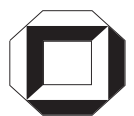


Stanislav Dogel

**Spectroscopic Ellipsometry of
Interfacial Phase Transitions in
Fluid Metallic Systems:
 $K_x(KCl)_{1-x}$ and $Ga_{1-x}Bi_x$**

ISBN 3-937300-08-2



universitätsverlag karlsruhe

Dissertation, Universität Karlsruhe (TH), 2004

Impressum

Universitätsverlag Karlsruhe
c/o Universitätsbibliothek
Straße am Forum 2
D-76131 Karlsruhe

www.uvka.de

Alle Rechte vorbehalten
© Universitätsverlag Karlsruhe 2004

ISBN 3-937300-08-2

Content:

Zusammenfassung /Abstract.....	1
1. Introduction.....	5
2. Interfacial phenomena.....	9
2.1 Classification of wetting transitions, surface freezing and interfacial instabilities.....	9
2.2 Theoretical concepts of the effective interfacial potential.....	12
2.3 Long and short-range interactions - thickness of wetting layer.....	12
2.4 Overview of experimental and theoretical results on K-KCl and Ga-Bi surface transition studies.....	13
3. Characterization of surfaces and interfaces by spectroscopic ellipsometry	19
3.1 Interaction of light with matter.....	19
• Dielectric function and complex index of refraction.....	19
• Drude and Lorentz-oscillator models.....	19
3.2 Spectroscopic ellipsometry.....	20
• Basic definitions and principal setup.....	21
• Rotating analyser ellipsometer (RA).....	22
• Phase modulation ellipsometry.....	23
3.3 Simple models of the optical interfacial characteristics.....	25
• 2 phase model.....	25
• 3 phase model.....	26
4. Experimental apparatus and measuring procedure.....	29
4.1 High temperature construction for K-KCl measurements.....	29
• Experimental setup.....	29
• Calibration of Ψ , Δ and R	32
• Sample preparation, ellipsometry and reflectivity measurements	33
4.2 UHV chamber for in-situ measurements of liquid Ga-Bi alloys.....	35
• Design of UHV chamber	35
• Crucible and sample preparation.....	37
• In-situ surface cleaning	38
• Alignment and calibration of ellipsometer	41
5. Data evaluation and error analysis.....	45
5.1 Errors in measured quantities.....	45

5.2 Errors in optical constants and film thickness.....	51
5.3 Sensitivity and limitations.....	52
6. Experimental results.....	55
6.1 Results of the measurements of potassium-rich K-KCl melts.....	55
6.2 Results of Ga _{1-x} Bi _x alloy measurements	67
• Optical properties of pure liquid Ga and Bi	67
• Ellipsometric data and wetting behaviour approaching liquid-liquid coexistence.....	72
• Oscillatory behaviour of liquid alloy.....	82
• Ellipsometric measurement of surface the freezing transition.....	86
7. Discussion.....	93
7.1 Wetting and prewetting transitions at the fluid-wall interface of K-KCl.....	93
• Ellipsometric evidence of the wetting transition.....	93
• Microscopic structure of the film.....	94
• Tetra point wetting.....	98
• Characterization of the prewetting transition.....	104
7.2 Wetting and surface freezing transitions at the fluid/vapour interface of Ga-Bi alloys.....	107
• Complete wetting transition at the liquid-liquid coexistence line.....	107
• Ellipsometric characterization of the surface freezing transition.....	111
7.3 Spinodal decomposition and oscillatory instability at a fluid metal interface...	113
Appendix.....	119
Manufacturer list.....	135
References.....	137
Acknowledgments.....	145
Curriculum Vitae.....	147
List of publications.....	149

Zusammenfassung

In der vorliegenden Arbeit wird über Untersuchungen der Grenzflächenphasenübergänge in fluiden Systemen mit kurzreichweitigen Wechselwirkungen berichtet. Von besonderem Interesse sind folgende Phasenübergänge: Vorbenetzung und vollständige Benetzung, das neuartige Phänomen des *surface freezing* und neue Beobachtung von oszillatorischen Instabilitäten an Grenzflächen, die durch spinodale Entmischung hervorgerufen sind. Diese Phänomene wurden an zwei Systemen mit flüssig-flüssig Mischungslücke für unterschiedliche Konfigurationen untersucht: beim System K_xKCl_{1-x} an der Film-Wand-Grenzfläche und beim System $Ga_{1-x}Bi_x$ an der Grenzfläche zum koexistierenden Dampf. Zur spektroskopischen Charakterisierung der Grenzflächeneigenschaften, vor allem der Zusammensetzung und der Dicke des Filmes, und deren Änderungen mit der Zeit, Temperatur (bis 1000 K) und Konzentration der Probe, wurde die Methode der Ellipsometrie (und Reflektometrie) in großem spektralen Bereich (UV-VIS) eingesetzt. Die Messungen von $Ga_{1-x}Bi_x$ erforderten eine Neuentwicklung einer UHV-Anlage mit *in-situ* Phasenmodulationellipsometer. Die K_xKCl_{1-x} Experimente wurden mit Hilfe eines vorhandenen Rotationellipsometers durchgeführt.

Die neuen Ergebnisse der optischen Spektren der *wetting* Filme und deren Dicken entlang der fest-flüssig Koexistenzlinie sowie in flüssiger homogener Phase (*prewetting*) im K_xKCl_{1-x} werden im ersten Teil dargestellt. Im Film lässt sich die für die flüssige salzreiche Volumenphase typische F-Bande nachweisen. Die Zusammensetzung des Filmes kann aus der Bandenintensität und Halbwertsbreite abgeschätzt werden und entspricht $x_{KCl} \sim 0.9$, d.h. etwa das Ende der salzreichen flüssig-flüssig Koexistenzlinie am eutektischen Punkt. Die Halbwertsbreiten der F-Bande sind gegenüber der Volumenphase stark reduziert. Als mögliche Ursache kann die Ausbildung einer geordneten Struktur in den Benetzungsfilmen an der Grenzfläche Schmelze-Saphir angesehen werden. Oberhalb der fest-flüssig Koexistenz nehmen die Dicken der *wetting* Filme ab bei konstanter Zusammensetzung mit steigender Temperatur als auch bei konstanter Temperatur mit abnehmender Salzkonzentration. Dies wird für vollständige Benetzung (*complete wetting*) erwartet. Die gemessenen Filmdicken entlang der fest-flüssig Koexistenzlinie bei Annäherung an den monotektischen Punkt liegen im Bereich zwischen 30 und 440 nm. Diese Ergebnisse entsprechen dem Szenario des *tetra point wetting*. Für eine quantitative Beschreibung wurden die Freie Exzess-Enthalpien des Systems berechnet. Für manche Konzentrationen wurden Hinweise auf den Vorbenetzungsübergang (*prewetting transition*) gefunden. Die Lage der *prewetting* Linie wurde im Vergleich zu früheren Publikationen korrigiert.

Im zweiten Teil werden die Ergebnisse des *complete wetting*, *surface freezing* und der oszillatorischen Instabilitäten in $\text{Ga}_{1-x}\text{Bi}_x$ Legierungen dargestellt. Hochpräzise Spektren konnten bei Annäherung an die flüssig-flüssig Mischungslücke von der homogenen flüssigen Phase mit sinkender Temperatur aufgenommen werden. Diese Spektren wurden im Rahmen eines 3-Phasen-Modells mit einem *Effective Medium* als Substrate und einem Bi-reichen Film beschrieben. Die Filmdicke von 30 \AA wurde für unsere spezifische Geometrie der Probe bei flüssig-flüssig Koexistenz gemessen. Mit den gemessenen Filmdicken und bekannter Informationen der freien Exzess-Enthalpien des Systems wurde das *effective interfacial* Potential berechnet. Messungen bei Abkühlung von der homogenen flüssigen Phase in das Zwei-Phasen-Gebiet unterhalb der monotektischen Temperatur sind im Einklang mit dem *tetra point wetting* Szenario im Ga-Bi System. In dieser Arbeit wurde die erste ellipsometrische Untersuchung des *surface freezing* durchgeführt. „Erstarrte“ Filme erscheinen bei den Temperaturen deutlich oberhalb der Liquidus-Temperatur und bestehen aus reinem kristallinen Wismut. Unter den für diese Arbeit typischen Bedingungen (nämlich thermischer Gradient von $\sim 3 \text{ K}$) wachsen die Filme rasant und erreichen schnell Dicken, die im Nanometer-Bereich liegen. In der Mischungslücke wurden für verschiedene Konzentrationen und Temperaturen Oszillationen der optischen Eigenschaften der Oberfläche beobachtet. Die Einzelheiten dieses Phänomens sind gegenwärtig nicht vollständig verstanden, deshalb wird nur die qualitative Beschreibung gegeben.

Abstract

The objective of the present work was to investigate the interfacial phase transitions in fluid systems with short-range intermetallic interactions. The phase transitions of interest include prewetting and complete wetting, the novel and rarely studied phenomena of surface freezing, and, finally, the very recent observation of interfacial oscillatory instability induced by spinodal decomposition. These phenomena were studied in two systems exhibiting a liquid-liquid miscibility gap at different interfacial configurations: at the fluid/wall interface in fluid K_xKCl_{1-x} and at the fluid/vacuum interface of the $Ga_{1-x}Bi_x$ alloys. To characterize the respective interfacial changes, the composition and thickness of the segregated ultra thin films and their evolution with time, the spectroscopic ellipsometry and partly reflectometry were performed over a wide spectral range (VIS-IR) as a function of composition and temperatures partly up to 1000 K. Whereas in the experiments on K_xKCl_{1-x} an existing home build rotating ellipsometer could be used to extend measurements on this system in more details, a completely new UHV-apparatus including the in-situ phase modulation ellipsometer had to be developed for the experiments on the $Ga_{1-x}Bi_x$ alloys.

In the first part on the system K_xKCl_{1-x} new results on the wetting film spectra and on the film thickness at solid-liquid coexistence as well as in the homogenous liquid phase (prewetting) are presented. The film spectra show the typical absorption of the liquid state F-center which clearly indicates that the film is a salt-rich phase. Using the parameters of the F-bands (intensity and halfwidth) the concentration of F-centers can be determined, and as a result the composition of the wetting film is estimated. It corresponds to $x_{KCl} \sim 0.9$, i.e. values at the salt-rich end of the liquid-liquid coexistence curve. A strong reduction of the halfwidth of the F-band in the film in comparison to the bulk salt-rich phase can be explained by the formation of an ordered structure at the fluid/wall interface. In the homogenous region above the solid-liquid line the film thickness decreases at constant composition with increasing temperature and at constant temperature with decreasing salt concentration in agreement with complete wetting. The wetting film thickness strongly increases approaching the monotectic temperature along the liquidus line from 30 to 440 nm. Results along the solid-liquid curve strongly support the tetra point wetting scenario. For this interpretation a quantitative description of the excess Gibbs energy of the system has been developed. At some concentrations qualitative indications for prewetting transitions in the metal-rich K_xKCl_{1-x} homogeneous phase have been obtained. In comparison to the previously published works the location of prewetting line should be corrected.

In the second part on the system $\text{Ga}_{1-x}\text{Bi}_x$ the results on complete wetting, surface freezing and oscillatory interfacial instabilities are presented. The high-precision spectra have been recorded approaching the liquid-liquid miscibility gap of this system with decreasing temperature from the homogeneous liquid phase. These spectra have been modeled using a Ga-Bi effective medium approximation for the substrate covered by a film of liquid Bi. As one reaches the demixing regime the film of our particular sample geometry has a thickness of approximately 30 Å. From these results and the known excess Gibbs energy of liquid Ga-Bi alloys the effective interfacial potential has been obtained. Continuous measurements on cooling from the homogeneous region below the monotectic temperature give evidence of tetra point wetting in the Ga-Bi system. First ellipsometric study of the surface freezing in Ga-Bi system has been performed. It is found that a frozen film forms well above the liquidus line and consists of pure crystalline bismuth. Under the present conditions of slight temperature inhomogeneities of ~3 K the film grows rapidly, reaching a thickness in the nanometer range. Within the miscibility gap in the broad range of concentrations and temperatures a very interesting effect of surface and bulk oscillatory instability was observed. The details of this process at present are not well understood, but a qualitative description is given.

1. Introduction

Surface and interfacial characteristics are a traditional topic of physics and physical chemistry. Numerous interfacial phenomena (adsorption, desorption, spreading, stability and wave motion of the interface, etc) are essential for many natural and technological processes. Open liquid surfaces or liquid in contact with a substrate (liquid, solid, vapour) are especially interesting because of their mobility. In recent years significant progress has been made in the study of phase transitions at fluid interfaces. This became possible due to a development of surface specific techniques (among them ellipsometry is on the leading place) and much of theoretical understanding. Particular fruitful in sorting out (but at the same time adding new) intricacies of interfacial phenomena, and how those are influenced by surface interactions has been the study of surfaces in contact with critical binary liquid mixtures. Systematic study of such phenomena was initially stimulated by the seminar paper of J. Cahn [Cahn77] (or Ebner and Saam [Ebner77]), who predicted the presence of the *wetting transition* in the two-phase region of a critical liquid mixture. Using experimental results of the nucleation study in the system methylcyclohexane-perfluoromethylcyclohexane, that showed failure of nucleation theory near the critical point of the system, Cahn developed his theory of *critical point wetting*. Any two phase mixture of fluids near their critical point exhibit the *wetting transition*: approaching some temperature T_w (*wetting temperature*) one of the critical phase completely wets the third phase and excludes contact with the other critical phase [Cahn77]. Interrelated with the wetting transition there is a *prewetting transition* (the terminology and details of the wetting transitions will be presented in Chapter 2.1).

For binary fluid systems there were a number of claims of the first order wetting transition (starting from publication by Moldover and Cahn [Moldover80]). But despite considerable efforts the prewetting transition remained to be observed experimentally. It was performed only decades later by Rutledge and Taborek [Taborek92] studying adsorption of helium on caesium substrate and one year later in the system methanol-cyclohexane – one of the oldest systems – in the study of the wetting transition by Kellay et al. [Kellay93]. Study of binary liquids revealed also a large number of experimental difficulties, mainly concerning the long equilibration time in these systems, this led to the consensus that the systems are in general very hard to study (see Kayser et al. [Kayser86a]). In one-component systems second order wetting transition [Vani83] and critical wetting [Ragil96] have been found.

Research has been focused mostly on non-metallic systems with long-range interactions. Systems powered by short-range interactions, for example screened Coulomb interactions, are

even today quite rare. Up to now the wetting transitions were found only in several binary metallic systems like Ga-Bi, Ga-Pb, Ga-Tl and in K-KCl - alkali-alkali halide molten salt solution. Latest achievements in the study of wetting related phenomena will be described in Chapter 2.4, concentrating on the systems K-KCl and Ga-Bi. So, in the following only a brief introduction and goal-settings will be given.

These two systems exhibit a miscibility gap [Johnson58], [Predel60] (see Fig. 6.1 and 6.2.5). Within this region, from the monotectic temperature, T_{mono} , up to the critical temperature, T_c , two liquid phases of different concentrations coexist. Below T_{mono} liquid coexists with solid phase. In both systems all temperatures and concentrations of interest are relatively easy accessible – particularly true for the Ga-Bi system. The vapour pressure of the liquid Ga-Bi alloys is relatively low, which enables one to study the fluid interface under UHV conditions. This is impossible in the case of K-KCl system – the vapour pressure of liquid potassium is above 1 atm at ~800...900 K [Borgstedt87] (typical temperature range of the experiments), so the sample requires a firmly tight sapphire cell which should also sustain corrosive alkali metal under these conditions (material choice and problems which it causes are discussed in Chapter 4.1).

There is one common advantage of both systems for an optical study – the optical properties of the components in Ga-Bi (Fig. 6.2.3 and 4) and K-KCl systems are very different. In the latter system in addition the salt-rich phase is identified by its F-center absorption (Fig. 6.1.1). This special optical feature of alkali halides, which is observed in solid as well as in liquid state (maximum of absorption is 2.1 and 1.3 eV, respectively), allows to discriminate a state of wetting film. The optical properties will be described in Chapters 6.1 and 6.2.

Ellipsometry, the experimental technique of this work, is a primary method in the field of wetting studies (Chapter 3.2). It is the most sensitive visible light optical method available for measurement of the thickness and optical properties of thin films. In some cases an information on composition and structure can be obtained. Modern ellipsometry is also very fast, allowing to study the processes *in-situ*. However, the interpretation of the ellipsometric signal can be very complicated because many effects, such as gradients of composition, surface roughness, different kinds of anisotropy of optical properties etc, contribute or influence the measurement [Azzam77]. Generally, to interpret ellipsometric results one requires a model of the interface. The generic models in ellipsometry are 2 and 3 phase models, when the former presents a substrate plus ambient and the latter a substrate with a film on it (Chapter 3.3). A correct choice of model for the interfaces is crucial in ellipsometry to obtain reliable optical properties and the thickness of the film.

The aim of the first part of this experimental work is to extend spectroscopic rotation ellipsometry and reflectivity) investigations of the wetting and prewetting transitions in the metal-rich K_xKCl_{1-x} solution at a sapphire interface. These studies were started in the thesis of Staroske [Staroske00]. Special emphasis in the present work is on the measurements along the solid-liquid coexistence line approaching T_{mono} (751 °C) and above this line in the homogeneous liquid region. The main objective is to characterize the wetting films in this system, their composition, thickness and optical properties. For this purpose the thermodynamic calculations of the Gibbs free energy of the metal-molten salt mixture were carried out. The results will be introduced within the *tetra point wetting scenario* [Dietrich97]. The discussion will concentrate on two particularly striking features of the wetting films in this system: their unusual thickness and peculiar microscopic structure.

The second part is dedicated to the Ga-Bi system. Here wetting, surface freezing and interfacial oscillatory instabilities of $Ga_{1-x}Bi_x$ alloys were studied at the fluid/vapour interface under UHV conditions by means of phase modulation ellipsometry. For this aim a new UHV-setup was designed and built. Special attention has been paid to the cleanness of the alloy surface therefore different techniques of in-situ cleaning had to be integrated in the setup. Contrary to the study of K_xKCl_{1-x} melts where only a few measurements at constant temperatures could be recorded for one concentration, the $Ga_{1-x}Bi_x$ alloys could be studied continuously on cooling or heating in the so-called *kinetic* measurements. However, they are more difficult to be interpreted quantitatively than spectroscopic ellipsometry data, but at the same time are very illustrative and informative to show the dynamics of the system.

Study of $Ga_{1-x}Bi_x$ alloys required a precise knowledge about the optical properties of both pure components – they were determined at the beginning of this study in a broad temperature and spectral range. This data was later used to build up the optical interfacial models.

The discussion will focus on the complete wetting observed in the homogeneous liquid region approaching the liquid-liquid line. Measured thickness of the wetting film will be presented as a function of Gibbs free energy. From this dependence the information about the effective interfacial potential is obtained. In the next part on the surface freezing transition the first results of the spectroscopic characterization of the frozen film will be described. Very unusual effect of the surface periodical instability observed for the first time in the Ga-Bi system is presented in the last part of discussion. A simple model to explain the observations will be offered and possible mechanisms that qualitatively account for the oscillatory behaviour will be discussed.

2. Interfacial phenomena

The phenomenon of the critical wetting transition predicted independently by J. Cahn [Cahn77] (and at the same time by Ebner and Saam [Ebner77]) has received great deal of attention. Over the last decades, tremendous progress has been made both in experimental studies and theoretical understanding. Numerous excellent reviews on the subject appeared, which include the following references: [Tarazona83], [deGennes85], [Sullivan86], [Dietrich88], [Schick90] and [Bonn01]. Between them the material is covered in great details.

2.1 Classification of wetting transitions, surface freezing and interfacial instabilities

Let's consider a liquid droplet on a solid (non-deformable) substrate as is depicted in Fig. 2.1a. Different *wetting states* (see Fig. 2a-c) can be defined with the help of the contact angle Θ - the angle between solid/liquid and liquid/vapour interfaces:

- a. $0^\circ \leq \Theta \leq 90^\circ$ - *partial wetting*: surface is only partially covered by liquid (but in general there is a microscopic adsorbed film around the droplet),
- b. $\Theta = 180^\circ$ - *complete drying*: liquid no longer “likes” a contact with substrate,
- c. $\Theta = 0^\circ$ - *complete wetting* - uniform liquid film covers solid surface.

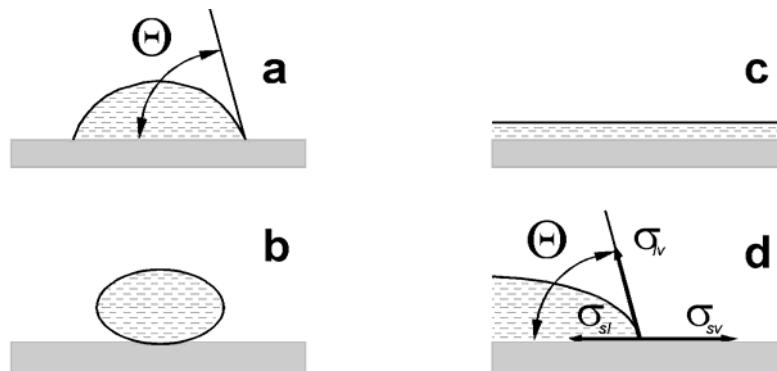


Fig. 2.1. Wetting of a liquid droplet on a solid substrate: (a) partial wetting, (b) complete drying, (c) complete wetting, (d) force balance at the three-phase contact line.

In the case of a partial wetting, the relation between the cosine of the contact angle and the surface tensions is given by the Young's equation (Eq. 2.1). This equation can be interpreted as a force balance for the line of three-phase contact and expresses the mechanical equilibrium at that line (Fig. 2.1d):

$$\sigma_{sv} = \sigma_{sl} + \sigma_{lv} \cos\Theta, \quad 2.1.$$

where σ_{ij} are the surface tensions between phases in contact.

Change of the thermodynamic variables (p, T, x_i) will alter the surface tensions (Eq. 2.1), hence the *wetting state* may be changed (Cahn's scaling argument [Cahn77]) and *wetting transition* might occur. The *wetting transition* is a transition between the partial and complete wetting. If the system is studied as a function of temperature, the transition temperature is called the wetting temperature – T_w .

The wetting transition is reflected in the evolution of the thickness of the wetting film. It can be assumed that the film thickness is directly proportional to the excess surface density Γ_i , defined as the excess density (n_i^s) of a component i per unit surface:

$$\Gamma_i = \frac{n_i^s}{A}, \quad n_s = N - n_b V, \quad 2.2.$$

where N is the total number of particles and n_b is the number of particles per unit volume in the bulk phase.

The classification of the different wetting transition will be given on the example of a binary system of two liquids α and β exhibiting a miscibility gap with an upper critical point T_c as shown in Fig. 2.2 (see also [Freyland98]). Let's consider the different paths of a change of the thermodynamic state on this schematic bulk phase diagram (Fig. 2.2):

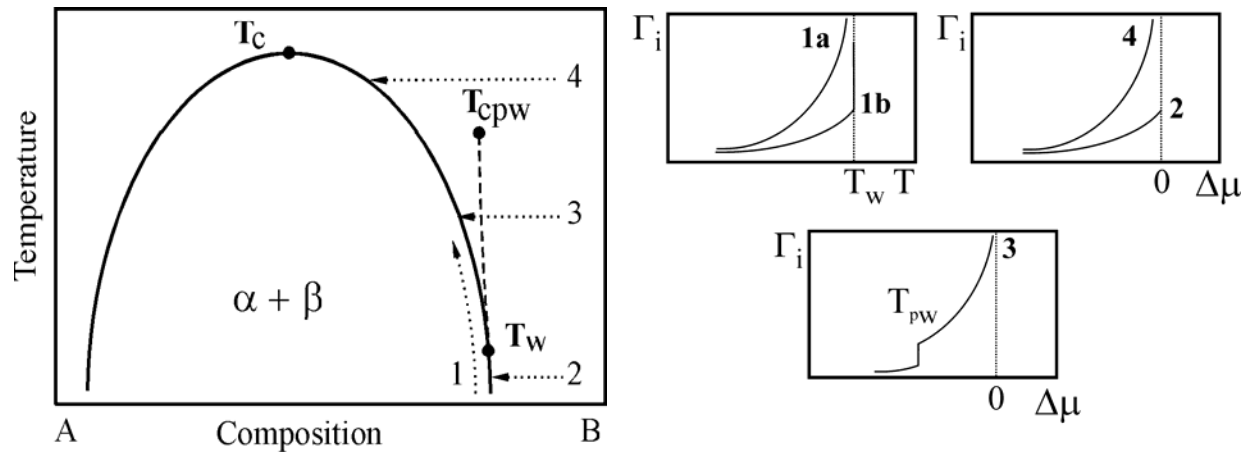


Fig. 2.2. Schematic phase diagram of binary system with miscibility gap (solid line). Prewetting (dashed) line starts at T_w and ends at T_{cpw} . Several paths of a change of the thermodynamic state are included: 1- behaviour of the surface excess density, Γ_i , along the coexistence curve approaching T_w : 1a and 1b – second and first order wetting transitions; 2,3,4 – Γ_i approaching coexistence: below T_w , $T_w < T < T_c$ and $T_{cpw} < T < T_c$ ($\Delta\mu$ is the chemical potential relative to that at coexistence, see p. 15).

1. On the *path Nr. 1* along the coexistence line two scenarios are possible:
 - a. Γ_i increases continuously for $T < T_w$ and diverges at T_w , this is called a ***critical wetting transition*** (second order), Fig. 2.2. (**1a** inset).
 - b. Γ_i is finite (low) for $T < T_w$ and diverges at T_w , this is a ***first order wetting transition***, Fig. 2.2. (**1b** inset).
2. Three possible paths have to be considered if coexistence is approached from the homogeneous phase region:
 - a. For $T < T_w$ (*Path Nr. 2* in Fig. 2.2), Γ_i possesses the microscopic values approaching the coexistence line (Gibbs adsorption), Fig. 2.2. (**2** inset).
 - b. $T > T_w$ (*Path Nr. 4* in Fig. 2.2), Γ_i diverges approaching coexistence line – this is the characteristic of ***complete wetting***, Fig. 2.2. (**4** inset).

The *Path Nr. 3* in Fig. 2.2 deserves special attention. Moving along this line at conditions off of coexistence the *thin-thick* transition occurs [Dietrich97]. The location of such transitions defines the ***prewetting line*** predicted by Cahn [Cahn77] and independently by Ebner and Saam [Ebner77]. The prewetting line starts on coexistence at T_w , moves away from it tangentially [Rowlinson82 and Hauge83] and ends at the critical prewetting point, T_{cpw} . The behaviour of the surface excess density on *path Nr. 3* is shown in Fig. 2.2. (**3** inset).

The film thickness at the prewetting transition, even though changing from the thin to the thick, remains finite. This is due to the fact that the film is thermodynamically unstable for conditions off of coexistence. The jump in Fig. 2.2 (**3** inset) gets larger as the prewetting line is crossed closer to coexistence. Above T_{cpw} the step disappears (but some “bump” still can be observed, not shown in Fig. 2.2. (**4** inset)).

Surface freezing and melting are peculiar types of wetting transitions (for a review see [Löwen94]). In the latter case the surface of the solid, at uniform temperature below the melting point of the bulk material, has a thin coating of its melt. A famous extensively studied example is ice, but the phenomena was also observed on molecular solids and first reported for metals [Dash89], [Pluis90]. In comparison with the surface melting, less experimental observations and theoretical studies are available so far for the surface freezing transition. Here an ordered solid-like surface film coexists with the bulk liquid at temperatures above the bulk freezing temperature. Among the best-studied examples are alkanes [Maeda00] and liquid crystals [Swanson89]. Very rare studies (only two examples are known up to now) of binary metal systems will be introduced in the following chapter.

Oscillatory instabilities in systems with an interface, like an open liquid surface or fluids with a multilayer configuration, are well described in the literature [Nepomnyashchy02],

[Miller85]. In general, interfacial oscillations and waves occur when a “perturbation switches on some compensating mechanism that tries to diminish this disturbance” (*negative feedback*). It is essential, that the stabilizing and destabilizing forces have different time scales leading to a certain, effective time delay [Nepomnyashchy02]. The well-known examples of such competing mechanisms are the thermocapillarity (Marangoni) effect and the Rayleigh-Bernard convection [Nepomnyashchy02].

2.2 Theoretical concepts of the effective interfacial potential

Only a brief introduction to this topic will be given in the following, for detailed treatment see [Dietrich88], [Schick90]. Considerable understanding of wetting phenomena was gained using the so-called van der Waals theory. In this theory attractive molecular interactions are treated in the mean-field approximation, so that one can define a grand canonical potential $\Omega(\rho(z);T,\mu)$. Minimizing Ω with respect to the density profile $\rho(z)$ one constructs the *effective interfacial potential* $\Omega^{\text{eff}}(d;T,\mu)$, where d is the wetting film thickness [Dietrich88]. For two coexisting phases α and β in contact with substrate γ , Ω^{eff} is given by:

$$\Omega^{\text{eff}}(d;T,\mu) = d\Delta\mu + \sigma_{\alpha\beta} + \sigma_{\alpha\gamma} + \omega(d) + \omega_g(d), \quad 2.3.$$

where $\Delta\mu$ is the difference in the chemical potentials relative to the coexistence line (see Fig. 2.2 and p. 15) and $\sigma_{\alpha\beta}$ and $\sigma_{\alpha\gamma}$ are the surface free energies (β is the nonwetting phase). The term $\omega(d)$ is the mean field correction to the surface energy, which arises from the fact that the wetting film has finite thickness d . $\omega_g(d)$ is the gravitational energy term equal to $g\Delta\rho Ld$ ($\Delta\rho$ is difference in mass densities of the coexisting phases, L is the height of nonwetting phase).

Knowing the type of interaction - long- or short-range forces (see next chapter) and minimizing $\Omega^{\text{eff}}(d;T,\mu)$ one can determine the equilibrium film thickness d_0 .

2.3 Long- and short-range interactions – thickness of wetting layer

To evaluate the equilibrium wetting film thickness the discussion must focus on the term $\omega(d)$, which essentially describes the interaction between film and substrate phase. First, the case of van der Waals forces will be considered. In this case the effective interfacial potential is given by [deGennes81]:

$$\Omega^{\text{eff}}(d;T,\mu) = d\Delta\mu + \sigma_{\alpha\beta} + \sigma_{\alpha\gamma} + \frac{A}{d^2} + g\Delta\rho Ld, \quad 2.4.$$

where A is the Hamaker constant [Israelachvili92]. After minimization of $\Omega^{\text{eff}}(d;T,\mu)$ it is straightforward to obtain the equilibrium thickness of wetting film, from Eq. 2.4:

$$d_0 = \left(\frac{2H}{g\Delta\rho L + \Delta\mu} \right)^{\frac{1}{3}}. \quad 2.5.$$

In the case of exponentially decaying short-range interactions, assuming the same strengths and screening lengths, λ^{-1} , of both liquid-liquid and film-substrate potentials, the term $\omega(d)$ can be approximated by $\omega(d)=\sigma_0\exp(-\lambda d)$ [Widom78]. The equilibrium film thickness after minimization of Eq. 2.4, is given by [Pandit82]:

$$d_0 = \frac{1}{\lambda} \ln \left(\frac{\lambda\sigma_0}{g\Delta\rho L + \Delta\mu} \right). \quad 2.6.$$

In certain experimental situations the gravitational term is very small and can be neglected. It has to be pointed out that the thickness of the wetting film measured in an experiment can be influenced by a number of other factors [Kayser86a] not included in Eq. 2.5 and 2.6. Examples are: diffusion and convection in liquid phases, electric charging of the substrate. The heat transfer through the sample can control the rate of approach to an equilibrium. These effects will be discussed to some extent in Chapter 7.

2.4 Overview of experimental and theoretical studies of surface phase transitions in K-KCl and Ga-Bi systems

This chapter summarizes a part of previous work on surface phase transitions in K-KCl and Ga-Bi fluid metallic mixtures. Studies of our lab are highlighted in Ref. [Dogel03], [Turchanin02], [Freyland03], [Tsekov03].

• Wetting and prewetting transitions in a metal-molten salt, K_xKCl_{1-x} , solution

First indication of a wetting transition at the fluid/wall (sapphire) interface in metal-rich K_xKCl_{1-x} melts has been obtained by reflectivity measurements [Nattland88a]. On heating the melts along the solid-liquid coexistence line a discontinuous change in the reflectivity was detected near $x_{KCl}\approx 0.01$ and $T_W\approx 500$ °C. The optical constants at the melt/sapphire interface exhibit a clear change once the wetting transition at coexistence is passed. This was confirmed later by ellipsometry [Juchem90] and SHG [Tostmann96].

In an effort to understand the nature of this wetting transition a detailed SHG investigation of this system has been performed. SHG is a very surface specific (resolution of several monolayers) nonlinear optical method. The SH-signal is determined by the nonlinear susceptibility and is strong for metals but small for a molten salt or salt-rich solutions. Using SHG several sections of the phase diagram were probed along different paths [Tostmann96]. The SH-intensities exhibited two maxima on heating from the two-phase region into the

homogeneous liquid phase region. The first maximum near 500 °C was found to be independent of composition and strongly connected with the wetting transition [Tostmann96] whereas the second was shifting with higher salt concentrations to higher temperatures. The appearance of the second maximum was explained in the following way. The wetting salt-rich film, which segregates at 500 °C, is characterized by localized electron defects like F-center. (In the crystalline solid, the F-center - from German “Farbzentrum“ - is a localized electronic state – the excess electron trapped in an anion vacancy. The evidence of the existence of F-center like species in liquid state alkali halides has been found by Freyland et al. [Freyland84]. They were studied extensively experimentally by ESR [Nicoloso83], NMR [Warren84] and optical absorption [Nattland93], as well as theoretically by computer simulations [Parrinello84], [Selloni87] and [Koslowski97]). These defects have high polarizability and strong optical excitations in the visible range. With rising temperature the concentration of these defects increases [Freyland99]. Hence the SH-intensity rises approaching second maximum. The decrease of the SH-signal beyond the second maximum has been explained by a reduction of the concentration of the electronic defects. This corresponds to a transition from high to low adsorption of the salt-rich phase at the interface with increasing temperature, which is a signature of the prewetting transition. So, the positions of the second maximum reflect the location of the prewetting line.

Later results of spectroscopic ellipsometry combined with reflectometry measurements strongly supported this interpretation [Staroske00]. Experiments have been carried out at conditions along the coexistence line and off of coexistence on the metal-rich side of the bulk phase diagram. Analysis of the liquid F-center absorption spectra gave valuable insight into the nature, composition and structure of the wetting films. The composition has been determined from the absorption coefficients of the F-center band, and corresponds to ~90 mole % of salt. The excitation energy of the F-bands at 1.3 eV clearly indicated the liquid nature of the wetting films [Nattland93], [Blankenhagen99].

The occurrence of the liquid F-center-like states up to 200 K below the monotectic temperature (see Fig. 6.1) gave evidence of a strong undercooling of the wetting films with respect to the bulk phase. Reduction of the F-band halfwidth was related to a charge ordering at the sapphire interface and strong charging interactions, which obviously play an important role for the unusually thick wetting films in K_xKCl_{1-x} system [Staroske01]. Strong increase of the wetting film thickness from 30 nm at 530 °C up to 300 nm at 720 °C [Staroske01], approaching monotectic temperature of 751 °C, has been described by the *tetra point wetting scenario* for binary fluids [Dietrich97].

• Tetra point wetting scenario

The *tetra point wetting scenario* was introduced by Dietrich and Schick [Dietrich97] for the interpretation of the wetting phenomena in binary fluid systems exhibiting a liquid-liquid miscibility gap in the bulk liquid phase. Four-phase coexistence (solid-liquid₁-liquid₂-vapour) in a two-component system is considered by analogy with the *triple point wetting* in a one-component system [Pandit83]. The idea can be explained with the help of the schematic phase diagram shown in Fig. 2.3. The true first-order wetting transition is located at T_W on the metastable extension of the liquid-liquid demixing line into the solid-liquid region.

As was already shown above, a prewetting line extends tangentially into the homogeneous phase and ends at the prewetting critical point T_{cpw} (see also Fig. 2.2). Since the extrapolated liquid-liquid line lies in the solid-liquid phase region, the prewetting line eventually breaks through the equilibrium coexistence curve at some temperature T_W' . This is the temperature where the wetting film can be observed for the first time on heating the system along the coexistence (usual experimental path). Therefore, all data points between the prewetting and coexistence line correspond to prewetting states. They are off of coexistence with respect to the metastable extensions of the liquid-liquid region.

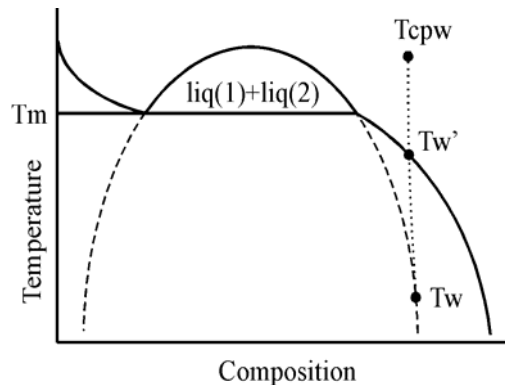


Fig. 2.3 Schematic representation of a binary phase diagram with a miscibility gap. Solid lines: equilibrium phase lines. Dashed lines: metastable extensions of the liquid-liquid demixing binodals. Dotted line: prewetting line. T_m , T_W and T_W' refer to monotectic and wetting temperatures and the intersection of the prewetting line and solid-liquid phase line of bulk diagram, respectively. T_{cpw} designates the critical prewetting end point.

Thus approaching the monotectic point along coexistence above T_W' corresponds to the path which probes the *complete wetting* (similar to *path Nr. 4* Fig. 2.2). On such approach the distance $\Delta\mu = \mu_{sl} - \mu_{112}$ continuously decreases between T_W' and T_{mono} . Here μ_{sl} is the chemical potential of the wetting phase at the solid-liquid coexistence line and μ_{112} is its value at the metastable extension of the liquid-liquid demixing line [Dietrich97]. As a consequence the film thickness should increase with increasing temperature and finally diverge at T_{mono} .

Studying the functional dependence of the film thickness on $\Delta\mu$ ($d \propto \ln(1/\Delta\mu)$ or $d \propto (\Delta\mu)^{-1/3}$) one could distinguish between screened Coulomb and algebraically decaying van der Waals type interactions (see subsection 2.3 above).

• **Wetting, prewetting and surface freezing transitions in Ga-Bi alloys**

Following the observation of Perepezko et al. [Perepezko82] of an unusual segregation of a macroscopic Bi phase encapsulating a Ga rich core in undercooled Ga-Bi droplets, the first attempt to study this wetting phenomenon spectroscopically was done by means of ellipsometry [Nattland95, 96, 98]. The data clearly indicated a tetra point wetting transition approaching the monotectic temperature. The film thickness at $T_m=495$ K was estimated to be 50 Å with an error on account of experimental limitations of about 50 %.

Several X-ray reflectivity and grazing incidence diffraction measurements have been performed in Ga-rich alloys to study the microscopic structure of the liquid/vapour interface [Flom93], [Lei96], [Tostmann00]. From these data it was concluded that a complete monolayer of the low tension Bi-component segregates at the interface. Furthermore, it was found that the structure of this monolayer is like that of supercooled bulk liquid Bi. Above the monotectic temperature, T_m , Bi film grew up to 30 Å [Tostmann00]. In the very recently experiments of Huber et al. [Huber02, 03] the variation of the thickness of the wetting layer was studied along several phase boundaries on heating of a $\text{Ga}_{0.88}\text{Bi}_{0.12}$ liquid alloy and in the homogeneous phase region. The film grew up to 50 Å at approaching T_m along the solid-liquid coexistence line, stayed almost constant along the liquid-liquid line and disappeared moving off this line. The logarithmic $\Delta\mu$ -dependence of the wetting film's thickness allowed to obtain the short-range surface potential [Huber02]. A log-dependence was also found in a similar metallic system of Ga-Pb alloys. From Auger spectroscopy Chatain and Wynblatt [Chatain96] deduced that the growth of the wetting film thickness is proportional to $\ln(\Delta\mu^{-1})$. Analysing their surface energy measurements of the interface composition profile by a layering model [Wynblatt98] these authors concluded that complete wetting extends deep into the metastable regime of liquid-liquid coexistence [Serre98]. The wetting transition temperature in the Ga-Pb system was estimated to be well below 300 K. All these experimental evidences are consistent with the *tetra point wetting scenario*.

Knowledge of surface freezing phenomena in metallic systems is rather poor. The only two systems where it has been very recently observed are so far dilute Ga-Pb [Yang99] and Ga-Bi alloys. Surface freezing in Ga-Bi has been studied by SHG and plasma generation [Turchanin02] as well as by surface light scattering [Freyland03] for compositions between

the eutectic and monotectic points. In this composition range the formation of the solid-like films was observed at surface freezing temperatures T_{SF} clearly above the solid-liquid coexistence line. An important observation was the pronounced hysteresis on melting of these films, which indicates that the transition is of first order. The lines of surface freezing and respective melting temperatures merge the bulk liquidus curve approaching the monotectic point (Fig. 2.4) [Turchanin02]. Results of the light scattering measurements are in qualitative agreement with SHG-results. Approaching the surface freezing transition from above a discontinuous change in the slope of $\sigma(T)$ was detected, i.e. the surface entropy, $-\partial\sigma/\partial T$, jumps. This is an indication of a structural transition from liquid-like to ordered surface [Freyland03]. The light scattering experiments allowed also a first experimental observation of the prewetting transition in Ga-Bi alloys [Freyland03].

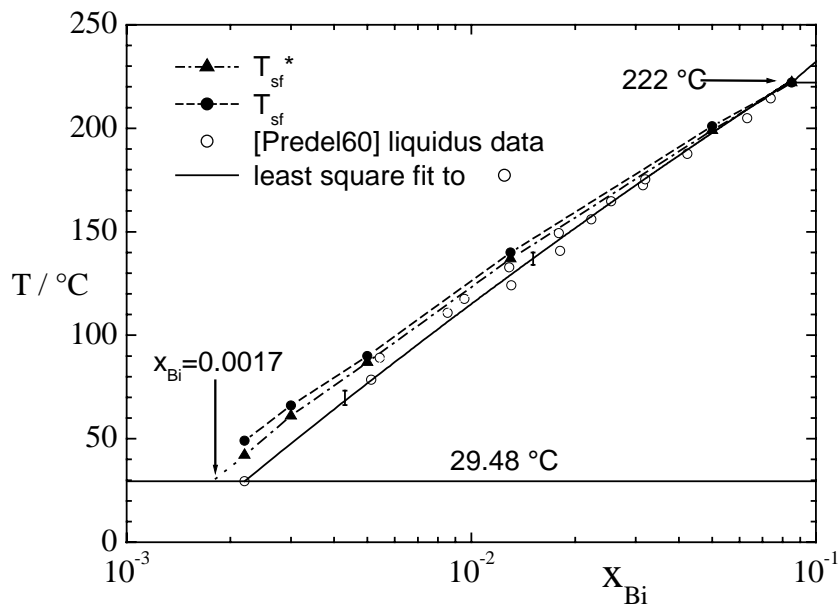


Fig. 2.4 Surface freezing (T_{sf}^* , \blacktriangle) and melting (T_{sf} , \bullet) lines detected by SHG on heating and cooling, Ga-rich side of bulk phase diagram. Solid line (liquidus curve) with error bars shows least square fit to experimental points of Predel [Predel60].

Although the surface freezing transition has been characterized by different experimental techniques, no information exists on the thickness of these solid-like films and their variation with T and concentration. The experimental observations of wetting, prewetting and surface freezing are supported by theoretical calculations of Tsekov and Freyland [Tsekov03]. Thermodynamic model calculations, which were performed, describe in particular the thickness of the films as a function of thermodynamic variables. The calculated dependence of the liquid film thickness predicts quantitatively adsorption and complete wetting transition. As a final result a complete diagram of the surface liquid-solid phase transitions on the vapour/liquid Ga-Bi interface was derived [Tsekov03].

3. Characterization of surfaces and interfaces by spectroscopic ellipsometry

3.1 Interaction of light with matter

Electromagnetic waves and polarized light are treated in depth in the following textbooks: [Gunter90], [Born91]. Here only some salient features, which will be used later and which are directly related to the ellipsometry and reflectivity measurements, will be reviewed.

• Dielectric function

If a material is exposed to a harmonic electromagnetic wave and the field strength, $E(\omega)$, is not large, a linear relation between the applied field and the material's response holds:

$$P(\omega) = \chi \epsilon_0 E(\omega). \quad 3.1$$

The proportionality constant χ is called *dielectric susceptibility*. To describe the internal field the *electric displacement* (D) is used:

$$D(\omega) = \epsilon_0 E(\omega) + P(\omega) = (1 + \chi(\omega)) \epsilon_0 E(\omega). \quad 3.2$$

The *dielectric constant (or function)*, which describes the optical properties of media, is then defined from Eq. 3.2 as:

$$\epsilon(\omega) = 1 + \chi(\omega) = \epsilon_1(\omega) + i\epsilon_2(\omega), \quad 3.3$$

where ϵ_1 and ϵ_2 are real and imaginary parts of the dielectric function, ϵ .

• Complex index of refraction

Another way to describe the interaction of light with a material is the *complex index of refraction*, N , connected with the dielectric function by:

$$N = \sqrt{\epsilon} = n + ik, \quad 3.4$$

where n is the *index of refraction* and k the *extinction coefficient* of the medium. Combining equations 3.3 and 3.4 one can obtain following relationships:

$$\epsilon_1 = n^2 - k^2; \quad \epsilon_2 = 2nk. \quad 3.5$$

And correspondingly, relations for n and k are:

$$n = \sqrt{\frac{1}{2}(\sqrt{\epsilon_1^2 + \epsilon_2^2} + \epsilon_1)}; \quad k = \sqrt{\frac{1}{2}(\sqrt{\epsilon_1^2 + \epsilon_2^2} - \epsilon_1)}. \quad 3.6$$

• Drude and Lorentz-oscillator models

The optical properties (ϵ) of a material are frequency dependent – this effect is called *dispersion*. To explain the origin of material dispersion one needs to consider the interaction

between the electrical component of the incident electromagnetic wave and the electrons in the material. If the electrons of mass m are free the equation of motion in a simple classical description is:

$$\frac{\partial^2 x}{\partial t^2} + \gamma_D \frac{\partial x}{\partial t} = \frac{eE}{m}. \quad 3.7$$

Coordinate x can be replaced by the polarisation, $P = Nex$ (N is number density of electrons per unit volume) and using Eq. 3.1 and 3.3, Eq. 3.7 can be solved to obtain $\varepsilon(\omega)$:

$$\varepsilon(\omega) = 1 + \frac{\omega_p^2}{-\omega^2 + i\gamma\omega}; \quad \omega_p^2 = \frac{Ne^2}{\varepsilon_0 m}; \quad \gamma_D = \frac{\omega_p^2 \varepsilon_0}{\sigma_{DC}}. \quad 3.8$$

This result is the Drude free electron model, which describes conduction electrons in metals. The dielectric function is presented in terms of two parameters only: plasma frequency ω_p and damping frequency γ_D (σ_{DC} is dc conductivity). For the real and imaginary parts of the dielectric function, one can obtain the following expressions:

$$\varepsilon_1 = 1 - \frac{\omega_p^2}{\omega^2 + \gamma_D^2}; \quad \varepsilon_2 = \frac{\gamma_D}{\omega} \cdot \frac{\omega_p^2}{\omega^2 + \gamma_D^2}. \quad 3.9$$

In the classical Lorentz-oscillator model the essential modification is that the electrons are now bound to the positive charges (this is taken into account by a restoring force). The corresponding term ($\omega_0 x$) has to be added to the left side of Eq. 3.7. Solutions for both parts of the dielectric function are:

$$\varepsilon_1 = \varepsilon_\infty + \frac{\omega_p^2(\omega_0^2 - \omega^2)}{(\omega_0^2 - \omega^2)^2 + \gamma_D^2 \omega^2}; \quad \varepsilon_2 = \frac{\omega_p^2 \gamma_D \omega}{(\omega_0^2 - \omega^2)^2 + \gamma_D^2 \omega^2}. \quad 3.10$$

The definitions in Eq. 3.10 are the same as in Eq. 3.8. Epsilon infinity (ε_∞) takes into account all contributions from different sources like: valence electrons, lattice vibrations etc (for details see [Grosse79]). $\hbar\omega_0$ describes the binding energy of the electron.

3.2 Spectroscopic ellipsometry

Ellipsometry is a very sensitive optical technique for a characterization of the optical properties of surfaces and thin films. It is based on the measurement of the change in the polarization state of light after an interaction (in most cases reflection, but transmission mode is also applicable) with the sample. A detailed review of ellipsometry can be found in the book – “Ellipsometry and Polarized Light” written by Azzam and Bashara [Azzam77]. Ellipsometry is very attractive technique because of several reasons: it has an outstanding sensitivity to any minute interfacial changes, is essentially non-invasive and hence it can be

used for *in-situ* measurements and to obtain not just optical properties but also the thickness of thin films. Ellipsometry measurements can be performed under multiple angles of incidence (MAI) or/and at different wavelengths – *spectroscopic ellipsometry* (SE).

• **Basic definitions**

Incident and reflected (and transmitted) waves can be presented in terms of p and s components; p lies parallel to the plane of incidence (this plane contains both incident and reflected waves) and s is perpendicular to it. The reflected wave is connected with the incident wave through the reflection coefficients for both polarizations (Fresnel complex amplitude reflection coefficients [Guenther90]):

$$r_p = \frac{E_{rp}}{E_{ip}}; \quad r_s = \frac{E_{rs}}{E_{is}}, \quad 3.11$$

where “r” stands for reflected, “i” for incident wave.

If linearly polarized light is reflected from a surface, p and s components undergo, in general, different changes in the amplitude and phase – the reflected wave is elliptically polarized. The change of polarization upon reflection can be determined as a ratio of the complex Fresnel coefficients Eq. 3.11:

$$\rho = \frac{r_p}{r_s} = \frac{|r_p|}{|r_s|} e^{i(\delta_p - \delta_s)}, \quad 3.12$$

where $|r|$ is the ratio of the amplitude of reflected to the incident waves, δ gives the phase shift upon reflection, $\delta = \delta_{\text{refl}} - \delta_{\text{inc}}$. The ratio ρ is the quantity measured by ellipsometry. More precisely, two angles Ψ and Δ are measured: Ψ - the angle whose tangent is the ratio of the magnitudes of the reflection coefficients and Δ - the change in the phase differences that occurs upon reflection. From Eq. 3.12:

$$\tan\Psi = \frac{|r_p|}{|r_s|}, \quad \Delta = \delta_p - \delta_s. \quad 3.13$$

The *fundamental equation of ellipsometry* is then:

$$\rho = \tan\Psi e^{i\Delta}. \quad 3.14$$

• **Principle setup**

In Fig. 3.2.1 one can see a schematic diagram of an ellipsometer [Hauge80]. Collimated beam from a monochromatic source passes through a polarizer, which defines the polarization state of the incident light. Polarized light is then reflected from the sample and after passing the

analyser (another polarizer) is detected by a suitable detector. That is how, in principal, the null ellipsometer – the very first ellipsometry instrument – looked like. The null ellipsometer, which was driven manually, is replaced nowadays by the automatic modulation instruments.

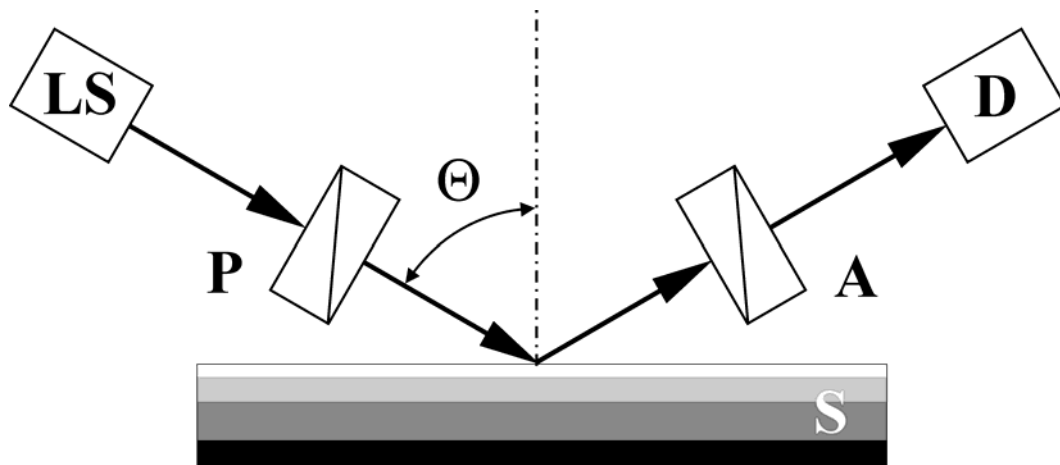


Fig. 3.2.1 Basic optical train of an ellipsometer: light source (LS), polarizer (P), sample (S), analyser (A) and detector (D). Θ is an incidence angle.

Measurements of the ellipsometric angles Ψ and Δ became more precise and much quicker. Review on the progress made in this field can be found again in [Azzam77].

In the present work two types of ellipsometry have been used: rotating analyser (RA) and phase modulation ellipsometry (PM), reviews of these types can be found in [Azzam77], [Aspnes75a], [Stobie75], [Jasperson69], [Drevillon82].

• Rotating analyser ellipsometer (RA)

For the RA [Aspnes75a] the arrangement of the optical elements is the same as for a null ellipsometer, and there is in addition a rotating polarizer placed before or after (makes practically no difference) the reflecting surface. In the following the system $PSA_{rot}A$ (**P**olarizer-**S**ample-**r**otating-**A**nalysers-**A**nalysers) will be described. This type of ellipsometer in a double-modulation configuration was introduced by Stobie *et al.* in 1975 [Stobie75]. The intensity of light on the detector after described above ellipsometer train can be written as a Fourier series [Stobie75]:

$$I = I_0 [a_0 + a_2 \cos(2\omega t) + b_2 \sin(2\omega t) + a_4 \cos(4\omega t) + b_4 \sin(4\omega t)]. \quad 3.15$$

Coefficients a_2 , b_2 , a_4 , b_4 are directly related to the ellipsometry angles [Stobie75]. To obtain these coefficients the signal on the detector is digitised and then Fourier transformation is applied. The novelty of this method was that it did not require signal-amplitude measurement (a_0 is not used!).

The RA instruments have one principal problem – the so-called *cos-problem*. They are limited to the detection of the quantities proportional to $\cos\Delta$ (and $\tan\Psi$). As a result, the experimental uncertainty increases dramatically when $\cos\Delta$ becomes unity, i.e. $\Delta < 20^\circ$ or $\Delta > 160^\circ$. Another problem of Δ measurement rises from the property of the cosine function: the sign of Δ cannot be unambiguously determined. This problem can be solved if additional optical element – quarter-wave plate is introduced into the optical train [Collins90].

To reduce the negative effect of the imperfections of the optical components (some optical defects, slight misalignment etc.) on the ellipsometric angles, the *zone-averaging* procedure [Azzam77] is normally performed. Ellipsometric angles are measured for different positions (*zones* – normally two or four) of polarizer and analyser and then averaged.

Present RA setup was used for high temperature measurements of K-KCl melts (Chapter 4.1). Due to the experimental limitation imposed by the construction of the sapphire cell, the spectroscopic ellipsometry measurements were possible only under single angle of incidence. In this way the dielectrical function and film thickness are difficult to define reliably. Therefore, an additional source of information was required, such as, for example, reflectivity measurements under normal angle of incidence. The reflectance, R , is defined as the ratio of the reflected light intensity to the intensity of the incident beam:

$$R = r^2 = \frac{|E_r|^2}{|E_i|^2}. \quad 3.16$$

Experimental details of the reflectometer construction are presented in Chapter 4.1.

• Phase modulation ellipsometry (PM)

PM ellipsometry is a relatively new technique and it is of interest to describe it in somewhat more detail than the previous one. The PM type of ellipsometer was first introduced by Jaspersen and Schnatterly in 1969 [Jaspersen69]. The ellipsometric angles are obtained by modulating the polarization state (phase) of the transmitted beam to produce the time-dependent intensity (same strategy as for RA). This is Fourier transformed or otherwise decoded to obtain the polarization change which occurred upon reflection.

The “heart” of the ellipsometer of this type is the *photoelastic modulator*. It consists of a rectangular fused silica block cemented to a piezoelectric quartz crystal oscillating at frequency of 50 kHz. An uniaxial sinusoidal standing strain wave is established in the block and induces a time varying birefringence. This in turn generates a periodic phase shift $\delta(t)$ between orthogonal amplitude components in the beam passing through the silica. The relative phase shift has the form:

$$\delta(t) = A_m \sin \omega t, \quad 3.17$$

where ω is the resonant angular frequency of the modulator unit and A_m the modulation amplitude. A_m is proportional to the excitation voltage applied to the crystal and to the wavelength of the light.

The theoretical expression of the intensity of a monochromatic light emerging from the sequence of polarizer(P)-sample-modulator(M)-analyser(A) takes general form [Drevillon82]:

$$I(t) = I_0 + I_S \sin \delta(t) + I_C \cos \delta(t), \quad 3.18$$

where the coefficients I_0 , I_S and I_C of the signal are related to the ellipsometric angles in the following way:

$$\begin{aligned} I_0 &= \frac{r_p^2 + r_s^2}{4} (1 - \cos 2A \cos 2\Psi), \\ I_S &= \frac{r_p^2 + r_s^2}{4} (\sin 2A \sin 2\Psi \sin \Delta), \\ I_C &= \frac{r_p^2 + r_s^2}{4} (\sin 2M (\cos 2\Psi - \cos 2A) + \cos 2M \sin 2A \sin 2\Psi \cos \Delta). \end{aligned} \quad 3.19$$

For simplification the equations 3.19 are given for the practical configuration of modulator and polarizer angle: $M-P=45^\circ$. In the instrument, the polarizer and modulator are connected together to increase the angular precision of their position in respect to one another and reduce the number of motors controlling their positions.

The Fourier expansions of $\sin \delta(t)$ and $\cos \delta(t)$ are:

$$\begin{aligned} \sin \delta(t) &= 2 \sum_{m=0}^{\infty} J_{2m+1}(A) \sin(2m+1)\omega t, \\ \cos \delta(t) &= J_0(A) + 2 \sum_{m=0}^{\infty} J_{2m}(A) \cos(2m)\omega t, \end{aligned} \quad 3.20$$

where $J_\nu(A)$ are Bessel functions of argument A and order ν . The ellipsometric angles Ψ and Δ can be extracted from the measurement of the ratio R_ω (*fundamental*) and $R_{2\omega}$ (*second harmonic*) to the dc component:

$$\begin{aligned} R_\omega &= \frac{2J_1(A)I_s}{I_0 + J_0(A)I_c}, \\ R_{2\omega} &= \frac{2J_2(A)I_s}{I_0 + J_0(A)I_c}. \end{aligned} \quad 3.21$$

Those expressions are simplified by adjusting A so that $J_0(A)$ is equal to 0 and by convenient orientations of the optical elements with respect to the incidence plane ($I_0 = 0$, see Eq. 3.19).

Two practical measurement configurations are retained:

a. Configuration I: $M-P=45^\circ$, $M=0^\circ$ and $A=45^\circ$

$$\begin{aligned} I_0 &= 0, \\ R_\omega &= 2J_1(A) \sin 2\Psi \sin \Delta, \\ R_{2\omega} &= 2J_2(A) \sin 2\Psi \cos \Delta. \end{aligned} \quad 3.22$$

b. Configuration II: M-P=45°, M=45° and A=45°

$$\begin{aligned} I_0 &= 0, \\ R_\omega &= 2J_1(A)\sin 2\Psi \sin \Delta, \\ R_{2\omega} &= 2J_2(A)\cos 2\Psi. \end{aligned} \tag{3.23}$$

Comparison of *both* presented ellipsometry techniques can be made at the end of this chapter:

- a. Because the rotation frequency of the analyser in RA is in the 50 to 100 Hz range, the time resolution, which provides an acceptable precision, is limited to several seconds. The PM technique with modulation frequency of 50 kHz allows to make single measurements in microseconds, which is particularly important for in-situ studies. But it also enables to acquire higher resolution spectroscopic data in a short time.
- b. RA instruments cannot measure ellipsometric angles for all materials (see above – “cos Δ -problem”) and define the sign of Δ . Introduction of quarter-wave plate solves the problem but increases a time for data acquisition and introduces certain error. PM is completely free from such uncertainty in Δ and allows an accurate and quick measurement of Δ , no matter what its value is.

3.3 Simple models of the optical interfacial characteristics

In the ellipsometric angles Ψ and Δ , all optical interfacial characteristics of the sample are hidden: optical constants $\varepsilon(\omega)$ of the film(s) and substrate as well as thickness of film(s). How to extract them from the experimental data will depend on the interfacial configuration (optical model) and also on the correctness of its application to the real experimental situation. The choice of the correct model is a crucial point in the interpretation of the ellipsometric data.

Two models are essential for the analysis of ellipsometric measurements: bare substrate – 2 *phase model* and substrate with a film – 3 *phase model*. All phases in both models are treated as homogeneous, optically isotropic, with ideally plane boundaries. For a detailed presentation of this topic see Ref. [Azzam77].

• 2 phase model

The two-phase model represents two semi-infinite media in contact: substrate (medium “1”) and ambient (medium “0”). The wave incident from medium “0” gives rise to a reflected wave in the same medium and a refracted wave in medium “1”. The amplitude and polarization of the reflected and transmitted wave can be determined, for a given amplitude and polarization of the incident wave, from the solution of Maxwell’s equations taking into

account the continuity of the tangential components of the electric (E) and magnetic (H) vectors across the interface. Finally, the equation connecting ρ (or Ψ , Δ) and the substrate dielectric function is [Azzam77]:

$$\varepsilon = N_1^2 = n_0^2 \sin^2 \Theta_0 \left[1 + \frac{(1-\rho)^2}{(1+\rho)^2} \tan^2 \Theta_0 \right]. \quad 3.24$$

This equation applies then medium “0” is perfectly transparent ($k_0=0$). The real and imaginary parts of the complex dielectric function can be found inserting the definition of ρ (Eq. 3.24) in the equation above:

$$\varepsilon_1 = n_0^2 \sin^2 \Theta_0 \left(1 + \frac{(1 - \tan^2 \Psi)^2 - 4 \tan^2 \Psi \sin^2 \Delta}{(1 + 2 \tan \Psi \cos \Delta + \tan^2 \Psi)^2} \tan^2 \Theta_0 \right), \quad 3.25$$

$$\varepsilon_2 = n_0^2 \sin^2 \Theta_0 \left(\frac{4 \tan \Psi \sin \Delta (1 - \tan^2 \Psi)}{(1 + 2 \tan \Psi \cos \Delta + \tan^2 \Psi)^2} \tan^2 \Theta_0 \right). \quad 3.26$$

An important point is, that the optical properties of unknown substrate can be directly found from the measured ellipsometric angles, i.e. from the analytical solution of Eq. 3.24.

• 3 phase model

This is the case of considerable importance in ellipsometry. As shown in Fig 3.3.1, there is a film of thickness d sandwiched between ambient and substrate. The transition between them is discontinuous and approximated as a step function. To define the model one needs to relate the complex amplitude of the resultant wave after reflection to the amplitude of the incident linearly polarized light wave. The procedure to be followed (originally due to Airy) is the summation of parallel partial waves, originating from multiple reflection inside the film and refraction into media “0” and “2” [Azzam77]. The total reflected amplitude can be written as an infinite geometric series:

$$R = r_{01} + t_{01} t_{10} r_{12} e^{-2i\beta} + t_{01} t_{10} r_{10} r_{12}^2 e^{-4i\beta} + \dots + \dots, \quad 3.27$$

where r and t Fresnel reflection and transmission coefficients, respectively.

The relation between the quantity measured by ellipsometry, the ratio ρ , and the reflection coefficients for the ambient-film-substrate system can be obtained as [Azzam77]:

$$\rho = \frac{r_p}{r_s} = \tan \Psi e^{i\Delta} = \frac{r_{01p} + r_{12p} e^{-2i\beta}}{1 + r_{01p} r_{12p} e^{-2i\beta}} \times \frac{1 + r_{01s} r_{12s} e^{-2i\beta}}{r_{01s} + r_{12s} e^{-2i\beta}}, \quad 3.28$$

where phase angle β (*film phase thickness*) – the phase change, which the multiply reflected wave experiences as it bounces between the film boundaries, is given by:

$$\beta = 2\pi \left(\frac{d}{\lambda} \right) \sqrt{N_1^2 - N_0^2 \sin^2 \Theta_0}. \quad 3.29$$

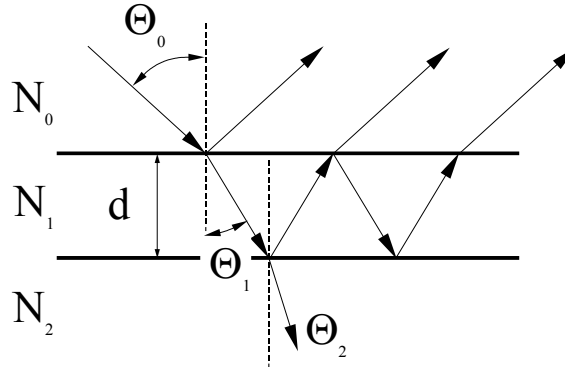


Fig. 3.3.1. Reflection and transmission of light by the ambient (0)-substrate (1)-film (2) system with parallel boundaries.

The functional dependence of Ψ and Δ on the parameters of the system can be symbolically written as:

$$\tan \Psi e^{j\Delta} = \rho(N_0, N_1, N_2, d, \Theta_0, \lambda). \quad 3.30$$

As one can see, ρ is explicitly dependent on nine real arguments (N is complex number, see Eq. 3.4). And although the function may appear deceptively simple from Eq. 3.28, it is in reality, quite complicated and, in general [McCrackin63], cannot be directly solved to yield the optical interfacial characteristics of the system. A solution requires a fitting iteration procedure in the frame of the appropriate interfacial model. But of course the number of unknown parameters should be at least equal to the number of measured quantities.

The general optimisation strategy will be shown for the example of K-KCl results. In this case, not all parameters of the system are unknown, and Eq. 3.30 actually reduces to:

$$\rho = \rho(N_{\text{film}}, d) = \rho(n, k, d). \quad 3.31$$

There are 3 unknowns (n , k and d) and only 2 measured parameters (Ψ and Δ). The missing information to solve the 3 phase model is obtained from the reflectivity measurements, since R depends on the same parameters as ρ :

$$R = R(N_{\text{film}}, d) = R(n, k, d). \quad 3.32$$

Now, there are enough independent equations to apply some numerical algorithm. This routine is aimed to find the parameter vector A , which minimizes the error sum χ^2 , defined as *biased estimator* [Jellison91]:

$$\chi^2 = \frac{1}{N} \sum_{i=1}^N \left(\left[\frac{\Psi^m(\lambda_i) - \Psi^c(\lambda_i, A)}{\Delta \Psi} \right]^2 + \left[\frac{\Delta^m(\lambda_i) - \Delta^c(\lambda_i, A)}{\Delta \Delta} \right]^2 + \left[\frac{R^m(\lambda_i) - r^c(\lambda_i, A)}{\Delta R} \right]^2 \right), \quad 3.33$$

$$N = n - g - 1,$$

where n is the total number of data point, g is the number of fitted parameters. The use of biased estimator has several advantages. One of them is, that the more accurate experimental points are automatically weighted more than inaccurate. They have bigger contribution to χ^2 . The superscripts m and c refer to the *measured* and *calculated* values, respectively. The parameter vector A has $2N+1$ components:

$$A = (n(\lambda_1), k(\lambda_1), \dots, n(\lambda_N), k(\lambda_N), d). \quad 3.34$$

The components of the parameter vector A for which χ^2 is smallest, are the solution of the system of equations 3.31 and 3.32. For the minimization of χ^2 the modified Levenberg-Marquardt conversion algorithm [Press86] is normally used. This is an efficient and stable optimisation method, based on the non-linear least-square routine. To launch the minimization routine some appropriate starting values of the unknowns should be guessed. The outcome, unfortunately, depends to some extent on their choice. For further details see [Azzam77].

In the case of Ga-Bi measurements, the parameters of based estimator will be I_s and I_c (Eq. 3.19). This delivers a certain advantage to the optimisation (will be described in details in Chapter 5). The interfacial 3 phase model (Chapter 6.2) for the metal alloys is simpler in comparison to the K KCl system – the thickness of the pure liquid Bi layer is the only fitting parameter. The optical properties of the substrate are calculated using the *effective medium approximation* (EMA). Just a few general words about the EMA. Overview with references concerning some special aspects of the EMA can be found in [Azzam77]. EMA is a powerful tool to study mixtures, rough layers, composite materials etc. This approximation allows to find the dielectric function of inhomogeneous materials from the dielectric functions of the components and their volume fractions. Of course, there is number of other parameters, which could contribute to the effective dielectric function like: size, shape and distribution of inclusions in the matrix phase. These effects are taken into account in the different modifications (Bruggeman, Maxwell-Garnet) of the working formula. Literature on the topic is abundant. It has to be noted that there are also situations where EMA fails. For example, if the component in the mixture changes its electronic properties in comparison to the pure state. Hence the applicability of EMA has to be proven in each case separately. In general it is impossible to predict how well it will describe a certain experimental situation. Such a check is easy to perform since the approximation is simple, straightforward and nowadays is included in all software treating the ellipsometric data.

The EMA was also applied to study the effect of sapphire corrosion in K-KCl measurements (Chapter 6.1).

4. Experimental apparatus and measuring procedure

4.1 High temperature construction for K-KCl measurements

As it was outlined in the introduction, the aim of this part of the present work was to extend the study of Staroske [Staroske00,01]. Special emphasis was given to the spectroscopic ellipsometry characterization of the wetting and prewetting transitions in the metal-rich K-KCl melts at temperatures near and above the monotectic point (751.5 °C; phase diagram of K-KCl system [Johnson58], see Fig. 6.1).

The investigation of the free melt surface is not possible since potassium is very volatile and strongly reacts with O₂. Its vapour pressure is around 250 kPa [Borgstedt87] at 800 °C. Hence the experiment requires a tightly closed optical cell. This imposes special demands on the choice of a transparent material. Only synthetic sapphire can sustain the attack of the highly corrosive alkali metal at high temperature [Freyland84]. Now a severe problem for ellipsometry arises: sapphire possesses a strong intrinsic birefringence [Jeppesen58], also after sealing of the cell a local stress birefringence is induced. Moreover, the birefringence is strongly temperature dependent [Nattand89]. To overcome those problems a meticulous in-situ calibration procedure (see p. 32) and precise temperature control of the high temperature probe are necessary.

• Experimental setup

In this chapter, the ellipsometer, the high temperature chamber and the cell construction will be briefly presented. Detailed description can be found in the thesis of Staroske [Staroske00]. The improvements of the setup made during this work will be summarized in the end of this chapter. The experimental setup is schematically shown in Fig. 4.1.1. It consists of a homemade PSA_{rot}A ellipsometer [Juchem95] and reflectometer [Staroske00]; also seen are the sapphire cell inside the chamber and the optical path of the light beam. In the present setup, a system of several cw lasers {see Manufacturer list} (spectral range $0.8 \leq h\nu \leq 2.2$ eV) was coupled to the ellipsometer with an optical fiber. A conventional light source (e.g. Xe-lamp) could not be used because of its low monochromaticity. Big differences in the phase shifts, induced in even narrow range of wavelengths after passing through the sapphire, could veil the true value of Δ from the sample [Jüchem95]. Only a light from a laser with very narrow bandwidth enables correct Δ measurements [Blankenhagen97].

For the ellipsometric measurements the linearly polarized beam enters the vacuum chamber through a quartz window. The beam diameter can be varied by the pinholes. In this study a

Ø1.5 mm beam was always used. The beam passes through the bottom sapphire prism and is reflected at the relevant sapphire-sample interface under an angle of incidence of 70°.

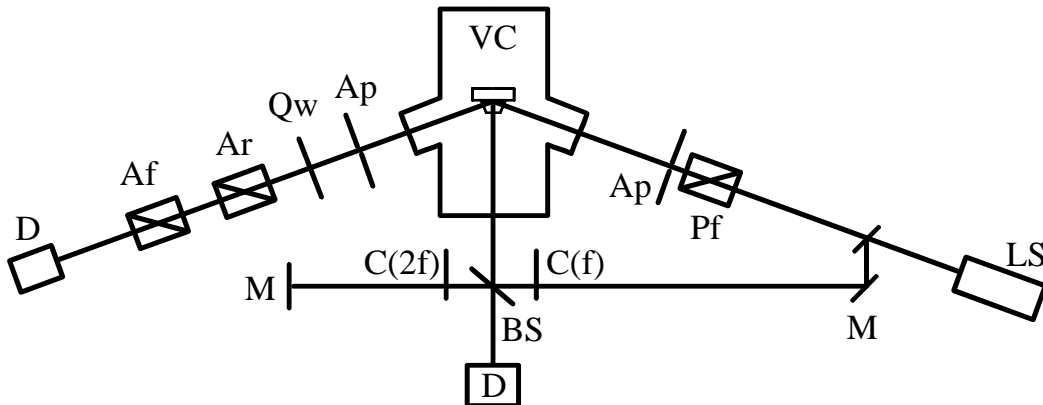


Fig. 4.1.1 Sketch of the ellipsometer system: (LS) laser system, (M) mirrors, (Pf) fixed polarizer, (Ap) pinholes, (VC) vacuum chamber, (Qw) retardation plate, (Af) fixed analyser, (Ar) rotating analyser, (D) detectors, C (f) and C (2f) wheels of chopper, (BS) beam splitter. Sapphire cell is magnified in Fig. 4.1.2 a.

The reflected beam is modulated by a rotating analyser ($\omega \sim 10$ Hz). It passes a fixed analyser and is then measured by suitable detectors (Si and Ge). The ellipsometric angles Ψ and Δ are computed from the Fourier coefficients of the modulated signal – see Chapter 3.2 [Stobie75]. The final improved data acquisition software has been written by Büscher [Büscher97], who also introduced an additional measurement with the quarter-wave plate (620 nm, 970 nm and 1540 nm), which can solve the uncertainty of the Δ measurements (Chapter 3.2). The plates are calibrated to eliminate the influence of multiple reflection effects [Blankenhagen97].

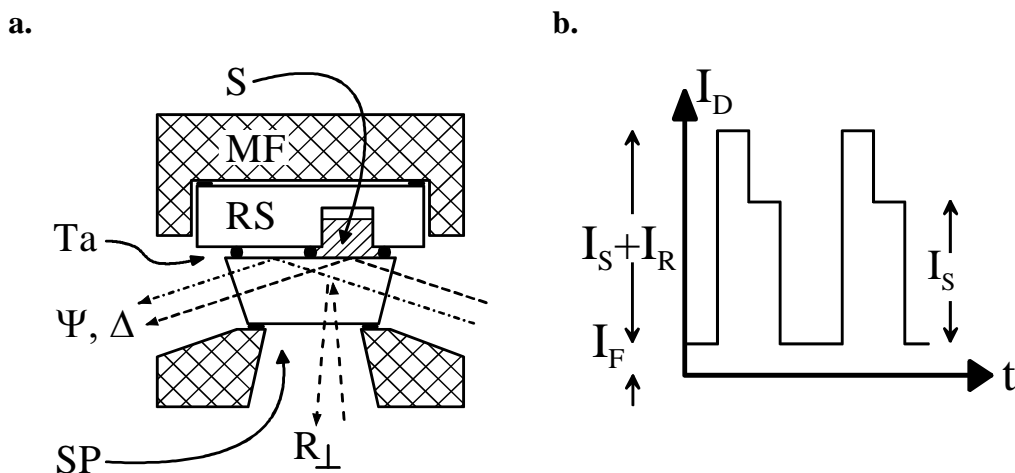


Fig. 4.1.2. (a) Cut through the optical cell and its steel holder: sapphire prism (SP), reservoir sapphire (RS), steel holder (MF), liquid sample (S), Ta-sealing-wire (Ta). There are graphite gaskets between metal holders and both sapphires. (b) I_D intensity of the signal at the detector D, I_F background radiation from the furnace, I_S reflected intensity from the sample, I_R reflected intensity from the reference mirror.

The cross section of the cell with its holder is shown in Fig. 4.1.2 a. The basic construction developed by Jüchem [Jüchem95] was modified later for additional reflection measurements [Staroske00]. The cell consists of two parts: the reservoir sapphire (RS) and single crystal synthetic sapphire prism (SP), which are squeezed together with tantalum wire (50 μm) in between. The sapphire prism has two sides inclined under the angle of incidence (Fig. 4.1.2 a) with respect to the cell base, to allow the laser light to enter and exit the cell under normal angle of incidence in order to avoid a change of the polarization state at this interface. The optical axis of the prism is perpendicular to the incidence plane. The reservoir sapphire is a round thick plate with a rectangular deepening for the sample, displaced with respect to the center of plate, Fig. 4.1.2 a. The holder, made from a high temperature resistant steel, has several holes for Ni-CrNi thermocouples. It has been shown that radial thermal gradients in the cell are negligibly small [Staroske00].

For the reflection experiment the unpolarized light beam can be deflected to the reflectometer [Metsch84]. The beam splitter (BS in Fig 4.1.1) serves to separate two light beams: one part at frequency f enters the chamber and is reflected at the prism plane - sample interface, the second part passes a $2f$ -chopper wheel mounted on the same axis as the f -chopper. It is reflected at a reference mirror and at the beam splitter again. Both signals merge and are detected by a single silicon detector; therefore the reflectivity spectral range is smaller than that of ellipsometry (Appendix, Results of K-KCl measurements).

For the determination of the sapphire-sample reflection coefficient, the intensity ratio $V(\lambda)$ can be defined from the intensity pattern (shown in Fig. 4.1.2 b):

$$V = (I_S + I_R) / I_S . \quad 4.1.1$$

The signals $V(\lambda)$ were averaged with a digital oscilloscope to achieve suitable signal-to-noise ratio. Light from the heater (I_F) in general doesn't influence the measurements; it just gives a certain offset to the signal. Taking into account the reflection and transmission coefficients of all interfaces on the beam path in the reflectometer, the reflectivity of sapphire sample interface R can be found from the following equation:

$$V = 1 + \frac{K}{R} , \quad 4.1.2$$

K is the constant obtained after the reflectivity calibration (see below).

The chamber, designed by Staroske [Staroske00] is a water-cooled vacuum (better than 10^{-5} mbar) vessel with the entrance and exit quartz windows. The resistance molybdenum heater (shaped as a long cylinder to minimize the temperature gradients) is controlled by PID-controller which allows to achieve high temperatures with a stability of $\Delta T < 0.1$ K. The chamber with the cell inside is positioned in the ellipsometer on a movable table (controlled

by a computer) with a precision of travel along both X- and Y-axis of 10 μm . The vertical position of the chamber can be also changed to compensate the vertical shift of the cell after heating [Blankenhagen97].

• **Calibration of Ψ , Δ and R**

The complete calibration procedure consists of several parts for all three measured quantities. They were developed in different PhD theses: [Juchem95], [Blankenhagen97] and [Staroske00]. Here only the final points are briefly summarized.

At 25.0 $^{\circ}\text{C}$ (held constant, ± 0.1 $^{\circ}\text{C}$, using water from thermostat), both compartments of the cell have clean reflection planes (sapphire/argon interfaces). That was insured by careful sample preparation (see ‘‘Sample preparation’’ below). Ψ and Δ profiles are recorded at approximately 20 points along the sample cavity (SC) and parallel to it along the reference compartment (RC) for selected wavelengths in the spectral range $0.8 \leq h\nu \leq 2.2$ eV. For the light reflected from the sapphire surface at an angle of incidence of 70 $^{\circ}$, the conditions of total internal reflection are fulfilled. Ψ , in this case, is expected to be 45 $^{\circ}$, but some deviations from this value (less than 0.5 $^{\circ}$) were always observed. In the assumption that one has to deal with linear effects, the true value of Ψ_{Sample} at the measurement temperature can be obtained using the following correction [Juchem95]:

$$\Psi_{\text{Sample}}(MT) = \arctan \frac{\tan(\Psi_{MT})}{\tan(\Psi_{RT})}. \quad 4.1.3$$

In this formula and later on MT is measurement temperature, RT stands for room temperature. For the angle Δ the calibration procedure is more complicated. The measurement at room temperature gives two Δ -profiles: $\Delta^{\text{RC}}(\text{RT})$ along the reference- and $\Delta^{\text{SC}}(\text{RT})$ along the sample-compartment. On heating, potassium melts and the liquid phase wets the prism base. Two profiles are recorded again: $\Delta^{\text{RC}}(\text{MT})$ and $\Delta^{\text{SC}}(\text{MT})$. The quantity of the interest, $\Delta_{\text{Sample}}(\text{MT})$, can be obtained taking the difference [Nattland88]:

$$\Delta_{\text{Sample}}(\text{MT}) = (\Delta^{\text{SC}}(\text{MT}) - \Delta^{\text{SC}}(\text{RT})) - (\Delta^{\text{RC}}(\text{MT}) - \Delta^{\text{RC}}(\text{RT})) + \Delta_{\text{Ar}}. \quad 4.1.4$$

The phase shift due to the presence of argon in the cell Δ_{Ar} must be also taken into account. It is calculated using the following equation [Pohl67]:

$$\tan\left(\frac{\Delta_{\text{Ar}}}{2}\right) = \frac{\cos(\Theta_0) \sqrt{(\sin^2(\Theta_0) - 1/n_{\text{Sapph}}^2)}}{\sin^2(\Theta_0)}. \quad 4.1.5$$

The temperature and wavelength dependence of n_{Sapph} are known [Mallitson62].

Calibration of reflectivity R was performed at a temperature around 400 °C. According to the phase diagram (see Fig. 6.1, p. 56), the liquid phase, which now wets nicely the bottom prism, consists of nearly pure potassium. Under those condition the reflectivity at the sapphire-potassium interface is:

$$R_k = |r_k|^2 = \frac{(n_k - n_{Sapph})^2 + k_k^2}{(n_k + n_{Sapph})^2 + k_k^2}. \quad 4.1.6$$

In this equation n_k and k_k are the optical constants of pure potassium at corresponding temperature, which are calculated using the free-electron Drude model (Chapter 3.1) with input data: N_e , electron density, and the electrical conductivity σ_{DC} taken from Ref. [Achener68]. Now the calibration constant K can be obtained from R_k and the experimentally measured V_k (Eq. 4.1.2.):

$$K = (V_k - 1)R_k. \quad 4.1.7$$

This constant is then used to calculate the values of the reflectivity at different temperatures using equation Eq. 4.1.2.

• Sample preparation, ellipsometry and reflectivity measurements

The subtle details of the experiment can be found in Ref. [Staroske00]. All samples have been prepared in a glove box (O_2 , H_2O less than 1 ppm). A small amount of Ti powder was added in the hole of the reservoir sapphire and covered by liquid potassium. Finally, the desired amount of high purity KCl crystals was pressed tightly into the already solidified metal surface. It is important that during calibration at room temperature no components of the sample will have a contact with the prism since during assembling the cell is turned upside down. A net like structure of Ta wires (50 μm) was spanned on the surface of sapphire and covered by the prism. Sapphires were squeezed together (it is important that sapphires have no direct contact with the metal parts of the holder – there are graphite gaskets ~0.2...0.4 mm thick between them) and the cell is placed inside the chamber. The chamber was fixed on the movable table and evacuated. Now the first part of the calibration can be done. For the measurements in the full spectral range, one needs to change different lasers and couple each into the optical fiber, align Dye and Ti:Sapphire lasers for lasing at different wavelengths. Alignment and re-alignment of a single laser is a tedious procedure of unpredictable duration, which required much physical efforts and a lot of patience from the experimentalist. A single ellipsometric measurement at one wavelength and one point along the prism took around 1 minute, hence 15-20 points along one compartment required ~10 minutes, plus same time for the second compartment. Hence room temperature calibration alone normally took around 15

hours. After the room temperature calibration of the ellipsometric angles has been finished, the sample was slowly heated to 150 °C and kept here for two days. During this time Ti powder functions as an oxygen getter and reduces the amount of oxides in-situ. After that the calibration of R was performed at 400 °C. The setup is now ready for the high temperature measurements. Normally, around a day was given for the thermal stabilization and homogenisation of the probe at a high temperature. One measurement of ellipsometry at a fixed temperature combined with reflectometry took 18-20 hours.

Practically all experiments had been done on heating since the cell leaks during cooling due to the inhomogeneous relaxation of stress in the holder and, in particular, the inelastic behaviour of the tightly squeezed Ta-wires on cooling.

In comparison to the previous experiments several improvements have been done in the present investigation:

- a. A new diode laser (1.165 eV) has been introduced in several measurements to complete the set of discrete wavelengths between 0.9 and 1.3 eV.
- b. The construction of the bottom window of the vacuum chamber has been changed. Used before standard UHV viewport-flange should survive the bake-out up to 400 °C by the specification. However, it proved to be unreliable and often cracked already at 650 °C. In this work, a thick (10 mm) quartz window had been installed in a specially designed water-cooled bottom flange. It became possible to perform a large number of measurements at temperature higher than 700 °C.
- c. To reduce the time of the measurement the number of wavelengths has been reduced from 18 [Staroske00] to 15. This did not decrease the resolution in n and k of the film. So, the measurements in the experimental sets were performed faster, hence the influence of some negative effects, such as for example high temperature corrosion of the sapphire or even breakage of the cell, could be minimized.
- d. Special attention has been drawn to the choice of the measurement conditions: concentration and temperature. Previous measurements were performed partly in the solid-liquid region of the phase diagram. It might introduce uncertainty in the optical properties of the film and its thickness, due to an unknown distribution of the undissolved solid phase and light scattering from it. Measurements in the present study have been done either very close to the solid-liquid coexistence line or in the homogeneous liquid phase region.

4.2 UHV chamber for in-situ measurements of liquid Ga-Bi alloys

The second part of this work was focused on the in-situ ellipsometric investigations of the wetting and surface freezing transitions as well as oscillatory instability at the liquid/vapour interface of Ga-Bi alloys.

Any surface study, particularly of liquid metals, requires ultra high vacuum conditions to enable an access to the free metal surface (without oxides and other impurities). Ultra high vacuum (UHV) in this context means 10^{-9} mbar and better. From kinetic gas theory it is easy to show that only in such vacuum a monolayer film of impurities forms on the surface on a time scale of hours, which is longer than the time of an experiment.

In this chapter the detailed construction and performance characteristics of the apparatus, which has been developed and used during this work, will be introduced.

• Design of UHV chamber

The requirements to the setup can be divided in two groups. First, it should be possible to create an atomically clean surface of the sample, i.e. maintain a vacuum better than 10^{-9} mbar and clean the sample surface in-situ. Second, the basic needs of the ellipsometric measurement have to be fulfilled, including the flatness of the liquid alloys surface, reduction of the vibrations and the possibility of an alignment.

First and foremost, to obtain the UHV conditions the material selection should be carefully considered. In the design the following points are essential: chamber volume, capacity and speed of a pumping system, flanges and connecting lines (diameter and length should be optimised), possibility of bake-out, choice of view-port and electrical feedthrough, heating element, sample transport, sealing technique etc.

Let's start from the chamber, the front cut of it is shown in Fig. 4.2.1. The chamber with all (except of few parts) its inner components was made from a high quality stainless steel (DIN E EN 10088; X6CrNiMoTi 17-12-2) special for the UHV applications. Before assembly (after machining) all parts were scrupulously cleaned, because even one finger-print (fat) can incapacitate the UHV setup for a long time.

The main vessel of the vacuum chamber has two big arms, inclined under an angle of 70° , with flanges for the modulator (Nr. 1, see Fig. 4.2.1) and the analyser head (Nr. 2) of the UVISEL ellipsometer {Jobin Yvon}. The liquid nitrogen trap (Nr. 3, volume appr. 2.5 litres) is placed on the upper flange, which also has a small viewport to illuminate the sample from above (see Fig. 4.2.2, Nr. 6).

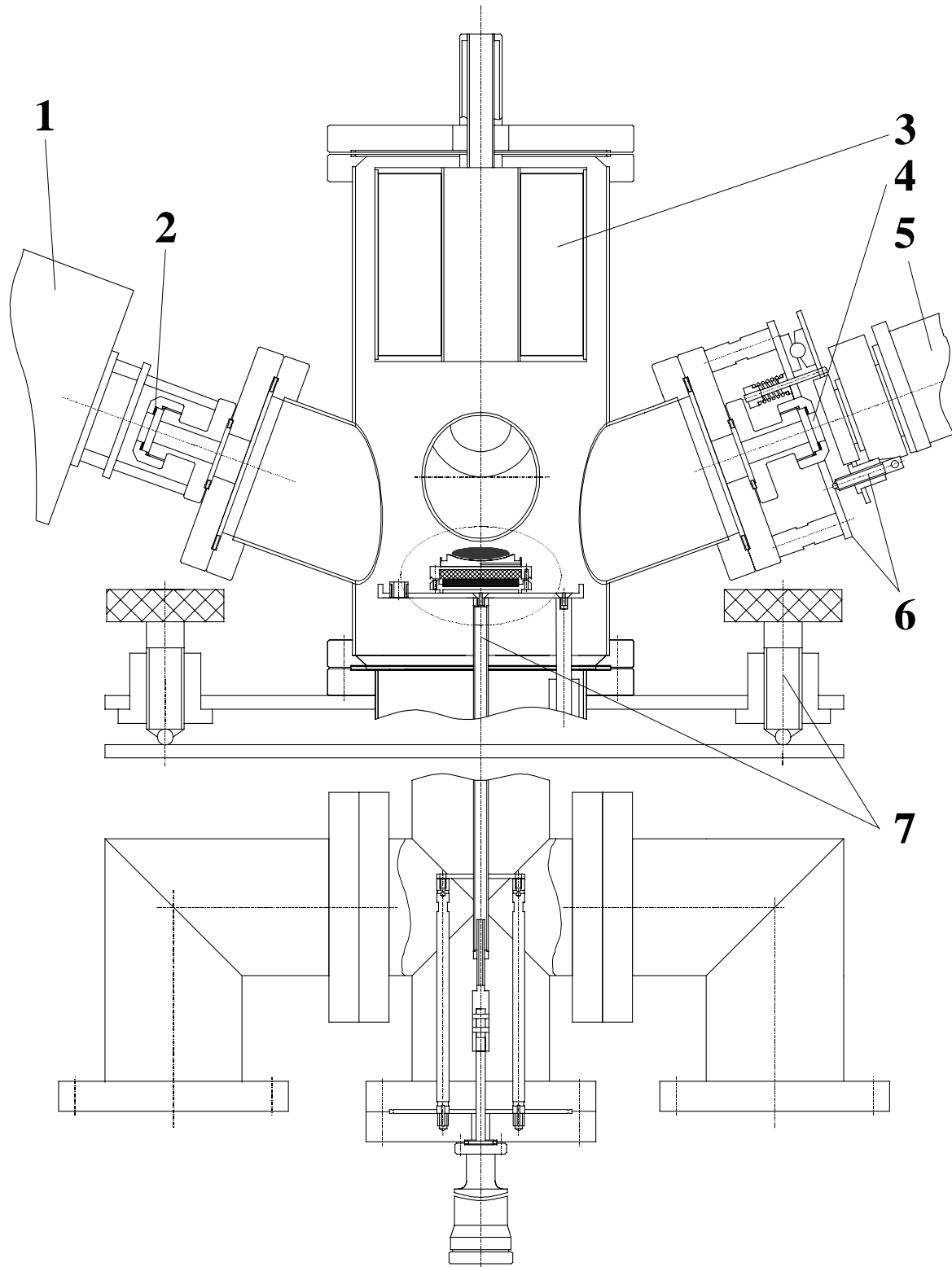


Fig. 4.2.1 Frontal cut of the chamber: 1, 5 – modulator and analyser heads of UVISEL modulation ellipsometer; 2, 4 – low-stress windows; 3 – liquid nitrogen trap; 6, 7 – alignment mechanisms. For details see the text.

There are two observation windows from quartz on CF40 flanges on the front side of the chamber. Whereas all flanges of the apparatus have been sealed using standard copper-rings

(CF gaskets), a special technique has been applied to achieve UHV sealing of the quartz window on the metal flange [Noble94]. For this aim the standard copper gasket is modified by machining a knife edge into one its faces and the knife is deformed on the surface of the window. This technique works very well and is much cheaper than commercial view-ports. The ellipsometric windows are sealed differently. The window (Nr. 2 and 4) inside the holder with nut is screwed to the body of the view-port with an In-wire ring in between. In this way less stress is induced in the optical windows, which is important for the ellipsometric measurements (Chapter 5).

The pumping system consisting of an oil-roughening pump, a turbo- and ion-pump, is connected to the U-shape bottom part of the chamber. With this combination of pumps a vacuum of nearly 10^{-10} mbar can be achieved (after bake-out and using the liquid nitrogen trap). Bake-out heating elements are coiled around all parts of the construction and are able to warm them up to 110-120 °C. Higher bake-out temperatures cannot be used, because of the ellipsometric windows (melting point of In is 157 °C). For safety, the windows are air-cooled during the bake-out.

The design of the heating element deserves special attention in UHV application and in the present measurement in particular. In this work a Mo-wire heater with Al_2O_3 ceramic insulation is enclosed in a casing from pure copper. The upper surface of the casing is polished to provide good heat transfer to the crucible. For the temperature control a Ni-CrNi thermocouple and PID-controller are used, allowing the temperature stability better than ± 0.5 K.

The whole setup is installed on a passive vibration insulating system of 4 air-pillows. It was found that such a simple system is sufficient and successfully damps almost all vibrations, which are always present in any lab.

• Crucible and sample preparation

Pure liquid Ga and its alloys have very high surface tension and strive for a curved free surface. This is not suitable for optical reflectivity studies, because the light beam diverges after the reflection. To avoid this in the present work, a crucible with hemispherical cavity has been used. The optimal shape was found experimentally. The advantage of such construction is that a nearly flat surface can be obtained using relatively small amounts of the expensive components. The cavity alone is not a guaranty of success: a liquid metal sample does not spread on the crucible surface in the presence of oxides. Their origin does not matter – both interfaces, crucible itself and the sample, must be perfectly clean.

As a material for the crucible Mo has been chosen. It is inert for both components (Ga and Bi) in the full temperature range of this study. The crucible was polished, rinsed with solvents (acetone and methanol), then heated up to 1100 °C and held for several hours at this temperature in the high-frequency furnace under vacuum better than 10^{-5} mbar. As it is well known oxides of Mo are volatile at this temperature. After the thermal treatment, the cooled crucible still under vacuum was transported in the glove-box (O_2 , H_2O less than 1 ppm).

Ga (99.99999 %) and Bi (99.9999%) {AlfaChemicals} had to be cleaned before use since these purities only refer to metal impurities. Melted without additional purification the metals revealed a thick layer of some impurities, essentially oxides. The cleaning procedure is very easy for Ga (melting point 29.8 °C). It was done by simply running liquid Ga through glass capillaries in the glove-box. In the case of Bi ($T_{\text{melt}}=271.4$ °C) it was more complicated. Bismuth has been cleaned in the same way but under vacuum in the high-frequency furnace. After purification both Ga and Bi were always kept in the glove-box.

Now alloys can be prepared. Liquid Ga has been poured in the Mo-crucible using a glass syringe and the respective amount of solid Bi was added. The sample was solidified and quickly transported on air into the chamber. In spite of all described above precautions, after melting of the sample in the chamber under vacuum, some clearly visible remainders of impurities were still present on the sample surface.

• *In-situ* surface cleaning

In the case of liquids, due to the high mobility of the elements and impurities on the sample surface, the cleaning is not that straightforward as for a solid surface. To obtain atomically clean surfaces the setup is equipped with the three systems: an Argon sputter-gun (1); homemade mechanical tungsten wire-cleaning device (2) and a lock (3) (details of all systems are shown in the Fig. 4.2.2).

Placed into the chamber, the sample stood on the cooling plate (11, Fig. 4.2.2) inside the lock. After a modest vacuum of 10^{-7} mbar was achieved, a bake-out procedure could be started. During the bake-out the sample was kept solid (running tap-water through the plate holder), otherwise the liquid metal surface could collect some additional impurities in the relatively bad atmosphere. When the bake-out was finished, the sample was shifted onto the heating element using the linear driver of the lock. Before actual experiments, the sample was heated up to 250-300 °C, depending on concentration, for a homogenisation of the alloy. After several hours the cleaning could be started. The successive stages of the cleaning procedure are documented in Fig. 4.2.3. As was already mentioned, after the melting, the liquid surface appeared to be covered by a substantial layer of some impurities, presumably oxides.

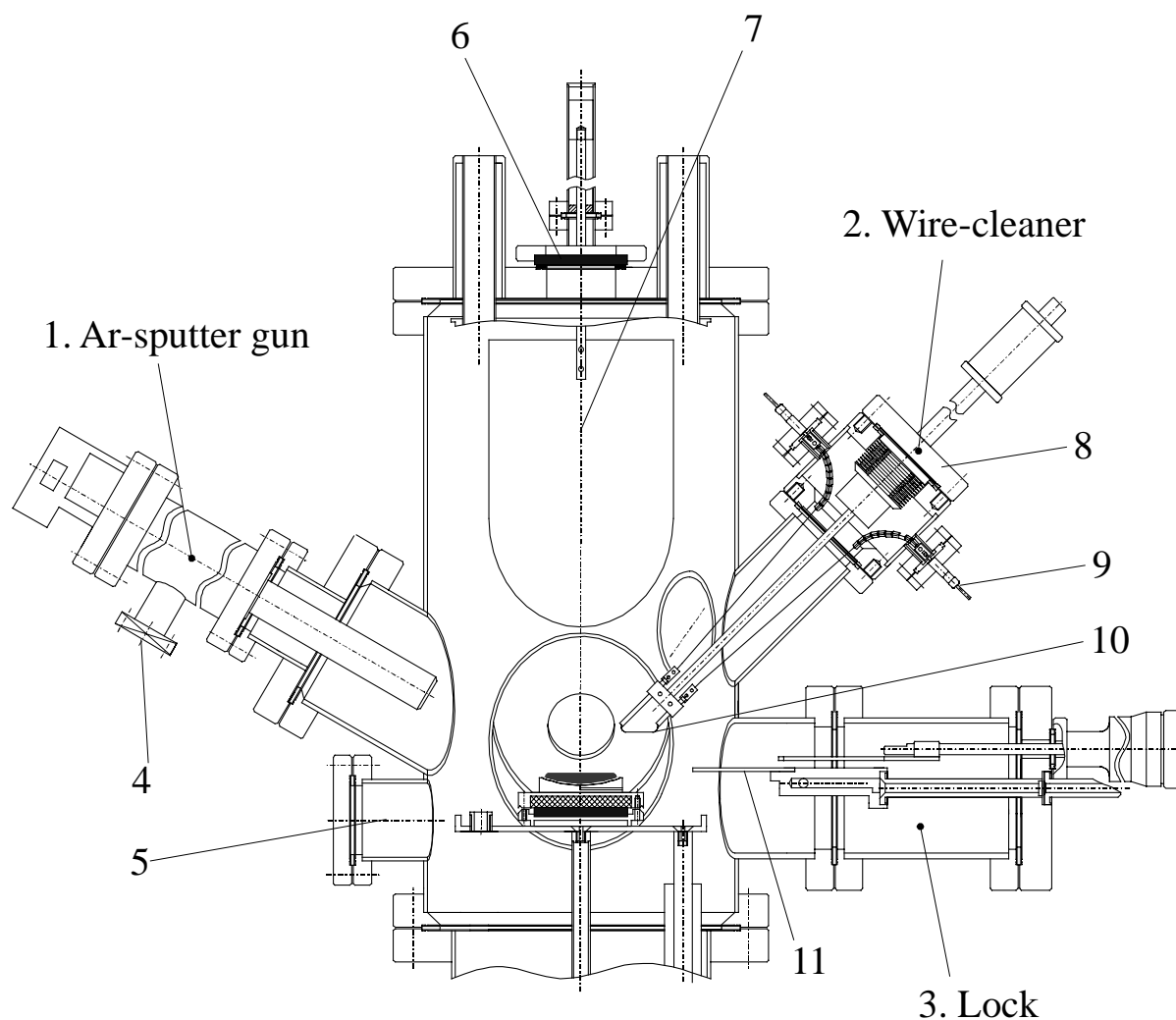


Fig. 4.2.2 Side cut of the chamber. Cleaning devices are shown: Ar-sputter gun (1), tungsten wire-cleaning device (2), lock (3). The remaining number refer to: Ar supply and fine leak valve (4); protective container (5); illumination window (6); magnetically driven shields (7); W-wire, electrical feedthrough, wobble-stick of the mechanical cleaner (10, 9, 8).

It seemed to be, that they come from Bi, which was purified obviously insufficiently and retained high amount of oxides. The thick complete layer of oxides can be seen in Fig. 4.2.3 (A). One can also notice that at this stage the sample does not wet the crucible at all. The next picture (B) shows the sample after 15 minutes of sputtering. For the cleaning a broad sputter gun beam of high intensity (5 kV) was used. Ar-flow through the chamber was controlled by a fine-leak valve (4, Fig. 4.2.2). Sputtering was very efficient until the oxide film was complete, but after some time (around 15-20 minutes) the film broke into islands, which floated on the clean mirror-like metal surface. The oxides were collected by the beam on the opposite of the sputter-gun's footprint at the crucible's rim, Fig. 4.2.3 B.

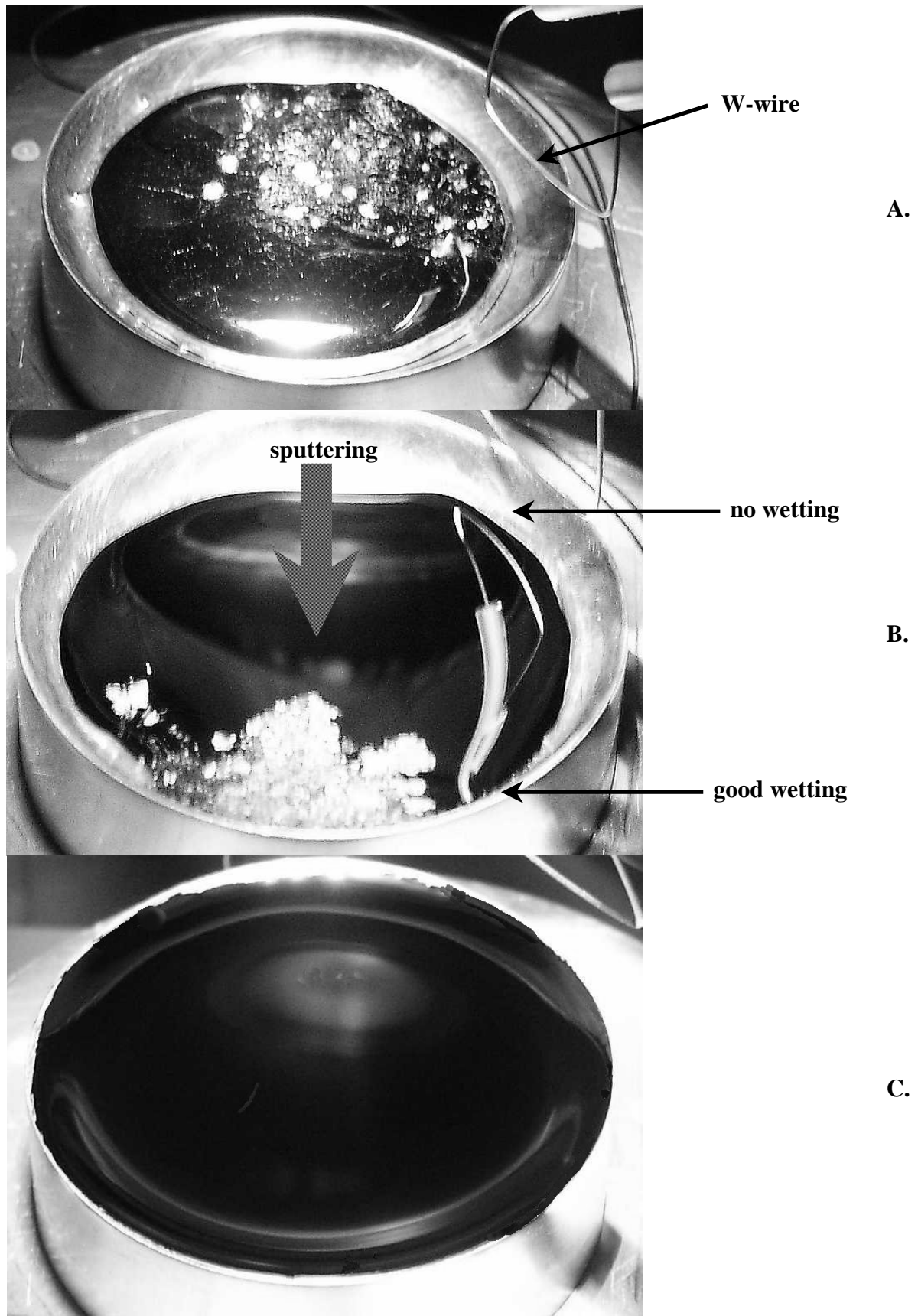


Fig. 4.2.3 Stages of the sample cleaning: **A** – after melting, **B** – after sputtering, **C** – finally cleaned and plane surface ready for measurements. W-wire of mechanical cleaner (A) and its reflection in the alloy (B), can be seen.

It should be noted that, this part of the crucible is now wetted by the liquid sample, Fig. 4.2.3B. At this stage sputtering becomes almost useless since the oxides are just moved outside the ion beam spot but not removed by this beam. Therefore, the W-wire cleaning device was applied (shown in Fig. 4.2.2, Nr. 3). The device worked similar to that described in work of Indlekofer et al. [Indlekofer87]. It consists of a tungsten wire (\varnothing 0.7 mm, ~10 mm long (10)) fixed on the wobble-stick (Nr. 8), which allows all degrees of freedom to reach the whole surface of the liquid sample. The wire is brought into contact with the oxides; they stick to it and are then mechanically removed. The wire is cleaned inside the protective container (Nr. 5) by heating it with a current up to 10 A (Nr. 9) for several seconds to evaporate stuck to it impurities. For the good sticking, it is also important that the wire has temperature around 300 – 400 °C. At such temperatures the oxides start to melt and wet it. It was experimentally found that for all concentrations (including pure Ga and Bi) this optimal temperature of the tungsten wire was achieved using current of ~2.5 A. The surface was sputtered again – this was done to collect residual micro impurities. The mechanical wire-cleaner was applied again. After repetitive runs it was possible to remove *all* visible oxides.

The final result, ready for the measurement surface can be seen in Fig 4.2.3 (C). There are no oxides and the surface is perfectly clean. It might be even more important that the crucible surface is now completely wet by the clean liquid alloy. This implies that during the cleaning procedure a thin oxide film on the crucible/sample interface has also been removed or dissolved. In this way the liquid alloy can completely wet the pure Mo surface – metals wet metals – which is not the case for a MoO_x -covered surface, where the surface tension is roughly an order of magnitude lower than that of the metallic alloy. This together with the crucible cavity leads to a flat surface ideal for ellipsometry. All samples independently of the thermal treatment were always maintained in the vacuum of 10^{-9} mbar and no formation of oxides was noticed for weeks.

During sputtering and particularly during evaporation of the impurities from the wire-cleaner, it was important to protect the ellipsometric windows against deposition of some film on them. The windows were shielded with the help of the magnetically driven metal screens, Fig. 4.2.2, Nr.7. This helped to keep them clean during all experiments of this work.

• Alignment and calibration of ellipsometer

In-situ ellipsometers are in general more difficult to operate than the conventional ones fixed to a goniometer. This is due to two main reasons:

1. incident angle can not be changed and/or measured quickly, furthermore, it has to be found at the beginning with a reliable precision from some additional measurement,
2. the sample has to be handled from outside of the chamber, which causes complications to align it; even positioning and transfer of the sample inside the chamber can be hindered.

Especially for the measurements on liquid surface, an additional problem for the alignment arises. The liquid surface itself cannot be oriented and stays always horizontal.

In this chapter solutions of those difficulties will be offered and modulation ellipsometer will be briefly introduced.

The UVISEL phase modulation ellipsometer {Jobin Yvon} consists of a high stability Xe-lamp, the analyser and detector heads, a monochromator and computer for control and data processing. The lamp and monochromator are coupled with the instrument with optical fibers. The flexibility of the fibers together with the compact design of both ellipsometer heads allows an accurate assembly of the instrument on the UHV-chamber. Use of the phase modulation ellipsometer has several advantages, which make it particularly suitable to study the interfaces of liquids. The ellipsometer has no mechanically moving parts; hence it does not produce vibrations. It possesses rapid and high precision data acquisition, which makes it principally insensitive to vibrations from different sources.

Coming to the alignment and calibration, a few words should be said about the operations made during the manufacturing and testing of the instrument at Jobin Yvon Company. These are: the calibration of the modulation amplitude A and electronic calibration. During the first one, $J_0(A)$ is set equal zero and during the second, the factors correcting the birefringence of the modulator and the electronic bandpass are determined [Drevillon82].

After assembly of all setup components on the chamber, the incidence angle (Θ) has to be checked, corrected and determined. For this aim the Al-mirror was inserted into the chamber and placed in the middle of the heater casing on the table. The table was brought in the position where light strikes the center of the mirror. It was achieved using the linear driver on the bottom flange of the chamber (Fig. 4.2.1). The path of reflected beam was judged. The main criteria are the maximum intensity transmitted through the ellipsometer to the detector and a correct alignment of all optical components. The path could be adjusted by orienting the plate on the "ball and socket" joint (Nr. 6 in Fig. 4.2.1) with analyser head on it, using two screws. When this operation was accomplished the screws were secured with glue and the angle of incidence was set. Next step was to find the zero position of analyser and modulator, which both were mounted manually as precisely as possible in the incidence plane. Scanning

the analyser angular position in small $\pm 0.05^\circ$ steps the minimum in R_ω (Chapter 3.2) was found. The analyser was set to 0° . In the same way, but now analysing $R_{2\omega}$, zero-position of the modulator was found and set. After this, the Al-mirror was replaced by an aged silicon wafer sample (Si (111) covered by a film of native SiO_2). The reflection conditions were restored by the height adjustment only. This was sufficient, since both samples have the plane-parallel surfaces. The ellipsometric spectra have been taken in the full range $0.8 \text{ eV} \leq h\nu \leq 4.65 \text{ eV}$. The result was fitted with the 3 phase model. In this model the optical properties of both the Si-substrate and the SiO_2 -layer are known. The thickness of the SiO_2 film, which is approximately 110 \AA , and the angle of incidence were the fitting parameters. If the experimental and theoretical spectra overlap (χ^2 is an indication of discrepancy) and obtained thickness agrees with the known one, then the second fit parameter, the value of Θ , can be taken and used in all future experiments. The incidence angle was found to be $\Theta = 71.15^\circ \pm 0.05^\circ$, which is in the good agreement with 70° planned during the design of the setup. The instrument was ready for the investigations.

When the liquid alloy is introduced into the ellipsometer, corrections are required to restore the reflection conditions. The reflection plane of the liquid surface should coincide with the defined reflection plane of the ellipsometer. The sample orientation, with respect to the instrument geometry, is aligned exclusively by varying the sample height (Nr. 7 in Fig. 4.2.1) and tilting the complete UHV-chamber-ellipsometer construction. The whole setup stood practically on three points – one rigid and two massive screws with grips (Fig. 4.2.1). They allowed a precise controllable tilt of the ellipsometer reflection plane.

The carefully aligned sample with the flat thoroughly cleaned surface required later only a slight, if at all, vertical correction in the whole experimental run for the one concentration.

5. Data evaluation and error analysis

For the evaluation of the ellipsometric and reflectivity data both 2 and 3 phase models have been applied. Whereas the 2 phase model can be solved analytically, the 3 phase model has to be solved numerically (Chapter 3.3).

The general parameters of 3 phase models can be summarized as follows:

a. K-KCl experiment:

- ambient* – sapphire : n and k are known [Mallitson62], the T dependence of n and k are corrected according to the citation [Nattland88b];
- film* – KCl-rich phase : n, k and thickness are fit parameters;
- substrate* – K-rich phase : $\epsilon(\omega, T)$ have been approximated using Drude model (Eq. 3.17) on the base of $N_e(T)$ and $\sigma(T)$ taken from the literature [Achener68].

b. Ga-Bi experiment:

- ambient* – vacuum : n=1, k=0;
- film* – pure liquid Bi : thickness is a fit parameter, $\epsilon(\omega)$ was measured in this work;
- substrate* – Ga-Bi alloy : $\epsilon(\omega, x_{Bi}, T)$ have been calculated from the EMA-approximation using measured data of pure Ga and Bi of this work.

In the K-KCl measurements the input parameters of the fitting procedure were ellipsometric angles Ψ , Δ and reflectivity R. In the Ga-Bi experiments the ellipsometer software analysed the intensities I_S and I_C instead of conventional ellipsometric angles. This is a clear advantage not only because I_S and I_C are original experimental quantities but also because both values lie in the same range from 0 to 1. Hence they will have the same statistical weight during fitting (Eq. 3.33, Chapter 3.3). This is not the case if ellipsometric angles Ψ and Δ are used, since in the present study Ψ is several times smaller than Δ .

In this chapter all kinds of experimental errors will be presented and discussed. Some of them are common for these both systems; but when necessary the distinction in the error analysis between K-KCl and Ga-Bi experiments will be discussed.

5.1 Errors in measured quantities

• Error of concentration

This error depends essentially on the precision of the balance used, but also on the way of preparation and the following treatment of the sample. To weigh the components a “Sartorius R 160P” piezo balance ($\delta m = \pm 0.1$ mg) was always used. Preparation of the samples was

described in Chapter 4.1 and 4.2. Starting with the measurements of K-KCl, from the definition of molar concentration the propagation of the error is straightforward:

$$x_K = \frac{\frac{m_K}{M_K}}{\frac{m_K}{M_K} + \frac{m_{KCl}}{M_{KCl}}}, \quad 5.1.1$$

$$\Delta x_K = \left| \frac{\partial x_K}{\partial m_K} \right| \delta m_K + \left| \frac{\partial x_K}{\partial m_{KCl}} \right| \delta m_{KCl}; \quad \Delta x_{KCl} = \left| \frac{\partial x_{KCl}}{\partial m_K} \right| \delta m_K + \left| \frac{\partial x_{KCl}}{\partial m_{KCl}} \right| \delta m_{KCl}.$$

The same procedure applies for Δx_{Bi} in the case of the Ga-Bi alloys. Errors $\Delta x_K, \Delta x_{Bi}$ estimated for all measured concentrations in both systems were less than 3 %.

At high temperature, some part of the potassium of a K-KCl sample will be in the vapour phase. But this amount is negligible since the empty space left inside the cell during preparation was very small (around 10 % of total sample volume).

In the measurements of Ga-Bi alloys an additional error contribution may arise due to the sputtering and mechanical cleaning of the liquid surface. Some unknown amount of Ga and Bi metals can be removed from the sample together with oxides, thus leading to a shift of the sample composition. Fortunately, this effect can be easily controlled. After the measurements had been completed, samples were weighed again. Loss of weight was found to be always around 0.25 g only (from total ~40 g). It is concluded that shift of the weighed concentration was negligibly small. In the total, estimated error of the concentration for the studied systems is less than 5 %. These errors will not be shown in the graphs later on.

• Error of temperature measurement

The temperature in both experiments was measured with a Ni-NiCr thermocouple (absolute accuracy is $\pm 0.5\%$ from the measured value of T). In the case of the K-KCl experiment, taking into account homogeneous heat distribution inside the high temperature furnace [Staroske00] and close position of the thermocouple to the sample, the temperature reading was very accurate. The situation was different for the Ga-Bi alloys. Separation of the thermocouple and the surface of the studied liquid alloys was around 10 mm. In this case the vertical and radial thermal gradients estimated in our lab [Nattland95] can be up to 3 K. Gradients can be also different for spectroscopic and kinetic measurements.

• Errors of ellipsometric measurements

The theoretical precision is discussed in the literature for different ellipsometer systems [Aspnes75b]. For *in-situ* studies of some processes in vacuum (or under pressure, in liquid etc.) the most important error, which if not carefully avoided can influence the results

strongly, stems from the presence of windows of the cell or apparatus [Stagg93]. They can function as additional optical elements inside the ellipsometer arrangement, the elements which are furthermore not necessarily stable in time. Force applied to the window to achieve vacuum sealing, leads to a stress birefringence (in general unequal in the entrance and exit window). Difference in the pressure and temperature on the both sides of the windows also has an effect on the stress distribution. In the K-KCl setup this problem was partially solved by the zone-averaging procedure (Chapter 3.2). But the negative effect of window birefringence was more pronounced at high temperatures when the windows became warm due to the thermal radiation from the furnace. In the Ga-Bi experiments special *low-stress* windows were used; in addition, the ellipsometer was calibrated under conditions similar to experiment (under vacuum around 10^{-7} mbar). During the measurements the air-conditioning machine allowed to keep the temperature in the lab stable, hence temperature of the windows was stable too. In the following the errors of the ellipsometric quantities will be presented separately.

A. Ellipsometric errors in the measurements of the K-KCl system.

The detailed analysis of errors of rotating-analyser ellipsometry can be found in Ref. [Nijs88] and references therein. For our particular ellipsometer, the following contributions are of interest:

- **Errors of Ψ**

Systematic errors in Ψ as a consequence of slight misalignment of polarizer and analyser in the ellipsometer are eliminated with the zone-averaging procedure described in the Chapter 3.2. But there are still the errors caused by the deviations in the angular positions of polarizer and analyser. These errors depend very strongly on the absolute value of Ψ [Stobie75]. The upper limit of such an error in this study is 0.2° [Juchem95], which together with statistical contributions gives 0.5° as the final error of the angle Ψ .

- **Error of Δ**

For the angle Δ , the zone averaging improves the systematic errors as in the case of Ψ . In our particular study the angle Ψ was always around 45° (see experimental data in the Appendix), in this case the influence of errors in the angular positions of polarizers on the angle Δ can be neglected [Stobie75]. The main source of errors in the angle Δ is the birefringence of sapphire (see Chapter 4.1). The assumption about equal changes of the birefringence in the both cell compartments (Eq. 4.1.4) does not hold exactly. Tests with the empty sapphire cells showed deviations of about $\pm 2^\circ$. The adjustment of the vertical position of the cell after heating

endows another $\pm 2^\circ$ uncertainty [Blankenhagen97]. In the last error the inaccuracy of the linear displacement of the chamber during the measurement was also included. There remain of course the error contributions due to the slight fluctuations of temperature during acquisition of the ellipsometric spectra (approx. 20 hours, Chapter 4.1). But they are so small under careful control of the temperature (deviations of ± 0.4 K only), that they can be neglected in comparison with the other above-mentioned contributions. So, the estimated upper limit of the angle Δ error is 4° .

• **Error of reflectivity, R**

All possible contributions in the error of the reflectivity have been discussed in the thesis of Staroske [Staroske00], who performed test measurements and estimated them. The main source of errors in his work was the turbidity of the bottom window, which he always observed after the heating. He related this effect to the deposition of some impurities evaporated from the chamber furnace at high temperature. In the present work this effect was avoided in the following manner. The furnace in the empty chamber was backed for several hours at $\sim 400^\circ\text{C}$ and cooled down under vacuum. After that, the cell was quickly inserted in it, so that the baked inner components of the chamber (heater, wall, holders etc.) were only several minutes in contact with air. Any contamination of the bottom window has never been observed in this study. Still possible error sources are: the precision of the cell position – the chamber was moved manually; the errors of the oscilloscope's reading; slight changes of the reflection geometry on the temperature rise due to the inhomogeneous expansion of the cell holder construction. All contributions enumerated above were estimated as 10-15 % error of the reflectivity measurement.

• **Error of λ**

The wavelengths obtained from the different lasers were directly checked before the measurements with the wavelengths-meter from Spectra Physics company {Spectra Physics}. The specified precision of this device is ± 0.5 nm.

It is important to remember that the calibration measurements (Chapter 4.1) of Ψ , Δ and R could suffer from some of the above-mentioned errors also. This will add some certain contributions to the final error of the quantities measured in the experiment.

B. Ellipsometric errors in the measurements of the Ga-Bi system.

It's is of relevance to give at the beginning the performance characteristics specified by the manufacturer for the ellipsometer mounted on the goniometer (for silicon wafer as a sample):

- a. accuracy of Ψ and Δ is $\pm 0.1^\circ$; repeatability of Ψ is $\pm 0.015^\circ$, of Δ is $\pm 0.08^\circ$,

b. accuracy of λ is ± 0.15 nm and repeatability is ± 0.005 nm.

The parameters listed under (a) needed to be checked in this study after the splice of the ellipsometer together with UHV-chamber and in particular for the measurements of the liquid metal surface. The final test has been done with the $\text{Ga}_{0.998}\text{Bi}_{0.012}$ alloy at a constant stable temperature of ~ 280 °C in a vacuum of $5 \cdot 10^{-9}$ mbar. In Fig. 5.1.1 one can see the ellipsometric angles Ψ and Δ , which were recorded continuously every 10 seconds for the period of about 7 hours. The signal variations of the long-time performance of the setup include the stability of: the crucible and room or respectively windows temperatures, mechanical vibrations, which are always present up to some level and the precision of the ellipsometer itself.

The statistical data for a period of time of appr. 7 hours are: $\Psi = 38.94 \pm 0.01^\circ$ and $\Delta = 121 \pm 0.05^\circ$. As can be clearly seen the quality and precision of the ellipsometer measurements was not lost in the in-situ measurements of the liquid Ga-Bi alloys.

One of the very important questions in ellipsometry is how the output of the ellipsometric measurement depends on the alignment of the sample in the instrument. Normally, this point is omitted, since it is assumed that the sample is aligned as good as it could be done. But in the case of time dependent *kinetic* measurement (for definition see Chapter 6.2, p. 67), if the reflection geometry changes, the influence of this effect on the measured quantities had to be investigated. All *kinetic* measurements with the Ga-Bi alloys were performed on cooling (the reason will be explained in Chapter 6.2, p. 80), so (i) the surface of alloy sinks, due to the thermal retraction and (ii) the surface tension of alloy changes, hence wetting of the liquid alloy and crucible may change too. So, in general, the shape and vertical position of the reflecting surface might vary with temperature.

The effects listed in (ii) were practically eliminated after the surface cleaning, where perfect wetting of the crucible and the flat surface of liquid alloy were routinely achieved. Effect (i) was not expected to be big. Since the temperature range in all *kinetic* measurements very rare exceeded 100 K, the maximum thermal retraction can be estimated as $30 \mu\text{m}$: $\Delta h = \alpha_L L \Delta T$; where $\alpha_L = 0.3 \times 10^{-4} \text{ K}^{-1}$ [Takamichi93], typical crucible depth $L = 10$ mm, $\Delta T = 100$ K. (In principle retraction of all parts - heater casing, table and its support - has to be included to obtain precise number). To see the influence of such height variation, Ψ and Δ were continuously recorded during the manual change of the vertical sample position from the silicon wafer sample. The shift could be done with micrometer resolution. No changes in Ψ and Δ were noticed until Δh clearly exceeded 0.05 mm which, as was shown above, could never happen in the experiments. Besides, the alignment before and after each measurement

was carefully checked and compared. No visible changes were detected (except in *surface freezing* study - see Chapter 6.2).

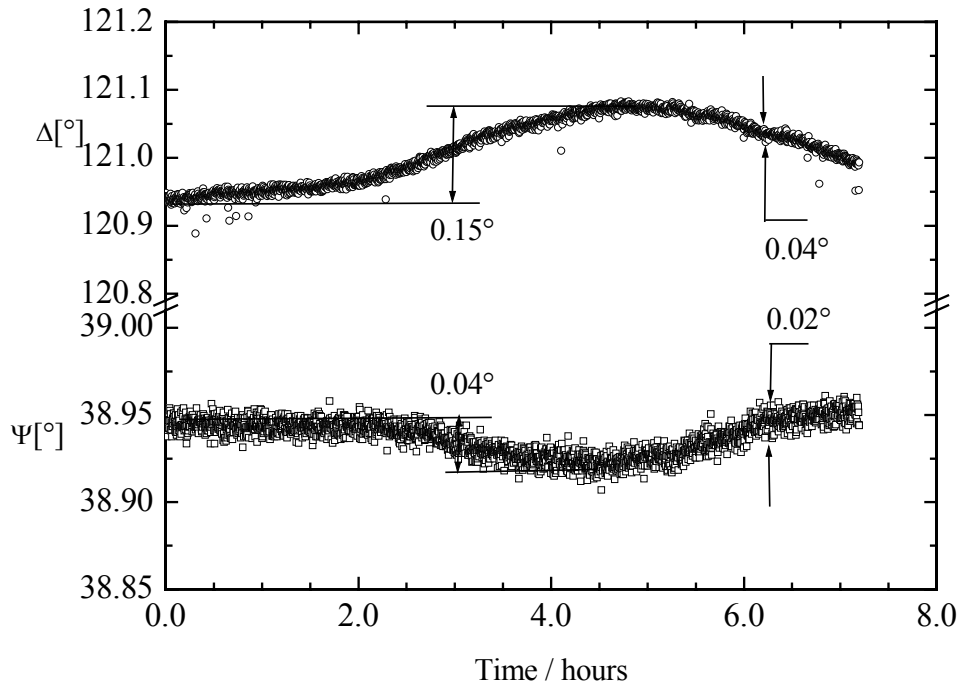


Fig. 5.1.1 Long-time stability and reproducibility of present in-situ ellipsometric setup on the example of liquid $\text{Ga}_{0.998}\text{Bi}_{0.012}$ alloy at constant stable temperature ~ 280 °C in vacuum $5 \cdot 10^{-9}$ mbar. Ψ and Δ were recorded every 10 seconds at $\lambda=450$ nm. Attention: scales of Ψ and Δ are different.

On the other hand, the thermal retraction of the liquid surface produced a very interesting effect, which was observed practically in all kinetic measurements. This effect gives indirect insight on the sensitivity of the setup. In Fig. 5.1.2 the intensity of the polarized light is shown as a function of time (bottom axis) and temperature of the crucible (upper axes). This is a “quasi-reflectivity” measurement with polarization of incident light of 45° at an angle of incidence of $\Theta=71.15^\circ$. It was taken on cooling of the $\text{Ga}_{0.99}\text{Bi}_{0.01}$ alloys with 2 K/h. The origin of the periodical variation of the reflectivity (minimum every 0.5 K) can be explained in the following way: the system “entrance window – liquid alloy surface – exit window” is nothing else but the interferometer in which the length of the beam path changes.

Using the above formula and taking into account the incidence angle for $\Delta T \sim 0.5$ K (shown in the Fig. 5.1.2 temperature difference between two minima in reflectivity) one can estimate $\Delta l = 460$ nm ($\Delta l = \Delta h / \cos(\Theta)$). This value nicely agrees with the wavelength of 450 nm used in this measurement. That is why the interference conditions are fulfilled every 450 nm of the height variation on cooling. Disregarding the periodical variation, the overall stability of the

reflectivity upon temperature variation of 20 K is very good. The described periodical change could be sometimes seen in the ellipsometric angles Ψ and Δ (not shown here).

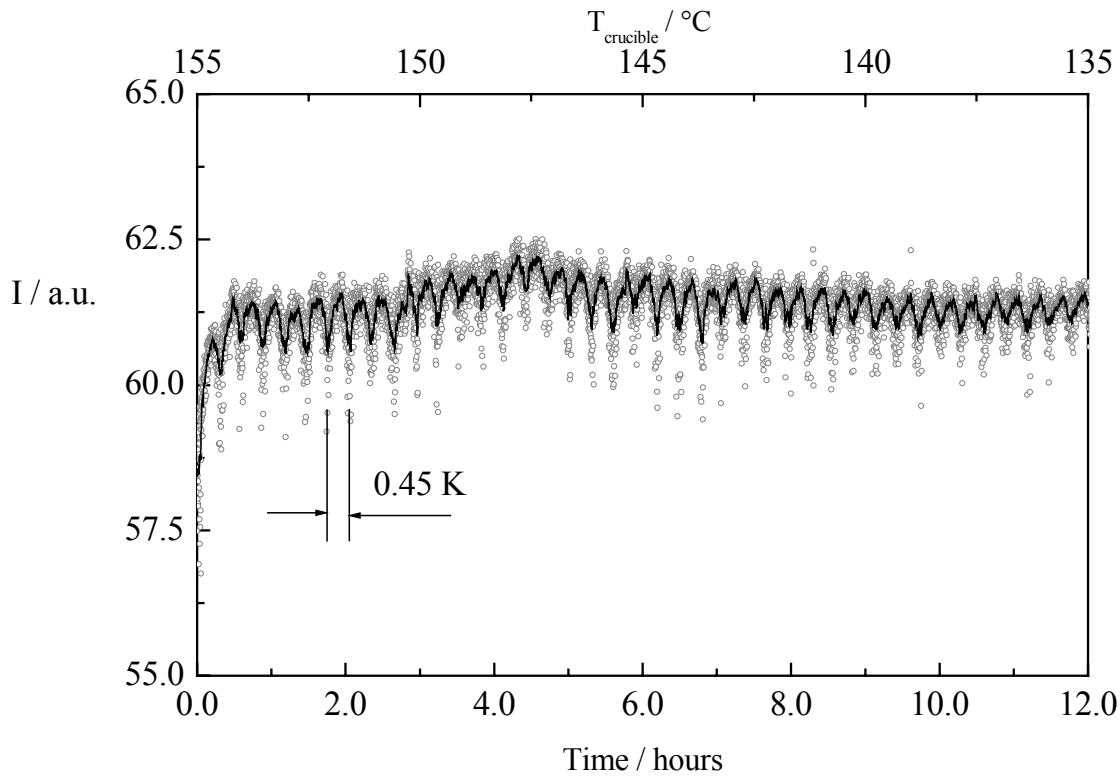


Fig. 5.1.2 Reflectivity of polarized (45° , incidence angle 71.15°) light ($\lambda=450$ nm) in arbitrary units, measured on cooling with 2 K/h of liquid $\text{Ga}_{0.99}\text{Bi}_{0.01}$ alloy (\circ) as a function of time (crucible temperature). Line is an average through the points (is shown for convenience).

5.2 Errors in optical constants and film thickness

• 2 phase model

Since there is the analytical relation between measured ellipsometric angles (Ψ and Δ) and the dielectric function ε of the substrate, the error of ε can be also found analytically:

$$\Delta\varepsilon = \left| \frac{\partial\varepsilon}{\partial\Psi} \right| \delta\Psi + \left| \frac{\partial\varepsilon}{\partial\Delta} \right| \delta\Delta. \quad 5.2.1$$

The contributions of the incidence angle uncertainty and anisotropy of the sapphire* to the final error of the dielectric functions of the potassium-rich phase in the K-KCl measurements can be neglected [Blankenhagen97]. In the case of the Ga-Bi alloys the 2 phase model was applied to the measurements of the pure components. Maximum errors of $\varepsilon_{\text{Ga}}(\omega)$ and $\varepsilon_{\text{Bi}}(\omega)$ are around 1.

* In principle, Eq. 3.25 and 3.26 were obtained for the isotropic media.

• 3 phase model

It is not a trivial task to give the error limits for the components of the parameter vector A (Chapter 3.3). Thorough treatment of this problem can be found in Ref. [Press86]. Variation of the components of vector A during fitting algorithm leads to the change in $\Delta\chi^2$. This change can be defined with the help of the curvature matrix, K , the elements of which are given by:

$$K_{ij} = \frac{\partial^2 \chi}{\partial A_i \partial A_j}. \quad 5.2.2$$

From Eq. 5.2.2 the inverse curvature matrix (K^{-1}) can be found [Press86]:

$$(\Delta A_i^{corr})^2 = (K_{ii})^{-1}. \quad 5.2.3$$

The diagonal elements of the inverse matrix yield the correlated errors of the i 'th element of the vector A . These errors can be later used as an estimation of the maximum error of calculated values. The off-diagonal elements give the cross-correlation coefficients, which are the measure of the correlation between parameters. In reality, it is not possible to define rigorously the error limits of the fitted parameters if there is any correlation between them [Press86].

Modern software for evaluating ellipsometric data incorporates the error analysis with the calculation of curvature matrix, the cross-correlation coefficients and most important errors of the quantities obtained after fitting.

In this work “Film Wizard” {Scientific Computing International, SCI} and “DeltaPsi 2” {Jobin Yvon} programs were used for the data evaluation of K-KCl and Ga-Bi measurements, respectively.

5.3 Sensitivity and limitations

Under the “sensitivity” in this study the smallest reliably measurable film thickness will be understood (minimum measurable thickness); under the “limitation” – the maximum measurable thickness.

For the K-KCl experiment thorough analysis had been done by Staroske in his thesis [Staroske00]. Only one point will be mentioned here. From the model calculation alone, the sensitivity of the K-KCl setup was estimated to be ~5 nm. This value seems to be very optimistic taking into account the severe experimental conditions. In the present work it will be shown that sensitivity is somewhat worse and the uncertainty of the thickness determination arises already at 20 nm. Anyway, all measured salt-rich films had thicknesses

above 100 nm and very high sensitivity was needed in one experiment exclusively (Chapter 6.1, Measurement Set 1, $T=650$ °C, p. 58).

In this work the error analysis of the Ga-Bi setup has been done. To estimate the minimum and maximum measurable film thickness a simple example was considered: pure liquid Bi as a film and the $\text{Ga}_{0.8}\text{Bi}_{0.2}$ alloy as a substrate. The optical properties of the latter were simulated on the basis of EMA approximation (Chapter 3). In Fig. 5.3.1 results of this model calculation for Ψ and Δ are shown as a function of film thickness. The calculation is shown here for a single wavelength of 450 nm but the results are representative for the whole spectral range.

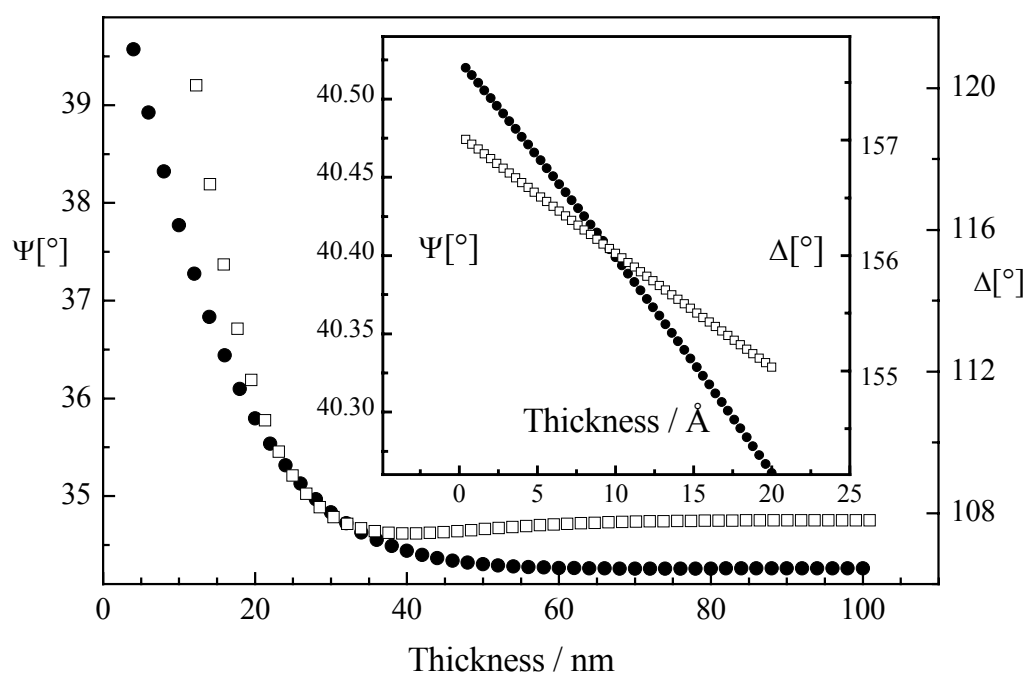


Fig. 5.3.1 Calculations of Ψ (●) and Δ (□) as a function of thickness of the liquid Bi-film on top of the $\text{Ga}_{0.8}\text{Bi}_{0.2}$ liquid alloy substrate. In the inset a small range of the thickness is magnified. Scales of graph and inset are different.

As can be seen in Fig. 5.3.1, for thickness above 500 Å ellipsometric angles Ψ and Δ stay constant – an ellipsometer is “not able to sense” the substrate through such thick film. The values of the ellipsometric angles in this case correspond to those of the pure liquid Bi. The sensitivity is a more subtle and important topic in the study of the wetting phenomena of the Ga-Bi system. At some conditions only a few (or even one) monolayers of Bi are expected (see Chapter 2.4). Can such ultra-thin film be measured in the present setup? One can compare one- and two-monolayer films in the frame of 3 phase model in the inset of Fig. 5.3.1, where small range of thickness is magnified. The contrast in angle Δ is almost 2° ,

which is an order of magnitude more than the accuracy of Δ measurement (see above). Contrast in angle Ψ is considerably less, but even though more than the measurement accuracy. Moreover, the spectroscopic analysis to find the film thickness is made for a broad range of wavelengths. This additionally increases the film thickness resolution. Such remarkable Å-precision is (theoretically) possible for this system due to the already mentioned pronounced difference in the optical properties of liquid Ga (and Ga-Bi alloy) and liquid Bi (for comparison the data can be found in the Appendix, p. 131 and 132).

Similar interfacial model, but with solid Bi film on the top of the $\text{Ga}_{0.9}\text{Bi}_{0.1}$ substrate has been investigated as well. The results – minimum and maximum measurable film thickness, are practically the same as for the calculations above. Solid film becomes a “bulk phase” for ellipsometer when its thickness is above ~50 nm. These results will be used later in the study of the surface freezing transition.

In the conclusion it has to be mentioned that theoretical modeling is, of course, not perfect representation of the real situation and gives only an estimations of sensitivity and limitation of the Ga-Bi setup. The accuracy of the determination of the wetting film thickness was found to be in the range from 2 to 5 Å, i.e. ranging from 100 %, for extremely thin, to ~15...20 %, for thickest film. This estimation can be done if one studies the influence of the single parameter (like: Θ , starting values of d_w and concentration) of the model on its outcome.

In this liquid metal system there is also another principal problem to measure accurately the film of one monolayer – the capillary waves, which should be included in the 3 phase model as a roughness of both interfaces of the film. The amplitude of capillary waves at the conditions (x , T) of all measurement performed here can be estimated as 1.5...2 Å [Ayyad03]. In the following chapter, where the results of ellipsometry measurements of Ga-Bi alloys will be presented, the error bars of wetting film thickness correspond only to an average error of several fits to the measurements at the same temperature (but not to the total error of measurements estimated above).

6. Experimental results

6.1 Results of the measurements of potassium-rich K-KCl melts

In this chapter the results of combined spectroscopic ellipsometry and reflectometry measurements of potassium-rich K-KCl melts are presented. The optical properties as well as the thickness of the wetting film were determined from the ellipsometric angles Ψ , Δ and reflectivity R (raw experimental data can be found in Appendix, p. 119-130) using the 2 or 3 phase models (see Chapter 5).

In all measurements it was relatively easy to distinguish between two interfacial scenarios: sapphire in a contact with a homogeneous bulk metallic liquid and a segregated film of thickness d between sapphire and a metallic liquid. Ellipsometry angles Ψ and Δ for the latter case have visible peculiar structure around 1.3 eV, which is the finger print of F-center absorption expected for KCl in the liquid state (Chapter 2.4). Also the reflectivity measurement is extremely indicative. Its low values show immediately the presence of absorbing film on the otherwise highly reflecting metal-rich phase. In the case of homogeneous bulk metallic phase, i.e. when the 2 phase model is applicable, the real and imaginary parts of dielectric function of K-rich phase are shown. In the case of the 3 phase model the results are given in terms of the refraction n and absorption k coefficients (and thickness of the salt-rich film). This presentation has the advantage of a direct comparison with the literature data of the metallic bulk melts (usually given as ϵ_1 and ϵ_2 spectra) and the salt-rich melts, where absorption measurements exist [Blankenhagen99].

In the following the results are presented as a sequence of experiments or *measurement sets* according to the nominal sample concentrations. Their locations are shown in the K-KCl phase diagram in Fig. 6.1. In each measurement set, if possible, data have been recorded first along liquid-solid coexistence line or a few degrees below it, near the prewetting line (as given by Tostmann et al. [Tostmann95]), above this line and finally after cooling to the liquid-solid coexistence line again.

Errors of n , k and film thickness after evaluation with the 3 phase model are relatively large. To make the graphs more readable the representative error bars are shown only for a few experimental points. So big uncertainty of the determined quantities considerably complicates any quantitative analysis.

A common feature for all measurements is, that the dispersion of the refraction index is not very clearly discernible; this is also true for the previous results [Staroske00]. Anyway, n always lies in the range between 0.5 and 2.0, which is in agreement with the optical properties

of pure KCl [Palik85]. Maxima in the absorption coefficients are relatively high and the halfwidth of the peaks are narrow. The discussion of these optical features of k and the unusual thicknesses of the wetting films will be given in Chapter 7.1. The parameters of the F-center absorption peaks for all measurements are summarized in the Table 6.1.1 at the end of this chapter.

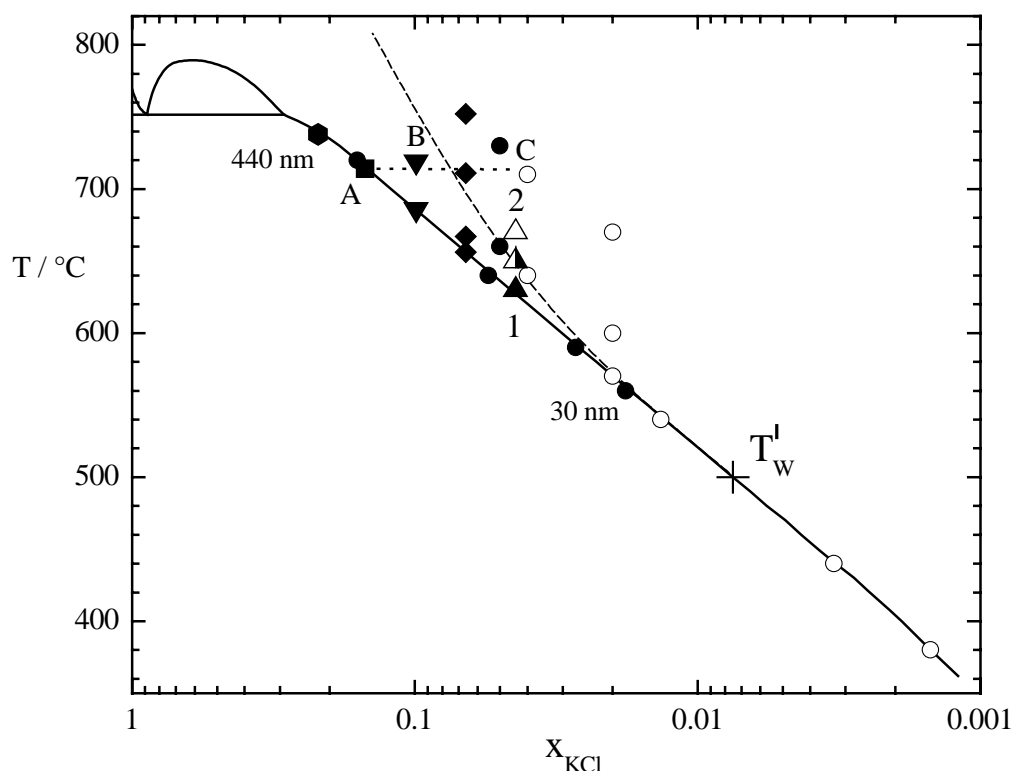


Fig. 6.1. Wetting characteristics of the metal-rich fluid K-KCl system. Solid lines: K-KCl phase diagram [Johnson58]. Dashed line: suggested prewetting line [Tostmann95]. Temperature T'_w (+) is the temperature where the wetting film can be observed for the first time on heating along coexistence. Open symbols present ellipsometric and reflectivity spectra with clear metallic character; full symbols refer to spectra exhibiting wetting character. Circles (●,○) refer to previously obtained results [Staroske], other symbols are new measurements of this work: (▲) – Set Nr. 1, (◆) – set Nr. 2, (▼) – Set Nr. 3, (■) – Set Nr. 4, (●) – Set Nr. 5. Some of the markings made in this figure will be used later in the Chapter 7.1. The spectra at nearly constant temperature along the cut A-B-C are presented in Fig. 7.1.1 in the chapter “Ellipsometric evidence of the wetting transition”. The symbols (▲, △) will be described in the Chapter “Characterization of the prewetting transition”.

1. Measurement Set 1 ($x_K = 0.956$)

Three measurements have been carried out: (1) at 630 °C (solid-liquid coexistence), (2) 650 °C (prewetting line) and the last one (3) at 675 °C.

The concentration of salt in this set is very low in comparison to the other experiments. All three temperatures lie below 700 °C, above which a slight corrosion of the sapphire cell may occur and influence the optical measurements. Hence, the data of this set should be free from this problem. Indeed, after the measurements no traces of corrosion were found on the sapphire surface. Staying below 700 °C has an important advantage to give the system enough time for homogenization after the temperature change. The interval between two measurements in this set was 3 days in comparison to 12 – 16 hours in the other experiments. The ellipsometric angles and reflectivity, measured at 630 °C, give clear evidence of the presence of the wetting film: low value of reflectivity R around 40 % (lower section of Fig. 1A, Appendix), the characteristic maximum in Δ at 1.3 eV (middle section of Fig. 1A). So, the data were interpreted in terms of the 3 phase model. The results – the optical constants n and k - are shown in Fig. 6.1.1.

The 3 phase model gives a fairly good fit to the initial data (Fig. 1A, Appendix) and the obtained film thickness of 220 ± 35 nm is in a good agreement with the previous measurement at similar conditions (x_K , T) [Staroske00]. Optical constants n and k , even though the errors are big, show the Kramer-Kronig consistency [Ashcroft76].

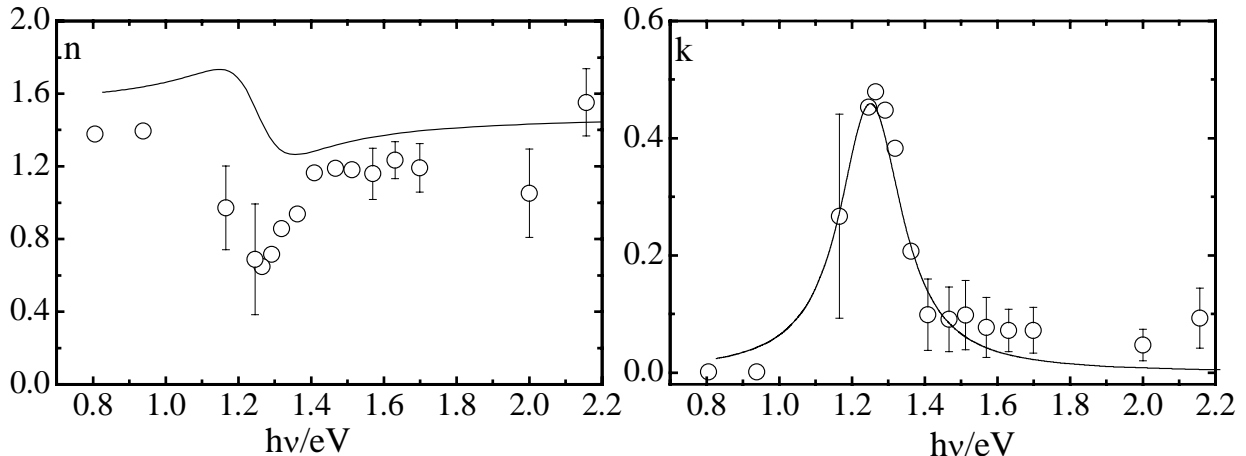


Fig. 6.1.1 Symbols refer to refractive index n (left) and absorption coefficient k (right), results of the 3 phase model analysis of ellipsometric and reflectivity measurements at sapphire/salt rich interface of $K_{0.956}KCl_{0.044}$ melt at 630 °C on coexistence. Lines: Drude-Lorentz fit to k (see the text).

The line in the right part of Fig. 6.1.1 is a Drude-Lorentz fit (Eq. 3.10, Chapter 3.1) to the experimental values of the absorption coefficient. The line in the left part of Fig. 6.1.1, which is in good qualitative agreement with experimental values of n , shows dispersion consistent with the absorption. This is one of a few measurements where such a fine quality and consistency of n and k has been achieved.

The second measurement at $T = 650\text{ }^\circ\text{C}$ seems to be an intermediate case between the clear wetting at $630\text{ }^\circ\text{C}$ and a non-wetting situation at the last temperature $675\text{ }^\circ\text{C}$ (see below). Therefore both the 2 (Fig. 6.1.2) and the 3 phase (Fig. 6.1.3) model had to be tried.

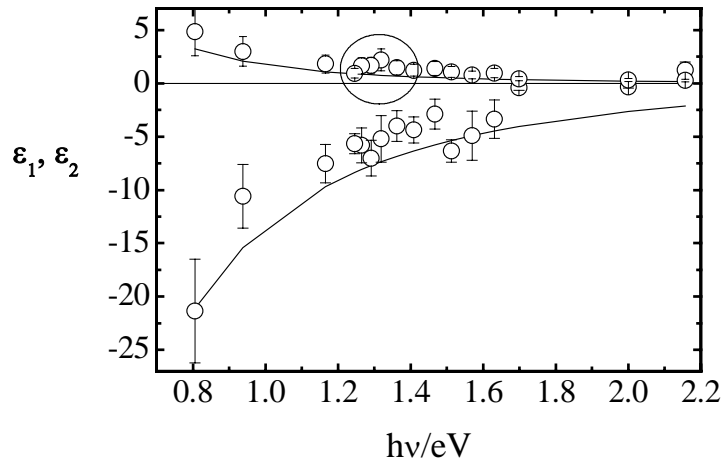


Fig. 6.1.2 Symbols: dielectric function of $\text{K}_{0.956}\text{KCl}_{0.044}$ melt at $650\text{ }^\circ\text{C}$ (near prewetting line) calculated on the base of the 2 phase model. Lines are free electron Drude model calculation using a number density of free electrons of $N_e = 1.066 \cdot 10^{22}\text{ cm}^{-3}$ and dc conductivity of $\sigma_0 = 16970\text{ }(\Omega\text{cm})^{-1}$. Circle marks position of a small maximum around 1.3 eV.

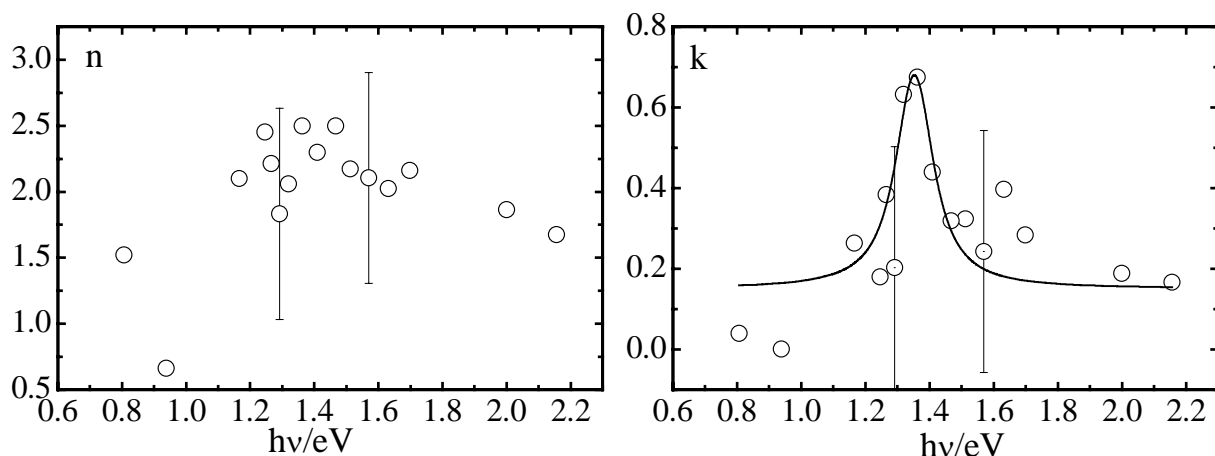


Fig. 6.1.3 Symbols refer to refractive index n and absorption coefficient k , results of the 3 phase model analysis of ellipsometric and reflectivity measurements at sapphire/ $\text{K}_{0.956}\text{KCl}_{0.044}$ interface at $650\text{ }^\circ\text{C}$ near prewetting line. Line in k serves in this figure as a guide for an eye only.

It is difficult to decide which model describes the situation better. The data-points in Fig. 6.1.2 are in agreement with the prediction of the Drude free electron model although a clear systematic deviation in ϵ_1 is apparent; in addition some small but a clear maximum (indicated in Fig. 6.1.2 with circle) in ϵ_2 around 1.3 eV is visible. The high values of reflectivity, nearly 80 % (Fig. 2A) indicate that the wetting film, if present, should be very

thin. Indeed the outcome of the 3 phase model for a thickness is 20 ± 15 nm. There is maximum in k at 1.3 eV, but n doesn't show any structure at all (Fig. 6.1.3). Both n and k show strong scattering and errors (only smallest are shown in Fig. 6.1.3) are dramatic.

Summarizing all above mentioned, one must conclude that such film is actually on the edge of sensitivity of this measurement.

At $T = 675$ °C one clearly detects a bulk metallic liquid in a contact with the sapphire. The spectra are drawn in Fig. 6.1.4 together with a satisfactory free electron model calculation using for the number density of the free electrons $N_e = 1.058 \times 10^{22} \text{ cm}^{-3}$ and $\sigma_0 = 16210 (\Omega\text{cm})^{-1}$ for the dc conductivity [Achener68].

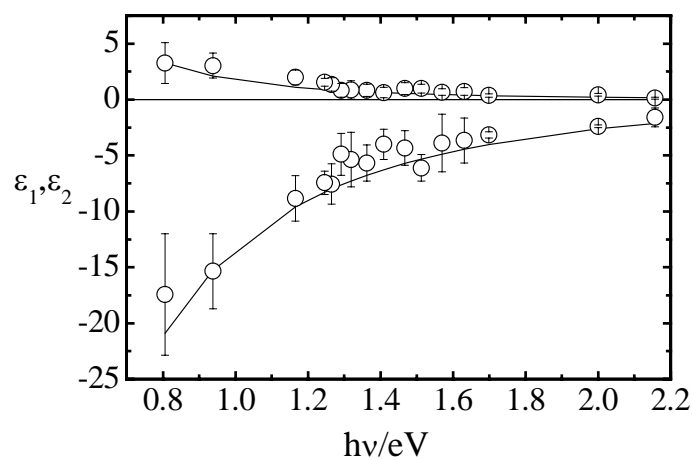


Fig. 6.1.4 Symbols: dielectric function of $\text{K}_{0.956}\text{KCl}_{0.044}$ melt at 675 °C (near prewetting line) evaluated on the base of the 2 phase model. Lines are free electron Drude model calculations using a number density of free electrons of $N_e = 1.058 \times 10^{22} \text{ cm}^{-3}$ and dc conductivity of $\sigma_0 = 16210 (\Omega\text{cm})^{-1}$.

The reflectivity also shows practically pure metallic values (Fig. 3A). There is an interesting feature in the reflectivity data, a slight minimum around 1.7 eV. A similar behaviour has been observed for Rb-RbCl system. This dispersion was related with the interband transitions [Nattland86]; however there might be another explanations for this feature in the present experiment.

No data could be recorded after cooling of this sample, since the cell leaked.

2. Measurement Set 2 ($x_K = 0.934$)

Four measurements have been performed: (1) at 656 °C (solid-liquid coexistence), (2) at 711 °C (slightly above prewetting line), (3) at 752 °C and the last one (4) after cooling the system back to coexistence at 667 °C. The disadvantage of this measurement set is the absence of one very important Nd:YAG laser, which was broken during the calibration. So, one point of the spectra at 0.93 eV is missing.

For the first temperature, as it is expected from the very low values of reflectivity and maximum in Δ around 1.3 eV (Fig. 4A), the 3 phase model, which has to be applied, will reveal a relatively thick wetting film. The results are shown in Fig. 6.1.5 and the determined film thickness is 220 ± 40 nm. The 3 phase model shows very good fit to the original data (Fig. 4A).

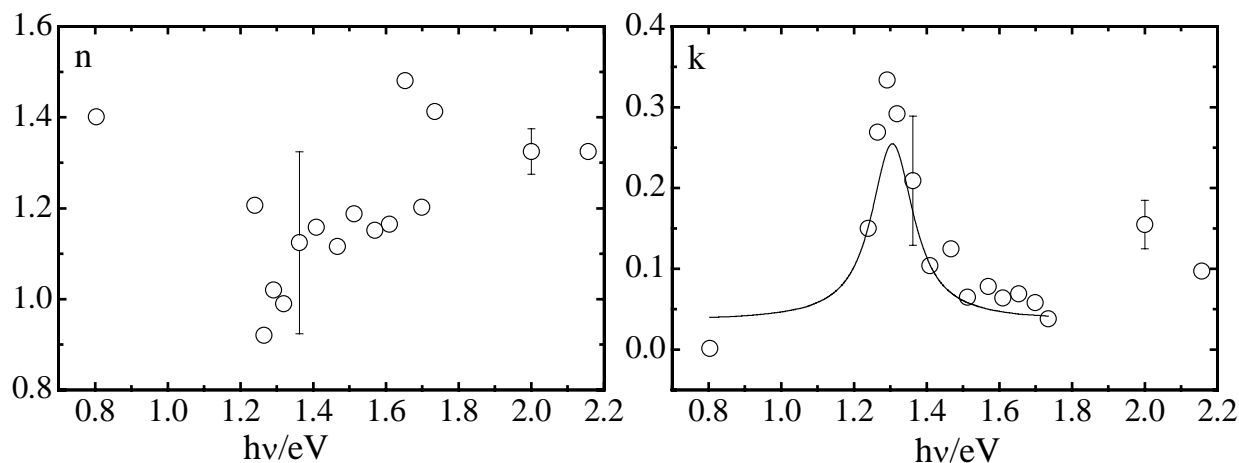


Fig. 6.1.5 Symbols refer to refractive index n and absorption coefficient k , results of the 3 phase model analysis of ellipsometric and reflectivity measurements at sapphire-salt rich interface of $K_{0.934}KCl_{0.066}$ melt at $656^\circ C$ on coexistence. Line in k is a function fitted to selected data points (see text).

F-center absorption at 1.3 eV in k and structure in refraction index n are clearly discernible. To obtain some parameters of the absorption band the following fit to k has been performed.

This is a fit of the Lorentz-type function $k = \frac{A}{B} \cdot \frac{1}{4(h\nu - h\nu_0)^2 + B^2}$ (generic form of Eq. 3.10

recalculated for k) to the selected experimental points (points obviously deviating from the common dependency were excluded). Error bars of k were not taken into account during the fit. This procedure allowed the estimation of the maximum absorption k_{\max} and halfwidth ΔE (A and B in the equation, respectively) of the absorption peaks. Lines in the all following figures of the absorption coefficient were drawn according to the described procedure.

There were no doubts for the application of the 3 phase model to interpret the results at $711^\circ C$. The optical constants are shown in Fig. 6.1.6. The film thickness decreases but remains relatively thick - 150 ± 50 nm. The decrease in the film thickness is in accordance with the wetting scenario and with the increase of the values of reflectivity (Fig. 5A).

The next temperature of $752^\circ C$ was a very difficult experimental task. The measurement had to be done quickly to avoid high temperature corrosion of the sapphire cell. It is also difficult to control such high temperature with the same precision as lower temperatures. The thermal radiation from the furnace can influence the ellipsometric measurement, since the

wavelengths are in the measurements range. The contribution of each effect alone was checked and proved to be small, but total influence is difficult to estimate.

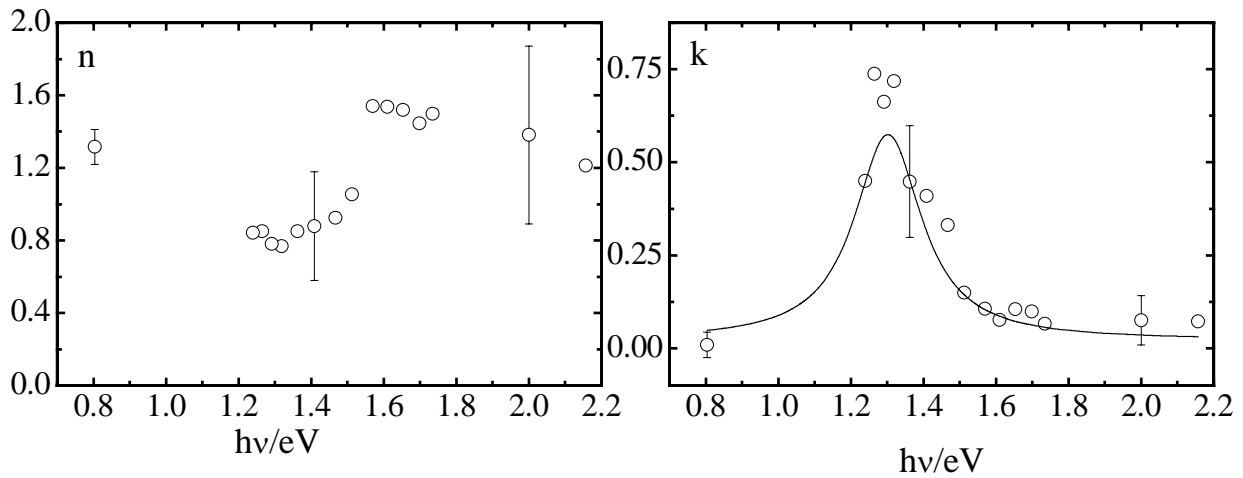


Fig. 6.1.6 Symbols refer to refractive index n and absorption coefficient k , results of the 3 phase model analysis of ellipsometric and reflectivity measurements at sapphire-salt rich interface of $\text{K}_{0.934}\text{KCl}_{0.066}$ melt at $711\text{ }^\circ\text{C}$ near prewetting line. Line in k is a function fitted to selected data points (see text).

Since above the prewetting line one could expect that the wetting film would disappear, as a first approach the 2 phase model was applied. It showed unphysical values ($\epsilon_1 > 0$) of the dielectric function of assumed metal-rich phase. The 3 phase model describes the results better. Even though the fit to the reflectivity is very poor, it is quite good for ellipsometric angles Ψ and Δ (Fig. 6A). The 3 phase model results are shown in Fig. 6.1.7.

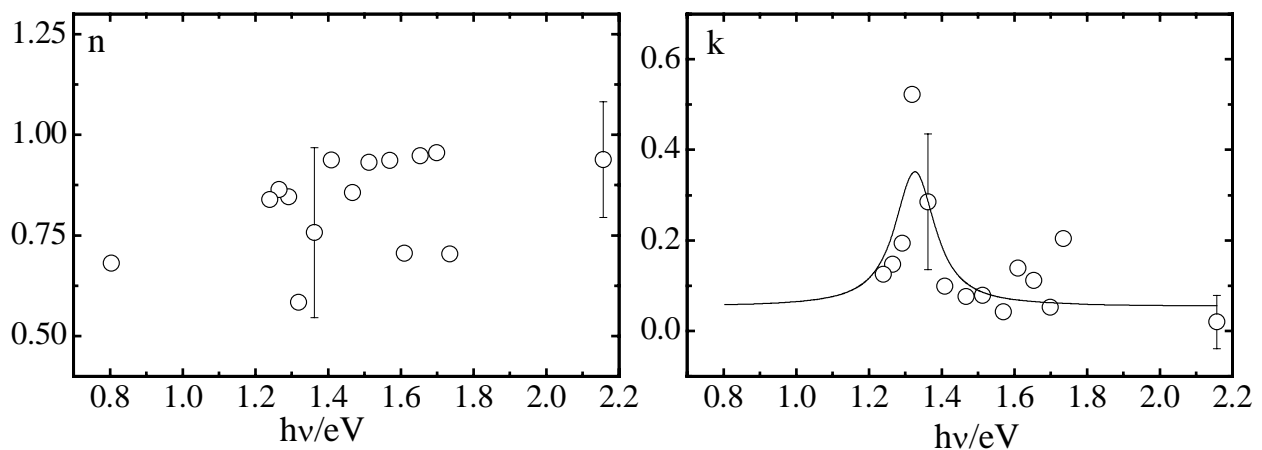


Fig. 6.1.7 Symbols refer to refractive index n and absorption coefficient k , results of the 3 phase model analysis of ellipsometric and reflectivity measurements at sapphire-salt rich interface of $\text{K}_{0.934}\text{KCl}_{0.066}$ melt at $752\text{ }^\circ\text{C}$ above prewetting line. Line in k is a function fitted to selected data points (see text).

The errors are large but one still can see the F-center absorption peak at 1.3 eV. The value obtained for the film thickness is 80 ± 40 nm. The big error of the thickness and scattering of

the optical coefficients can be explained by all experimental difficulties mentioned above. It was interesting to measure in the next experiment at the same temperature as at the beginning and compare both. This could directly show the influence of the sapphire corrosion on the results. But more important, that it could give very valuable insight in the different behaviour of wetting film on heating and on cooling (*hysteresis*), which is a major feature of the wetting transitions. Unfortunately, such experiment is almost impossible for the present setup. This is due to inhomogeneous relieve of the stress in the cell and its holder (see cell construction Chapter 4.1, p. 30). The cell usually becomes untight - does not matter how cautiously the temperature is reduced. Nevertheless, in this set such attempt was successful - the cell was still closed after the cooling. Only the final temperature 667 °C occurred to be slightly differed from the measurement (1). There can be the following explanation: there is a change in thermo-conductance conditions in the chamber-furnace-sample system after “annealing” it for some time at high temperature. So, in spite of the fact that the parameters for the temperature controller were exactly the same as used the first time, the difference was 11 K. It was too risky to try to cool the sample further.

Taking the temperature difference into account, both measurements (1) and (4) are in very good agreement. The 3 phase model was applied and the results are shown in Fig. 6.1.8. The fit to the experimental data is quite good (Fig. 7A).

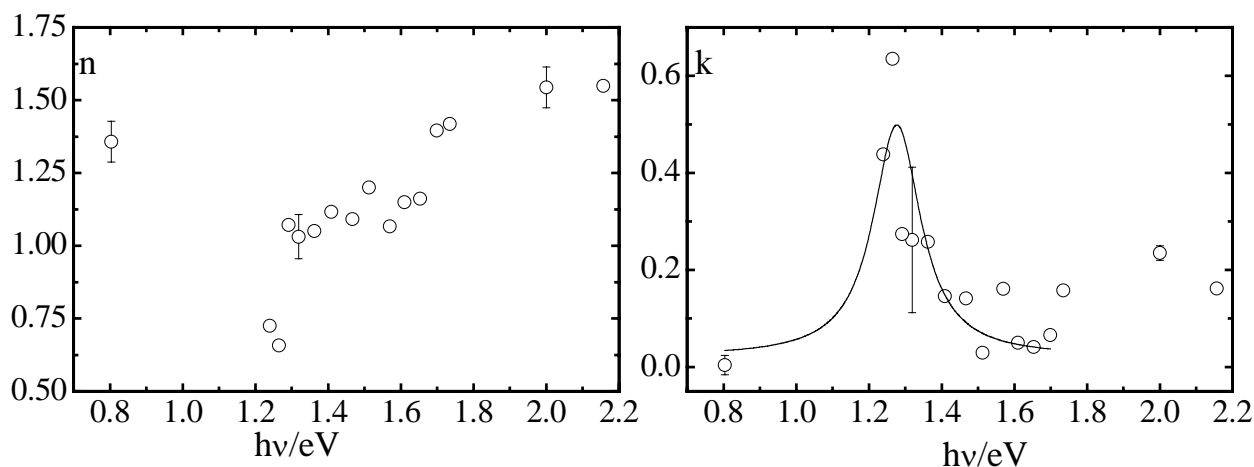


Fig. 6.1.8 Symbols refer to refractive index n and absorption coefficient k , results of the 3 phase model analysis of ellipsometric and reflectivity measurements at sapphire-salt rich interface of $K_{0.934}KCl_{0.066}$ melt at 667 °C slightly above coexistence. Line in k is a function fitted to selected data points (see text). (667 °C; $x_K = 0.934$).

One can compare Fig. 6.1.5 and 6.1.8. The optical constants are practically the same, the film thickness is 200 ± 20 nm, which is almost the same as in the first measurement (220 nm). At this point the influence of the corrosion on the experimental results can be discussed. Corrosion leads to the roughness of the sapphire interface. Such problem is normally treated

in the frame of the effective medium approximation [Azzam77] (see p. 28). The effective optical properties of the rough layer in the present work were combined from that of sapphire and the salt-rich phase. The model becomes complicated. There are now two films, which imply one more parameter – thickness of the rough layer. The fitting process in this case became unstable. As the outcome, it gave either unphysical results or extremely big errors for the calculated values. Any way, it was possible to track some common features in all performed approaches. First, the thickness of the rough layer decreases or even completely disappeared. And second, that the n and k of the EMA-layer tended to be the same as for the salt-rich film after use of the one-layer model. The conclusion was made, that the additional rough layer does not give better agreement between measured and calculated quantities. This shows that the effect of microscopic corrosion is very small or not detectable in our particular sophisticated (sapphire cell, high temperature) setup. Moreover, sapphire surface always was carefully examined after the cell was disassembled. In the present measurements only slight traces of corrosion were observed.

3. Measurement Set 3 ($x_K = 0.901$)

Two measurements have been performed: (1) at 681 °C - coexistence, (2) 719 °C - slightly below prewetting line. Due to the high temperatures required for this concentration, it was planned to approach the prewetting line after the measurement at coexistence in several steps. Unfortunately, at a temperature above 719 °C the cell leaked.

For the first measurement on coexistence at 681 °C the 3 phase model gives very good fit to experimental data (Fig. 8A), and shows the presence of a thick wetting film of 250 ± 50 nm. The absorption coefficient has typical F-center absorption features, Fig. 6.1.9. The refraction index shows the structure, which is consistent with F-center absorption.

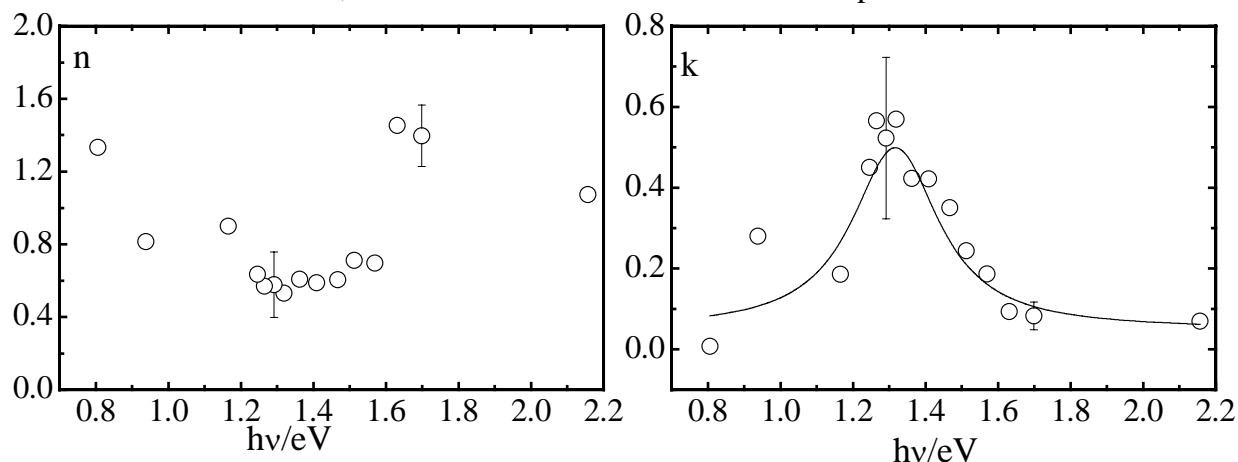


Fig. 6.1.9 Symbols refer to refractive index n and absorption coefficient k , results of the 3 phase model analysis of ellipsometric and reflectivity measurements at sapphire-salt rich interface of $K_{0.901}KCl_{0.099}$ melt at 681 °C on coexistence. Line in k is a function fitted to selected data points (see text).

The value of reflectivity remains still low at the next temperature of 719 °C, slightly below prewetting line. So, the 3 phase model was applied for this temperature too. It gives a very good fit to the experimental data (Fig. 9A).

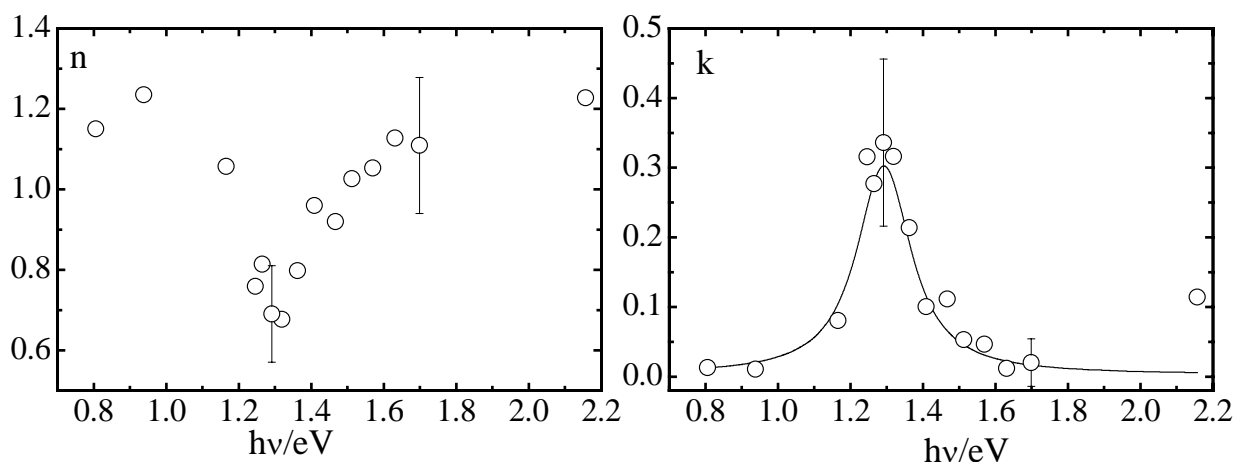


Fig. 6.1.10 Symbols refer to refractive index n and absorption coefficient k , results of the 3 phase model analysis of ellipsometric and reflectivity measurements at sapphire-salt rich interface of $K_{0.901}KCl_{0.099}$ melt at 719 °C on coexistence. Line in k is a function fitted to selected data points (see text).

The determined film thickness is 150 ± 60 nm. This value is quite big for the situation off-coexistence (but it is clearly less than at coexistence). The absorption and refraction coefficient are shown in Fig. 6.1.10. Taking into account the high temperature and all difficulties following from it, the quality of n and k is very good. Moreover, the coefficients are Kramer-Kronig consistent. One common feature for all measurements can be seen particularly well in this set. After leaving the coexistence the halfwidth of the absorption peak reduces (compare Fig. 6.1.9. and Fig. 6.1.10). Possible explanation of this effect will be offered in the Chapter 7.1.

4. Measurement Set 4 ($x_K = 0.75$ - filled, $x_K^I = 0.85$ – on the solid-liquid coexistence line)

Only one measurement at $T = 714$ °C on coexistence line could be performed for this concentration. After heating, the melt decomposed into salt-rich islands surrounded by the metallic phase (origin of both phases was confirmed by the reflectivity measurements). The ellipsometry could not be done in such situation, since the size of the islands was comparable with the diameter of the laser beam spot ($\varnothing 1.5$ mm). The main reasons for such behaviour of the melt probably are the shortages in the sample preparation and/or too quick temperature increase. For the preparation of so high concentration, the salt volume had to be almost the same as of the metal (Chapter 4.1). The crystals were also relatively big. This in turn required long times for their dissolution in the liquid potassium and increased the time for a homogenisation of the mixture. But waiting at the high temperature increased a risk of

corrosion. The measurements with high salt concentration (and at high temperatures) became extremely difficult and also unstable. Several of them were finished without any results at all. In this measurement, at temperature of 714 °C the concentration of the liquid phase at the sapphire/melt interface according to the phase diagram is 0.85 (the weighted sample concentration is $x_K=0.75$). For so high concentration the assumption of pure potassium as a substrate in the 3 phase model can be questionable. Anyway, applied here in the same way as before, 3 phase model gives quite good fit to experimental data (Fig. 10A). The determined optical constants are shown in Fig. 6.1.11. The film thickness of 330 ± 40 nm is in agreement with the extremely low reflectivity values (lower section of Fig. 10A).

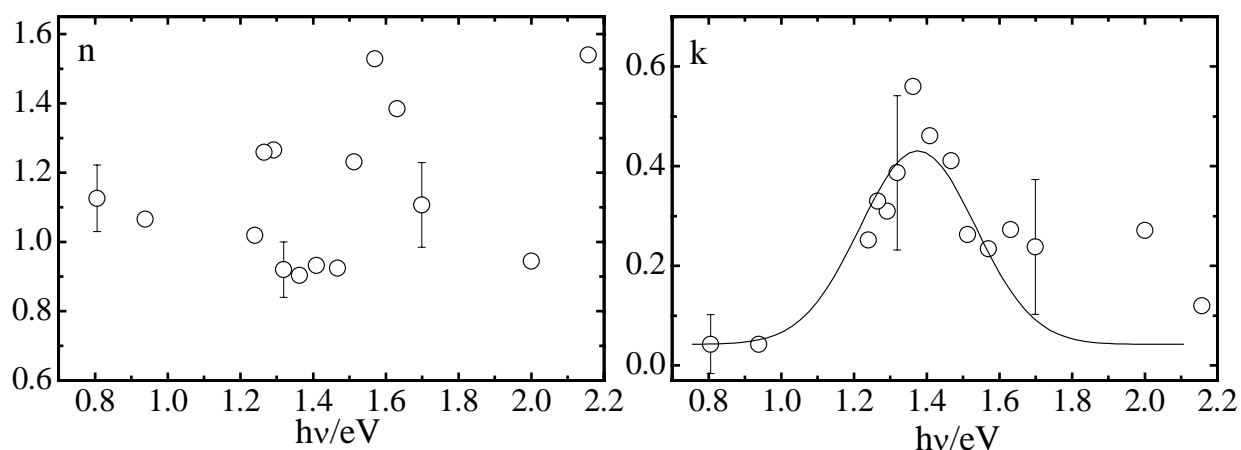


Fig. 6.1.11 Symbols refer to refractive index n and absorption coefficient k , results of the 3 phase model analysis of ellipsometric and reflectivity measurements at sapphire-salt rich ($x_K^I = 0.85$) interface of $K_{0.75}KCl_{0.25}$ melt at 714 °C on coexistence. Line in k is a function fitted to selected data points (see text).

The halfwidth of the absorption band is clearly broader than in the measurements before. The refraction index is unstructured and scattered a lot, but its values lie still in the physical range expected for the salt-rich phase.

5. Measurement Set 5 ($x_K = 0.78$)

Only one measurement at coexistence at 738 °C has been performed for this concentration too. This is the measurement with the highest salt concentration. So it is naturally endowed with the same problems as described in the previous subsection. The same phenomena of the phase decomposition happened here after the heating. The situation did not change even after several days of waiting at the second temperature. The visible islands did not grow or disappear. Though a single temperature only, this measurement was a success. In spite of all experimental difficulties the quality of experimental data (Ψ , Δ and R) values is surprisingly good. The conventional 3 phase model fits Ψ , Δ and R quite well. The results, n and k , are shown in Fig. 6.1.12. The determined thickness of the film is 440 ± 50 nm.

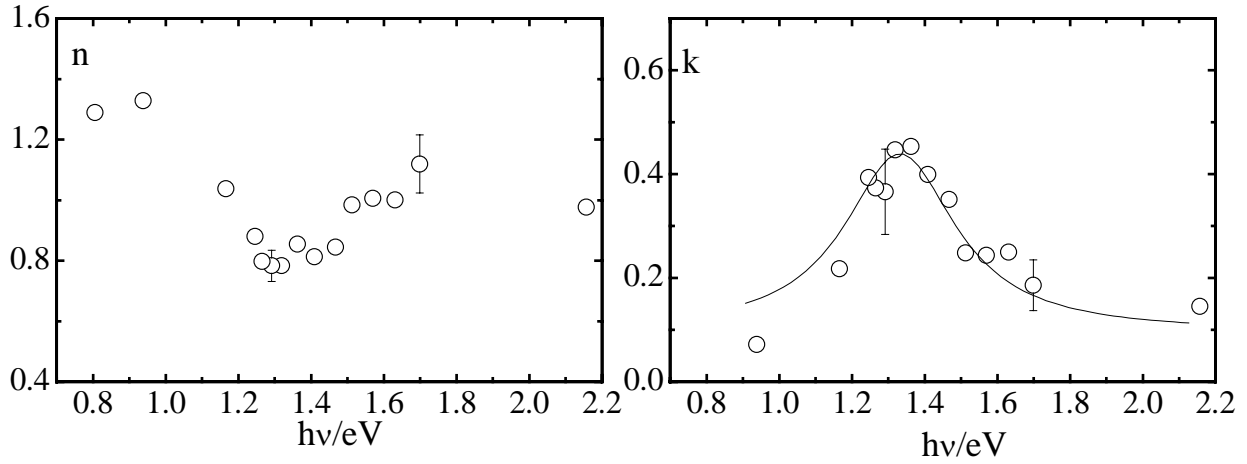


Fig. 6.1.12 Symbols are refractive index n and absorption coefficient k , results of the 3 phase model analysis of ellipsometric and reflectivity measurements at sapphire-salt rich interface of $\text{K}_{0.88}\text{KCl}_{0.22}$ melt at 738°C on coexistence. Line in k is a function fitted to selected data points (see text).

To facilitate an orientation on the “landscape of K-KCl results” (Fig. 6.1 at the beginning of the chapter) and further discussion, all results of the 3 phase model calculations are collected in the Table 6.1.1. It is divided into measurements “at” and “off” coexistence. The first column of the table shows the number of the corresponding figure in this chapter.

TABLE 6.1.1. Spectral parameters for salt-rich wetting films: x_K nominal potassium mole fraction, T temperature, $x_K^{(l)}$ composition of the liquid phase, E_0 energy of the absorption maximum, d thickness of the salt-rich film, k_{max} maximum absorption, ΔE estimated half width of the absorption band. Error of the film thickness is obtained after the 3 phase model calculation. For the error of k_{max} , the error of $k(E_0)$ determined from the 3 phase model was taken. Due to very big uncertainty of k , value of ΔE could be only estimated, its error run up to 50% or unfortunately even more.

Fig.	x_K	$T/^\circ\text{C}$	$x_K^{(l)}$	E_0/eV	d/nm	k_{max}	$\Delta E/\text{eV}$		
-	0.800	560	0.982	1.50 ± 0.10	30 ± 20	0.60 ± 0.20	0.60	[Staroske00]	at
-	0.950	580	0.973	1.35 ± 0.05	130 ± 40	0.23 ± 0.07	0.20	[Staroske00]	
6.1.1	0.954	630	0.954	1.30 ± 0.10	220 ± 35	0.47 ± 0.10	0.15	this work	
-	0.800	640	0.947	1.32 ± 0.05	200 ± 100	0.30 ± 0.05	0.50	[Staroske00]	
6.1.5	0.934	656	0.934	1.30 ± 0.05	240 ± 40	0.30 ± 0.15	0.21	this work	
6.1.9	0.901	681	0.901	1.35 ± 0.10	250 ± 50	0.50 ± 0.20	0.32	this work	
6.1.11	0.750	714	0.850	1.40 ± 0.20	330 ± 40	0.45 ± 0.20	0.42	this work	
-	0.800	720	0.840	1.32 ± 0.05	300 ± 100	0.70 ± 0.06	0.60	[Staroske00]	
6.1.12	0.780	738	0.780	1.35 ± 0.10	440 ± 50	0.50 ± 0.15	0.53	this work	
6.1.10	0.901	719	-	1.30 ± 0.05	150 ± 60	0.35 ± 0.10	0.20	this work	off
6.1.8	0.934	667	-	1.25 ± 0.10	200 ± 20	0.50 ± 0.10	0.20	this work	
6.1.6	0.934	711	-	1.30 ± 0.10	150 ± 50	0.60 ± 0.15	0.22	this work	
6.1.7	0.934	752	-	1.35 ± 0.10	80 ± 40	0.40 ± 0.15	0.18	this work	
6.1.3	0.954	650	-	1.35 ± 0.10	20 ± 15	0.60 ± 0.20	0.15	this work	
-	0.950	660	-	1.33 ± 0.05	90 ± 40	0.25 ± 0.10	0.2	[Staroske00]	
-	0.950	730	-	1.3	~ 60	0.15-0.3	-	[Staroske00]	

6.2 Results of Ga_{1-x}Bi_x alloy measurements

Selected results of spectroscopic modulation ellipsometry measurements of Ga-Bi alloys will be divided in four parts. In the first subsection the optical constants of the pure components will be presented. The dielectric functions of pure gallium and bismuth in a liquid state have been measured at several temperatures in a broad spectral range. In addition, the optical properties of the pure solid Bi were obtained (for convenience this data are described in the section about the surface freezing transition). The next section deals with the wetting behaviour of liquid Ga_{1-x}Bi_x alloys. The formation of the wetting films can be clearly seen from the ellipsometric data. The variation of the thickness along the different experimental paths in the phase diagram has been studied using the 3 phase model. Its applicability will be justified on two examples. The third section concentrates on a new effect, specific for a liquid alloy interface, an oscillatory interfacial instabilities, which indicate periodical bulk behaviour during the spinodal decomposition. It is characterized here for the first time by ellipsometry. In the last part an approach to study the surface freezing transition in Ga-Bi by ellipsometry will be presented (concentration choice and experimental strategy). Experimental difficulties and collected observations of this peculiar transition will be summarized.

For the sake of brevity, several features common for all measurements will be listed in this introduction. In this study of liquid Ga_{1-x}Bi_x alloys it was possible to perform two types of measurements: *kinetic* and *spectroscopic*. The name of the former is given after an acquisition routine of the program “PsiDelta2” used in this work {Jobin Yvon}. During *kinetic* measurements the data are recorded continuously every 1-10 seconds at a single wavelength 450 nm during some thermal treatment of the sample (mostly cooling). *Spectroscopic* (SE) measurements have been performed in the full spectral range of the ellipsometer from 0.8 to 4.65 eV, at different constant temperatures and compositions whenever a detailed characterization of the optical constants of the interface or the film thickness was of interest.

In all experiments perfectly clean and flat surfaces of the liquid metal were routinely obtained, independent of the initial contamination. For all concentrations and studied temperatures the vacuum was around $5 \cdot 10^{-9}$ mbar. No oxide formation after cleaning has ever been noticed. All preparations of the measurements are described in Chapter 4.2. Precision and accuracy of the setup was discussed in Chapter 5.

• Optical properties of pure liquid Ga and Bi

The data of the pure components will be crucial throughout the whole study. Their precision will influence all final model calculations and the conclusions drawn from them. At the

beginning the attempt was made to find such information in the literature. In spite of the fact that liquid metals are a topic of considerable technological and fundamental interest, no really thorough study of the optical properties of Ga and Bi was found. The data had been taken only at a limited number of photon energies and a single temperature practically in each study. Sometimes the experiments were done in an inert gas atmosphere, no specification of the metal surface was often mentioned. All this stimulated to conduct the measurements of both pure liquid metals.

Pure liquid Ga. The measurements have been performed at 5 temperatures in the range from 50 to 300 °C (Fig. 12A, “A” for Appendix). At each temperature up to 5 spectra were taken after several hours of a temperature stabilization.

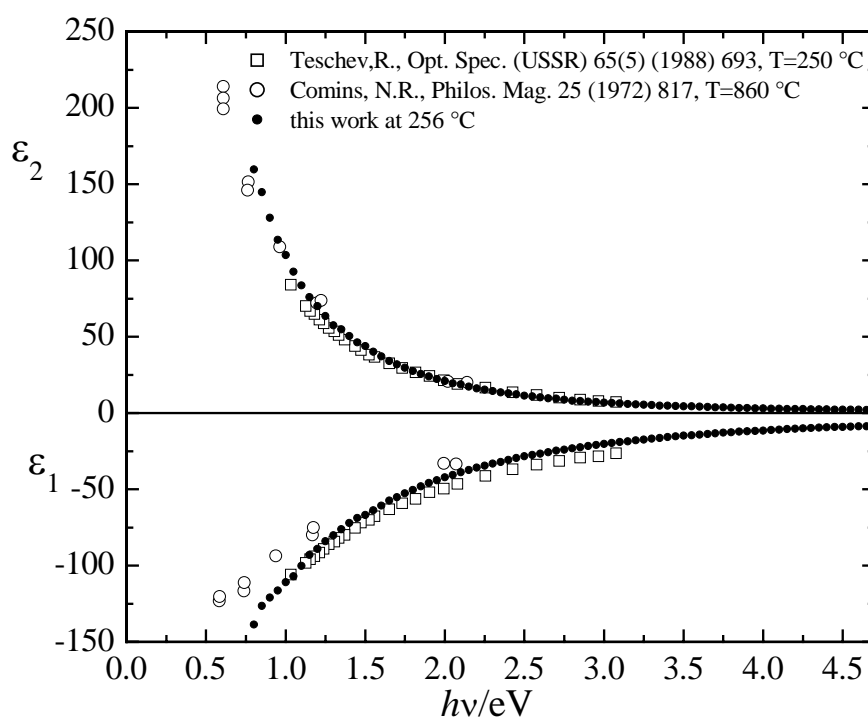


Fig. 6.2.1 Comparison of the dielectric function of liquid pure Ga at 256 °C (this work) with available literature data. Identification of the symbols and respective citations are given in the inset.

In Fig. 6.2.1 a comparison of one spectrum of this work for pure Ga at 256 °C with literature data is shown. Only two relevant publications were found: [Comins72] at 860 °C and [Teschev88] at 250 °C. The last reference is of particular interest, since several temperatures were measured and the spectral range is relatively broad (even though only half of the present spectra). But as one can see, there is a systematic deviation between the literature data [Teschev88] and those of this work for nearly the same temperature (in the values of the dielectric function and its line shape, especially visible in ϵ_1). The reason could be surface contaminations like oxides. Such information is not mentioned in [Teschev88], nor is the

purity of Ga given. In this respect our data is defined better: UHV, Ga purity and surface cleanness as mentioned above.

Our spectra of liquid Ga are in very good agreement with the simple free electron model. This can be seen in Fig. 6.2.3, for the spectrum taken at 256 °C – experimental points and free electron Drude model lines nicely agree. Details of this fit are presented below for both liquid gallium and bismuth together.

Pure liquid Bi. Six measurements have been made in the temperature range from 290 to 385 °C (Fig. 13A) in the same way as for pure liquid Ga. During these experiments the vacuum was worse than in all other measurements (see Table 6.2.2A).

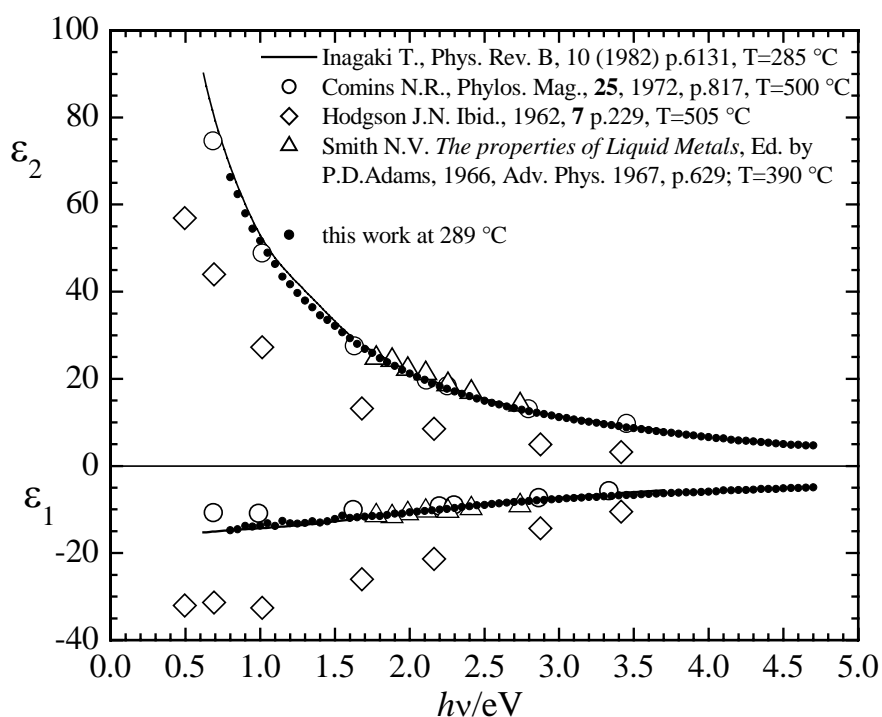


Fig. 6.2.2 Comparison of the dielectric function of liquid pure Bi at 289 °C (this work) with available literature data. Identification of the symbols and respective citations are given in the inset.

There can be several reasons for this. To melt Bi and achieve higher temperatures the heating element had to be at 350-450 °C. The outgas from furnace elements can be very strong. Also at such temperatures the vapour pressure of liquid Bi rises considerably. Anyway, even with a pressure increased up to 10^{-8} mbar no oxide formation was noticed.

In Fig. 6.2.2 one can see a comparison of several spectra found in the literature of liquid Bi with one spectrum at 289 °C of this work. A good agreement, especially with the very reliable study (UHV, in-situ cleaning) of Inagaki et al. [Inagaki82], is clearly seen.

In principle, the experimental spectra of liquid Ga and liquid Bi could be directly used without any further analysis. But it is interesting to extract some additional information from the optical data and compare it with the results of direct measurements.

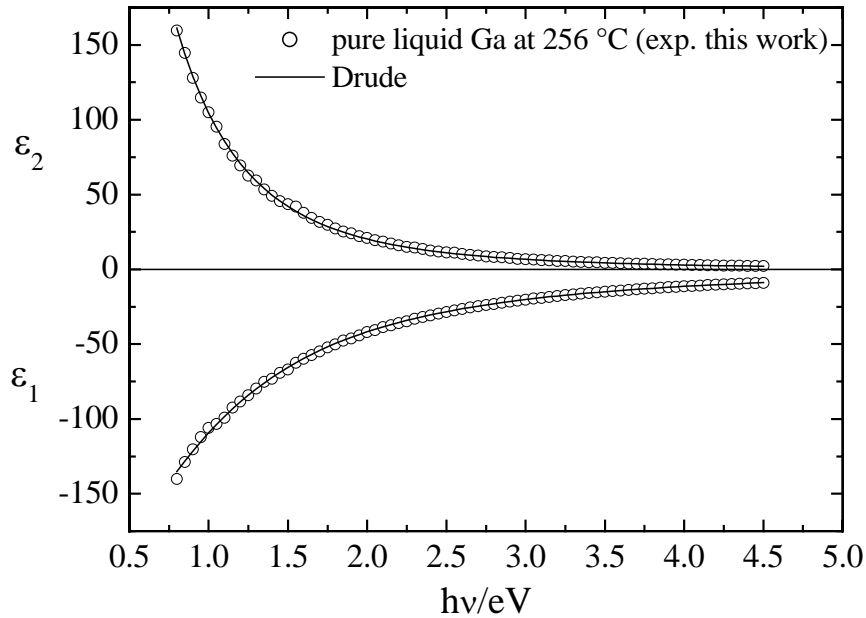


Fig. 6.2.3 Comparison of the experimental spectra of pure liquid Ga (\circ) at 256 °C with the free electron Drude model (lines). Parameters after the fit are $\omega_p=14.51$ eV, $\gamma_D=0.908$ eV.

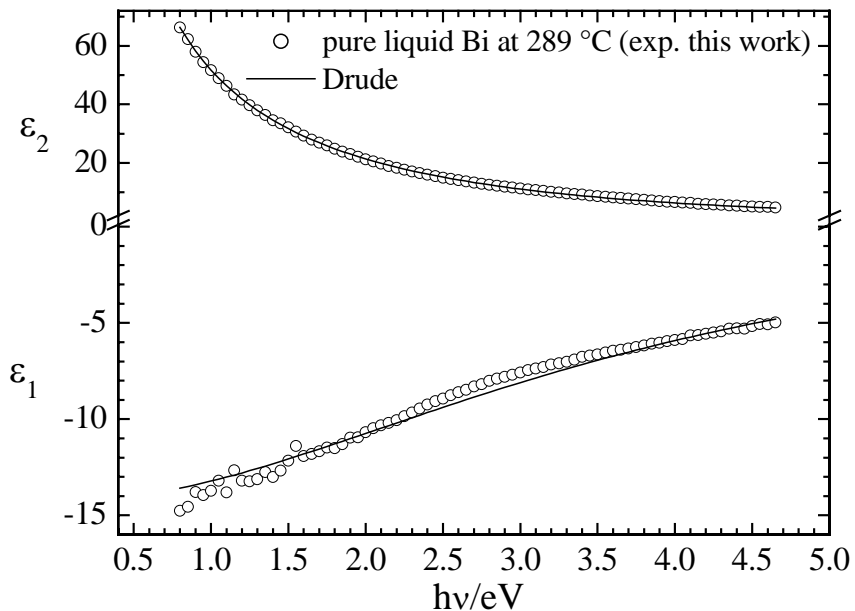


Fig. 6.2.4 Comparison of the experimental spectra of pure liquid Bi (\circ) at 289 °C with the free electron Drude model (lines). Parameters after the fit are $\omega_p=14.49$ eV, $\gamma_D=3.85$ eV. Attention: scales for ϵ_1 and ϵ_2 are different.

It is very easy to treat a liquid metal in the frame of the Drude free-electron model (Chapter 3.1). This simple model can be directly applied to the measured intensities I_C and I_S . Both intensities were fitted within the 2 phase model for the spectra of liquid metals to obtain $\omega_p(T)$

and $\gamma_D(T)$. The results of these fits are summarized in the Appendix, in Table 6.2.1A for Ga and 6.2.2A for Bi.

Here the quality of the fits to the spectra is shown in Fig. 6.2.3 for liquid Ga at 256 °C and for liquid Bi at 289 °C in Fig. 6.2.4. As one can see, the fit for the liquid Ga is perfect. This is not the case for the liquid Bi. The fit is good within the error bars of ϵ_1 and ϵ_2 (not shown here but maximum errors are ± 1.5), but even though the discrepancy in the line shape of ϵ_1 is clearly discernible. Obviously, the Drude model does not satisfactorily describe liquid Bi, a fact noticed in several studies, for example in Ref. [Inagaki82]. In the solid state Bi is semimetal, therefore it is not surprising that experimental ϵ_1 and ϵ_2 deviate from the free electron values [Hafner92].

The values $\omega_p(T)$ and $\gamma_D(T)$ determined from the fits were averaged for several measurements at a single temperature. These data can be used to calculate the electron density $N_e(T)$ and the dc-conductivity $\sigma(T)$ (see Eq. 3.8 in Chapter 3.1) for both liquid metals. In turn, the $N_e(T)$ and $\sigma(T)$ can be found from the direct measurements. Data of $N_e(T)$ were re-calculated from liquid metal density measurements [Steinberg74], conductivity σ was taken from the work of Cusack [Cusack59]. A comparison of these data with the spectroscopic results of this work is given in the Appendix: Table 6.2.1A and 6.2.2A, also shown in Fig. 6.2.3A and 6.2.4A (see pp. 131-133). Both liquid metals exhibit correct trends of $N_e(T)$ and $\sigma(T)$ with temperature and the values are close to the ones measured directly. The comparison shows that ϵ_1 and ϵ_2 of the Ga in liquid state are well described by the Drude free-electron model. This is not a completely new fact and was already noticed by a number of investigators but on the basis of limited to one temperature and few point's spectral data. Liquid Bi requires further analysis but in principle the free-electron model describes this metal satisfactorily. These pieces of information are very important since they allow to simulate the dielectric functions of liquid Ga and Bi if direct measurements at certain temperature or photon energy are not available.

In a brief conclusion of this section the following points are of particular interest:

- a. During this work high accuracy dielectric functions of pure Ga and Bi have been obtained in a broad spectral and temperature range. Good general agreement with the spectroscopic data available in the literature indicates that the whole setup works properly and the measurements were performed correctly.
- b. Taking into account the surface cleanness and the achieved UHV conditions together with the wide energy range covered by the spectra in this work, the present data are clearly improved the comparison with existing literature values of ϵ_1 and ϵ_2 of Ga and Bi. Therefore later in the models for Ga-Bi alloys exclusively the data of pure components measured in this work will be used.

• Ellipsometric data and wetting behaviour approaching liquid-liquid coexistence

Possible experimental paths to study a wetting transition were discussed in Chapter 2.1. The easiest experimentally accessible thermodynamic variable of the system is the temperature. For example heating a $\text{Ga}_{1-x}\text{Bi}_x$ sample of a certain concentration (x_{Bi} between monotectic ~ 0.085 and critical ~ 0.3 concentrations) one could in principle investigate the wetting transitions along solid-liquid curve approaching the monotectic point, along Ga-rich part of liquid-liquid demixing line and in homogeneous liquid region of Ga-Bi phase diagram (see Chapter 2.4). Exactly in this way the measurement of Huber et al. has been performed [Huber02]. In this work, due to the reasons that will be described below (see p. 80), it was impossible to reproduce such heating experiment. Here the wetting transition was studied on cooling with the help of kinetic and spectroscopic measurements for several concentrations, which lie inside the miscibility gap ($x_{\text{Bi}}=0.085, 0.12, 0.2, 0.33$ and 0.43).

In the first part of this section all results of the spectroscopic measurements performed in this system will be presented: they correspond to the points shown in the Ga-Bi phase diagram [Predel60] in the Fig. 6.2.5.

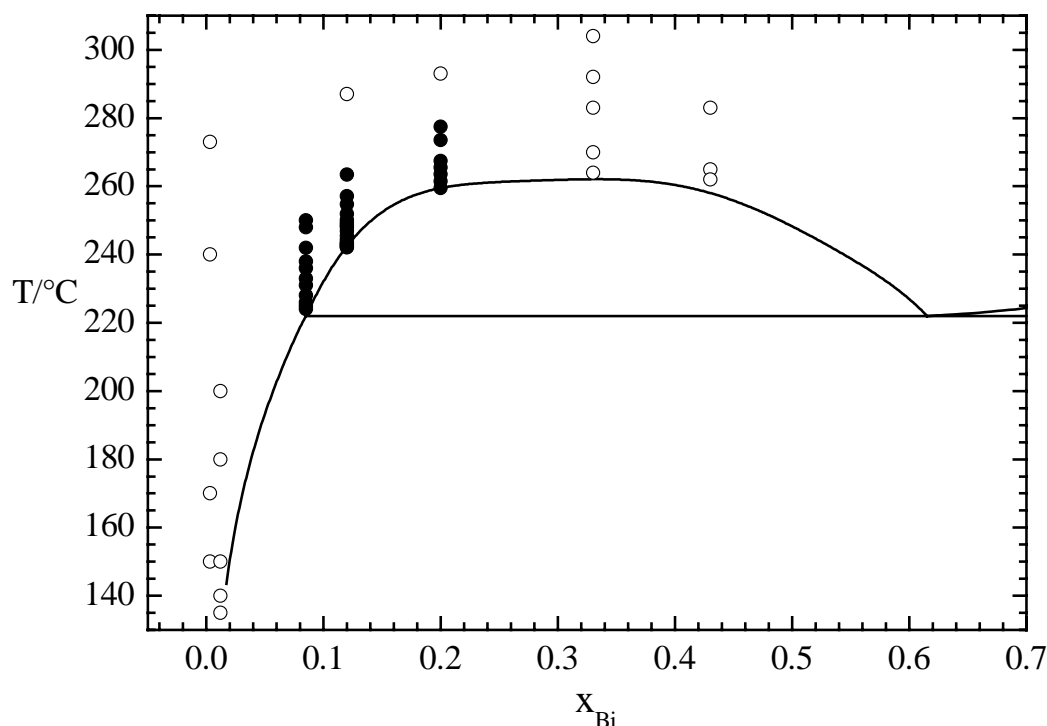


Fig. 6.2.5 Wetting characteristics of the liquid $\text{Ga}_{1-x}\text{Bi}_x$ alloys. Solid lines: part of the Ga-Bi phase diagram [Predel60]. Open symbols refer to ellipsometric spectra described within the 2 phase model; full symbols refer to spectra consistently described by the 3 phase model. For details see text.

Application of effective medium approximation (EMA). Spectroscopic ellipsometry measurements in the homogeneous region of the phase diagram, for temperatures above

280 °C, undoubtedly show that EMA can be applied as a good approximation of the dielectric functions of the $\text{Ga}_{1-x}\text{Bi}_x$ alloys. This will be exemplified on the $\text{Ga}_{0.67}\text{Bi}_{0.33}$ alloy at 283 °C. At this temperature this alloy represents homogeneous mixture of both components (there is always one or two monolayers of Bi at the liquid alloy/vacuum interface [Ayyad02], [Tostmann00] but in the present setup the accuracy is too low to detect it, Chapter 5). Hence the 2 phase model can be used to fit the measured ellipsometry data I_C and I_S . In this model only the concentration x_{Bi} in the substrate is unknown. For liquid Ga the spectrum taken at 256 °C (Fig. 6.2.1) and for liquid Bi taken at 289 °C (Fig. 6.2.2) were utilized. Results of the very good fit ($\chi^2=0.25$) are shown in Fig. 6.2.6. The Bi content in the alloy obtained from the fit corresponds to 46 ± 1 vol. %. Recalculated into molar fraction this gives $x_{\text{Bi}}=0.32\pm 0.01$. This nicely coincides with the filled fraction of $x_{\text{Bi}}=0.33$. Same results were observed for all points drawn with open circles in the phase diagram, Fig. 6.2.5. This provides a good proof for the application of EMA in this study of $\text{Ga}_{1-x}\text{Bi}_x$ alloys.

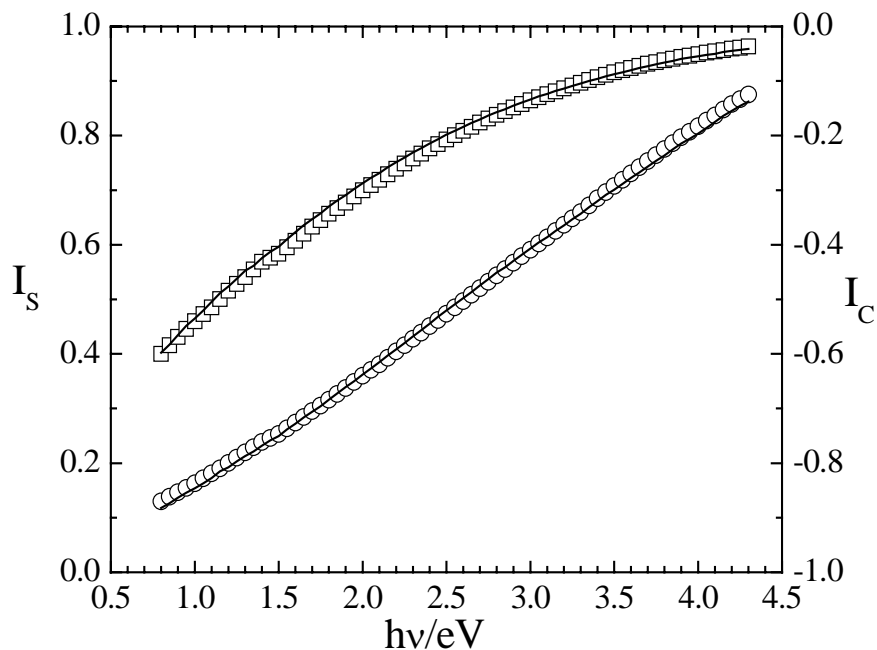


Fig. 6.2.6 Points are experimental ellipsometric intensities I_S (\square) and I_C (\circ) measured for the $\text{Ga}_{0.67}\text{Bi}_{0.33}$ alloy at 283 °C. Lines show the 2 phase model (EMA-substrate) fit. The alloy concentration determined from the fit is $x_{\text{Bi}}=0.32\pm 0.01$.

Origin of the film. Even though there is enough information about the origin of the wetting film in Ga-Bi system (Chapter 2.4) it is interesting to show it on the base of the ellipsometric results of this work. A selection from the spectroscopic ellipsometry measurements of the Ga-Bi alloy with $x_{\text{Bi}}=0.2$ is presented in Fig. 6.2.7. Ellipsometric results at several temperatures were evaluated using the 2 phase model. Results of the real part ε_1 of the pseudo-dielectric

constant for the $\text{Ga}_{0.8}\text{Bi}_{0.2}$ alloy together with ϵ_1 of liquid Ga and Bi are shown. One can clearly see how the character of spectra changes from that of Ga-like at high temperature (spectrum 1) to a Bi-like as the liquid-liquid line is approached (spectrum 4 at 258 °C; this temperature is slightly higher than that at the liquid-liquid coexistence corresponding to this alloy).

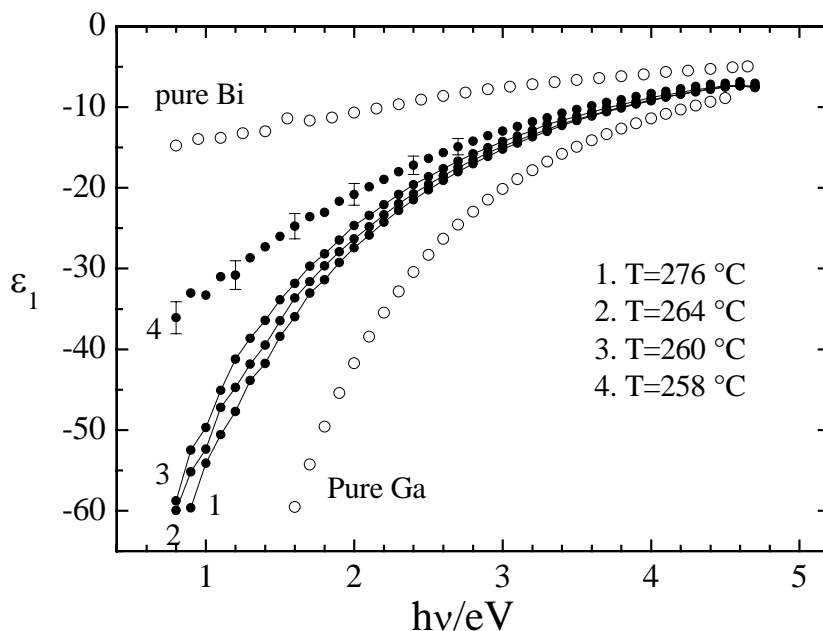


Fig. 6.2.7 ϵ_1 -spectra of pure Ga and Bi (\circ) and pseudo-dielectric functions of $\text{Ga}_{0.8}\text{Bi}_{0.2}$ alloy (\bullet). The alloy spectrum with the highest ϵ_1 -values corresponds to the lowest temperature. Thin lines in spectra are the guides for an eye.

It should be pointed out that the 2 phase model was used here only for an illustrative purpose; it of course delivers wrong dielectric function of the alloy, because the substrate with the wetting film (actually the 3 phase model) on it was substituted in this treatment for one homogeneous phase. In any case, this analysis provides additional (Chapter 2.4) evidence that the wetting film is a Bi-rich phase.

Choice of the model. If the wetting film is present, one needs to apply the 3 phase model to evaluate the results of the spectroscopic ellipsometry. The details of such a model for a liquid/liquid interface can be very complicated. The model should include a roughness of all interfaces given by the capillary waves amplitudes, diffuse boundaries (*gradient layers*) etc. Different configurations of the model were tried at the beginning. It was found that a very simple model could consistently describe all spectroscopic ellipsometry measurements conducted in the present work. This model, shown in Fig. 6.2.8, comprises pure liquid Bi (spectrum of this work taken at 289 °C) as a film and Ga-Bi alloy (EMA calculates from the spectra of this work for pure liquid Ga at 256 °C and pure liquid Bi at 289 °C) as a substrate.

The application of EMA as an approximation of the dielectric function of Ga-Bi alloy was checked in the frame of the 3 phase model again (see above). To fit the ellipsometric spectra there were two unknowns in the model: the thickness of pure Bi film and the molar fraction of Bi in the substrate.

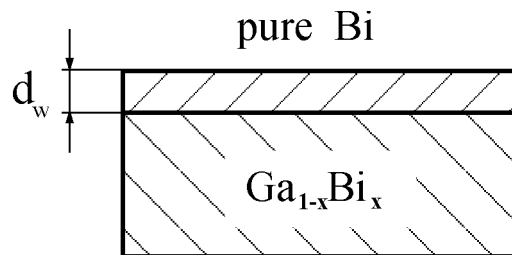


Fig. 6.2.8 The 3 phase model applied to evaluate the thickness of the wetting film (d_w): substrate – EMA spectra of $Ga_{1-x}Bi_x$ (pure liquid Ga at 256 °C and pure liquid Bi at 289 °C), film – experimental spectra of pure liquid Bi.

Results of such a fit to the spectra of $Ga_{0.8}Bi_{0.2}$ alloy at 264 °C are shown in Fig. 6.2.9. The fit is very good ($\chi^2=0.32$), the volume fraction of 34 ± 1 vol.% (corresponds to $x_{Bi}=0.22\pm 0.015$) approaches the weighed mole fraction of the sample ($x_{Bi}=0.2$), and the wetting film thickness is around 4 ± 2 Å.

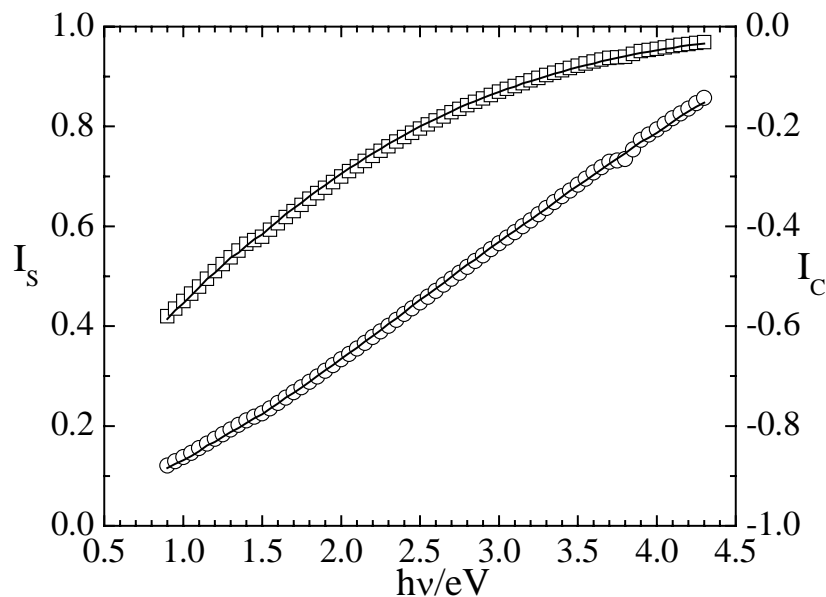


Fig. 6.2.9 Points are experimental ellipsometric intensities I_S (\square) and I_C (\circ) measured for the $Ga_{0.8}Bi_{0.2}$ alloy at 264 °C. Lines show the 3 phase model fit (see text). The substrate concentration determined from the fit is 34 ± 1 vol.% of Bi (or $x_{Bi}=0.21$) which is in a good agreement with the weighed sample concentration $x_{Bi}=0.2$. Thickness of the film is 4 Å.

This consistency of the experimental results with the EMA approximation was observed for all spectroscopic measurements performed on wetting (see below). So, in the following the substrate concentration was fixed to the weighed one for the respective samples.

In a simplified model the thickness of the film, d_w was the only fitting parameter. Such simplicity of the model is an obvious disadvantage. Indeed, it was noticed that slight discrepancies between the model and the experimental results arise at some points. But, as was already mentioned above, this simple 3 phase model delivers better fits than any other.

Complete wetting transition (SE). Locations of the spectroscopic ellipsometry measurements where a change of the wetting film thickness has been observed, are shown as solid points in Fig. 6.2.5. Three experiments have been performed. The very first experiment has been done at $x_{\text{Bi}} \sim 0.085$, very close to the monotectic point. Unfortunately, in this measurement reliable data acquisition was possible only in the spectral range $1.5 \leq h\nu \leq 3.2$ eV, due to a technical problem that was later solved. Since the concentration of Bi is low, pure Ga has been used as a substrate in the 3 phase model for this measurement. The variation of the Bi film thickness is shown in Fig. 6.2.10 for two measurement runs. Both were performed for the same sample with an interval of several days between them, practically at the same temperatures. During this time the sample was always in the vacuum of 2×10^{-9} mbar. The surface was not cleaned between these measurements.

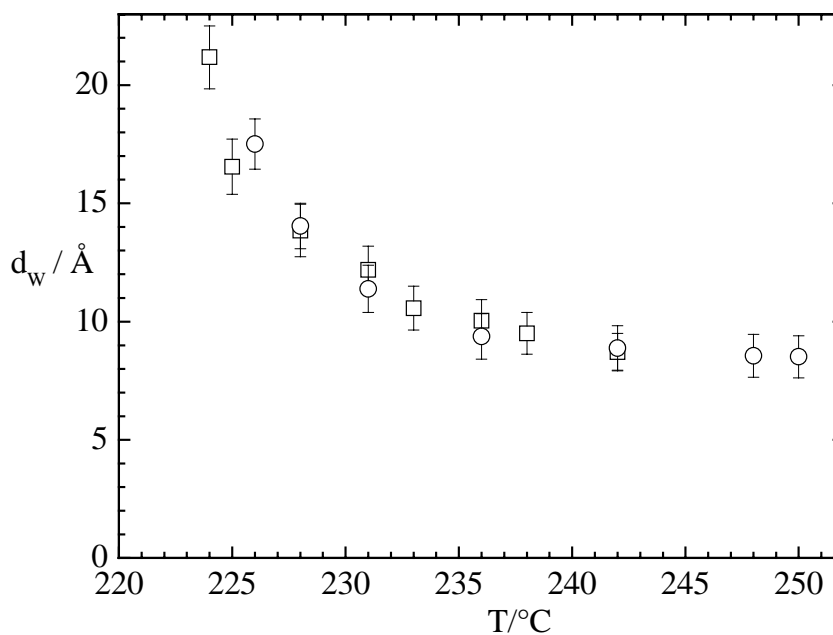


Fig. 6.2.10 Thickness of the wetting Bi film as one approaches the miscibility gap from the homogeneous liquid region (sample concentration is $x_{\text{Bi}}=0.085$). Symbols (○, □) present different measurement runs performed with an interval of several days.

This measurement will not be included in the following discussion. Nevertheless, one can make a very important experimental observation: there is no detectable influence of the possible oxidation of the liquid alloy surface over several days.

The next concentration was that with $x_{\text{Bi}}=0.2$. The results of the 3 phase model fit - thickness of the wetting film - are shown in Fig. 6.2.11. One can clearly see the strong and continuous increase from 5 Å to 20 Å in a small temperature range of about 10 K. This is expected for the approach to a complete wetting transition at coexistence (Chapter 2.1). For this concentration, according to the phase diagram the binodal is crossed at 258 °C.

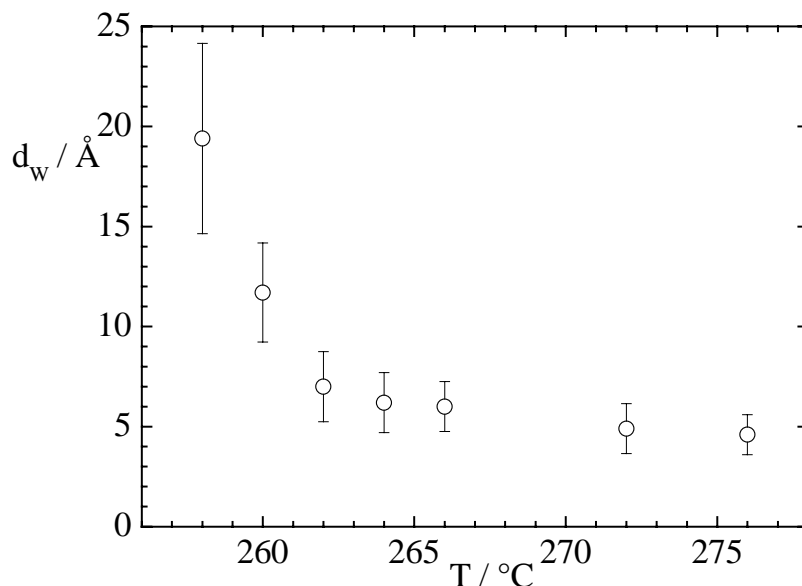


Fig. 6.2.11 Thickness of the wetting Bi film as one approaches the miscibility gap from the homogeneous liquid region evaluated on the base of the 3 phase model for the sample with $x_{\text{Bi}}=0.2$.

For the next concentration the experimental plan was to acquire at least 10 points (or more) in the temperature range close to the liquid-liquid line. It was decided to study the sample with $x_{\text{Bi}}=0.12$. This concentration is in between of the above-described ones and is the same as in study of Huber et al. [Huber02]. So, the results of both studies could be later compared. For this concentration according to the phase diagram the binodal is crossed at 242 °C. Special precautions were taken here: at each temperature 3-4 hours were given to the system for homogenisation and thermal stabilization, 3-5 spectra were recorded and evaluated using the 3 phase model. The results of d_w were then averaged. Variation of the Bi film thickness is demonstrated in Fig. 6.2.12. One can see that the average error of the thickness grows for thicker films (for total error estimation see the end of Chapter 5). The following discussion will be concentrated exactly on this measurement.

From a simple thermodynamic argument (see the book of Rowlinson and Widom [Rowlinson82] on p. 230) the wetting transition must be absent for concentrations above the critical $x_{\text{Bi}}=0.3$ [Predel60]. To demonstrate this, two concentrations were chosen, $x_{\text{Bi}}=0.33$ and 0.43. As can be seen from Fig. 6.2.5 no wetting film was observed even in the close vicinity to liquid-liquid line (spectroscopic ellipsometry results can be consistently described

within the 2 phase model – concentration of Bi in the substrate accurately agreed with the composition of alloys).

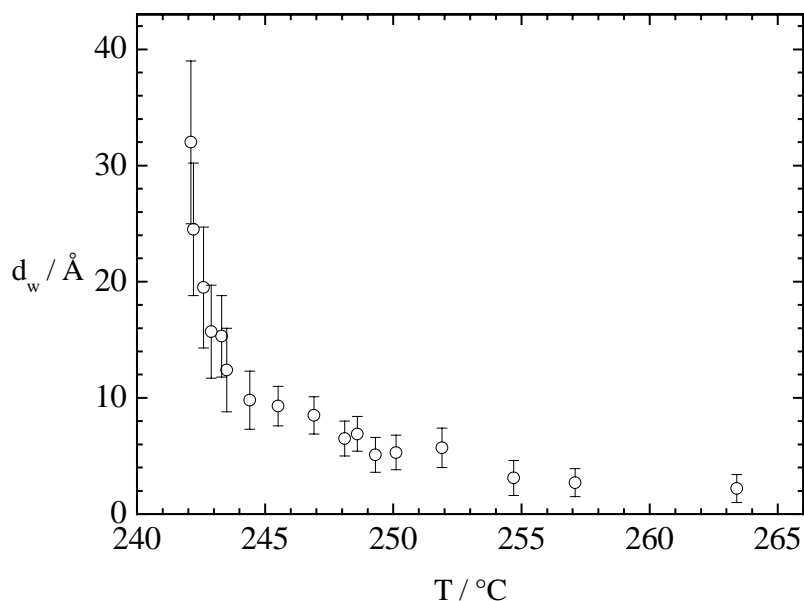


Fig. 6.2.12 Thickness of the wetting Bi film as one approaches the miscibility gap from the homogeneous liquid region evaluated on the base of the 3 phase model for the sample with $x_{\text{Bi}}=0.12$.

Complete wetting transition (kinetic measurements). With the knowledge gained from the spectroscopic ellipsometry measurements the *kinetic* measurements can be analysed. Kinetic measurements have been performed for four compositions with $x_{\text{Bi}}= 0.12, 0.2, 0.33, 0.43$ (all except 0.085). Samples were cooled down from the homogeneous liquid region (practically always from $T \sim 280$ °C) with different cooling rates (from 3 to 20 K/h). Two experiments for $x_{\text{Bi}} < 0.3$ and $x_{\text{Bi}} > 0.3$ will be shown. Observed similarities and differences will be highlighted. The result of one measurement on cooling of the $\text{Ga}_{0.8}\text{Bi}_{0.2}$ alloy from $T(\text{A})=276$ °C to $T(\text{C})=210$ °C with ~ 3 K/h (cooling rate of the furnace is slightly higher than that of crucible), is depicted in Fig. 6.2.13. Only one ellipsometric angle Ψ is shown (Δ changes in the same way). Cooling from A to C on the schematic bulk phase diagram of Ga-Bi corresponds to the following relevant paths for measurement at the alloy/vacuum interface: (i) **A**→**B** in the homogeneous liquid region; (ii) **B'**→**M'** – in the demixing region, the liquid with the lower surface tension (namely Bi-rich phase) is more favourable at the interface; (iii) **M'** ($x_{\text{Bi}}=0.085; T=222$ °C)→**C'** ($0.067; 210$ °C) on liquid-solid coexistence line. It can be clearly seen how precisely and sensitively the ellipsometry signal (Ψ) reflects all changes at the alloy's interface.

Several remarks are of interest before the kinetic data will be analysed. Unfortunately, it is very difficult to extract *quantitative* information e.g. film thickness from the kinetic measurement in ellipsometry. It can be done only if the 2 phase model is valid or with an

additional information from another measurement, for example spectroscopic ellipsometry study of the same process. That is why the results of SE were presented in this section first. However, it has to be taken into account that spectroscopic and kinetic ellipsometry results must not perfectly agree, due to the clear difference in the measurement conditions (stepwise and continuous cooling, respectively).

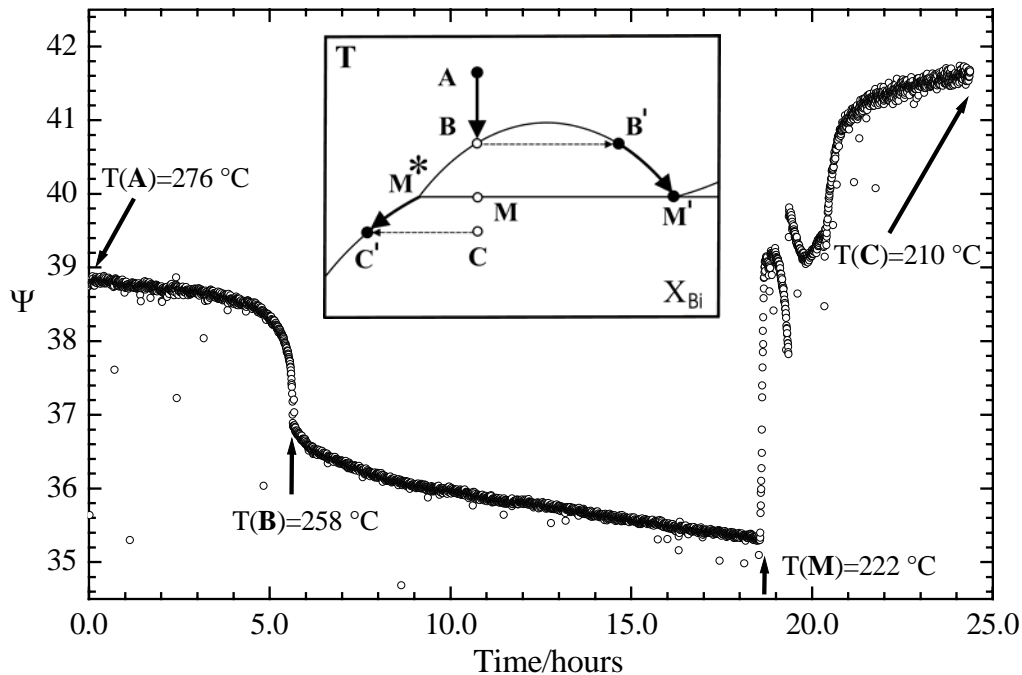


Fig. 6.2.13 Ellipsometric angle Ψ recorded every 20 seconds on continuous cooling $\text{Ga}_{0.8}\text{Bi}_{0.2}$ alloy from 276 to 210 $^{\circ}\text{C}$ with ~ 3 K/h. In the inset the positions of the characteristic points are shown in the schematic phase diagram: experimental “interfacial” path relevant for this study is indicated as thick lines with arrows (for details see text).

At point “A” the value of Ψ of 38.7° calculated on using the 2 phase model (substrate EMA) for $\text{Ga}_{0.8}\text{Bi}_{0.2}$ alloy agrees very well with measured in experiment value of $38.8^{\circ} \pm 0.1^{\circ}$. On the path AB (Fig. 6.2.13, inset) one can notice that the way of Ψ variation is generically the same as that of wetting film thickness d_w in Fig. 6.2.11 (same alloy). Hence, a decrease of Ψ indicates the wetting film growth and its rapid increase towards a finite value (~ 30 Å in this study) near the liquid-liquid line. It has to be emphasized that this variation is the same with respect to the cooling rates (3, 5, 10 and 20 K/h were tried) and the same picture was observed for $x_{\text{Bi}}=0.12$. Continuous decrease of Ψ in the liquid-liquid region, path B’M’, reflects either further growth of the film or an enrichment of Bi of the substrate adjacent to the film (or both). It can be shown that within the 2 phase model increase of Bi concentration corresponds to decrease of Ψ . No SE measurements were done at those conditions (see below).

The last part of the Ψ spectrum M^*C' , recorded from T_{mono} into solid(Bi)-liquid(Ga-rich) region, exhibits several features. One can see a jump at T_{mono} and, following after some time (~ 1 hour), a discontinuous rupture in the spectrum. Such behaviour is difficult to explain. The points to consider are the following: below T_{mono} a solid Bi-rich phase should appear. It was observed with the naked eye as several (not more than 5) relatively big ($\text{\O}3\text{-}5$ mm) crystals on the liquid surface (in all kinetic measurements, $x_{\text{Bi}}= 0.12, 0.2, 0.33, 0.43$). The surface obviously offers very attractive nucleation sites for the new phase: high Bi content and smallest from the whole volume temperature (due to the thermal gradient). These crystals did not sink because of the anomaly of Bi density - ρ of solid Bi is smaller than that of liquid Bi. The surface became no longer flat and the reflection conditions were distorted to some extent. Sometimes completely if the crystals emerged under the footprint of the light. This is possible explanation of the rupture in Ψ spectrum of $\sim 2^\circ$ at 19.5 hours. If the last part of spectrum in Fig. 6.2.13 will be moved down on $\sim 2^\circ$ the value of Ψ at 210°C will be about 39.5° (41.6° in Fig. 6.2.13 minus shift of $\sim 2^\circ$) which is in a good agreement with 40.2° estimated using the 2 phase model for $\text{Ga}_{0.933}\text{Bi}_{0.067}$ alloy at 210°C . Anyway, in the last part of the spectrum in Fig. 6.2.13 one can clearly recognise same behaviour of Ψ as along the path AB. This is expected from the tetra point wetting scenario, since along both paths AB and M^*C' the complete wetting is probed in the vicinity of liquid-liquid coexistence: moving away from M^* wetting film thickness decreases and disappears in the same way as it grew approaching B.

These observations are in direct agreement with the results of Huber et al. [Huber02] obtained on heating of $\text{Ga}_{0.88}\text{Bi}_{0.12}$ (see Chapter 2.4). In this study the experiment on heating could not be conducted due to the presence of Bi-rich crystals on the liquid surface after cooling of the alloy. The heating experiment could not be started at the beginning due to the sample preparation and necessity of the surface cleaning (see Chapter 4.2): the final preparations of sample to the measurement were done in the homogeneous liquid region.

The kinetic measurements for the alloy with a concentration higher than the critical one will be presented next. In the same way as in the previous example, the result of cooling of the $\text{Ga}_{0.57}\text{Bi}_{0.43}$ alloy from $T(\text{A})=280^\circ\text{C}$ to $T(\text{C})=185^\circ\text{C}$ with ~ 10 K/h is depicted in Fig. 6.2.14. As one can see from the inset in the figure, the measurement trajectory is almost the same, only the path AB approaches the demixing line on the other side of the miscibility gap. The value of Ψ of 35.7° at point "A" agrees well with the prediction of the 2 phase model $\Psi=36.5^\circ$. In this measurement there is no change of Ψ on the path AB – as expected, the formation and growth of the wetting film do not take place. This agrees with the SE result

(Fig. 6.2.5) which undoubtedly shows an absence of the film in the homogeneous liquid region for both concentrations $x_{\text{Bi}} = 0.33$ and 0.43 .

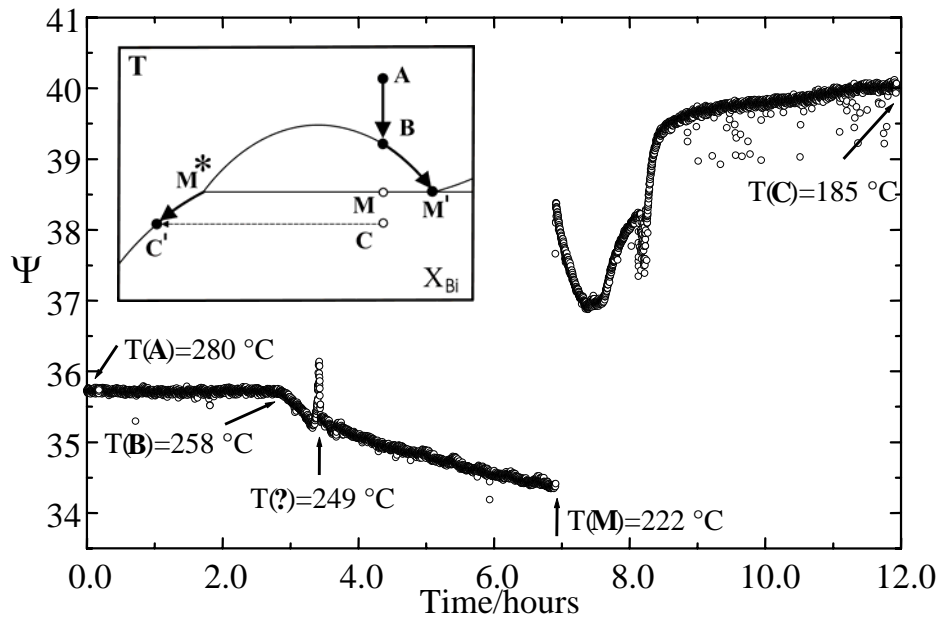


Fig. 6.2.14 Ellipsometric angle Ψ recorded every 5 seconds on continuous cooling $\text{Ga}_{0.57}\text{Bi}_{0.43}$ alloy from 276°C to 210°C with $\sim 8\text{ K/h}$. In the inset the positions of the characteristic points are shown in the schematic phase diagram: relevant for this study experimental path is indicated as thick lines with arrow (for details see text). To be compared with Fig. 6.2.13.

Path BM' for $\text{Ga}_{0.57}\text{Bi}_{0.43}$ alloy exhibits the same variation of Ψ , even the magnitude nicely coincides with that of the signal for $\text{Ga}_{0.8}\text{Bi}_{0.2}$. This confirms the interpretation given for the corresponding variation in Fig. 6.2.13. But there is some maximum in Ψ at $T = 249^\circ\text{C}$ (~ 3.5 hours), which cannot be attributed to any measurements artefacts like oxides, vibrations etc. This new feature was reproducibly obtained for this concentration and it has been never observed for other alloys. Its origin will be discussed in the next section.

At the monotectic temperature the crystals of the Bi-rich phase appeared, but fortunately remotely enough from the place of reflection and did not disturb measurement on the path $\text{M}^*\text{C}'$. The signal variation expected for the tetra point wetting, could be observed.

No spectroscopic ellipsometry measurements were performed to characterise the interface of alloy on the path BM' . The reason for this was the very interesting effect, which occurred for all concentrations at temperatures within the miscibility gap. The SE spectra are normally taken at constant temperature, so the sample was cooled down into the liquid-liquid region and the controller was stopped – keeping the furnace temperature constant. Cooling and stabilization process were followed by the kinetic measurement. The ellipsometric signals and the temperature variation of the crucible were surprising and quite opposite to expected “stabilization”. The results are presented in the next section below.

• Oscillatory behaviour of liquid alloys

The experimental conditions are described above: cooling from the homogeneous liquid region and stop in the miscibility gap. In Fig. 6.2.15 the results of ellipsometric angles Ψ and Δ as well as temperature of the crucible are shown as a function of time.

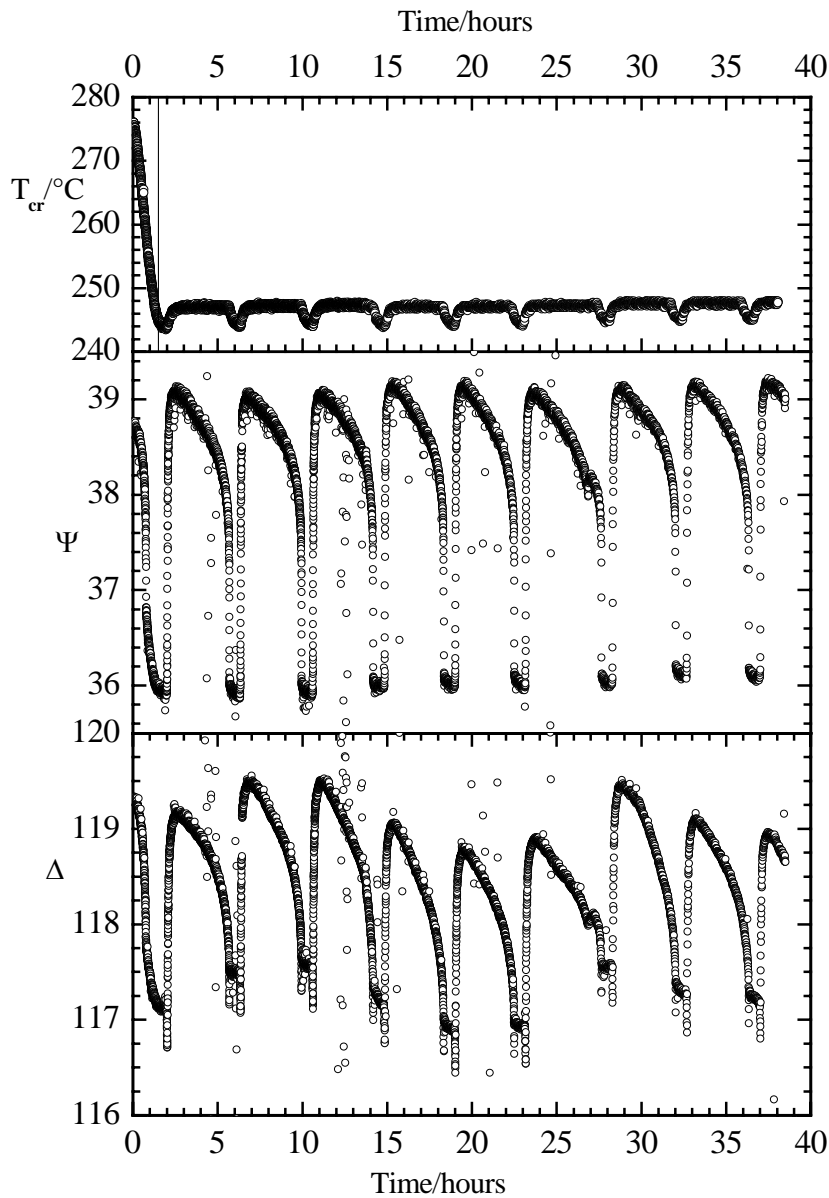


Fig. 6.2.15 T_{crucible} , Ψ and Δ (at 2.75 eV) for the $\text{Ga}_{0.8}\text{Bi}_{0.2}$ alloy over a period of 40 hours. Sample was cooled from 278 °C (homogeneous liquid) to 245 °C (inside the miscibility gap) with 20 K/hour. After 1.5 hour (marked with vertical line in T) the furnace temperature was stable within ± 0.1 K till the end of the measurement. Oscillation period of observed variations is ~ 5 hours.

As the temperature of the furnace becomes constant, strictly periodical changes of all three quantities are observed. These variations do not decay over very long time of (40 hours, only for this experiment “B” in Fig. 6.2.16 the signals were recorded for such a long time, other

were recorded only 15...20 hours). It seems that the system oscillates between two different states. It is necessary to mention that no changes were visually detected at the interface of the alloys. The reproducibility of the oscillations (line shape, amplitude and period) is remarkable. This is particularly true for Ψ and less for Δ , but this is not surprising since Δ is more sensitive quantity (by its nature).

A number of similar experiments have been performed. Their locations inside the miscibility gap are shown in Fig. 6.2.16. For concentrations above the critical ($x_{\text{Bi}} > 0.3$) this study was more systematic: four temperatures for the experiments marked as **C** ($\text{Ga}_{0.67}\text{Bi}_{0.33}$) and **D** ($\text{Ga}_{0.57}\text{Bi}_{0.43}$) and only one for each experiment with $x_{\text{Bi}} < 0.3$: **A** ($\text{Ga}_{0.88}\text{Bi}_{0.12}$) and **B** ($\text{Ga}_{0.8}\text{Bi}_{0.2}$).

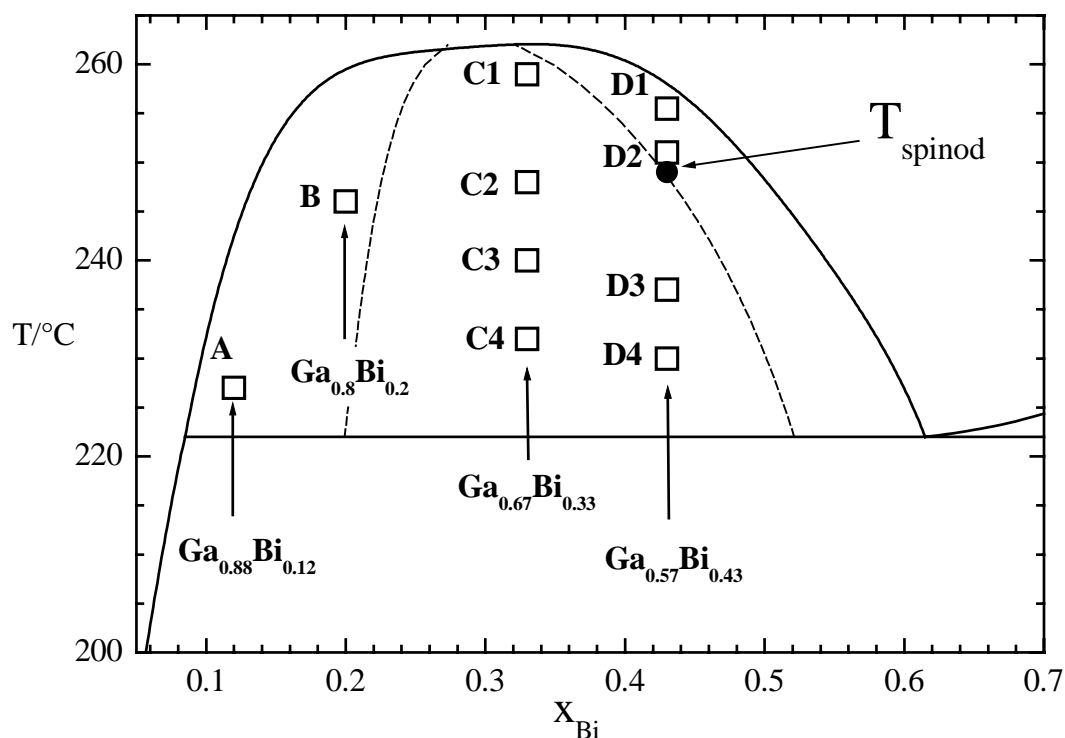


Fig. 6.2.16 The miscibility gap of the bulk Ga-Bi phase diagram [Predel60] is shown as solid lines. Dashed lines indicate the positions of the spinodal curves (see discussion). Points (□) mark the average temperature of the crucible during oscillations. Size of the points approximately represents the temperature instability. Filled circle (●) lies on the spinodal (see text).

The experimental conditions for all measurements were practically the same: starting temperature around 280 °C and cooling rate of 10 K/h.

Several interesting features can be noticed in Fig. 6.2.15. They are common for all experiments (A,B,C and D): (i) when the oscillations have started Ψ , Δ and T_{cr} increase simultaneously, whereas a decrease of the ellipsometric angles occurs at almost constant temperature (will be shown in details in Fig. 7.3.4); (ii) the increase in Ψ and Δ proceeds

several times faster than the respective decrease, which seems to be a “self-accelerating” process (see next Fig. 6.2.17 B).

Some insight into the mechanism and nature of this oscillatory process can be obtained by comparison of the experiments with concentrations on the opposite side of the miscibility gap.

Measurements “B” ($\text{Ga}_{0.8}\text{Bi}_{0.2}$) and “C3” ($\text{Ga}_{0.67}\text{Bi}_{0.33}$) are shown in Fig. 6.2.17.

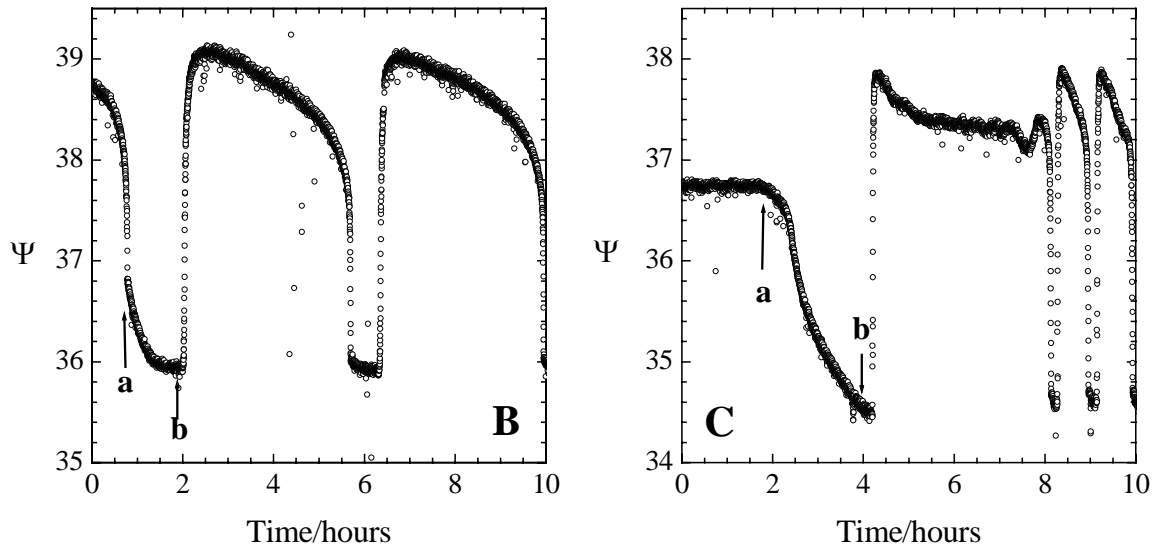


Fig. 6.2.17 Initial stage of the oscillatory change in Ψ for $\text{Ga}_{0.8}\text{Bi}_{0.2}$ ($x_{\text{Bi}} < 0.3$) in left (B) - and $\text{Ga}_{0.67}\text{Bi}_{0.33}$ ($x_{\text{Bi}} > 0.3$) - right part (C3). Entrance into demixing region is marked as “a”, “b” indicates the time when the cooling process was stopped. Cooling for exp. “B” was ~ 2 times faster than for “C3”.

The main differences between both experiments can be summarized as follows (see in Fig. 6.2.17). The oscillations in “B” start immediately after a constant temperature is achieved, whereas for the oscillations in the experiment of type “C” there is some transient time of ~ 4 hours. During this time small oscillations in Ψ develop increasing in the amplitude. Another evident difference exists in the period of the oscillations: 4 hours for “B” in comparison to 1 hour for “C”. It has to be pointed out that this difference is independent of the initial cooling rate. Its influence was studied for measurement “B” only - no noticeable change was observed for cooling rates ranging from 5 to 20 K/h.

It is interesting to note that the oscillations were never observed on continuous cooling within the demixing region. This observation provides a new insight on the kinetic measurements in Fig. 6.2.13 and 6.2.14: at T_{mono} the first crystals of solid Bi appear and the temperature stays constant for some time depending on the cooling rate; this time can be enough to initiate the jump of Ψ .

In the study of oscillations it was found that their amplitude and period in all three measured quantities depend strongly on the location of the “stop” inside the miscibility gap (points in

Fig. 6.2.16). It will be shown on the examples of the “C1” and “C4” measurements of $\text{Ga}_{0.67}\text{Bi}_{0.33}$ alloy, which are presented in Fig. 6.2.18. As one can see the amplitude and frequency of the oscillations increase strongly for the experiment “C4” which lies deeper inside the miscibility gap. Experiment “D” showed the same dependence of Ψ , Δ and T_{cruc} on the location in the demixing region. But it also exhibited some new features that were not observed for other concentrations. This feature was shown in Fig. 6.2.14 – there is a sharp peak in Ψ (and Δ , not shown) when a temperature around $T(?) = 249\text{ }^\circ\text{C}$ is crossed. This peak was reproduced at the same temperature in measurements “D3” and “D4”. This temperature for $\text{Ga}_{0.57}\text{Bi}_{0.43}$ alloy corresponds to the crossing of the spinodal, which is shown as a broken line in Fig. 6.2.16. This line was obtained from thermodynamic calculation of the phase diagram made by Huber et al. [Huber03] (see discussion Chapter 7.2). Such a direct observation of the spinodal has been made for the first time in a metallic system. As can be seen in Fig. 6.2.16 the spinodals could not be crossed in all other measurements (even on cooling of $\text{Ga}_{0.8}\text{Bi}_{0.2}$ alloy below T_{mono}).

In the end of this section the most interesting observations are briefly summarized:

- a. the oscillations were observed for different concentrations and at different temperatures inside the miscibility gap;
- b. indispensable condition to observe this oscillatory behaviour of Ga-Bi alloys is cooling from the homogeneous liquid region into the demixing regime and “stop” at constant furnace temperature; T_{start} and the cooling rate do not seemingly influence the oscillatory characteristics;
- c. even though there is a difference (see Fig. 6.2.17) in the oscillatory behaviour for alloys with $x_{\text{Bi}} < 0.3$ (which enter the miscibility gap with the wetting film at liquid/vapour interface, Fig. 6.2.13), and $x_{\text{Bi}} > 0.3$ (no wetting film up to the liquid-liquid coexistence Fig. 6.2.14), the initial presence of the Bi rich *film* before entering the 2 phase region is not a necessary condition for the oscillatory instability to occur;
- d. at constant temperature the period of the variations in Ψ , Δ and T_{cruc} strongly decreases with increase of Bi concentration in the alloy whereas the amplitude is almost constant;
- e. at constant concentration the period decreases but the amplitude of the variations in Ψ , Δ and T_{cruc} increases for lower temperature within the miscibility gap (figure below).

Explanation of this interesting correlation between the interfacial and bulk behaviour will be discussed in Chapter 7.3. The effects that can account for the oscillations will be introduced. At present moment only quantitative approach can be given. Also the model developed by

Turchanin et al. [Turchanin04] for similar oscillatory behaviour observed in a Ga-Pb alloy will be introduced. Similarities and differences of Ga-Bi and Ga-Pb systems and of the observed phenomena will be summarized.

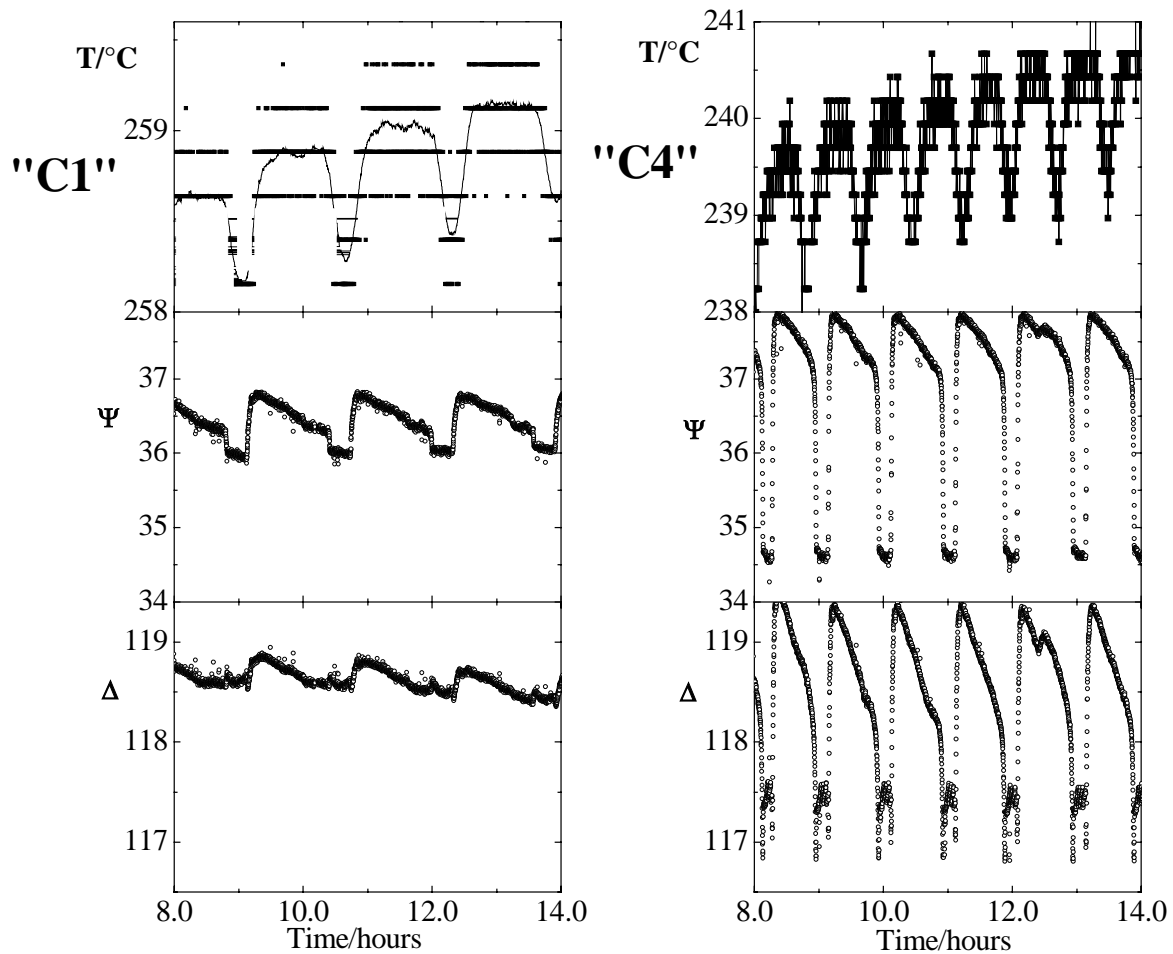


Fig. 6.2.18 Comparison of measurements “C1” (see Fig. 6.2.16) (left) and “C4” (right) for $\text{Ga}_{0.67}\text{Bi}_{0.33}$ alloy. Period of time from 8 to 14 hours corresponds to well established, reproducible oscillations. Line in graph of temperature is average drawn for convenience.

• Ellipsometric measurement of the surface-freezing transition

The aim of the following part of this study was an optical characterization of the surface freezing film in Ga-Bi and determination of its thickness.

The locations of this transition were described in Chapter 2.4 on the basis of a previous SHG study [Turchanin02]. The surface phase diagram of liquid alloy is shown for convenience here again in Fig. 6.2.19. It also includes the experimental path of kinetic and spectroscopic measurements of the present study. Two alloys have been investigated: $\text{Ga}_{0.997}\text{Bi}_{0.003}$ and $\text{Ga}_{0.988}\text{Bi}_{0.012}$. An advantage of the first concentration is clearly seen from the surface phase diagram (Fig. 6.2.19): the distance between surface freezing and liquidus lines increases for

alloys closer to the eutectic. In this measurement it is important to stop cooling of the crucible before the solid-liquid coexistence line is crossed. It is difficult since during the surface freezing transition the heat balance of the sample is changing which can lead to a rapid cooling. As a consequence, a Bi-rich solid phase might nucleate on the frozen Bi-rich film and would thicken it leading to wrong estimations of the thickness.

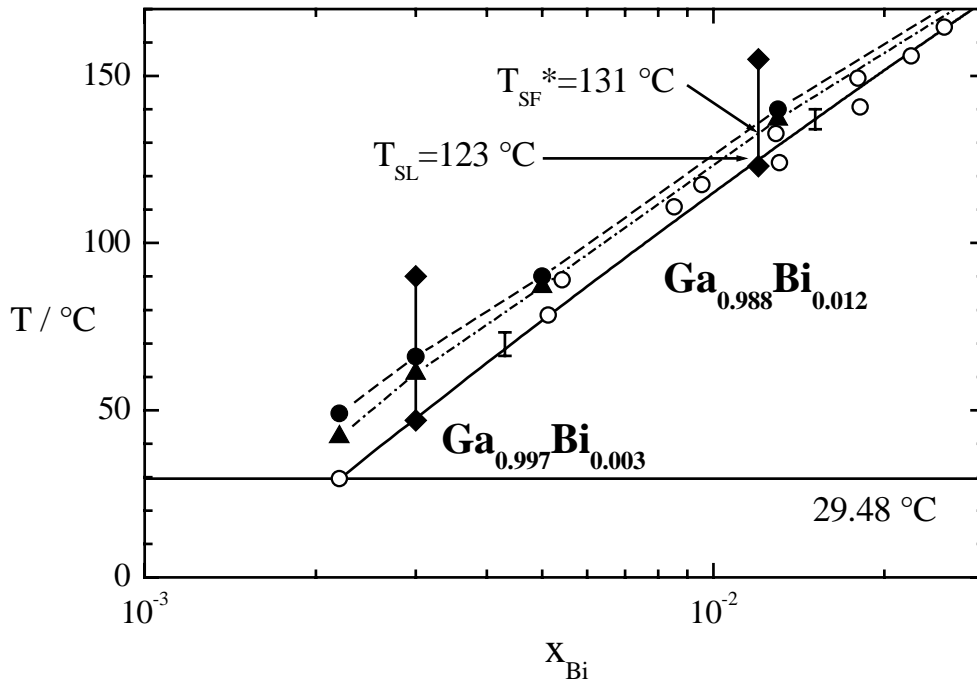


Fig. 6.2.19 Experimental paths of the ellipsometric measurements are shown as vertical lines with symbols (◆). For definition of other lines and points see Fig. 2.8. For the alloy $\text{Ga}_{0.988}\text{Bi}_{0.012}$ the surface freezing temperature $T_{\text{sf}}^* = 131$ °C and the temperature at solid-liquid coexistence $T_{\text{SL}} = 123$ °C are shown.

The transition is undoubtedly identified already from the cooling curve recorded for the crucible. An example is shown in Fig. 6.2.20. Particular feature of this cooling curve is an acceleration of cooling after a solid film appeared on the surface (indicated with an arrow in Fig. 6.2.20). This drop occurs even though the temperature of the furnace remains constant. The reason for this behaviour will be explained in Chapter 7.2.

The effect of the transition on the ellipsometric quantities was pronounced. First it has to be mentioned that for the $\text{Ga}_{0.997}\text{Bi}_{0.003}$ alloy the transition could be sensed and followed even with the naked eye – the film was visible. Several valuable observations have been made:

- *dynamics of the film growth* - first crystal-like nuclei of the film appeared always near the rim of the crucible, after that in seconds the film spread over the whole surface,
- *structure of the film* - growing of the film resembled in some way a crystallisation process. Coarse grains and dendrite structure could be clearly seen. The film surface

exhibited a roughness on macroscopic (up to 3 mm in amplitude waves) and microscopic (visible due to strong scattering of the light) scale.

Such a situation is unfavourable for ellipsometry (as for any other optical study) because of a big loss of the signal intensity by scattering and reflection and some unpredictable misalignment of the instrument. These facts made the results obtained for $\text{Ga}_{0.997}\text{Bi}_{0.003}$ alloy useless for any quantitative analysis.

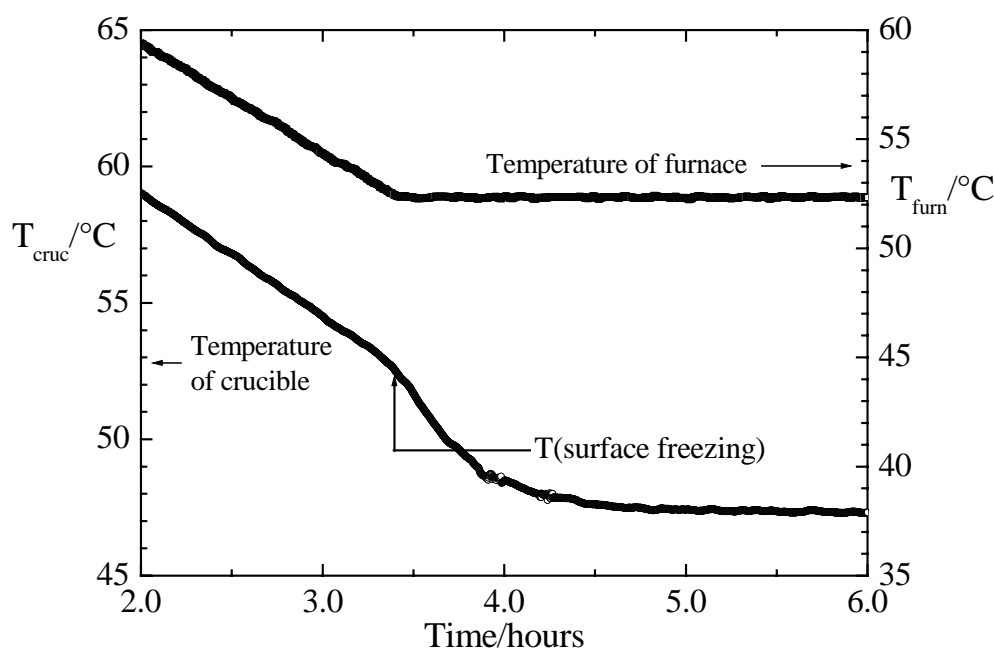


Fig. 6.2.20 Typical cooling curves taken on cooling with 5 K/h of $\text{Ga}_{0.997}\text{Bi}_{0.003}$ alloy. Temperature of the furnace is also shown (scales of T_{cruc} and T_{furn} are shifted!). Appearance of the film is marked with arrow.

Since the concentration near the eutectic happened to be very bad choice for the ellipsometric measurements another concentration was tried - $\text{Ga}_{0.988}\text{Bi}_{0.012}$ (with higher x_{Bi}). The structure and quality of the surface of frozen films for this alloy were radically different. To say only one fact - the frozen film could not be visually distinguished from the liquid surface any more. No changes upon the transition could be seen with the naked eye. But it was clearly detected by ellipsometry and by cooling curves. One of the kinetic measurements for the $\text{Ga}_{0.99}\text{Bi}_{0.01}$ alloy is shown in Fig. 6.2.21.

For this concentration no changes in the alignment of the sample were observed. The frozen film could be seen as a very viscous layer on the liquid surface which quickly damped the vibrations and waves induced by gentle knocking and shaking of the setup (one can see that Ψ and Δ in Fig. 6.2.21 are less noisy after ~6 hours).

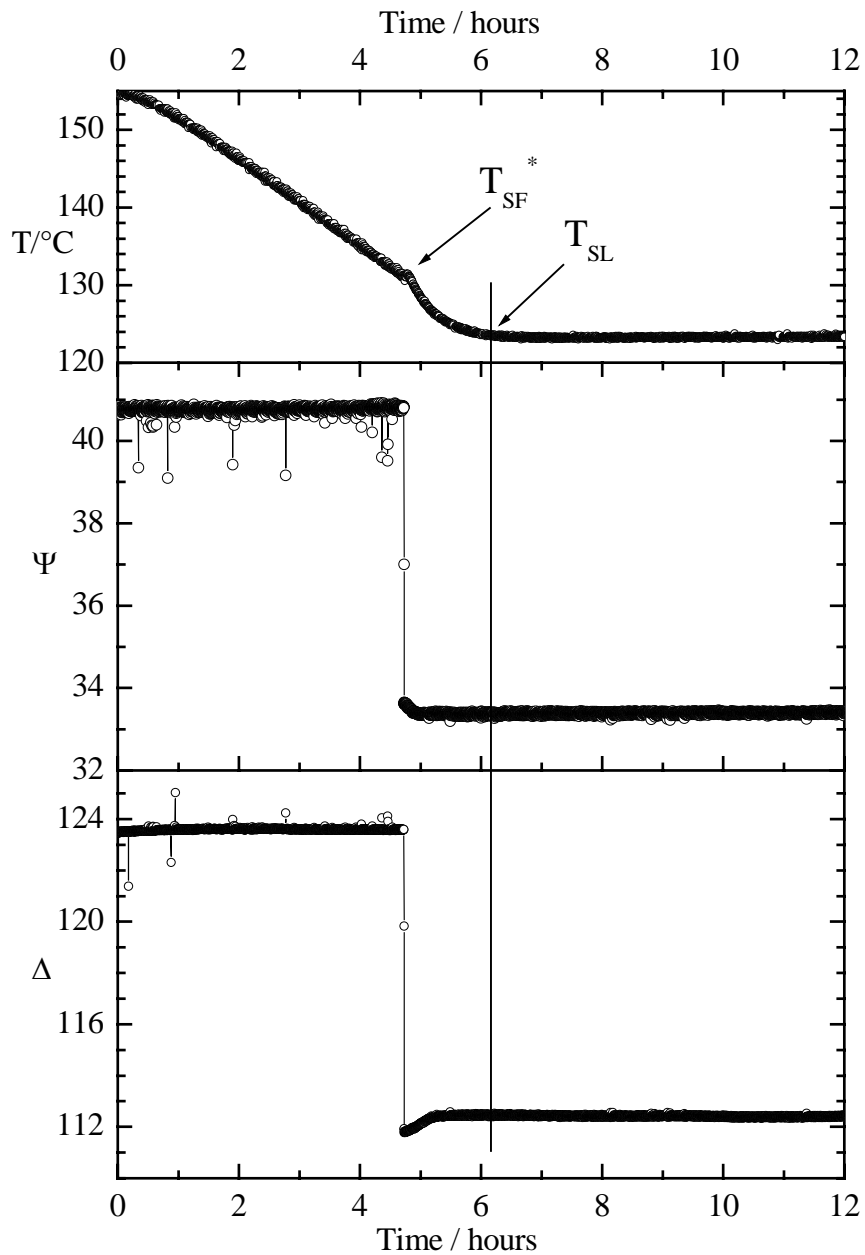


Fig. 6.2.21 Ellipsometric angles Ψ and Δ (two lower sections) recorded every 5 seconds on continuous cooling the $\text{Ga}_{0.988}\text{Bi}_{0.012}$ alloy from 156 to 123 °C with ~ 7 K/h. In the upper section the cooling curve of the sample for crucible is shown: temperature T_{SF}^* and T_{SL} are indicated with arrows.

The observations made during this measurement (Fig. 6.2.21) are summarized below:

- the transition temperature $T_{SF} = 131$ °C reasonably agrees with that of Turchanin et al. [Turchanin02];
- there are no changes in Ψ and Δ up to T_{SF} . This was confirmed by the SE measurements at $T=200, 180, 150, 140$ and 135 °C, which were consistently interpreted as Ga-rich alloy without the film (“monolayer-problem” was described above);

- c. the transition is abrupt and pronounced: acquisition time in kinetic measurement was 5 second, hence change of 8° for Ψ and 12° for Δ occurred in ~ 10 seconds. During this time the surface transition was completed in the footprint of the light spot ($\sim \varnothing 3$ mm),
- d. there is a little change of the ellipsometric angles after the “jump” within 30-40 minutes,
- e. as can be seen the cooling continued into the solid-liquid region. In order to suppress quick temperature drop one needs certain changes in the setup: (i) special thermal treatment which will include slight heating of the sample after T_{SF}^* is reached or (ii) additional heater from above to reduce vertical and radial thermal gradient in the crucible,
- f. T_{SL} marks the entrance into the two-phase region (vertical line at 1.5 hour after the surface freezing transition in Fig. 6.2.21). There is no indication of it in the Ψ and Δ -curves. The signals have already become stable long before the liquidus line, and stay constant after.

To determine the thickness of the frozen film the spectroscopic ellipsometry has been performed after the film formation. The first spectrum has been taken at 5.5 hours (Fig. 6.2.21) – at this time any variations of the ellipsometry signals in kinetic measurement have already subsided. The next spectra were recorded every hour. They are all the same, which additionally confirms the results of the kinetic measurements (point “d”, above).

The appearance of the interfacial model for this situation is straightforward – almost pure Ga substrate and solid Bi-rich film on top. As a first approach a pure bulk solid Bi film was assumed. The difficulty to find optical data relevant for this measurement was already described above for pure liquid Ga and Bi. The same is true in the case of solid Bi. It is not easy to obtain a plane atomically clean crystal surface that is why there are not many publications on the topic (no study of solid crystalline Bi in vacuum was found). Several publications available could not be used as a reference, so a spectrum of pure solid bismuth had been measured.

Pure solid Bi. Apart from the mentioned above difficulties to prepare such sample, in the present setup there is one insurmountable limitation - no solid probe can be aligned. Hence the measurement had to be done in the following way: pure Bi was cleaned in the UHV chamber in the liquid state (actually the same sample after SE study of liquid Bi was used). It was cooled down very slowly and solidified (all under UHV). Since the molar volume of Bi in the solid state is larger than in the liquid small swelling (some kind of “hill”) appeared in the middle of the crucible after solidification. Apart from it the surface was sufficiently plane (only 5×5 mm space was required). The solid sample was taken out of UHV chamber and immediately measured on air with the ellipsometer mounted on a goniometer table. This table

allowed alignment of the sample reflection plane. Different orientations have been tried, but no significant anisotropy was found – indicating that sample was polycrystalline. This was also observed under an optical microscope. The results of this measurement, which are shown in Fig. 6.2.22 as real and imaginary part of the dielectric function, have no pretensions of high quality (on air, an oxidation of the surface immediately took place), but the spectrum is good enough (in reasonable agreement with found publications) to continue the analysis of the surface frozen films.

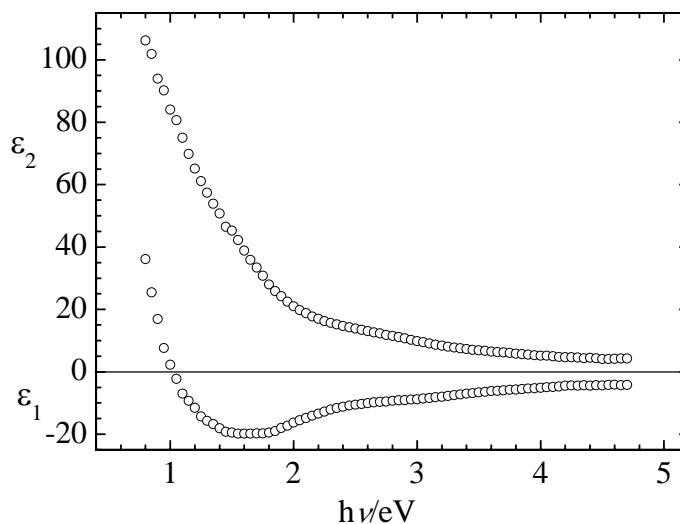


Fig. 6.2.22 Dielectric constant of pure solid Bi (○) measured on air at room temperature.

The 3 phase model (film – solid Bi, spectrum in Fig. 6.2.22, thickness (*unknown*); substrate - pure liquid Ga, spectrum at 130 °C) was applied to the spectra of the frozen films and revealed the following results. The fit to the experimental data was very good but as an outcome the thickness of about 1500 Å was obtained. It was shown in Chapter 5.3 that the limit of this measurement is ~50 nm; the ellipsometer is not able to “see” a substrate through thicker films. In this respect obtained thickness of ~0.1 μm indicates that the ellipsometric results can be described within the 2 phase model. So, the dielectric function of the frozen film can be found directly from experimental I_C and I_S values (Eq. 3.25 and 3.26 were written for Ψ and Δ values). The result is shown in Fig. 6.2.23.

In Fig. 6.2.23 the results of O. Hunderi [Hunderi75] are also shown. In his work the amorphous and crystalline Bi films (from 150 Å to 100 nm) were studied. Special care was taken to the preparation of the films: they were evaporated on a sapphire substrate and annealed under UHV (10^{-9} Torr). Any surface oxidation processes, which have a pronounced effect on the optical properties of the films, were completely excluded. Thick films of 100 nm always indicated the crystalline state [Hunderi75]. Having such a thickness they can be treated

as bulk crystalline Bi. The spectra (\bullet in Fig. 6.2.23, [Hunderi75]) are in strikingly good agreement with those of the surface frozen films (\circ in Fig. 6.2.23, this work). Both data sets agree well with the optical constants of pure solid bulk Bi (Fig. 6.2.22, this work).

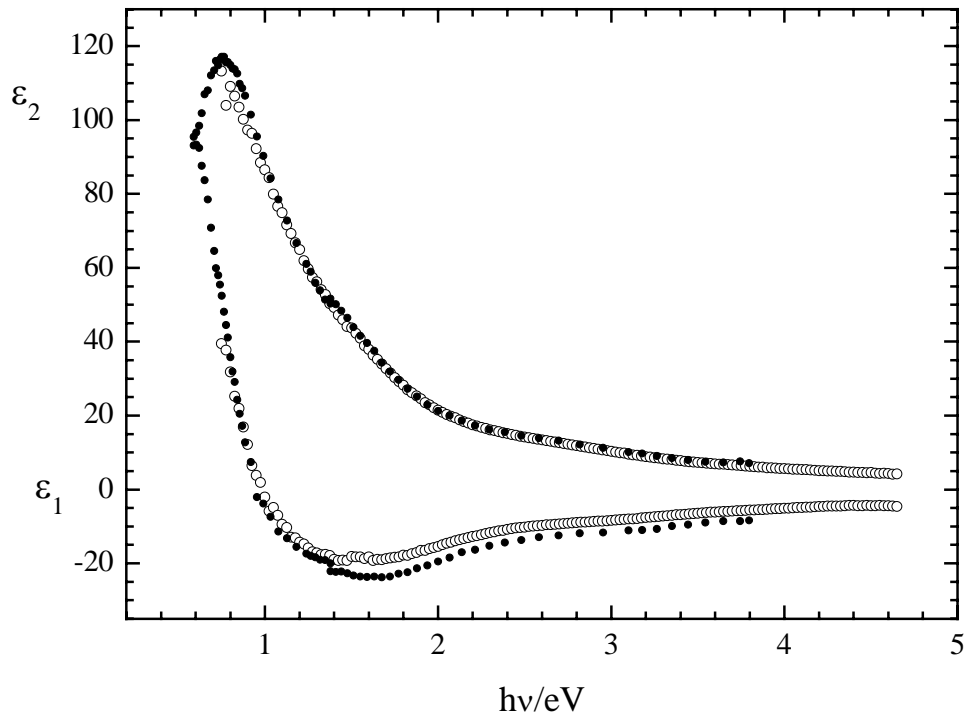


Fig. 6.2.23 Comparison of the real and imaginary parts of the dielectric function of the frozen film calculated on the base of 2 phase model: (\circ) this work at 123 °C and (\bullet) crystalline, 100 nm thick Bi films from the work of Hunderi [Hunderi75].

7. Discussion

7.1 Wetting and prewetting transitions at the fluid-wall interface of K-KCl

New and more detailed measurements of spectroscopic ellipsometry and reflectivity obtained in this work at the fluid K_xKCl_{1-x} /sapphire interface allow to revisit some specific wetting properties of this metal-molten salt system (Chapter 2.4). The first part of this chapter is dedicated to the ellipsometric evidence of the wetting transition. In the next part two particularly striking features of this transition will be discussed: (i) peculiar microscopic structure of the film, which is reflected in the optical spectra and (ii) unusual thickness of the films. New observations will be emphasized. In the third section the results along the solid-liquid coexistence line will be discussed in the framework of tetra point wetting. For this purpose an estimation of ΔG ($\Delta\mu$ in Chapter 2.4) was developed on the basis of the phase diagram calculations. The fourth section deals with the prewetting transition. For the first time in this system it was so clearly observed in the new measurements off of the solid-liquid coexistence. The results of this work give a new insight of the location of the prewetting line in K-KCl system.

• Ellipsometric evidence of the wetting transition

The system K-KCl exhibits different and clearly distinguishable wetting states at the interface with an inert wall (Chapter 6.1: Fig. 6.1 and Table 6.1.1). For an overview, these are exemplified in Fig. 7.1.1, on the path A-B-C for three compositions at constant temperature of about 710 °C (The corresponding loci in the phase diagram are marked in Fig. 6.1). This path also corresponds to the path Nr. 3 in Fig. 2.2 where on the approach to coexistence *complete wetting* is studied.

Spectrum A corresponds to a state at bulk solid-liquid coexistence. The wetting film has a thickness of 330 ± 40 nm. The optical constant $k(\omega)$ gives clear indication of the F-center absorption. Spectrum B was obtained in the homogenous phase and the salt rich film corresponds to a prewetting state. At roughly the same temperature the film thickness is much thinner (150 ± 60 nm), as it is expected for the situation off of coexistence. One can notice also the reduction of the F-center halfwidth. Further away from the coexistence one obtains spectrum C (taken from Ref. [Staroske00]), which represents the non-wetting side of the prewetting transition. Here, no salt rich film is present and the dielectric function corresponds to that of bulk metallic potassium with a small amount of potassium chloride ($x_{KCl}=0.04$).

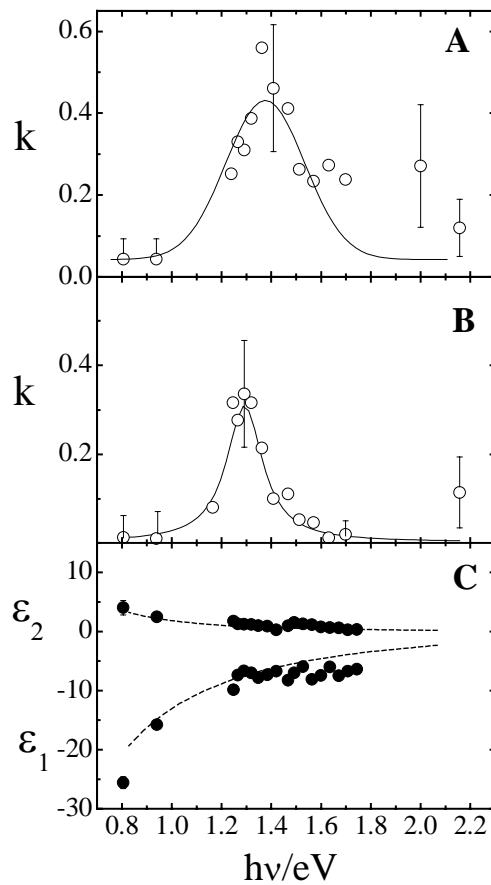


Fig. 7.1.1. Comparison of the optical properties of the K-KCl system at approximately the same temperature, around 710 °C. (A) and (B) absorption coefficients (*this work*, \circ) vs. energy of a salt-rich film at coexistence and near prewetting line, correspondingly. Solid lines are fits to selected points (see Chapter 6.1). (C) dielectric functions ϵ_1 and ϵ_2 (\bullet) measured in homogeneous liquid region [Staroske00]. For location of A, B and C in the phase diagram of K-KCl see Fig. 6.1.

• Microscopic structure of the film – information from F-center absorption band

The new experimental results of this work and older measurements, summarized in the Table 6.1.1 (p. 66), show several peculiar features:

- (i) The absorption band of the film spectrum has its absorption maximum in the range between 1.3 eV and 1.5 eV (for example Fig. 7.1.1) with an error of the order of 0.1 eV. In comparison to spectra of thermodynamically stable bulk phase F-centre solutions [Blankenhagen99] the absorption band of the wetting film shows a distinct reduced halfwidth.
- (ii) The films are very thick, a factor of 10 to 100 in comparison with the wetting films of other systems likes methanol-cyclohexan [Bonn94] or Ga-Bi [Huber02] at fluid/vapour interface. With improved accuracy the new data of this work nicely coincide with the older ones within experimental errors. Most interesting for the following discussion is the development of the film thickness along the solid-liquid coexistence curve illustrated in Fig.

7.1.6. Starting from 200 nm to 250 nm at temperatures around 650 °C the film thicknesses increases strongly by a factor of two as one approaches the monotectic temperature.

The position (energy) of absorption maximum is an unambiguous characteristic for the liquid state of the wetting layer, since the K_xKCl_{1-x} F-band in the solid state lies at 2.1 eV at temperatures near the melting point [Mollwo33]. Analysis of the absorption coefficient of the wetting film can reveal its composition [Blankenhagen99]. First, the concentration of the F-center has to be estimated. An estimation of F-center concentration, n_F , in the salt-rich wetting film can be performed with the help of the Smakula-equation [Fowler68]:

$$n_F = 8.21 \cdot 10^{16} \text{ cm}^{-3} \frac{1}{f} \frac{n}{(n^2 + 2)^2} \int K dK . \quad 7.1$$

In this equation K is absorption constant ($K = 4\pi k/\lambda$), n is index of refraction and f is oscillator strength. If the Lorenz-shape of the absorption band is assumed, Eq. 7.1 can be simplified [Fowler68]:

$$n_F = 1.29 \cdot 10^{17} \text{ cm}^{-3} \frac{1}{f} \frac{n}{(n^2 + 2)^2} K_{\max} \Delta E , \quad 7.2$$

where K_{\max} is absorption constant at maximum of the F-center absorption band and ΔE is halfwidth of it. All relevant parameters of Eq. 7.2 are taken from Table 6.1.1, for f a value of 0.8 typical for the F-center in the solid state is taken [Lüty60]. Results of this estimation are shown in Fig. 7.1.2 for the measurements of this work along the coexistence line. These results qualitatively agree with the previous estimations [Staroske00] and also present a new feature not detected and discussed before - continuous trend of n_F as a function thermodynamic variables (x_K , T). On approach to the monotectic point the concentration of F-center clearly increases (possible explanation will be given below), although by a small amount and in the very fine range. The values of n_F for the films off of coexistence are the same as on the coexistence around 10^{21} cm^{-3} but no trends can be found. Such magnitude of n_F corresponds to a salt concentration of 90 mole % in the wetting film (or $x_K \approx 0.1$); this result has been already noticed in the previous studies described in Chapter 2.4.

Coming now to another feature of the absorption band of the wetting salt-rich film, it is necessary to say, that although the physical mechanism underlying for its peculiar reduced band width is not quite clear yet, the following aspects seem to be important for further understanding. First, the strong undercooling of a liquid salt rich phase relative to T_{mono} should slow down the dynamical properties in the film on a molecular scale. The film may be regarded as being stabilized by the presence of the interface. This may also lead to a change of the microscopic structure compared to the bulk liquid. Therefore, longer life times of the

participating electronic states and smaller bandwidths are possible (were indeed observed in the femtosecond measurements of wetting films [Unterreiner 2002, unpublished]).

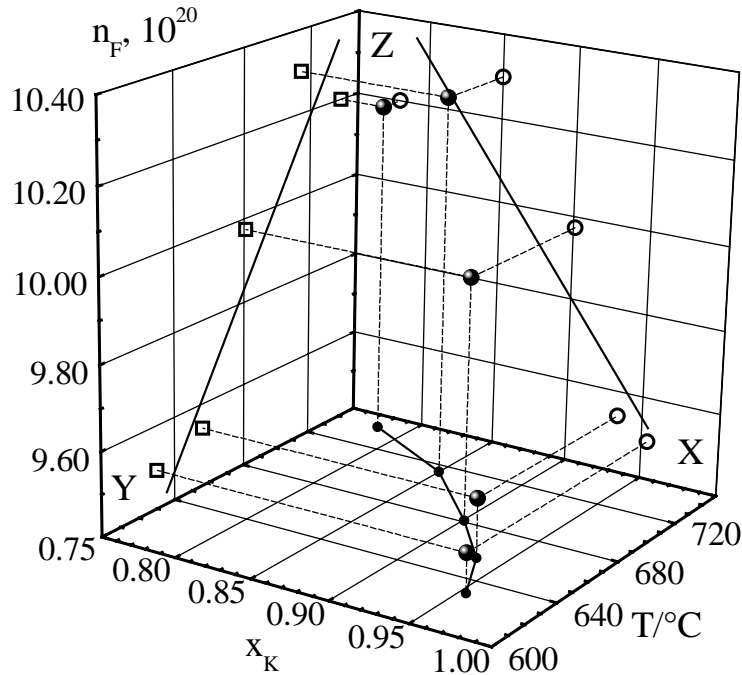


Fig. 7.1.2 Concentration of F-center, n_F (big volumetric circles) as a function of temperature, T and sample concentration, x_K . Points (\bullet) in the X-Y plane connected by a line represent the solid-liquid coexistence curve. Temperature variation of n_F in the Y-Z plane is shown by (\square). Variation with x_K (\circ) is shown in X-Z plane. Lines in both dependencies serve only as guides for the eyes. Dotted lines allow to identify a projection of n_F on corresponding plane.

Second, a charging of sapphire surface can occur. There are two mechanisms: (a) the charge can be generated by a partial electron transfer from the alkali metal to the alumina or (b) by the adsorption of oxide impurities, presumably K_2O at the interface [Rodriguez96] (their formation at certain conditions was clearly detected by SHG-study of [Tostmann97]). Charged surfaces and the inherent property of alkali halides to build up a pronounced local structure may lead to some charge ordering in adjacent to the surface layer. The possibility of such ordering was shown in the computer simulations, performed with a molten KCl film between smooth walls (with and without external electric field of 10^9 V/m), by Heyes and Clarke [Heyes81] (for recent calculations see [Booth01]). They found that whereas the average structure of the salt and interionic distances corresponds to that of bulk liquid, there is a long range ordering in the z plane of the electrified film and no evidence of such quasicrystalline ordering in the tangential planes. Possibly, F-center band of the wetting film reflects these structural characteristics (detailed discussion can be found in [Staroske01]). The halfwidth of absorption peaks of the wetting films on coexistence as a function of the sample

concentration is shown in Fig. 7.1.3 a. For comparison a typical value of ΔE of the bulk K_xKCl_{1-x} phase from an optical absorption measurement [Blankenhagen99] is shown by the symbol (\square). The errors are quite big and definitely complicate any quantitative analysis. Anyway, the continuous increase of ΔE approaching the value of bulk phase is clearly discernible. In the concentration range considered in Fig. 7.1.3 the wetting film thickness along the solid-liquid coexistence curve increases roughly by an order of magnitude from 30 nm to 400 nm (see Fig. 6.1), the increase of ΔE with x_K also reflects a continuous change of the microscopic structure of the films. Whereas at low film thickness the charge ordering may prevail, this is certainly not the case for thicker films - ΔE approaches its bulk value. This fact could not be resolved in the previous study [Staroske00]. Unfortunately, at the moment there are no theoretical model calculations which can explain the T- and x-variation of ΔE as plotted in Fig. 7.1.3a.

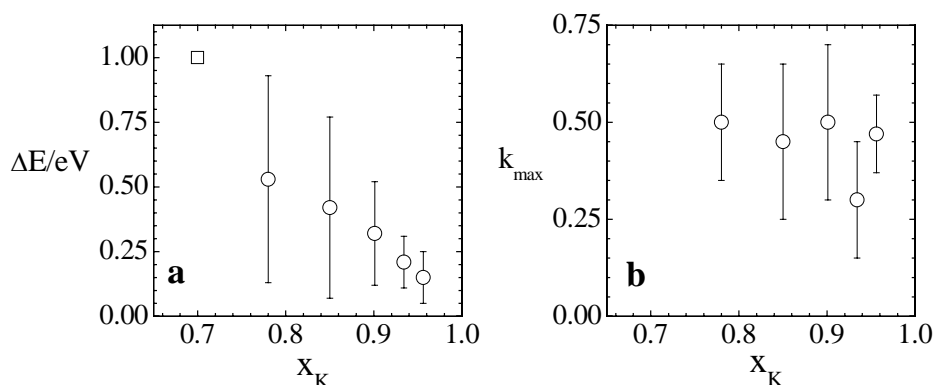


Fig. 7.1.3 Features of the F-center bands of the wetting films, measured in this work along the solid-liquid line (\circ). Square (\square) represents the result of absorption measurement of bulk K_xKCl_{1-x} [Blankenhagen99].

Off of coexistence ΔE stays almost constant (Table 6.1.1, p. 66). The behaviour of the absorption coefficient at maximum, k_{max} is also interesting – it stays practically constant at ~ 0.45 for the measurement along the solid-liquid line (Fig. 7.1.3 b) and slightly scatters, but still around the same value, off of coexistence (not shown here). Since in the absorption studies of the bulk phase it was found that k_{max} sensitively reflects the salt concentration, from the present measurements one can conclude that the composition of the film stays practically constant. In the previous study of Staroske [Staroske00] k_{max} had a large uncertainty. This is probably due to a possible influence of the remaining solid salt on the optical properties. The previous measurements were made in the solid-liquid region, which was avoided in the present measurements (see Chapter 4, point “d” on p. 34 and Chapter 6.1, p. 55).

The assumption of a surface charge can also help to explain qualitatively another still open problem (ii) of the study of wetting in K-KCl – unusual thickness of the films up to 400 nm

(see Table 6.1.1). The effect of the surface charge on the wetting film was first described by Langmuir [Langmuir38] and then generalized by Kayser to liquid mixtures of polar and nonpolar components [Kayser86b]. The double layer interactions lead to the disjoining pressure, which thickens the wetting film. Calculations made in work of Staroske [Staroske01] give 10 nm as an estimation of the thickness of electrified film. This approaches right order of magnitude in comparison to the observed experimental values. But the problem still remains open.

• Tetra point wetting

The strong undercooling discussed in the previous section indicates a metastable state of the salt-rich wetting phase in contact with a wall. Also a strong increase of the wetting film thickness at liquid-liquid coexistence as the monotectic temperature is approached can be clearly seen from the ellipsometric results (see Table 6.1.1 on p. 66). These facts are in a good agreement with the scenario of tetra point wetting [Dietrich97] (outlined in Chapter 2.4, p. 15). In this context it is important to develop a thermodynamical description of the K-KCl system, namely its total free enthalpy $G(x_{KCl}, T; p)$, which describes a respective equilibrium. Since we are particularly interested in the extrapolation of the demixing binodals, the liquid-liquid equilibrium of the miscibility gap has to be considered. One way would be the use of thermodynamic data of the enthalpy of mixing. Unfortunately, suitable data are practically not available. There is recent experimental study of Schmutzler et al. [Schmutzler96], who measured the activity of potassium in the K-KCl melt at temperatures from 1030 to 1250 K and determined ΔG_{mix} . But it is impossible to convert the tabulated and graph's data of the G as a function of temperature and concentration.

Another approach is to use the phase diagram calculations (see for a review [Kattner97]). First, one needs to choose some appropriate analytic expression of the free enthalpy. The unknown coefficients of the polynomial expression for $\Delta_{\text{mix}}G$ are then fitted to the known phase diagram data. Most thorough study of molten alkali metal-halide systems, including K-KCl, has been performed by Bredig et al. [Bredig64]. Hence in this work, exclusively their data of the K-KCl phase diagram has been used for the thermodynamic calculations.

In general, the free enthalpy of a binary solution can be approximated by a regular solution-type model [Kattner97]:

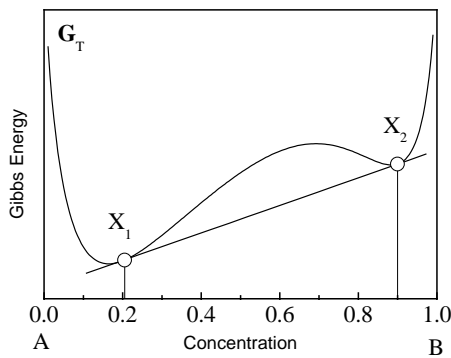
$$G = x_K G_K^o + x_{KCl} G_{KCl}^o + RT(x_K \ln x_K + x_{KCl} \ln x_{KCl}) + G^E. \quad 7.3.$$

Sum of the first two terms in Eq. 7.3 corresponds to a standard enthalpy of the K and KCl constituents of the phase, next term is the Gibbs energy of mixing for an ideal solution and

last G^E is the so-called excess term. Usually to approximate G^E the Redlich-Kister polynomials are used [Kattner97]:

$$G^E = x_{KCl}(1-x_{KCl}) \left(\sum_{n=0}^i A_n (1-2x_{KCl})^n \right), \quad A_n = a_n - b_n T. \quad 7.4.$$

The data for pure potassium and potassium chloride have been taken from the thermodynamical database JANAF [JANAF85]. The polynomial was limited to the third order. The 8 unknown coefficients a_n and b_n (*enthalpy* and *entropy* parameters) were determined by finding the double tangent to the Gibbs energy given by Eq. 7.3 in the temperature range between T_{mono} and T_c . To find the common tangent the shooting method (Eq. 7.5 and 7.6) has been applied. The principle is shown schematically in Fig. 7.1.4.



$$\left. \frac{\partial G_T}{\partial x} \right|_{x=x_1} = \left. \frac{\partial G_T}{\partial x} \right|_{x=x_2}, \quad 7.5$$

$$G_T(x_1) + \left. \frac{\partial G_T}{\partial x} \right|_{x=x_1} (x_2 - x_1) = G_T(x_2). \quad 7.6$$

Fig. 7.1.4 Schematic visualisation of the shooting method to find common tangent line to the Gibbs energy of binary mixture A-B. X_1 and X_2 correspond to the opposite points of miscibility gap at the same temperature. Eq. 7.5 and 7.6 are mathematical realisation of the common tangent line.

The system of eight equations was composed in the following way. Four temperatures T_j ($j=1\dots 4$) within the miscibility gap have been chosen. For each temperature from the K-KCl phase diagram one can read two concentrations (x_1 and x_2 in the Eq. 7.5. and 7.6) lying on the opposite sides of the binodal. Two linear equations containing only a_n and b_n could be written using Eq. 7.5 and 7.6. The linear system of eight equations with eight unknowns can be easily solved. The shooting method and manipulations with the thermodynamic data was performed with the help of Maple7 (mathematic software).

In spite of apparent clarity and unambiguous solution of system of linear equation, the fitting had to be done several times. The obtained polynomials of $G(x_{KCl}, T)$ had slightly different coefficients depending on the choice of the temperatures T_j . However, the correctness of the polynomial expression could be easily checked. First of all, it should correctly describe the

critical point of the phase diagram K-KCl, $x_{KCl}^C=0.61$, $T_C=1063$ K [Johnson58], and hence satisfy the following equation:

$$\frac{\partial^2 G(x_{KCl}^C = 0.61, T_C)}{\partial T^2} = 0. \quad 7.7$$

Secondly, the polynomial has to reproduce the liquid-liquid line. The parameters of the best-found polynomials are listed in the Tab. 7.1. The reconstruction of the miscibility gap in the Fig. 7.1.5 is quite good (open points nicely coincide with liquid-liquid lines), which gives a confidence in the obtained expression of $G(x_{KCl}, T; p = \text{const})$.

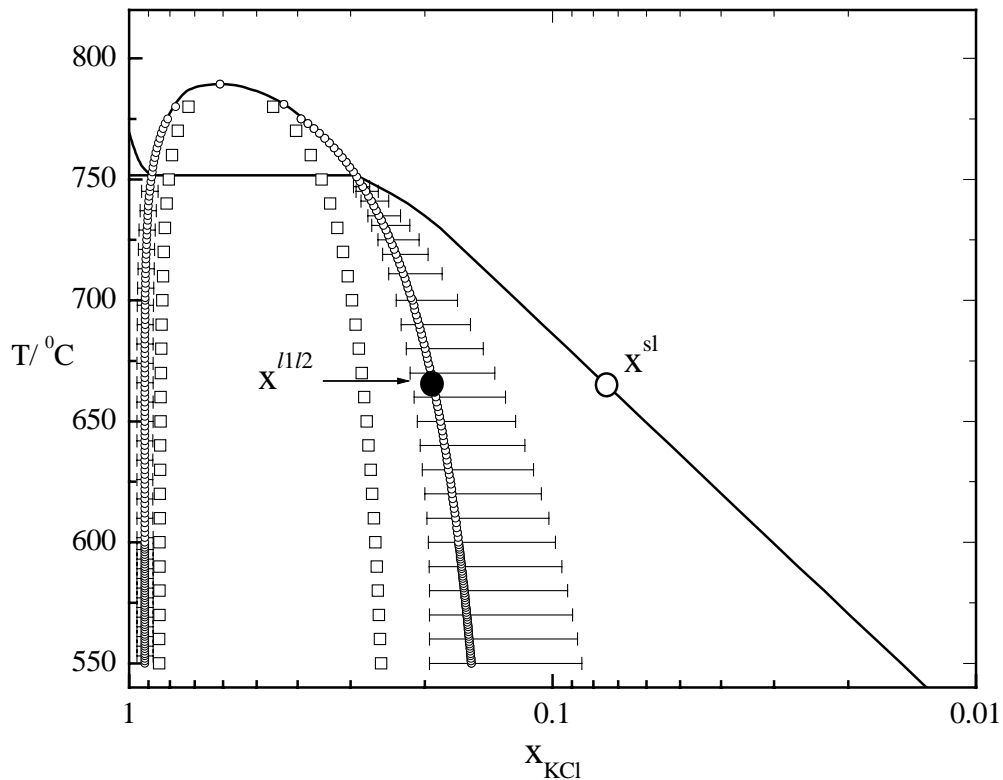


Fig. 7.1.5 High temperature part of the phase diagram of K-KCl [Johnson58], full lines; the circles (\circ) present a fit to the miscibility gap (for clarity not all circles are shown) and its metastable extensions below the monotectic temperature; the squares (\square) show the spinodals. The error bars have been determined from the different polynomial fits of G (see text). Big open and filled circles visualize the salt concentrations x^{sl} and $x^{1/2}$, which are used in Eq. 7.8.

Table 7.1. Enthalpy and entropy parameters a_n and b_n (Eq. 7.3 and 7.4) found after the fit to the miscibility gap of the K-KCl diagram.

n	a_n / Jmol^{-1}	$b_n / \text{Jmol}^{-1} \text{K}^{-1}$
0	11156.9	-2.8
1	39577.8	46.5
2	-93084.9	-84.8
3	-180520.9	-162.7

It has to be pointed out again, that the Redlich-Kister polynomials in the present calculations are based on the shape of the miscibility gap alone. So, the obtained expression is only an estimation. Moreover the error bars are quite large. They were obtained from the comparison of several solutions of the polynomial fitting.

From the Gibbs energy a number of thermodynamic properties can be determined, such as the spinodal and metastable extension of the miscibility gap, see Fig. 7.1.5, as well as the aim of this calculation - the difference in the Gibbs energy, ΔG . This is the relevant quantity for a two-component mixture, since it includes the chemical potentials of both components, whereas $\Delta\mu$ is usually related to one component, normally the major component of the wetting phase (see for example [Staroske01] and [Dogel03]). It has to be noticed, that in the literature no uniform approach to the estimation of $\Delta\mu$ exists. In general, the scaling parameter should possess the following properties: it has to contain the maximum information about the system and should become zero on the approach to certain state, which will correspondingly reflect the divergence of the wetting film to macroscopic values. Considering the usual experimental situation, one could choose the following scaling parameters, which would satisfy more or less the above mentioned requirements. For example, it can be $\Delta T = T_{\text{exp}} - T_{ll/2}$ at constant concentration, see [Schick90] and [Bonn01], or $\Delta x = x_{\text{exp}} - x_i$ (where x_i could be x_{mono} , see [Winblatt98], or x_{coex}). The choice of the parameter should not influence the nature of the scaling behaviour (short- or long-range) of the wetting film on approach to the liquid-liquid coexistence, but the quantitative outcome of the fitting will be different.

Value of ΔG in this work was directly calculated from Eq. 7.3 and 7.4, using data from Table 7.1, according to the following expression:

$$\Delta G = G_{sl} - G_{ll/2} = G(x_{KCl}^{sl}, T_{\text{exp}}) - G(x_{KCl}^{ll/2}, T_{\text{exp}}), \quad 7.8$$

where G_{sl} corresponds to the Gibbs free energy at the solid-liquid coexistence line at the experimental temperature and concentration, and $G_{ll/2}$ is its value at the metastable extension of the liquid-liquid demixing line at this experimental temperature (see Fig. 7.1.5).

The wetting film thickness results (this work and [Staroske00]) along the coexistence curve can be now discussed for the first time more quantitatively as a function of ΔG , see Fig. 7.1.6. For this aim the reduced error bars of this work are essential. Even though very thick, the film remains finite approaching the monotectic point or in other words the liquid-liquid coexistence curve, which is in agreement with the tetra point wetting scenario. According to it, all measurements on and off of coexistence correspond to the prewetting states with respect to the metastable extensions of the liquid-liquid lines (Fig. 7.1.5). And the measurements along the solid-liquid coexistence probe the complete wetting approaching the

monotectic point. A strong increase of the film thickness approaching the monotectic temperature is clearly discernible (Fig. 7.1.6).

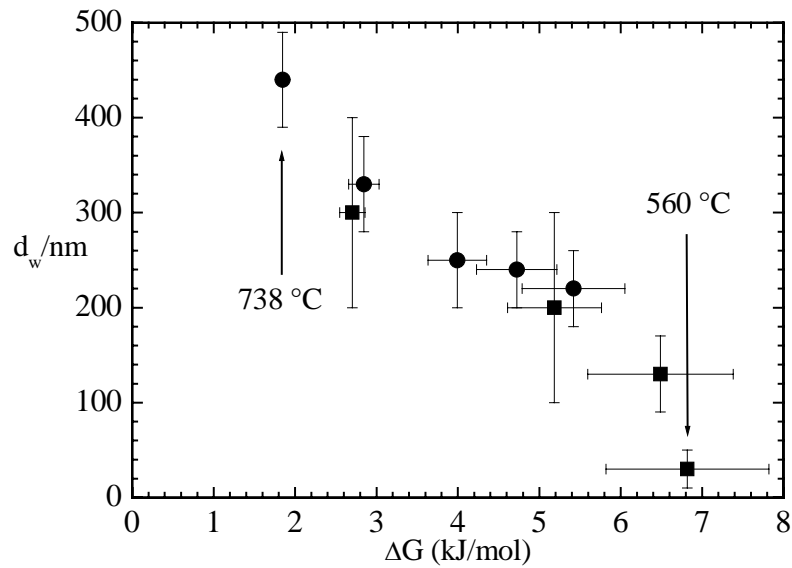


Fig. 7.1.6. Experimental data of the wetting film thickness along the coexistence line approaching the monotectic temperature as a function of ΔG (Eq. 7.8): (■) previous results, (●) results of this work.

It would be interesting to study the functional dependence of the film thickness on ΔG (instead of $\Delta\mu$ introduced in Chapter 2.3): $d \propto \ln(1/\Delta G)$ is expected for screened coulomb interaction; and $d \propto (\Delta G)^{-1/3}$ for algebraically decaying van der Waals type interactions. But first, both dependencies, Eq. 2.8 and 2.9, were simplified. In this experiment $L \sim 0.5$ cm and $\Delta\rho \sim 0.8$ g/cm³, which yields $\omega_g \sim (10^2 \text{ J/m}^3) \times d$. Comparing this value with the contribution of $\Delta G \times d$, which is of order $(10^{6 \dots 7} \text{ J/m}^3) \times d$ the gravitational term could be neglected. The experimental point at $d = 30$ nm [Staroske] was not considered during fitting, since it definitely deviates from the common trend of the film thickness.

Even though a logarithmic dependence seems to be slightly better than the other one, both theoretical dependencies show quite poor fits to the experimental data, Fig. 7.1.7 (dashed and dash-dotted lines). The discrimination is difficult due to the following reasons. Even with improved determination of the film thickness in this work, errors of d_w are still relatively big. The estimation of ΔG brings an additional uncertainty, which also increases for thinner films (determined by the errors in polynomial expression for the Gibbs energy). Moreover, it is difficult to expect from a molten salt in contact with a charged substrate to exhibit some distinct scaling behaviour. Furthermore, at $x_{\text{mono}}, T_{\text{mono}}$ the film could undergo metal-non-metal transition.

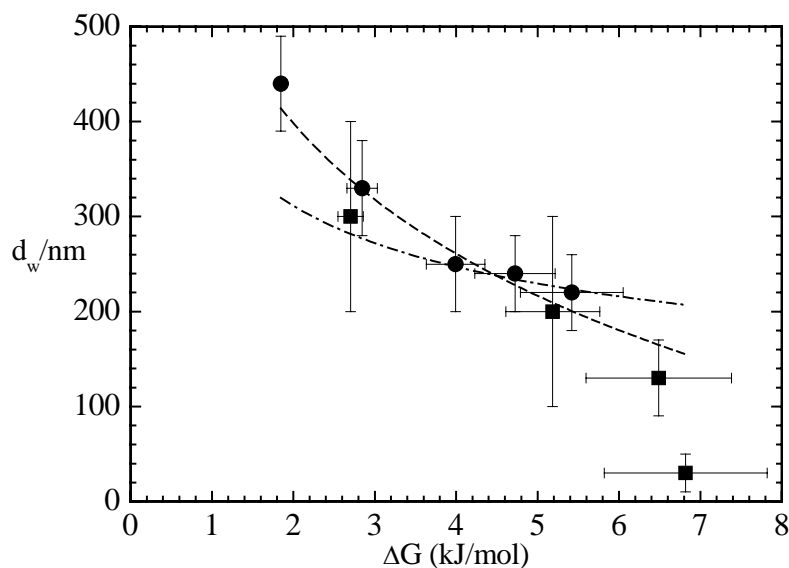


Fig. 7.1.7. Experimental data (this work, ●, and previous results, ■) of the wetting film thickness along the coexistence line approaching the monotectic temperature as a function of $\ln(1/\Delta G)$ – dashed line and function $(1/\Delta G)^{1/3}$ – dash-dotted line.

It can be also seen from Fig. 7.1.6 and 7.1.7 that more measurements are required especially in the close vicinity of the monotectic point. So, the present situation is very complex from both experimental and theoretical point of view. No theory has been so far found, which could give an quantitative explanation of the observed behaviours of the film thickness.

An important consequence of the tetra point wetting scenario concerns the wetting transition temperature T_w and location of the prewetting line. T_w should lie on the metastable extension of the liquid-liquid demixing curve and the prewetting line should leave this curve tangentially at T_w . One can compare Fig. 6.1 and Fig. 2.7, both are shown for convenience in Fig. 1.7.8, which includes also metastable extensions of liquid-liquid lines (from Fig. 7.1.5).

It is apparent that the dashed prewetting line cannot fulfil above-mentioned condition. As was already described in the Chapter 2.4 this line was originally derived from distinct patterns of the second harmonic signal (SHG) with continuously increasing temperature [Tostmann96]. In his work it was assumed that the transition to complete wetting occurs along the solid-liquid coexistence curve with the apparent wetting temperature T_w' . In the light of the results of this work a clearly higher slope of the prewetting line has to be anticipated. Such new prewetting line would also help to separate points of wetting (full symbols) from those at nonwetting (open symbols) in Fig. 7.1.8. The position of the true wetting temperature T_w remains unknown.

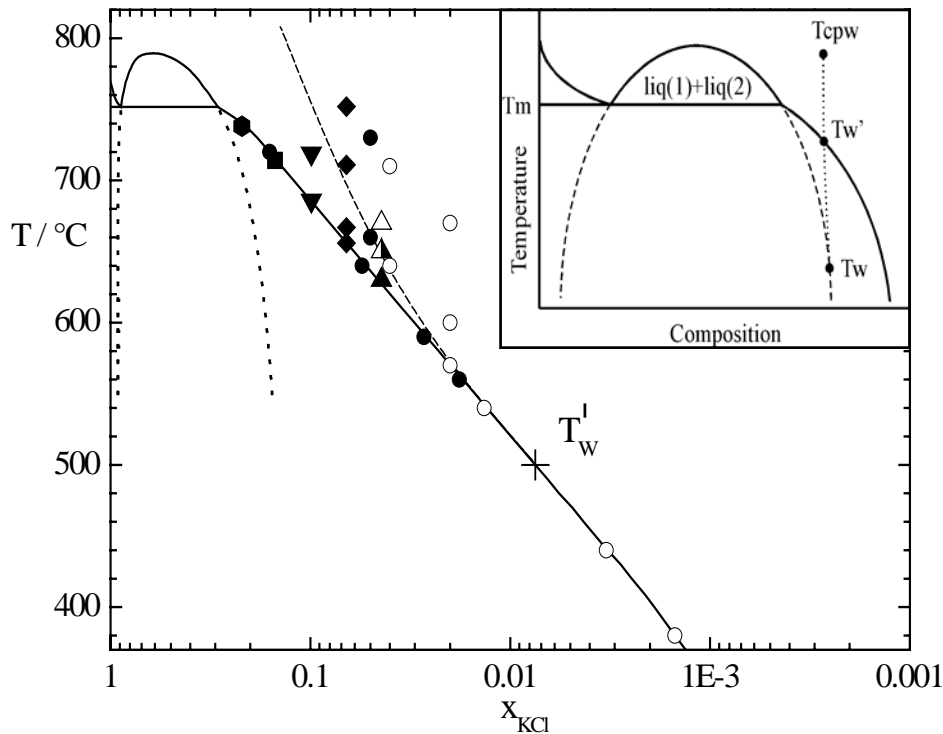


Fig. 7.1.8 Combination of Fig. 6.1 (all experimental results, Chapter 6.1) and liquid-liquid demixing curves taken from Fig. 7.1.5. In the inset schematic illustration of tetra point wetting scenario (Fig. 2.3).

• Characterization of the prewetting transition

In this section the experiments performed off of solid-liquid coexistence line are discussed.

On the high temperature side of the prewetting line, but restricted to a maximum salt concentration of $x_{\text{KCl}}=0.05$, non-wetting conditions are indeed observed (open symbols in Fig. 7.1.8 above). However, at higher salt concentrations the wetting case is always found, i. e. a salt rich film spreads between the sapphire window and the bulk metallic liquid (Fig. 6.1 or 7.1.8). It is possible that this discrepancy, with expected metallic liquid for the situation above the prewetting line, arises from the hysteresis effects that sometimes strongly influence wetting transitions [Bonn01]. This means that occurrence and disappearance of the wetting film may be triggered by the experimental conditions such as heating and cooling rates or residual impurities. In general one also expects for metastable states a dependence on the experimental history.

In the context of the prewetting transition the experiment marked with triangles (\blacktriangle in Fig. 6.1 or 7.1.8) at a composition of $x_{\text{K}}=0.954$ is of special interest. For the lowest temperature ($T=630$ °C, point 1 in Fig. 6.1) the spectra give clear evidence of the presence of a wetting film. The data, evaluated within the 3 phase model, are shown in Fig. 6.1.1 in terms of n and k . The film thickness is 220 ± 35 nm. Increasing the temperature by 20 K to 650 °C (half filled triangle in Fig. 6.1.13) the ellipsometry-reflectometry spectra were obtained, which could be

modelled with the 2 phase as well as with the 3 phase model (Chapter 6.1, p. 58). This situation can be treated as either some intermediate state or the accuracy limit. At next temperature of 670 °C the transition from the wetting to the non-wetting case proceeds (point 2 in Fig. 6.1). Now a bulk metallic liquid in contact with the sapphire is clearly detected. The spectra of dielectric function are drawn in Fig. 6.1.4 together with a satisfactory free electron model fit using for the number density of the free electrons $N_e=1.058 \times 10^{22} \text{ cm}^{-3}$ and for the dc conductivity $\sigma_e(0)=16210 (\Omega\text{cm})^{-1}$.

Such an unambiguous indication for the prewetting transition was not observed at higher compositions. However, the experiment at a metal composition of $x_K=0.934$ (♦ in Fig. 6.1) shows a clear trend for the wetting film thickness with increasing temperature as can be seen from Table 6.1.1. From this, one gets two pieces of information. First, with increasing temperature the film thickness decreases significantly, even though the prewetting transition is not observed. Second, there is some insight into the problem of a possible hysteresis. Starting from the measurement at $T=656$ °C in close vicinity to the liquidus line, the temperature was increased to 711 °C and then to 752 °C. The last experiment was done at $T=667$ °C. There is no indication for a wetting film thickness hysteresis since the latter data point nicely fits into the sequence of those obtained on heating.

7.2. Wetting and surface freezing transitions at the fluid/vapour interface of Ga-Bi alloys

• Complete wetting transition at the liquid-liquid coexistence line

As was shown in Chapter 6.2, the results of the modulation ellipsometry measurements at the fluid/vapour interface of $\text{Ga}_{1-x}\text{Bi}_x$ strongly support the scenario of tetra point wetting (Chapter 2.4). This can be seen in Fig. 6.2.13, where the behaviour of the ellipsometric angle Ψ is undoubtedly identified as a growth of the wetting film approaching the liquid-liquid coexistence on the path AB and disappearance of the wetting film leaving the coexistence along the solid-liquid line. The same path M^*C' was probed again for the alloys with the concentration of bismuth higher than the critical one ($x_{\text{Bi}}=0.3$) and exhibits the same behaviour of Ψ (Fig. 6.2.14); hence the same decrease in wetting film thickness occurs. Furthermore, this second measurement provides an experimental evidence of the absence of a wetting transition in the homogeneous liquid region for alloys with $x_{\text{Bi}}>0.3$ (see p. 77, 181).

To proceed with the scenario of tetra point wetting one needs the thermodynamic data on the system. For the Ga-Bi system this analysis has been performed relying on the data sets from the CalPhaD initiative [Burton96] (see Ref. [Huber03]), practically in the same way as described above for K-KCl. The Redlich-Kister polynomial for the Gibbs free energy, $G(x,T)$, was determined (see Appendix, p. 134). It has to be mentioned that the polynomial fit was based on the phase diagram of Predel [Predel60] only; hence it might possess some deficiency and should be treated critically. Recent experimental results of the study of the Ga-Bi phase diagram deviate from that of Predel, the demixing lines have lower temperatures (systematically by 2 K) but moreover the miscibility gap has a different shape [Khairulin02].

As in the previous chapter the difference in the free Gibbs enthalpy, $\Delta G(x_{\text{Ga}}, T, p=\text{const})$, will be used for a quantitative analysis. According to the experimental situation the value of ΔG was calculated using the following expression (analogue to Eq. 7.8):

$$\Delta G = G_{\text{exp}} - G_{\text{lll2}} = G(x'_{\text{Ga}}, T_{\text{exp}}) - G(x''_{\text{Ga}}, T_{\text{exp}}), \quad 7.9.$$

where G_{exp} corresponds to the Gibbs energy of the Ga-Bi mixture at the experimental temperature (T_{exp}) and concentration (x'_{Ga}) in the homogeneous liquid region, and G_{lll2} is its value at the liquid-liquid demixing line (x''_{Ga}) at this temperature (concentrations x'_{Ga} and x''_{Ga} correspond to open and solid points in the inset to Fig. 7.2.1).

The thickness of the wetting films obtained in this work (in Fig. 6.2.11 and Fig. 6.2.12, the T-dependence of d_w are shown) for two concentrations $x_{\text{Bi}}=0.12$ and 0.2 is presented now in terms of ΔG in Fig. 7.2.1. Both data sets are comparable within the experimental errors. But unfortunately, the number of points at $x_{\text{Bi}}=0.2$ (\square) is not sufficient for a quantitative analysis

since only three from seven temperatures lie below critical temperature of Ga-Bi system of 262.8 °C [Predel60] and hence can not be treated within tetra point wetting scenario. However, a thickness of the “wetting film” of ~ 5 Å was measured above T_C for $x_{Bi}=0.2$. Measurement above T_C for $x_{Bi}= 0.12$ reveals an apparent film of ~ 2 Å.

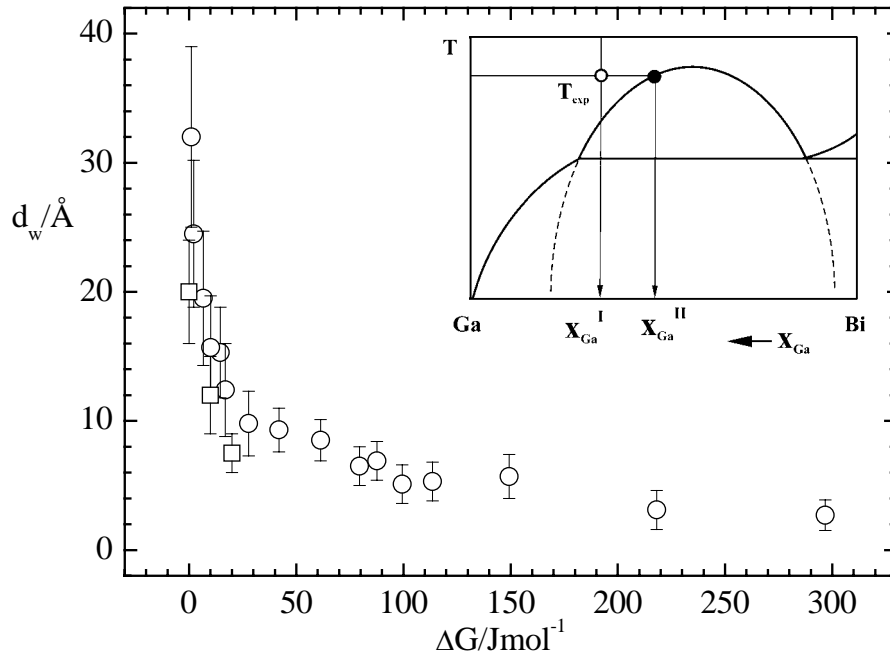


Fig. 7.2.1 Relation between ΔG and thicknesses of the wetting films determined for two alloys $\text{Ga}_{0.88}\text{Bi}_{0.12}$ (\circ) and $\text{Ga}_{0.8}\text{Bi}_{0.2}$ (\square). The inset shows a schematic Ga-Bi diagram, open point marks the location of the measurement: x'_{Ga} is nominal molar fraction of Ga in alloy ($x_{Ga}= 0.88$ and 0.8), filled point indicates the x''_{Ga} at the liquid-liquid demixing line at temperature of measurement, T_{exp} (see text).

These values can be treated as an offset or inaccuracy of the present measurements. This is not surprising if one takes into account the simplicity of the 3 phase interfacial model, which was used to evaluate the ellipsometric results, and experimental difficulties (liquid surface etc). This would also explain the difference in d_w (Fig. 7.2.1) approaching the liquid-liquid coexistence for two concentrations. So, the uncertainty of the film thickness determination in this measurement is unfortunately relatively high. Anyway, in principle we are interested in the relative change of the thickness, i.e. in the nature of the increase in wetting film in the limit $\Delta G \rightarrow 0$. This increase is clearly seen in both data sets. From the fit to the experimentally determined thickness the part $\omega(d)$ of the *effective interfacial potential* Ω^{eff} (Eq. 2.3) can be found. In the case of the Ga-Bi system with screened Coulomb interactions (short-range) the following dependence of the equilibrium wetting film thickness is expected: $d_w = 1/\lambda \ln(\Phi/\Delta G)$ [Pandit82] (see Eq. 2.6, in this equation $\Delta\mu$ has to be substituted for ΔG and $\lambda \cdot \sigma_0$ for Φ).

From the fit, Fig. 7.2.2, the following parameters of the interfacial short-range potential were found: correlation length, $1/\lambda$, $4.4 \pm 0.2 \text{ \AA}$ and $\Phi = 380 \pm 44 \text{ Jmol}^{-1}$.

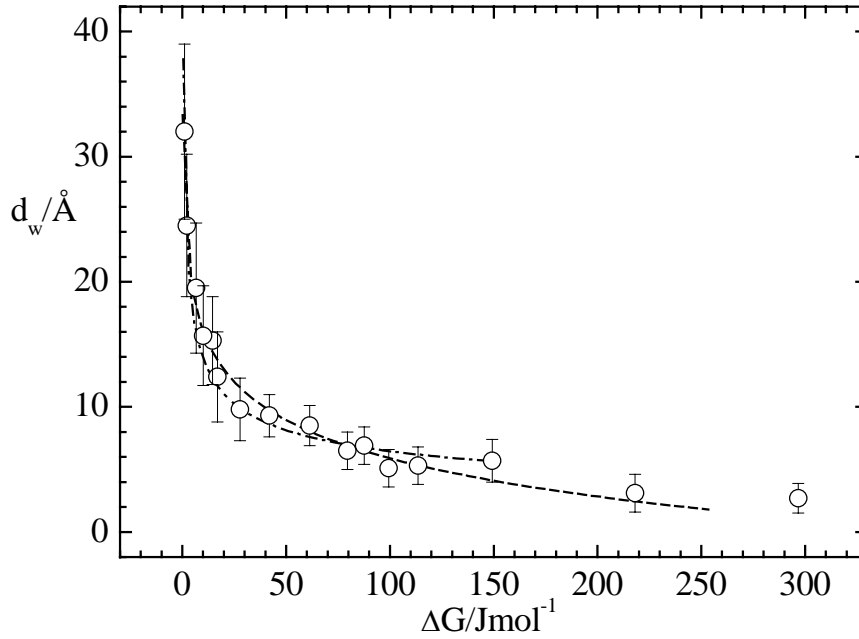


Fig. 7.2.2 Comparison of two fits to the experimental points of the wetting film thickness determined for the $\text{Ga}_{0.88}\text{Bi}_{0.12}$ alloy (\circ): dashed curve corresponds to $d_w \propto \ln(\Delta G^{-1})$, for the fit parameters see text; dash-dotted curve corresponds to $d_w \propto \Delta G^{-1/3}$.

During the fitting and in the formula for d_w above it was tacitly assumed that the gravitational contribution ($g\Delta\rho Ld$, see Eq. 2.6) is negligibly small. This fact can be easily proven:

$$\frac{\omega_g}{d} = 9.8 \frac{m}{s^2} \cdot (8.5 - 6.9) \times 10^3 \frac{kg}{m^3} \cdot 10 \times 10^{-3} m = 156.8 \text{ Jm}^{-3} \text{ or } 2.7 \times 10^{-3} \text{ Jmol}^{-1},$$

here g is the gravitational constant, $\Delta\rho$ is the difference in the density for two phases with x'_{Ga} and x''_{Ga} at coexistence and L is the thickness of substrate, defined by the crucible construction (all material properties are taken from Ref. [Takamichi93]). Indeed, above the liquid-liquid coexistence line the contribution of gravity to the thickness of the wetting film is negligibly small (compare 380 and 0.003 Jmol^{-1}) but it becomes important and finally defines the film thickness at coexistence where $\Delta G = 0$. Using the parameters of the surface potential found from the fit and the above estimated gravitational contribution one can obtain:

$$d_w^{1/2} = 4.4 \text{ \AA} \cdot \ln \left(\frac{380 \text{ Jmol}^{-1}}{2.7 \times 10^{-3} \text{ Jmol}^{-1}} \right) \sim 55 \text{ \AA}.$$

It is possible to conduct such an estimation in another way: inserting $1/\lambda = 4.4 \text{ \AA}$ (found above) in Eq. 2.6 (Chapter 2.3), and using a value of the surface tension for $\text{Ga}_{0.88}\text{Bi}_{0.12}$ alloys, $\sigma_0 \sim 500 \text{ mNm}^{-1}$ [Ayyad03], the film thickness at liquid-liquid coexistence can be found as:

$$d_w^{1/2} = 4.4 \text{ \AA} \cdot \ln \left(\frac{500 \times 10^{-3} \text{ Jm}^{-2}}{4.4 \times 10^{-10} \text{ m} \times 156.8 \text{ Jm}^{-3}} \right) \sim 70 \text{ \AA}.$$

These two almost independent simple estimations indicate first, that the wetting film diverges to the finite mesoscopic rather than macroscopic values (this result will be used in the next section). And secondly, they agree with the thickness of $\sim 30 \text{ \AA}$, found in this work experimentally in the close vicinity of the liquid-liquid coexistence line (see Fig. 7.2.1).

A quantitative comparison of the maximum values of the wetting films measured in this work $30 \pm 6 \text{ \AA}$ and 50 \AA obtained in the work of Huber et al. is difficult since the authors do not give any estimation of the experimental error [Huber02]. Two moments can be considered to get an insight into the approximate magnitude of this uncertainty. First, the film thickness in X-ray reflectivity measurements is defined from the electron density profiles, which possess certain error. Furthermore, there is some uncertainty in the shape of density profile itself. In a work of Pohl et al. [Pohl96], for example, it was shown that the X-ray reflectivity data could be consistently represented using some variations in the form of electron density profile. The authors were able to account for the change in X-ray reflectivity as well as in ellipsometric data during surface freezing transition of liquid alkanes. Hence the uncertainty of the determination of d_w in the work of Huber et al. [Huber02] can be estimated to be $10 \dots 15 \text{ \AA}$ (same value was from P. Huber in a private communication). In this sense the comparison of the values of short-range surface potential found in this work and in Refs. [Huber02,03] is difficult as well. Moreover, the authors used another way to estimate ΔG , which they unfortunately do not publish.

A few critical comments on the logarithmic fit in Fig. 7.2.2 are necessary. Even though it is good within error bars, one can notice certain deviations for thicker films. It is also interesting to compare this fit a description for long-range interactions (van der Waals), i.e. $d_w \propto \Delta G^{-1/3}$ (dash-dotted line in Fig. 7.2.2). It is clear that within experimental accuracy of this measurement and leaving two last points out of consideration (since they are on the edge of sensitivity of this setup), the honest discrimination between exponentially and algebraically decaying forces is practically impossible, especially at large d_w values.

It can be shown that the data of other studies of metallic systems (Ga-Pb [Winblatt98] and Ga-Bi [Huber02]) suffer from the same uncertainty in the film thickness determination as these of the present experiment and a clear discrimination between $d_w \propto \ln(\Delta G^{-1})$ and $d_w \propto \Delta G^{-1/3}$ is very difficult.

The thermodynamic model calculations of surface phase transitions in Ga-Bi alloys performed by Tsekov and Freyland [Tsekov03] are in good agreement with the experimental

results of this work. The theoretical calculations predict a complete wetting at conditions where it was observed experimentally and calculated thickness of the wetting film ($\sim 8 \text{ \AA}$) is in qualitative agreement with present experimental data. For more detailed analysis of the experimental data the improvement of this measurement (better accuracy of d_w determination) would be challenging.

• **Ellipsometric characterization of surface freezing transition**

First, it can be stated that the ellipsometric measurements reported here clearly indicate a sharp change of the optical constants at the alloy surface at a temperature well above the liquidus line. The temperature corresponding to this drop in Ψ and Δ coincide within the experimental errors with the surface freezing transitions found recently by SHG [Turchanin02] and capillary wave spectroscopy [Ayyad03]. As for the determination of the thickness of the corresponding surface frozen films the ellipsometric measurements undoubtedly indicate two important features: (i) the appeared solid-like film very quickly (Fig. 6.2.21) grows to a thickness above 50 nm and (ii) consists of pure Bi.

A description of the experimental situation at the sample/vacuum interface during kinetic measurements can give a qualitative insight in the process of film growth (i). Liquid alloy was continuously cooled down from temperatures above the solid-liquid coexistence curve. Spectroscopic ellipsometry indicates that the alloy presents a homogeneous liquid - there is no detectable film on the top of it. In this work the cooling was stopped immediately after the temperature T_{SF} had been reached in the sample. At this temperature a solid Bi film appears [Turchanin02]. This film distorts the thermal balance at the sample/vacuum or now Bi film/vacuum interface because the emissivity of solid Bi is higher than that of the surface of the liquid alloy consisting of Ga mostly [HCP76]. As a consequence the sample cools more rapidly during the formation of the solid-like Bi film. This can be clearly seen in the thermal curve in Fig. 6.2.20, where the temperature of the sample drops even though the furnace temperature stays perfectly constant. The difference in $\Delta T = T_{Furn} - T_{Cruc}$ before the surface freezing transition takes place and after it is completed is pronounced. So, the temperature of the crucible drops, and under this conditions the film grows further and a drainage of heat becomes even faster because the emissivity increases with increase of film thickness [Pigeat98], hence the process accelerates itself. In a short time the film has achieved its maximum value but now one can see that it grew in the non-stable conditions – a steep temperature gradient – so its thickness does not represent the equilibrium state. In principle, in the present setup the experiment had to be conducted in the following way: first cooling to the

temperature where the surface freezing occurs and then heating of the sample to compensate the thermal loss due to film formation. This is of course not easy to do in a real experiment. Another possibility would be a reflecting screen above the sample or even better additional heating element in this way one could get rid of the thermal vertical and radial thermal gradients completely.

It has to be mentioned that there are up to now no published measurements of the thickness of the frozen films in a metallic system. Existing theoretical calculations [Tsekov03] are consistent with observations made in this work. According to these calculations the thickness of the frozen film diverge to macroscopic (not measurable by ellipsometry) values within several degrees below T_{SF} .

Another very important point has to be addressed: the ellipsometric quantities, in particular “jumps” in Ψ and Δ in Fig. 6.2.21 were up to now interpreted as a “growth” of the frozen film. It must be mentioned that there could be the following alternative explanation of the observed feature. Let’s consider the front of the relatively thick frozen film which grows in the interface plane rather than in thickness, hence it moves and covers the liquid surface. In this way the jump in Ψ , for example, simply indicates how the slab appears and moves across the footprint of the light. Sometimes this front could be even seen because the reflection condition at the junction liquid/solid surface were different and liquid surface was slightly distorted by the moving front. Speed of this front could be visually estimated as 0.5...1 mm/s which would correspond to the time of about 5...10 second to cover the surface under the footprint of the light of \varnothing 3...5 mm.

On the one hand the point (ii) mentioned at the beginning is quite clear and does not require experimental confirmation: if the solid Bi phase appears it consists of pure Bi, since according to the phase diagram [Predel60] solubility of Ga in the solid Bi is negligible. However, in general, one could assume that as the frozen film just forms its concentration can be different from the solid Bi phase. But this deviation was not observed in the experiments.

7.3. Spinodal decomposition and oscillatory instability at a fluid metal interface

A general brief introduction of the oscillatory instabilities was given in Chapter 1. The references cited where contain a great number of experimental works concerning such phenomena. However, only non-metallic systems were studied. The first observation of an oscillatory instability in a metallic fluid was made very recently in a Ga-Pb alloy at conditions inside the liquid-liquid miscibility gap [Turchanin04]. It was found that oscillations of the surface properties – probed by SHG – induce periodic variations in the temperature of the bulk liquid. Stimulated by these observations, similar investigation of the Ga-Bi have been performed in this work at various positions inside the miscibility gap (see Fig. 6.2.16).

In contrast to dielectric liquids studied so far with respect to interfacial oscillations, Ga-based alloys have a specific distinction: a wetting film exists on the interface of fluid sample when entering the miscibility gap. This peculiarity is essential for the following discussion of the oscillatory behaviour of the measured ellipsometric quantities of Ga-Bi. We consider continuous cooling from the homogeneous liquid region into the miscibility gap. Such two paths are shown for two Ga-Bi alloys A ($x_{Bi} < x_c$) and B ($x_{Bi} > x_c$) in Fig. 7.3.1.

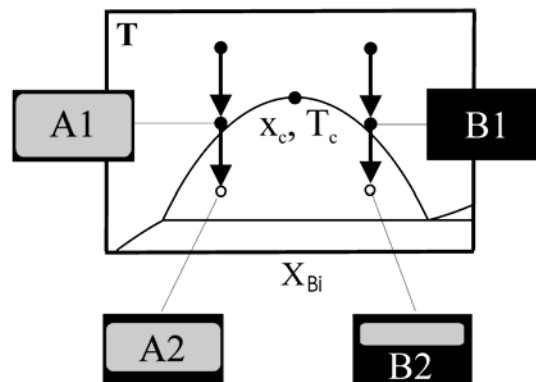


Fig. 7.3.1 Schematic phase diagram of Ga-Bi. The experimental paths for two Ga-Bi alloys A ($x_{Bi} < x_c$) and B ($x_{Bi} > x_c$) are shown. Physical appearance of the system is shown as rectangular slabs: grey is Ga-rich phase, black is a Bi-rich phase. Solid and open points represent the system in the homogeneous region (far off and close to the coexistence) and “stop temperature” where oscillations are observed, respectively.

When the alloy (A) approaches the liquid-liquid coexistence curve there is a wetting film of about 30 Å (see the previous chapter) on its top – state A1 in Fig. 7.3.1. At the liquid-liquid coexistence the wetting film which is governed by gravitation only ($\Delta G=0$) and could grow more (up to ~100 Å, p. 109). When it enters the miscibility gap the spinodal decomposition in the Ga-rich phase of the substrate occurs. From general considerations one would expect that the heavier Bi-rich phase would sink. But it should not be forgotten that this phase is favourable at the surface because it has the lower surface energy. So, mass transport of Bi due

to spinodal decomposition can proceed in both directions - to the bottom of the crucible and to the substrate/film interface where the Bi-rich layer already exists. Hence this layer can grow beyond its equilibrium value – state A2 in Fig. 7.3.1, where very thick layer of wetting phase is shown. The alloy (B) consists from the beginning of the future wetting phase so there are no changes with this alloy until the liquid-liquid line is crossed and the spinodal decomposition of the bulk phase starts. One can assume that some amount of Bi-rich phase will simply stay at the interface whereas rest of it will sink. The difference between both alloys is the amount of the Ga-rich phase – it is several times smaller for alloy B than in alloy A, Fig. 7.3.1. This obviously will influence the dynamics of the oscillatory process and might be also an explanation of the initial delay in the periodical changes, see Fig. 6.2.17. Anyway, the main feature for both alloys is the presence of two phases below the liquid-liquid demixing line: some layer of Bi-rich phase and Ga-rich phase as a substrate. And the fact that on constant cooling within the miscibility gap this film continues to grow (see Fig. 6.2.13 and 6.2.14). In the following the points which will be addressed are:

- stability of the wetting film (“wetting-dewetting” transition),
- possible competing mechanisms leading to interfacial oscillations,
- correlation of Ψ , Δ and T_{crucible} oscillations, variation of emissivity with Bi-rich film thickness and change of the heat balance.

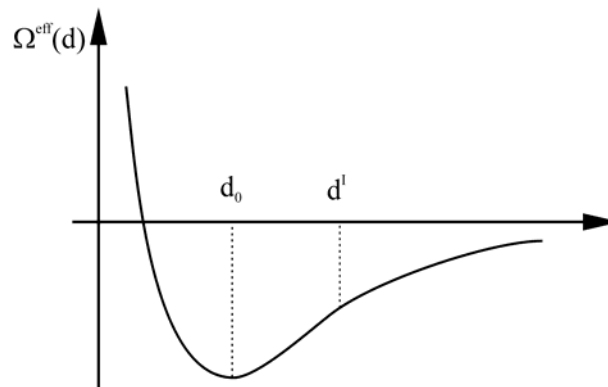


Fig.7.3.2 Schematic representation of the effective interfacial potential $\Omega^{\text{eff}}(d)$. Thickness d_0 corresponds to minimum in $\Omega^{\text{eff}}(d)$. Point d^I marks the position where second derivative of $\Omega^{\text{eff}}(d)$ changes its sign.

Qualitatively, the first point can be answered with the help of the effective interfacial potential $\Omega^{\text{eff}}(d; T, \mu)$ (Eq. 2.4, Chapter 2.3). For simplification the dependence of d only will be considered in the present case (after [Herminghaus99]). This potential is shown in Fig. 7.3.2 for the configuration when the film thickness at equilibrium would take a certain finite value d_0 which corresponds to the minimum in $\Omega(d)$. If the second derivative of $\Omega(d)$ is positive any fluctuation (thermal, concentration etc.) of the film thickness are ineffective and the equilibrium at d_0 is restored. However, for thicker films ($d > d^I$) $\Omega''(d)$ is negative as can be

seen from Fig. 7.3.2. The film becomes dynamically unstable and dewetting of a metastable film can occur. This scenario is consistent with the experimental observations. For example in Fig. 6.2.17 (left section B) in the kinetic spectrum of Ψ (same for Δ) it can be noticed that the maxima in the oscillating ellipsometric angle ($\sim 39^\circ$) practically coincide with the starting value of the measurement – no detectable Bi-rich film. As the decrease in Ψ definitely reflects film growth (Chapter 7.2), an increase corresponds to its disappearance or “dewetting”. It is interesting that the maxima in Ψ for the alloy with $x_{\text{Bi}} > x_c$ (Fig. 6.2.17, right section C) indicate a clearly different state (38°) in comparison to the initial one (36.8°). Basically the maxima for two alloys in Fig. 6.2.17 (B and C) agree very well. A very naïve assumption about the film thickness behaviour is shown in Fig. 7.3.3: the film simply homogeneously thins and thickens periodically which is reflected in the variations of the ellipsometric quantities.

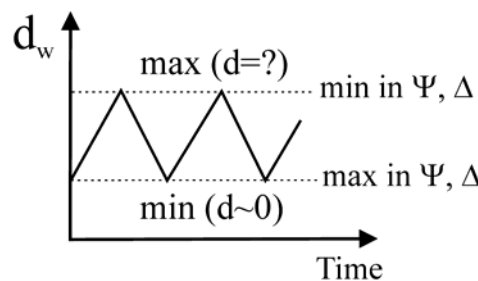


Fig. 7.3.3 The schematic time-dependence of the Bi-rich film consistent with the experimental observations: minimum in Ψ (and Δ) corresponds to maximum of Bi-rich film thickness, d_w (see text).

With this simple model, also the periodical change of the crucible temperature can be qualitatively explained. In the previous chapter it was already briefly discussed that a change of the film thickness composed of solid Bi on the liquid substrate will lead to a change of the heat balance at the sample/vacuum interface. The same is true in the present case of liquid Bi-rich layer. Furthermore, the emissivity, ε , increases when Bi-rich film grows [Pigeat98] and decreases when the film disappears. In general, the evolution of temperature in the crucible is described by a partial differential equation accounting for a diffusion, convection and production of heat in the sample, being coupled with the relevant boundary conditions. This differential will be equal to the heat supplied from the heater minus the loss of heat due to radiation in vacuum: $\alpha(T_{\text{furnace}} - T_{\text{crucible}}) - \varepsilon\sigma_0 T_{\text{crucible}}^4$ (where α is heat transfer coefficient, ε is emissivity coefficient, σ_0 is universal constant) [Turchanin04]. From this balance it becomes clear that the change of the film thickness will be coupled with the change of crucible temperature via the emissivity variation. Indeed this is in agreement with the experimental observations. Ellipsometric angles and T_{crucible} are shown in Fig. 7.3.4 where only one period of the oscillation is magnified.

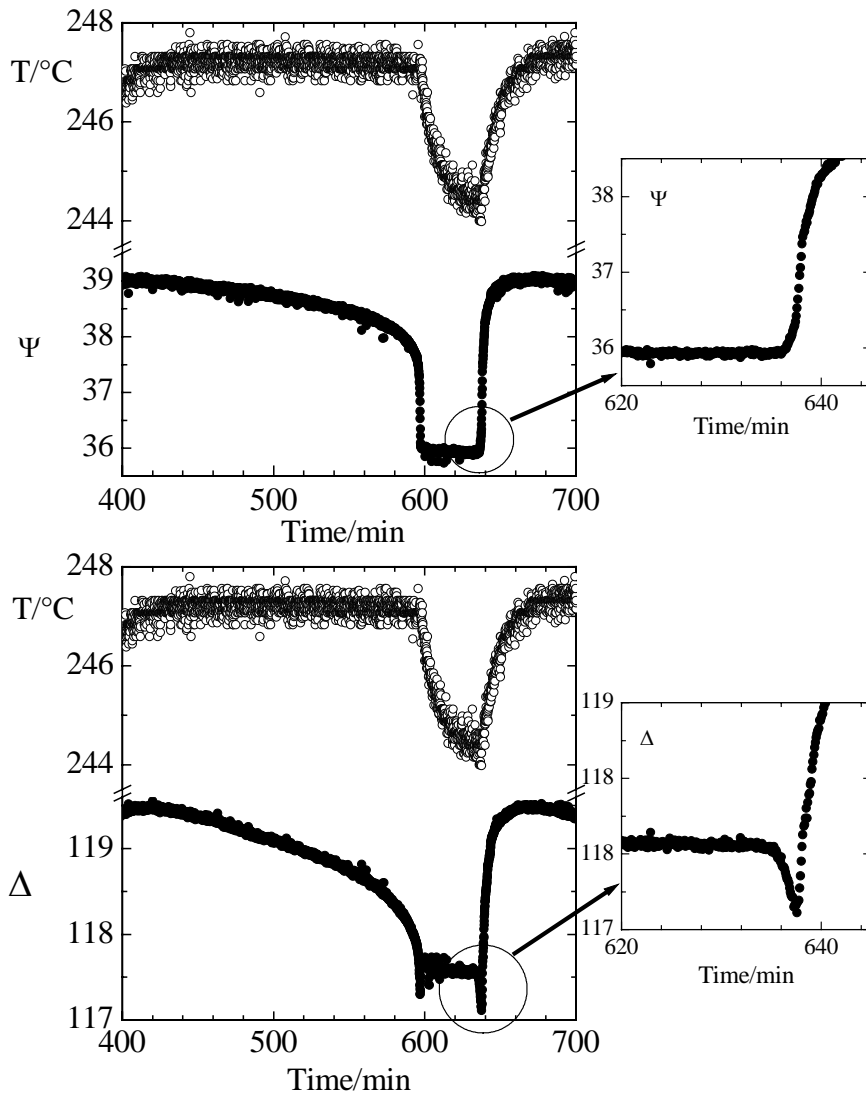


Fig. 7.3.4 Variation of the ellipsometric angles Ψ , Δ and T_{crucible} magnified for convenience in the time interval from ~ 7 to ~ 12 hours, see Fig. 6.2.15 for $\text{Ga}_{0.8}\text{Bi}_{0.2}$ alloy. Right sections show fine details of Ψ and Δ variations at ~ 637 min.

Thoughtful observation of the results in Fig. 7.3.4 reveals several features which disagree (or not included) in the simple model proposed above. First of all, it is clear that processes of the film growth (~ 200 min.) and its disappearance (~ 20 min.) have orders of magnitude different scales. The coupling between oscillations in Ψ , Δ and T_{crucible} is not direct - Ψ , Δ decrease whereas T_{crucible} is constant and vice versa. Furthermore, the plateau in ellipsometric angles is difficult to explain – it either means that (i) the film for some reason preserves certain thickness over relatively long time ~ 40 min. while the temperature drops almost by 3 K or (ii) that the film grows beyond the limit of the present setup (Chapter 5, p. 53). Second variant is highly improbable since for it the film should be thicker than ~ 500 Å and such thickness would disagree with the magnitude of Ψ and Δ change. Moreover, Δ exhibits very peculiar features at the beginning and the end of the plateau, which are completely absent in Ψ , right

sections in Fig. 7.3.4. It can be speculated that such features are an indication of the structural change at the sample/vacuum interface. Therefore it is of relevance to discuss the known mechanisms of dewetting: formation of the holes in the film [Redon91], [Herminghaus99] and formation of droplet [Turchanin04].

One of the first example of dewetting, which was studied extensively, is a gold film (later also Ni, Cu) on quartz, which was rapidly melted by a laser pulse heating [Bischof96]. In this case the dewetting can occur in two ways: first is a nucleation of holes in the film on any kinds of surface defects and their successive growth [Redon91] and second is based on the instability against the thermally activated surface waves [Herminghaus99]. The latter mechanism is called also spinodal decomposition - the 2D analogy of the spinodal demixing of the bulk. Main feature of this process is the formation of surface modulations and as a result some labyrinth structures with a characteristic wavelength. Essential in these examples is that wetting and dewetting occur at a fluid/solid interface. In the present case, dewetting at the fluid/fluid interface has to be considered. As a consequence interfacial inhomogeneities may develop as a function of time as qualitatively depicted in Fig. 7.3.3. Since the substrate is a fluid, the dewetting process might proceed in more complicated way including additional stages, see Fig. 7.3.5.

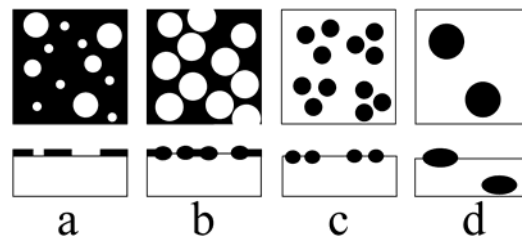


Fig. 7.3.5 The schematic changes in the structure of the sample/vacuum interface on a *microscopic* scale (view from above and side cut). Wetting phase is shown in black, substrate in white.

Appearance of such possible (*microscopic*) interfacial scenario depicted there is combined on the base of references [Krausch97], [Damman03] and [Turchanin04]. On the initial stage (not included in the figure, the wetting film grows to certain value and stays constant - temperature starts to decrease because emissivity ϵ is changed, Fig. 7.3.4. The film becomes unstable and the holes appear in it and start to grow, at this stage (Fig. 7.3.5 **a**) the remaining layer becomes even thicker. Further growth of holes leads to accumulation of material on the hole's rim – it looks like two droplets connected through a film in Fig. 7.3.5 **b**. The net-like interconnected structure breaks into separate small droplets to minimize the surface energy, Fig. 7.3.5 **c**. For the same reason several small droplets might coalesce into a bigger ones. Big droplet can reach certain critical radius and sinks. This is shown in Fig. 7.3.5 **d** as two droplets – one still grows at the interface and another, bigger in size ($r > r_c$), already settled at

the bottom of the crucible. Difference of this mechanism to the one described below is the size of the droplets – here the microscopic droplets form and sink. The final result is no wetting film at the sample/vacuum interface – all Bi-rich phase sank. This configuration is energetically unfavourable hence the wetting phase starts to segregate at the interface.

Second mechanism suggested in the work of Turchanin et al. [Turchanin04] for oscillatory instability in Ga-Pb alloy considers capillary-gravity instabilities, the local formation of single drop of the critical size (determined by capillary forces) in the wetting film. The droplet is limited by Rayleigh instability, which leads to detachment of it from the film. It sinks by gravity and in this way triggers an oscillatory instability. The time dependent changes at the interface are treated taking into account a viscous flow at the interface, mass and heat balance but neglecting in the first approximation the Marangoni effect. This type of instability is caused by the variation of the surface tension across the surface. Its change leads to the increase in tangential or shear stresses and generates or alters existing flows at the interface [Nepomnyashchy02]. This can play important role in this work since, as was already mentioned, the vertical and radial thermal gradients are up to 3 K (for this setup).

The main result of the model of Turchanin et al. [Turchanin04], calculations of non-linear differential equations of mass transport is, that it reproduces the observed by SHG oscillatory instabilities qualitatively correct, i.e. oscillation times of ~1 hour and temperature amplitudes of ~5-10 K. So, due to the similarity of the metal systems one could expect that this model would work in the present system as well. Indeed applied to Ga-Bi alloys it shows correct value of the period of the oscillations but fails in the magnitude of ΔT . This is may be not surprising since the systems differ from each other not only in physical properties of Pb and Bi (like: density, thermal conductivity, emissivity, surface tension and its thermal coefficient etc.) but also, most importantly, in the crucible configurations – liquid Ga-Bi sample has a lens shape whereas liquid Ga-Pb alloy was flat thin cylindrical tablet. This can lead to different mass and heat transport within both configurations and in turn to differences in the oscillatory behaviour, for example in Ga-Bi system the oscillations were never observed on continuous cooling as in Ga-Pb system.

To confirm or disprove this or offered above *microscopic* scenario the structural information of the film would be especially important, for example from the light scattering measurements or some optical microscopy (like SNOM).

In the conclusion it has to be mentioned that further understanding of the observed oscillatory instability requires additional experimental work and a development of the theoretical models.

Appendix

(i) Results of the measurements of potassium-rich K-KCl melts.

All original experimental data are presented as big open circles: ellipsometric angles $\Psi[^\circ]$ and $\Delta[^\circ]$, and reflectivity $R[\%]$. Full small circles show the same quantities generated after the best fit of the 3 phase model.

(ii) Results of Ga-Bi alloy measurements:

- a. optical properties of pure Ga and Bi,
- b. parameters of Drude model applied to both liquid metals and comparison with literature,
- c. Redlich-Kister polynomial for liquid-liquid coexistence [Huber03],

Original experimental spectra (ellipsometric intensities I_S and I_C) are not presented here because their interpretation is possible with the help of “PsiDelta” program {Jobin Yvon} only. But if needed they are available: Prof. Dr. W. Freyland, University Karlsruhe.

Details of the fitting procedure and the physical appearance of the models applied to certain experimental situation are given in Chapters 3.3, 5, 6.1 and 6.2. Errors are discussed in Chapter 5.

1. Measurement Set 1 ($x_K = 0.956$). (1) - $T=630$ °C. Results: n and k – Fig. 6.1.1; film thickness is 220 ± 35 nm.

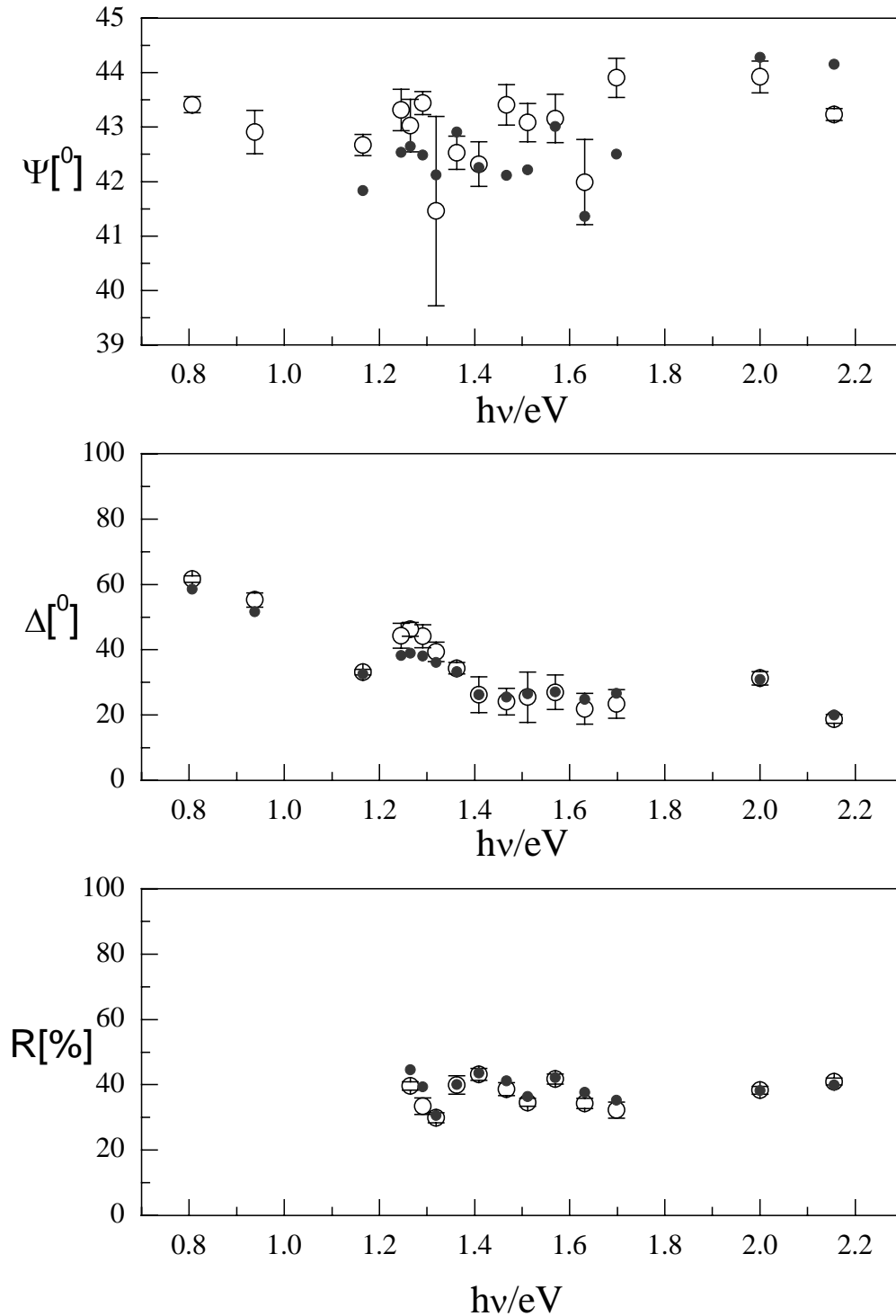


Fig. 1A

1. Measurement Set 1 ($x_K = 0.956$). **(2)** - $T=650$ °C. Results: n and k – Fig. 6.1.3; film thickness: 20 ± 15 nm, but see discussion in the Chapter.

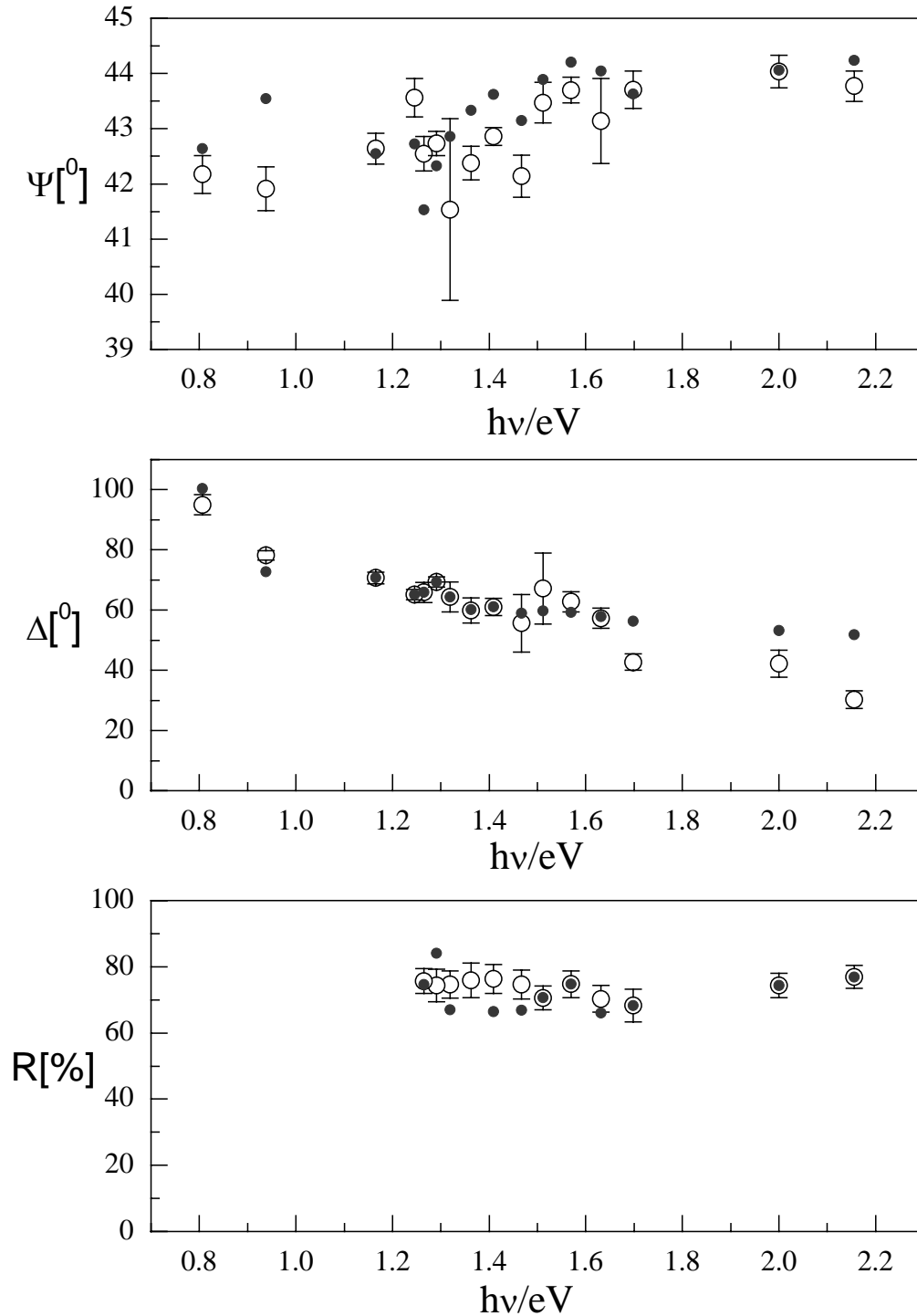


Fig. 2A

1. Measurement Set 1 ($x_K = 0.956$). **(3)** - $T=675$ °C. Results: ε_1 and ε_2 of metal-rich melt – Fig. 6.1.4.

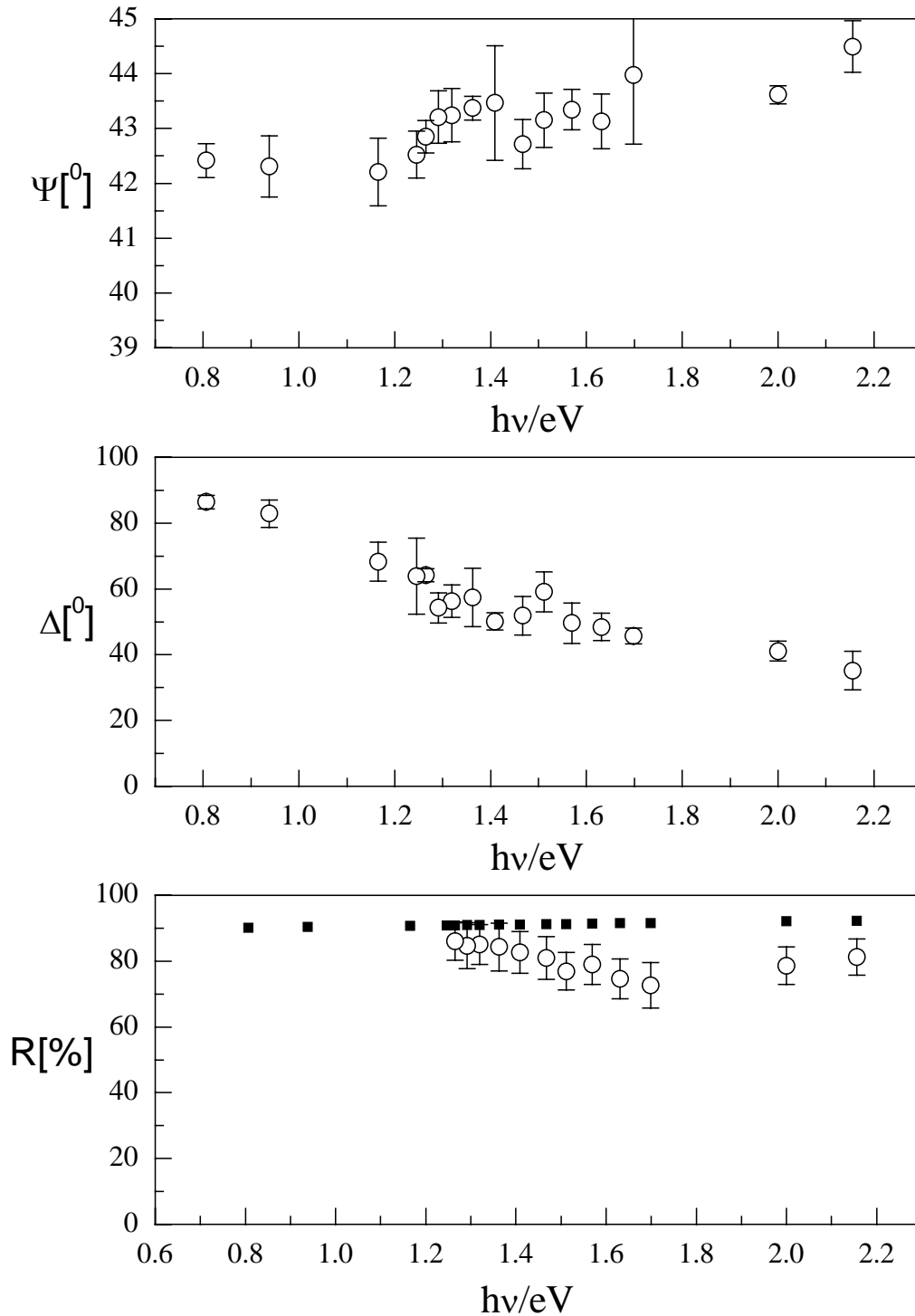


Fig. 3A In the lower section: experimentally measured reflectivity (○); ■ reflectivity of pure potassium at 675 °C.

2. Measurement Set 2 ($x_K = 0.934$). (1) - $T=656$ °C. Results: n and k – Fig. 6.1.5; film thickness: 220 ± 40 nm.

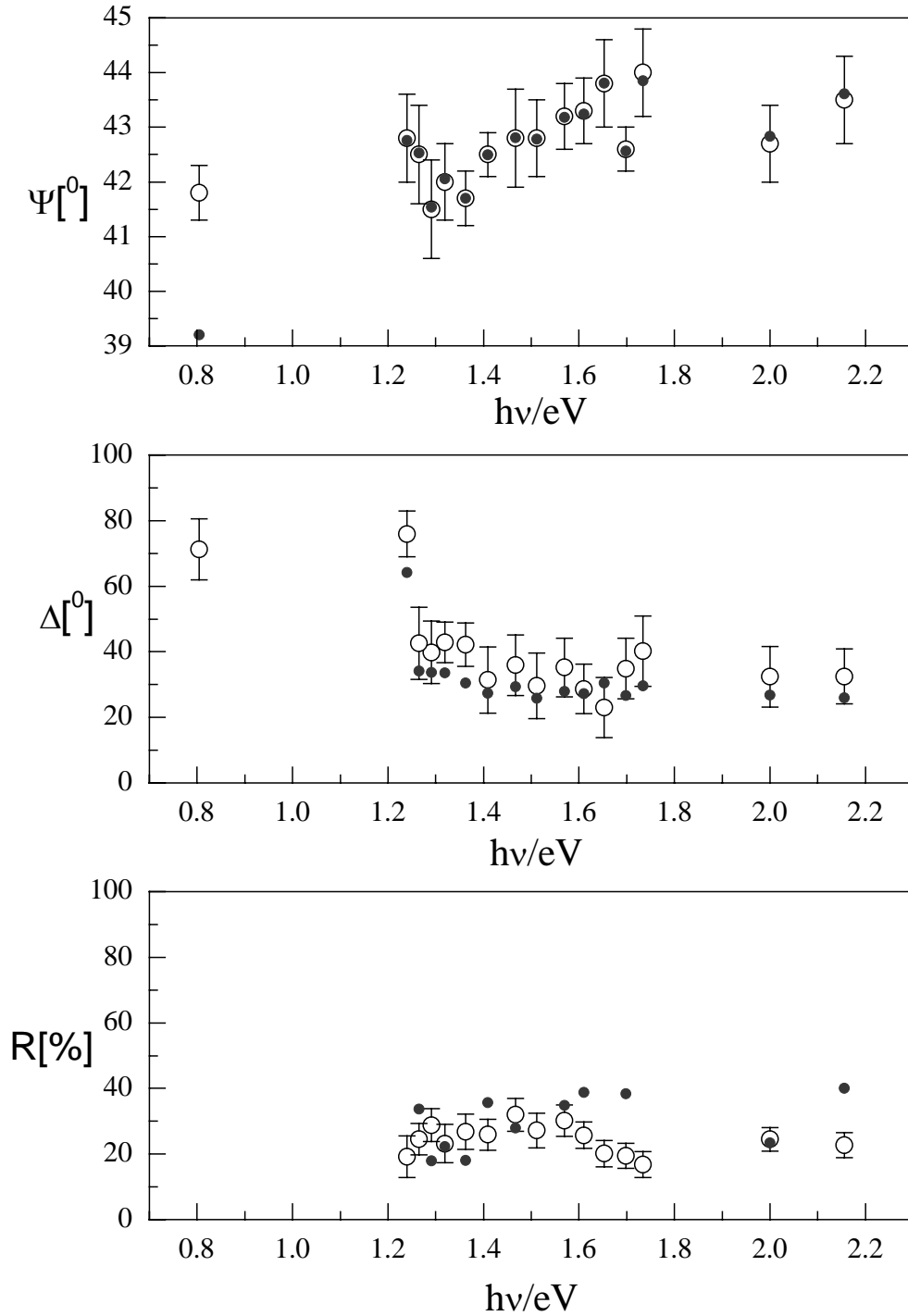


Fig. 4A

2. Measurement Set 2 ($x_K = 0.934$). (2) - $T=711$ °C. Results: n and k – Fig. 6.1.6; film thickness: 150 ± 50 nm.

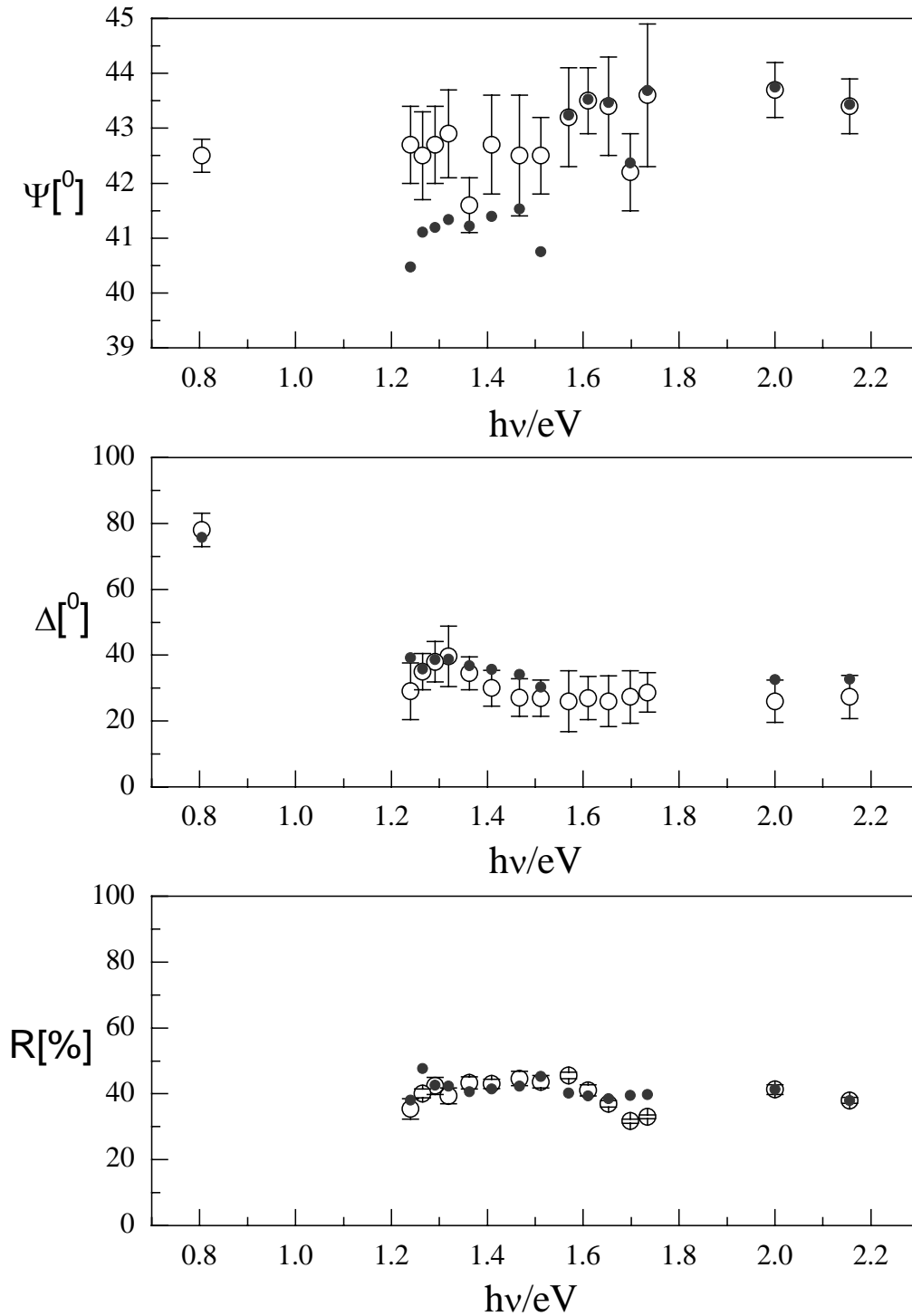


Fig 5A

2. Measurement Set 2 ($x_K = 0.934$). **(3)** - $T=752$ °C. Results: n and k – Fig. 6.1.7; film thickness: 80 ± 40 nm.

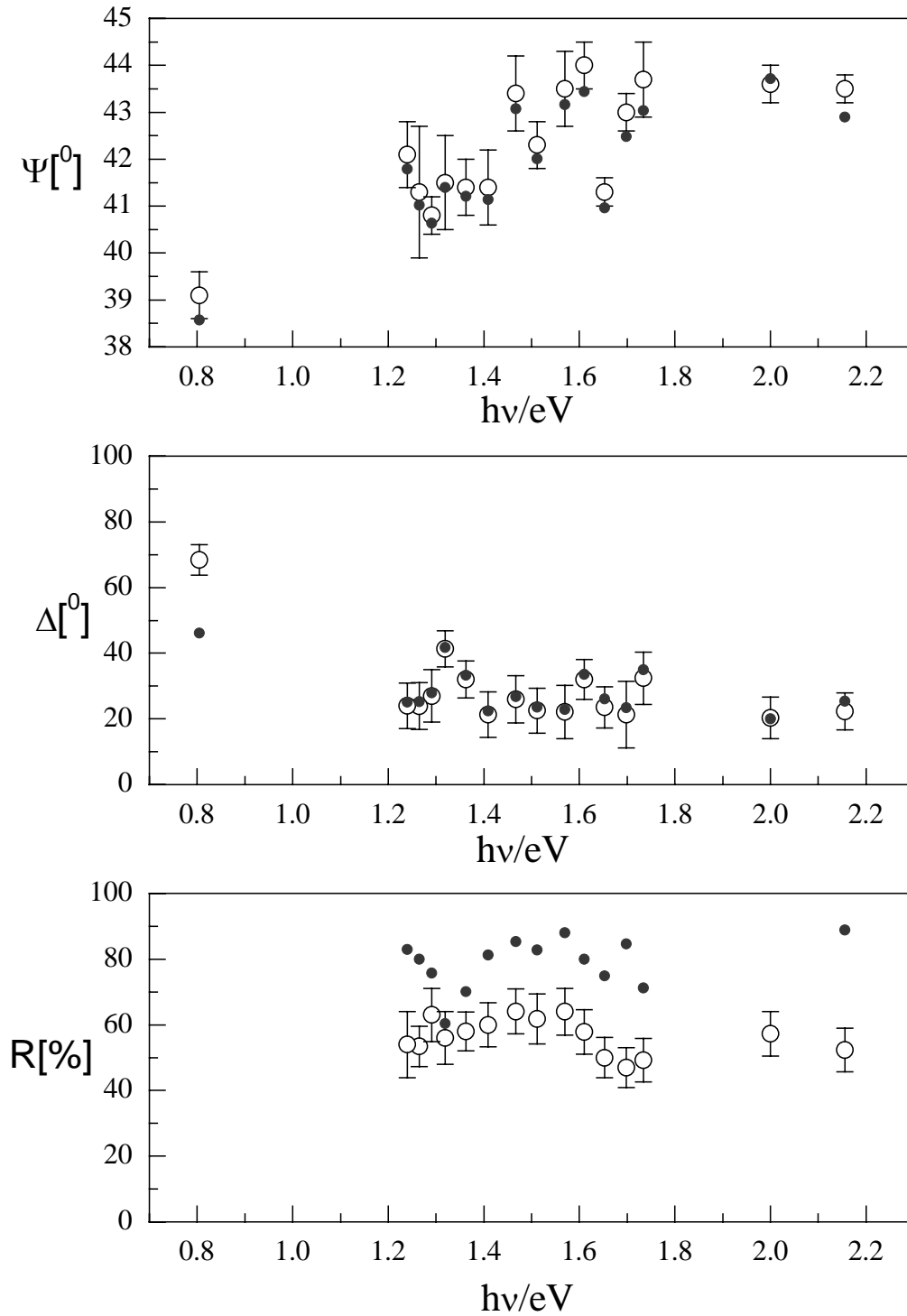


Fig. 6A

2. Measurement Set 2 ($x_K = 0.934$). **(4)** - $T=667$ °C. Results: n and k – Fig. 6.1.8; film thickness: 200 ± 20 nm.

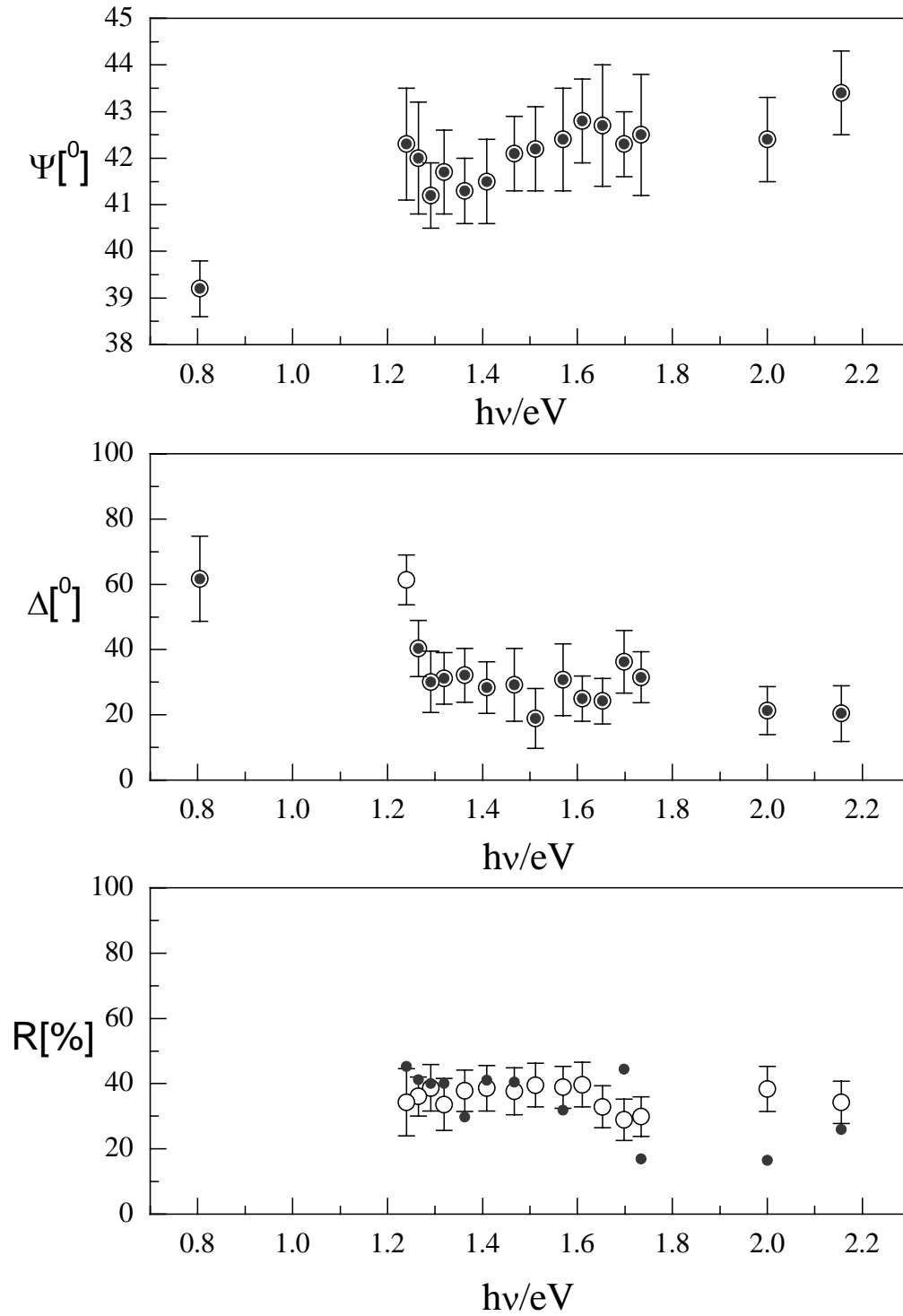


Fig. 7A

3. Measurement Set 3 ($x_K = 0.901$). (1) - $T=681$ °C. Results: n and k – Fig. 6.1.9; film thickness: 250 ± 50 nm.

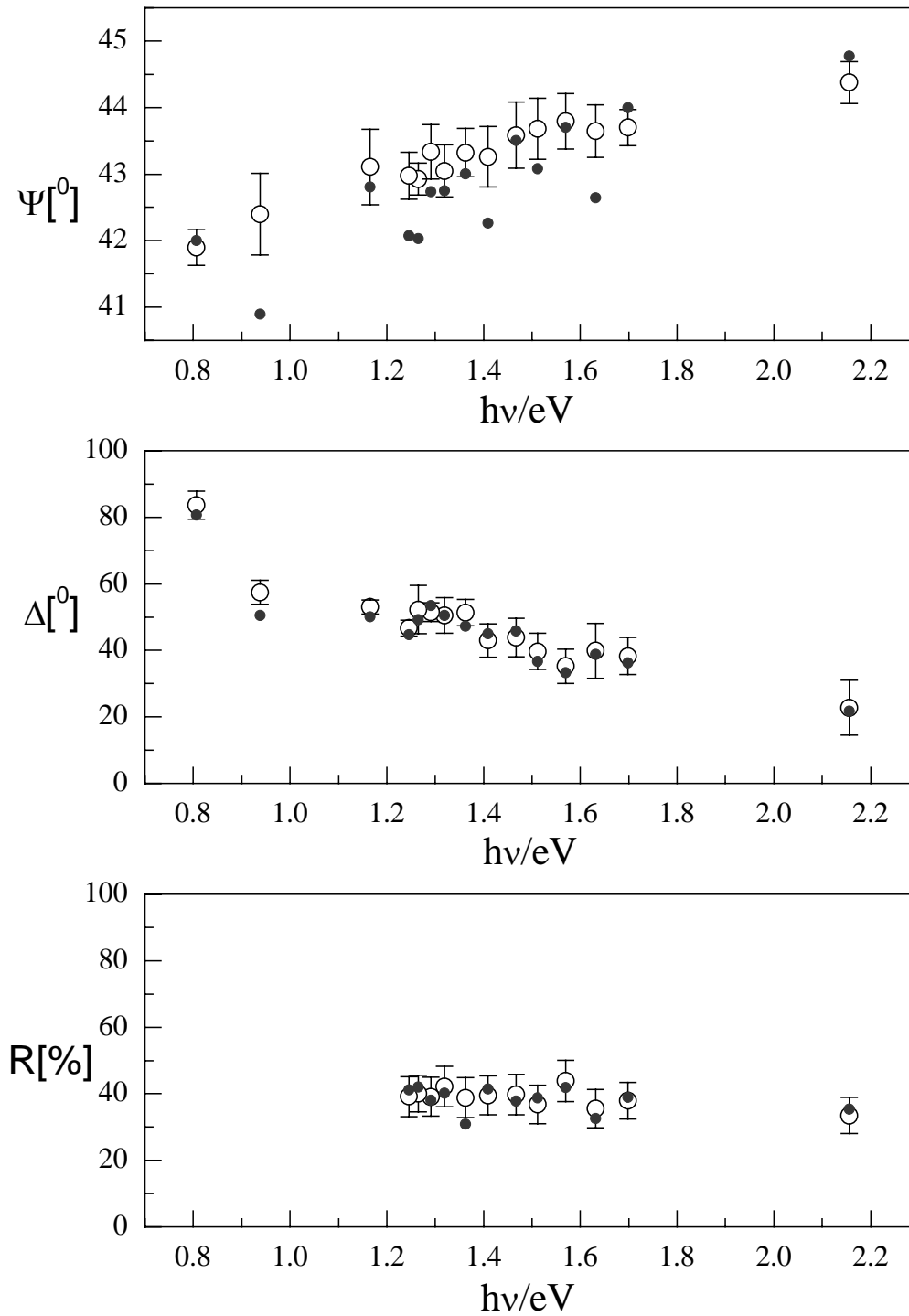


Fig 8A

3. Measurement Set 3 ($x_K = 0.901$). (2) - $T=719$ °C. Results: n and k – Fig. 6.1.10; film thickness: 150 ± 60 nm.

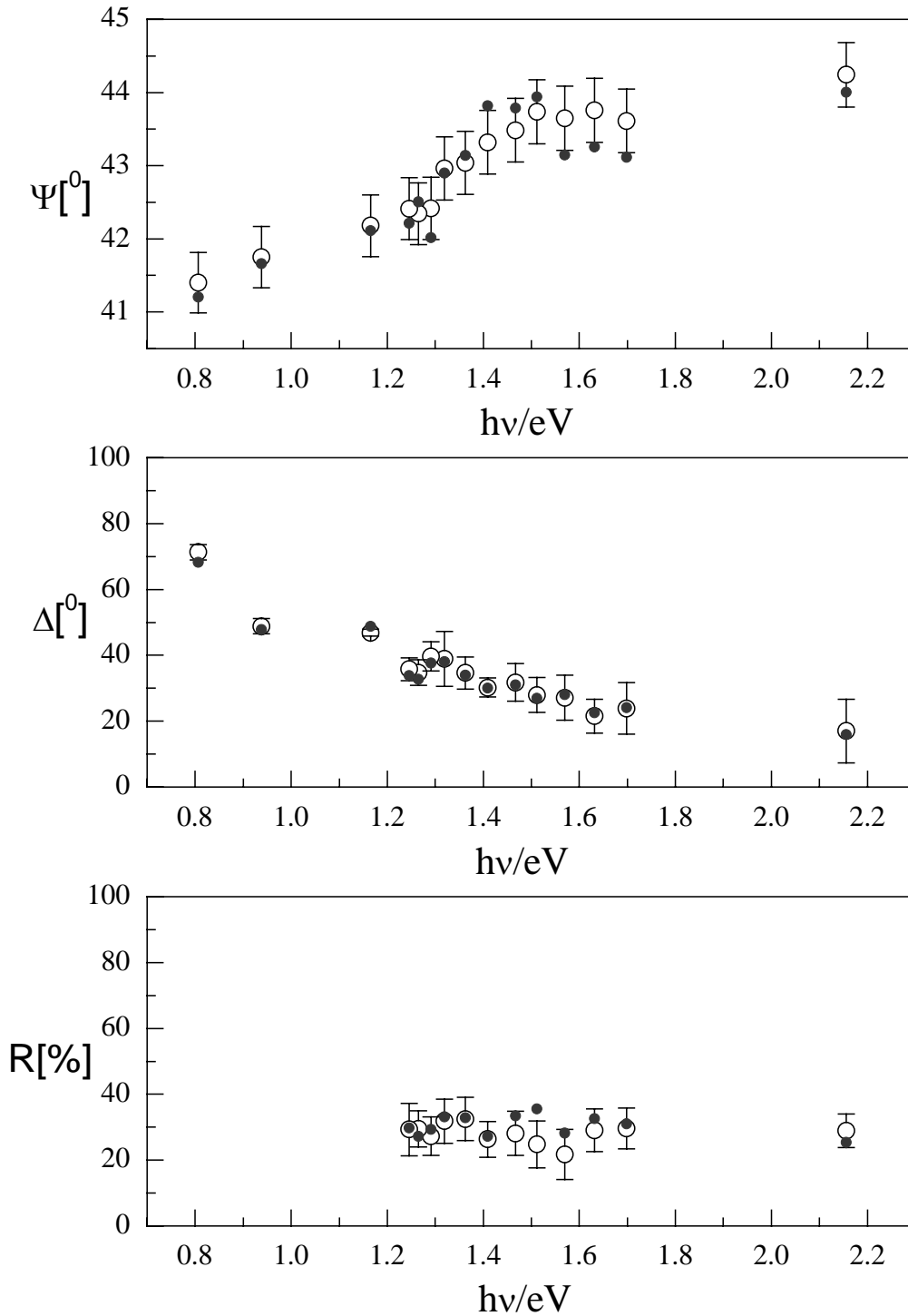


Fig. 9A

4. Measurement Set 4 ($x_K = 0.75$, $x'_K = 0.85$). (1) - T=714 °C. Results: n and k – Fig. 6.1.11; film thickness: 330 ± 40 nm.

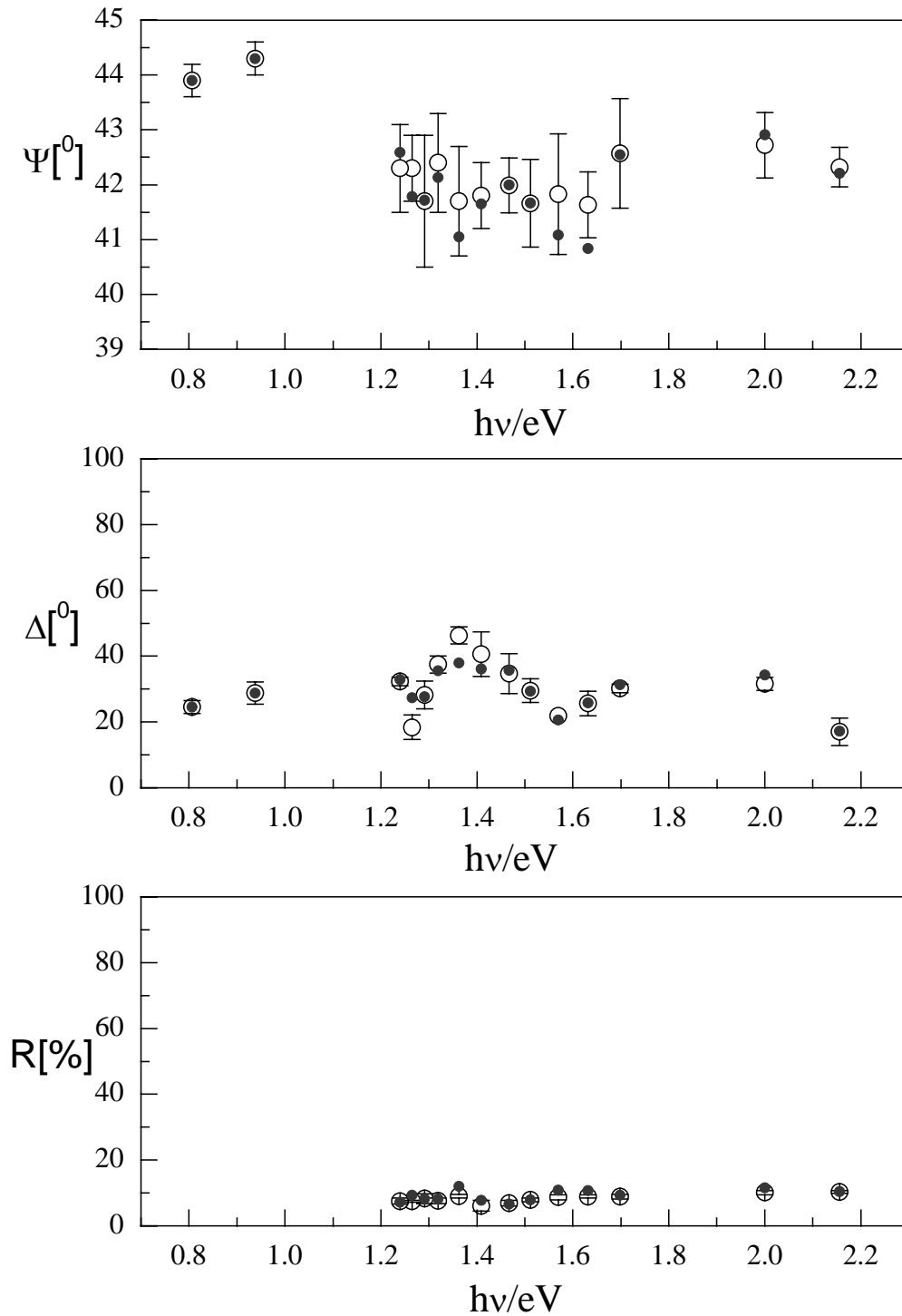


Fig. 10A

5. Measurement Set 5 ($x_K = 0.78$). (1) - $T=738$ °C. Results: n and k – Fig. 6.1.12; film thickness: 440 ± 50 nm.

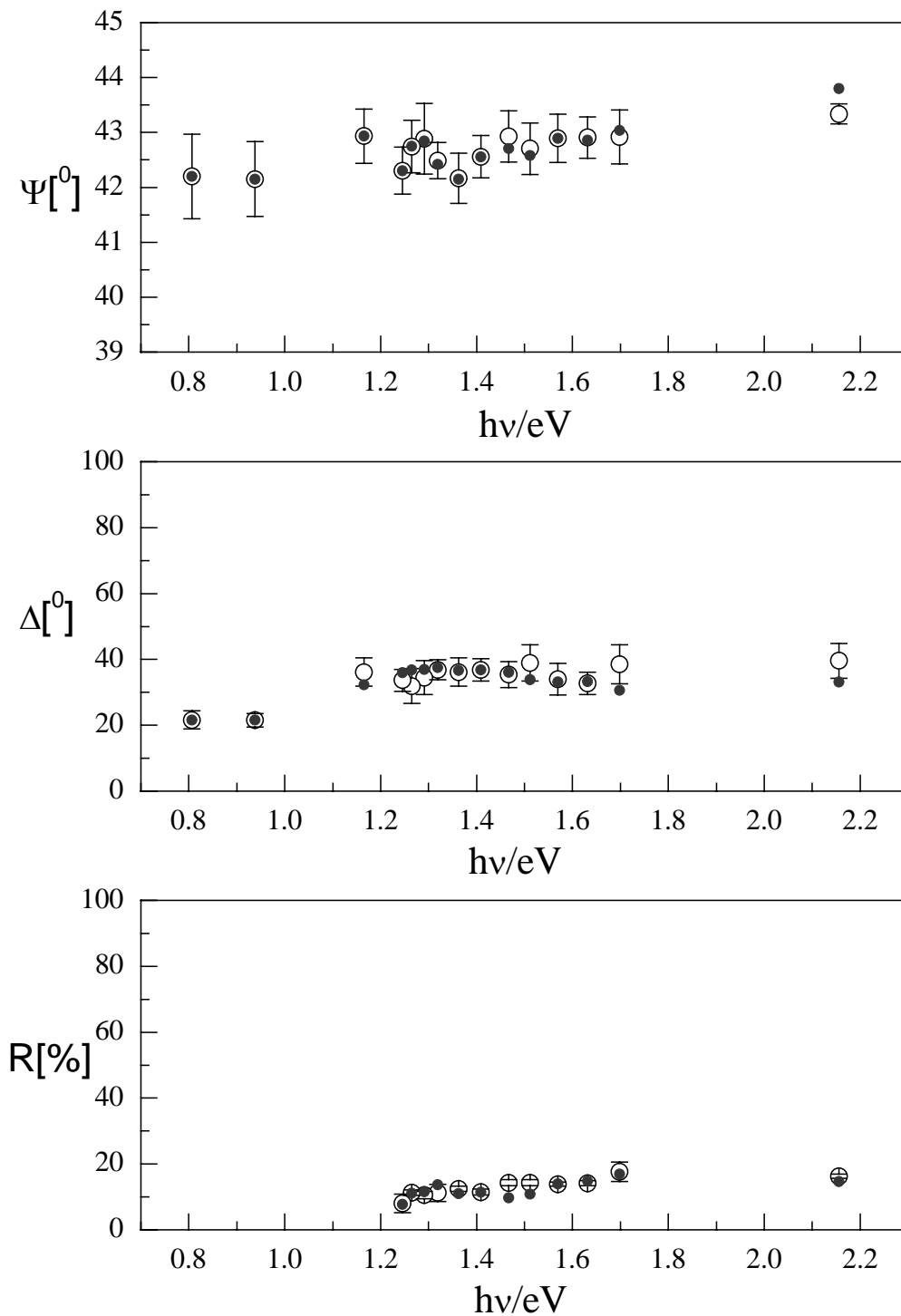


Fig. 11A

• Optical properties of pure liquid Ga.

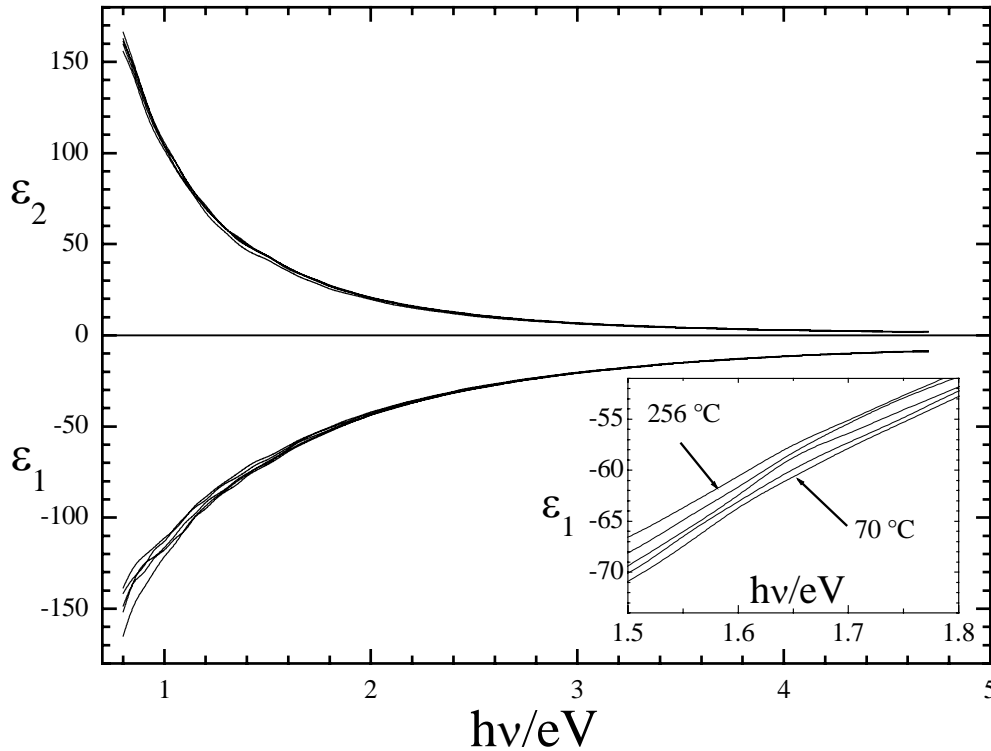


Fig. 12A. Real and imaginary parts of the dielectric function of liquid Ga. Parameters of the Drude free electron model fit to each temperature are summarized in Table 6.2.1A (below). In the inset the ϵ_1 is magnified in a small energy interval to show its temperature dependence.

Table 1A. Pure liquid Ga: experimental conditions, parameters of the Drude model obtained from fit to ellipsometric spectra (*this work*) and *literature data*: measurements of density [Steinberg74] and conductivity [Cusack59] (see also Fig. 6.2.3). The errors of ω_p and γ_D are less than 2%.

T/ °C	T/ K	$P_0/10^{-9}$ mbar	ω_p/eV	γ_D/eV	<i>this work</i>		<i>literature data</i>	
					$N_e/10^{23} \text{ cm}^{-3}$	$\sigma_0/10^4 \Omega^{-1}\text{cm}^{-1}$	$N_e/10^{23} \text{ cm}^{-3}$	$\sigma_0/10^4 \Omega^{-1}\text{cm}^{-1}$
70	343	1.1	14.62	0.829	1.551	3.564	1.574	3.75
130	403	1.2	14.60	0.833	1.547	3.447	1.565	3.592
173	446	1.4	14.59	0.859	1.544	3.333	1.560	3.494
215	488	2.1	14.53	0.886	1.533	3.208	1.553	3.391
256	529	2.3	14.51	0.908	1.527	3.112	1.547	3.301

• Optical properties of pure liquid Bi.

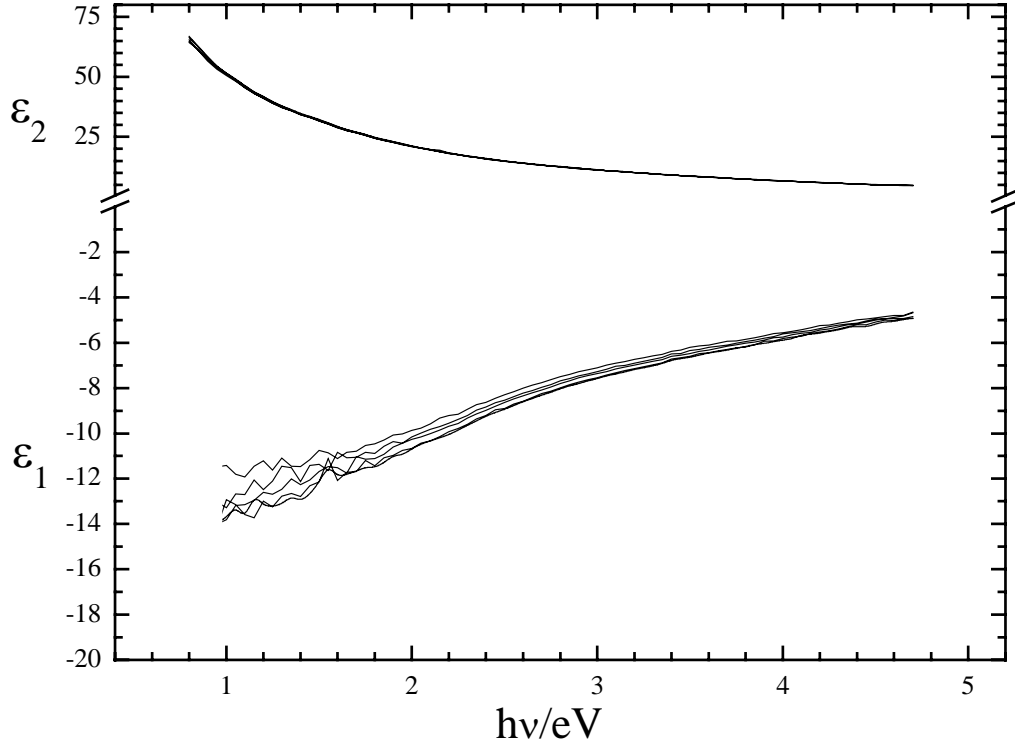


Fig. 13A. Real and imaginary parts of the dielectric function of liquid Bi. Parameters of the Drude free electron model fit to each temperature are summarized in Table 6.2.2A (below).

Table 2A. Pure liquid Bi: experimental conditions, parameters of the Drude model obtained from fit to ellipsometric spectra (*this work*) and *literature data*: measurements of density [Steinberg74] and conductivity [Cusack59] (see also Fig. 6.2.3). The errors of ω_p and γ_D are less than 2%.

T/°C	T/K	$P_0/10^{-9}$ mbar	ω_p/eV	γ_D/eV	<i>this work</i>		<i>literature data</i>	
					$N_c/10^{23} \text{ cm}^{-3}$	$\sigma_0/10^4 \Omega^{-1} \text{ cm}^{-1}$	$N_c/10^{23} \text{ cm}^{-3}$	$\sigma_0/10^4 \Omega^{-1} \text{ cm}^{-1}$
289	562	2.6	14.49	3.85	1.523	7.335	1.444	7.603
296	569	3.8	14.47	3.85	1.518	7.315	1.443	7.580
312	585	5.9	14.45	3.87	1.514	7.276	1.440	7.528
335	608	9.0	14.43	3.895	1.510	7.191	1.437	7.458
352	625	11	14.46	3.95	1.516	7.120	1.433	7.395
378	651	30	14.51	4.01	1.527	7.080	1.429	7.318

- Comparison of the Drude parameters from the fit to the ellipsometric spectra (*this work*) with the results of direct measurements (density [Steinberg74] and conductivity [Cusack59]) for pure liquid Ga and Bi: Fig. 14A and 15A, respectively.

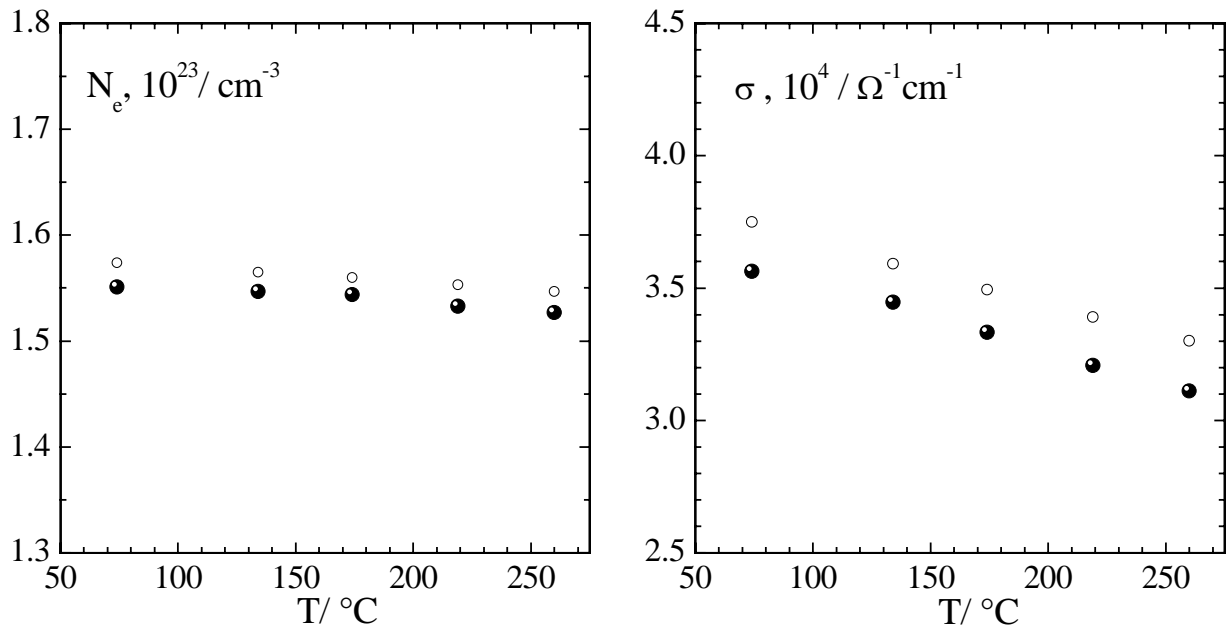


Fig. 14A Comparison of the N_e and σ from *this work* for pure liquid Ga (●) and *literature data* (○). For explanations see text above.

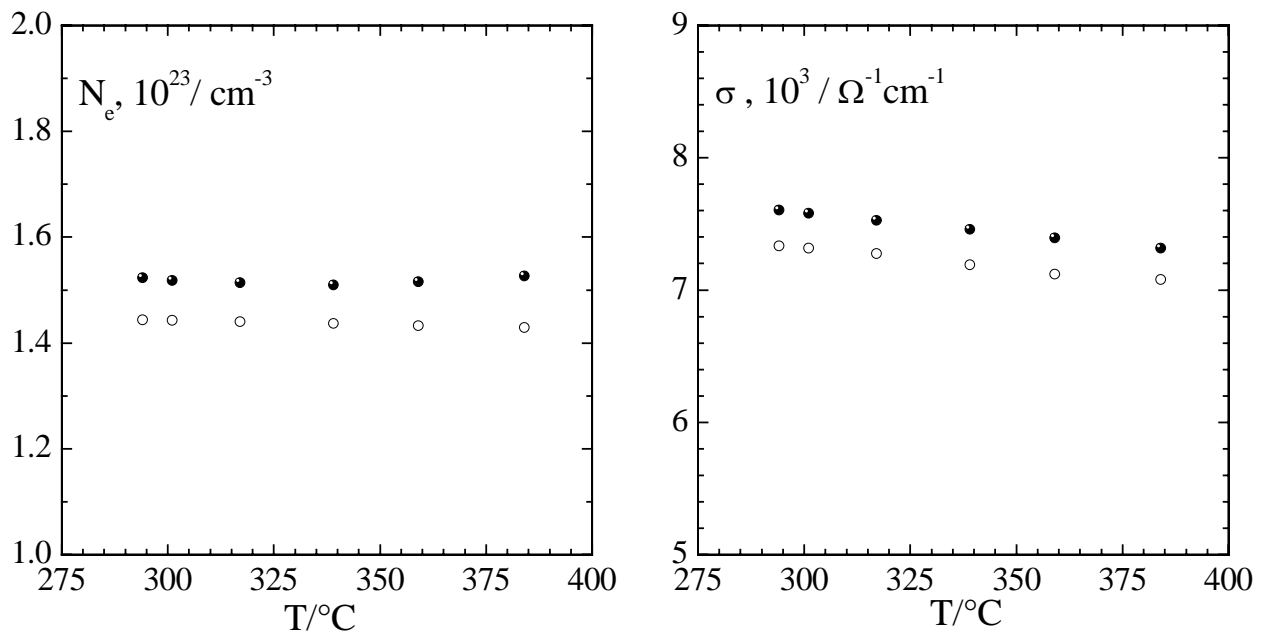


Fig. 15A Comparison of the N_e and σ from *this work* for pure liquid Bi (●) and *literature data* (○). For explanations see text above.

Redlich-Kister Polynomial for Ga-Bi equilibrium [Huber03]

1. The Gibbs free energy of Ga-Bi liquid system:

$$\begin{aligned}\Delta G(x_{\text{Ga}}, T) = & G_0\text{Ga}(T) \times c + G_0\text{Bi}(T) \times (1-c) + \\ & + R \times T \times (c \times \ln(c) + (1-c) \times \ln(1-c)) + \\ & + c \times (1-c) \times [L_0(T) + L_1(T) \times (1-2 \times c) + L_2(T) \times (1-2 \times c)^2 + L_3 \times (1-2 \times c)^3 + \\ & L_4(T) \times (1-2 \times c)^4 + L_5 \times (1-2 \times c)^5].\end{aligned}$$

For the definitions see Eq. 7.3 and 7.4.

2. The coefficients of the Redlich-Kister polynomial for $\Delta G(x_{\text{Ga}}, T)$ are:

$$L_0(T) = 8000 - 3388.8 \times T$$

$$L_1(T) = -4868.3 - 2.4 \times T$$

$$L_2(T) = -10375.3 + 14.1 \times T$$

$$L_3 = -4339.3$$

$$L_4(T) = 2653.4 - 9.4 \times T$$

$$L_5 = -2364.1$$

3. The Gibbs free energies of the pure Ga and Bi are:

$$G_0\text{Bi}(T) = \Delta H_{\text{Bi}} + (11245.9 - 7156.6) - (20.6 - 18.5) \times T - K(T) - 6.0 \times 10^{-9} \times T^7,$$

$$G_0\text{Ga}(T) = \Delta H_{\text{Ga}} + 5666.5 - 18.7 \times T - 1.7 \times 10^{23} \times T^{-9},$$

where

$$\Delta H_{\text{Bi}} = -7817.8 + 128.4 \times T - 28.4 \times T \times \ln(T) + 0.012 \times T^2 - 8.4 \times 10^{-6} \times T^3,$$

$$\begin{aligned}\Delta H_{\text{Ga}} = & -7055.7 + 132.7 \times T - 26.1 \times T \times \ln(T) + 1.5 \times 10^{-4} \times T^2 - 4.0 \times 10^{-8} \times T^3 - 118332 \times T^{-1} \\ & + 1.7 \times 10^{23} \times T^{-9}.\end{aligned}$$

Manufacturer list

• Ellipsometer and lasers

<u>Jobin Yvon</u>	UVISEL PM ellipsometer	16-18 rue du Canal 91165 Longjumeau Cedex (France) http://www.jobinyvon.com
<u>Spectra-Physics GmbH</u>	Ar-ion laser (pump), Ti:sapphir (710...1000 nm), Dye-laser (570...630 nm).	Guerickeweg 7 D-64291 Darmstadt (Germany) http://www.spectraphysics.com
<u>Coherent GmbH</u>	Ar-laser	Dieselstraße 5 b D-64807 Dieburg (Germany) http://www.coherent.de/
<u>LaserMax</u>	Diod-laser (1542 nm)	3495 Winton Place, Bldg. B Rochester, NY 14623 http://www.lasermx-inc.com
<u>Laser 2000 GmbH</u>	Diod-laser (1318 nm)	Argelsrieder Feld 14 D-82234 Wessling (Germany) http://www.laser2000.de
<u>Roithner Lasertechnik</u>	Diod-laser (1062 nm)	Schoenbrunner Strasse 7 A-1040 Vienna (Austria) http://www.roithner-laser.com

• Materials

<u>Goodfellow GmbH</u>	Ti powder, Ta-wire (annealed)	Postfach 1343 Bad Nauheim D-61213 (Germany) http://www.goodfellow.com
<u>AlfaChemicals</u>	K, KCl, Ga, Bi	A. Johnson Matthey Company Postfach 110765 D-76057 Karlsruhe (Germany) http://www.alfa.com
<u>Linios GmbH & CO.KG</u>	sapphire prism	LINOS Photonics GmbH & Co. KG Königsallee 23 D-37081 Göttingen (Germany) http://www.linios.de

• Thin Film Software

<u>FilmWizard</u>	http://www.sci-soft.com
<u>PsiDelta2</u>	http://www.jobinyvon.com



References

- [Achener68] P.Achener et al., *Thermophysical and Heat Transfer Properties of Alkali Metals* (Report No. AGN-8195 Vol. 1, Nuclear Division Aerojet-General Corporation, San Remo, 1968)
- [Ashcroft76] N.W.Ashcroft and N.D.Mermin, *Solid State Physic*, Saunders College, 1976
- [Aspnes75a] D.E.Aspnes and A.A.Studna, *High Precision Scanning Ellipsometer*, Appl. Opt. **14**(1) (1975) 220-228
- [Aspnes75b] D.E.Aspnes, *Precision Bounds to Ellipsometer System*, Appl. Opt. **14**(5) (1975) 1131-1136
- [Ayyad02] A.Ayyad, *Wetting, Prewetting and Surface Freezing Transitions in Fluid Ga-Bi and Ga-Pb Alloys: A Surface Light Scattering Study*, Dissertation, Karlsruhe (2002)
- [Azzam77] R.M.A.Azzam and N.M.Bashara, *Ellipsometry and Polarized Light*, NHPL (1977)
- [Bischof96] J.Bischof et al., *Dewetting Modes of Thin Metallic Films: Nucleation of Holes and Spinodal Dewetting*, Phys. Rev. Lett., **77**(8) (1996) 1536
- [Blanckenhagen97] B.von Blanckenhagen, *Spektroellipsometrie- und optische Absorptionmessungen zur Elektronenlokalisierung in $M_x(MX)_{1-x}$ -Schmelzen*, Dissertation, Karlsruhe (1997)
- [Blanckenhagen99] B.von Blanckenhagen et al., W.Freyland, *Systematic study of electron localization in salt-rich M_xMX_{1-x} melts by absorption spectroscopy*, J. Chem. Phys. **110** (1999) 2652
- [Bonn01] D.Bonn and D.Ross, *Wetting Transitions*, Rep. Prog. Phys. **64** (2001) 1085
- [Booth01] M.J.Booth and A.D.J.Haymet, *Molten salts near a charged surface: integral equation approximation for a model of KCl*, Mol. Phys. **99**(21) (2001) 1817
- [Borgstedt87] H.U.Borgstedt and I.Mathews, *Applied Chemistry of the alkali Metals*, Plenum Press, New York (1987)
- [Born91] M.Born and E.Wolf, *Principles of Optics*, Pergamon Press, (1991)
- [Bredig64] M.A.Bredig, *Mixtures of metals with molten salts*, in Molten Salt Chemistry, M.Blander (Editor) (1964)
- [Burton96] B. Burton et al., *Thermodynamic models and data for pure elements and other endmembers of solutions. Group 5: estimation of enthalpies and entropies of transition. CALPHAD: Computer Coupling of Phase Diagrams and Thermochemistry* (1996), Volume Date 1995, 19(4), 537-53

-
- [Cahn77] J.W.Cahn, *Critical Point Wetting*, J. Chem. Phys., **66** (1997) 3667
- [Chatain96] D.Chatain and P.Winblatt, *Experimental evidence for a wetting transition in liquid Ga-Pb alloys*, Surf. Sci. **345** (1996) 85
- [Collins90] R.W.Collins, *Automatic Rotating Element Ellipsometers: Calibration, Operation and Real-Time Applications*, Rev. Sci. Instrum., **61**(8) (1990) 2029-2062
- [Cusack59] N. E.Cusack and J. E.Enderby, *Resistivity of liquid alkali and noble metals*, Proceedings of the Physical Society, London **75** (1960) 395-401
- [Damman03] P.Damman et al., *Dewetting near the Glass Transition: Transition from Capillary Force Dominated to Dissipation Dominated Regime*, Phys. Rev. Lett., **91**(21) (2003) 216101-1
- [Dash89] J.G.Dash, *Surface melting*, Contemp. Phys. **30**(2) (1989) 89
- [deGennes81] P.G. de Gennes, *Some effects of long range forces on interfacial phenomena*, J. Physique Lettre **16** (1981) 377
- [deGennes85] P.G. de Gennes, *Wetting: Statistics and Thermodynamics*, Rev. Mod. Phys. **57** (1985) 827
- [Dogel03] S.Dogel, D.Nattland, W.Freyland, *Wetting transitions in fluid K_xKCl_{1-x} revisited*. Z. für Phys. Chem. (München, Germany) **217**(7) (2003) 879
- [Drevillon82] B.Drevillon, et al., *Fast Polarization Modulated Ellipsometer Using a Microprocessor System for Digital Fourier Analysis*, Rev. Sci. Instrum., **53**(7) (1982) 969-977
- [Dietrich88] S.Dietrich, *Wetting Phenomena*, in *Phase Transitions and Critical Phenomena*, C.Domb, J.L.Lebowitz (Editor), Academic Press, London 1986
- [Dietrich97] S.Dietrich, M.Schick, *Wetting at Solid-Liquid-Vapour-Tetra Point*, Surf. Science **382** (1997) 178
- [Ebner77] C.Ebner, W.F.Saam, *New Phase-Transitions in Thin Argon Films*, Phys. Rev. Lett. **38** (1977) 1486
- [Flom93] E.B.Flom et al., *In-plane structure of the liquid-vapor interface of an alloy: a grazing incidence x-ray diffraction study of bismuth: gallium*, Science **206** (1993) 332
- [Freyland84] W.Freyland et al., *Colour Centres and Clustering in Liquid Alkali Metal-Alkali Halide Solutions Approaching the Non-Metal-Metal Transition: An Optical Study*, J. Chem. Phys. **88** (1984) 3745
- [Freyland98] W.Freyland, D.Nattland, *Interfacial wetting transitions in ionic and metallic fluid mixtures*, Ber. d. Buns. Ges. Phys. Chem. **102** (1998) 1

-
- [Freyland99] W.Freyland, *Wetting transitions in fluid metallic mixtures*, Journal of Non-Crystalline Solids 250-252(Pt. 1) (1999) 199-204.
- [Freyland03] W.Freyland, et al., *Wetting, Prewetting and Surface Freezing Transitions in Fluid Ga-Based Alloys: A Surface Light Scattering Study*, J. Phys. Cond. Matt. **15**(1) (2003) S151
- [Grosse79] P.Grosse, *Freie Elektronen in Festkörpern*, Springer Verlag (1979)
- [Guenter90] R.D.Guenter, *Modern Optics*, WILEY, (1990)
- [Hafner92] J.Hafner and W.Jank, *Structural and electronic properties of the polyvalent elements*, Phys. Rev. B **45**(6) (1992) 2739
- [Hauge80] P.S.Hauge, *Recent Development in Instrumentation in Ellipsometry*, Surf. Sci. **96** (1980) 108
- [Hauge83] E.H.Hauge and M.Schick, *Continuous and First-order Wetting Transitions from the van der Waals Theory of Fluids*, Phys. Rev. **B 27** (9183) 4288
- [Herminghaus99] S.Herminghaus and K.Jacobs, *Strukturbildung in dünnen Filmen*, Phys. Blätter **55**(12) (1999) 35
- [Heyes81] D.M.Heyes and J.H.R.Clarke, *Computer simulation of molten salt interphases. Effect of a rigid boundary and an applied electric field.* J. of the Chem. Soc., Faraday Trans 2: Mol. and Chem. Phys. **77**(7) (1981) 1089
- [HCP76] *Handbook of Chemistry and Physics*, 57th Edition 1976-1977, **Press**, p. E-229
- [Huber02] P.Huber et al., *Tetra Point Wetting at the Free Surface of Liquid Ga-Bi*, Phys. Rev. Lett. **89** (2002) 035502
- [Huber03] P.Huber et al., *Short-range wetting at liquid gallium-bismuth alloy surfaces: X-ray measurements and square-gradient theory*, Phys. Rev. B **68** (2003) 085409
- [Hunderi75] O.Hunderi, *Optical properties of crystalline and amorphous bismuth films*, J. Phys. F: Metal Phys., **5** (1975) 2214-2225, (dielectric function of solid crystalline thick Bi film was obtained in the private communication)
- [Indlekofer87] G.Indlekofer et al., *New Preparation method for Liquid Alloy Surfaces and Their Characterization by electron Spectroscopy*, Mat Res. Soc. Symp. Proc., **83** (1987) 75-82
- [Israelachvili92] J.Israelachvili, *Intermolecular and surface forces*, Academic London (1992)
- [JANAF85] *JANAF Thermochemical Tables*, Third Edition, Part I and II, J. Phys. Chem. Ref. Data, Vol. 14, Suppl. 1, 1985

-
- [Jasperson69] S.N.Jasperson and Schnatterly, *An Improved Method for High Reflectivity Ellipsometry Based on a New Polarization Modulation Technique*, Rev. Sci. Instrum., **40**(6) (1969) 761-767
- [Jellison91] G.E.Jellison, *Use of based estimator in the interpretation of spectroscopic ellipsometry data*, Appl. Opt., **30**(23) (1991) 40
- [Jeppesen58] M.A.Jeppesen, *Some Optical, Thermo-Optical and Piezo-Optical Properties of Synthetic Sapphire*, J. Opt. Soc. Am. **48** (1958) 629
- [Johnson58] J.W.Johnson and M.A.Bredig, *Miscibility of metals with salts in the molten state III. The potassium-potassium halide systems*, J. Phys. Chem., **62** (1958) 604
- [Juchem90] R.Juhem et al., *Interfacial segregation and the wetting transition in fluid metal-salt systems*, Journal of Physics: Condensed Matter 2(Suppl. A) (1990) SA427-SA431.
- [Kattner97] U. R.Kattner, *The Thermodynamic Modelling of Multicomponent Phase Equilibria*, JOM, **49** (12) (1997) 14
- [Kayser86a] R.F.Kayser, et al., *What Controls the Thickness of Wetting Layers*, J. Chem. Soc. Faraday Trans. 2, **82** (1986) 1701
- [Kayser86b] R. F.Kayser, *Effect of surface ionization on wetting layers*, Phys. Rev. Lett. **56**(17) (1986) 1831
- [Kellay93] H.Kellay et al., *Prewetting in a binary liquid mixture*, Phys. Rev. Lett. **71** (1993) 2607
- [Khairulin02] R.A.Khairulin et al., J. Non-Cryst. Solids 297 (2002) 120.
- [Koslowski97] T.Koslowski, *The electronic structure of metal-molten salt solutions: a tight-binding approach*, J. Phys. Chem. **106** (1997) 7241
- [Krausch97] G.Krausch, *Dewetting at the interface between two immiscible polymers*, J. Phys.: Cond. Matter, **9** (1997) 7741
- [Langmuir38] I.Langmuir, *Repulsive forces between charged surfaces in water, and the cause of the Jones-Ray effect*, Science **88** (1938) 430; J. Chem. Phys. **6** (1938) 873
- [Lei96] N.Lei et al., *In-plane structure of the liquid-vapor interfaces of dilute bismuth-gallium alloys: X-ray-scattering studies*, J. Chem. Phys. **105** (1996) 4802; J. Chem. Phys. **104** (1996) 9615;
- [Löwen94] H.Löwen, *Melting, freezing and colloidal suspensions*, Phys. Rep. **237** (1994) 249
- [Lüty60] F.Lüty, *Höhere Anregungen von Festkörpern*, Z. Physik **160** (1960) 1

-
- [Maeda00] N.Maeda and V.V.Yaminsky, *Surface Supercooling and Stability of n-Alkane Films*, Phys. Rev. Lett. **84** (2000) 698
- [Mallitson62] I.H.Mallitson, *Refraction and Dispersion of Synthetic Sapphire*, J. opt. Soc. Am. **52** (1962) 1377
- [McCrackin63] F.McCrackin et al., *Measurements of the Thickness and Refractive Index of Very Thin Films and the Optical Properties of Surfaces by Ellipsometry*, J. of Research of the National Bureau of Standards-A. Physics and Chemistry, **67A**(4), 363-377 (1963)
- [Metsch84] G.Metsch, *Reflexionsmessungen an Alkalimetall-Suboxiden*, Dissertation, Stuttgart (1984)
- [Miller85] C.Miller and P.Neogi, *Equilibrium and Dynamic Effects in Interfacial Phenomena*, Ed.: M.Schick and F.Fowkes Surfactant science series; v. 17 New York
- [Moldover80] M.Moldover and J.Cahn, , Science **207** (1980) 1073
- [Nattland86] D.Nattland et al., *Metal-nonmetal transition in liquid alkali metal-alkali halide melts: electrical conductivity and optical reflectivity study*, Z. für Phys. Chemie (München) **149**(1), (1986) 1-15
- [Nattland88a] D.Nattland and W. Freyland, *Macroscopic Adsorption and Wetting Transition at the Solid-Fluid Interface of K_xKCl_{1-x} Solution*, Phys. Rev. Lett. **60** (1988) 1142
- [Nattland88b] D.Nattland, *Ellipsometrische Untersuchungen der optischen Konstanten des fluiden K_xKCl_{1-x}* , Dissertation, Marburg (1988)
- [Nattland93] D.Nattland et al., *Electron localization in metal-molten salt solutions: An optical study with in-situ variation of composition*, J. Chem. Phys. **98** (1993) 4429
- [Nattland95] D.Nattland et al., *Interfacial wetting in a liquid binary alloy*, J. Phys.: Condens. Matter **7** (1995) L457-462.
- [Nattland96] D.Nattland et al., *Wetting phenomena at the liquid-vapor interface of gallium-bismuth alloys studied by spectroscopic ellipsometry*, J. of Non-Cryst. Solids **205-207**(Pt. 2) (1996) 772
- [Nattland98] D.Nattland et al., *Interfacial properties of liquid alloys. An experimental study on Ga-Bi and Ga-Ge*, Ber. der Bunsen-Ges. **102**(9) (1998) 1151
- [Nepomnyashchy02] A.Nepomnyashchy et al., *Interfacial Phenomena and Convection*, Chapman&Hall/CRL Monographs and Surveys in Pure and Applied Mathematics 2002

-
- [Nicoloso83] N.Nicoloso and W.Freyland, *Electron spin resonance studies of electron localization in molten alkali metal-alkali halide solution*, J. Chem. Phys. **87** (1983) 1997
- [Nijs88] J.M.M.de Nijs and A.van Silfhout, *Systematic and random errors in rotating-analyser ellipsometry*, J. Opt. Soc. Am., **5**(6) (1988) 773-781
- [Noble94] A.Noble and M.Kasevich, *UHV optical window seal to conflat knife edge*, Rev.Sci. Instrum. **65**(9) (1994) 3042-3043
- [Palik85] E.D.Palik, *Handbook of Optical Constants of Solids*, **Academic Press** (1985)
- [Pandit82] R.Pandit et al., *Systematics of multilayer adsorption on attractive substrates*, Phys. Rev. B **26**(9) (1982) 5112
- [Pandit83] R.Pandit and M.E.Fisher, *Wetting Transitions near Bulk Triple Points*, Phys. Rev. Letters **51** (1983) 1772
- [Parrinello84] M.Parrinello and A.Rahman, *Study of an F-center in molten KCl*, J. Chem. Phys. **80**(2) (1984) 860
- [Perepezko82] J.H.Perepezko et al., in: G.E.Rindone (Ed.), *Material Processing in the Reduced Gravity Environment of Space*, **Elsevier** Publ. Inc., Amsterdam, (1982) 491
- [Pigeat98] P.Pigeat et al., *Calculation of thermal emissivity for thin film by a direct method*, Phys. Rev. B **57**(15) (1998) 9293
- [Pohl67] R.Pohl, *Optic und Atomphysik*, Springer Verlag, 12. Auflage (1967)
- [Pohl96] T.Pohl et al., *An ellipsometric study of the surface freezing of liquid alkanes*, Chem. Phys. Lett. **260** (1996) 82
- [Pluis90] B.Pluis et al., *Surface-induced melting and freezing. II. A semi-empirical Landau-type model*, Surface Science **239**(3) (1990) 282
- [Press86] W.Press et al., *Numerical Recipes: The Art of Scientific Computing*, Cambridge University Press (1986)
- [Predel60] B.Predel, Z. Phys. Chem. NF 24 (1960) 206; R. W. Ollinski, G. J. Abbaschian, in: T. B. Massalski, H. Okamoto, P. R. Subramanian, L. Kacprzak (Eds), *Binary Alloy Phase Diagrams*, ASM International, Ohio, 1990
- [Ragil96] K.Ragil et al., *Wetting of alkanes on water from a Cahn-type theory*, J. Chem. Phys., **105** (1996) 5160
- [Redon91] C.Redon et al., *Dinamics of dewetting*, Phys. Rev. Lett., **66**(6) (1991) 715

-
- [Rodriguez96] J.A.Rodriguez et al., *Interaction of Silver, Cesium, and Zinc with Alumina Surfaces: Thermal Desorption and Photoemission Studies*, J. Phys. Chem, 100 (1996) 18240
- [Rowlinson82] J.S.Rowlinson and B.Widom, *Molecular Theory of Capillarity*, Clarendon, Oxford 1982
- [Schick90] M.Schick in *Liquids at Interfaces*, Proc. Les Houches Summer School, Session XL VIII, J.Charvolin, J.F.Joanny, J.Zinn-Justin (Editor), North-Holland, Amsterdam 1990
- [Selloni87] A.Selloni et al., *Localization, Hopping and Diffusion of electrons in Molten Salts*, Phys. Rev. Lett. **59**(7) (1987) 823
- [Serre98] C.Serre et al., *Study of a wetting-related adsorption transition in the Ga-Pb system: 1. Surface energy measurements of Ga-rich liquids*, Surf. Sci. 415 (1998) 336
- [Staroske00] S.Staroske, *Spektroskopische Charakterisierung von Benetzungs- und Vorbenetzungsfilmen in Fluidem K-KCl*, Dissertation, Karlsruhe (2000)
- [Staroske01] S.Staroske et al., *Tetra-point wetting of liquid K-KCl mixtures: Spectroscopic characterization of mesoscopic wetting and prewetting films*, J. Chem. Phys. **115**(16) (2001) 7669
- [Steinberg74] D. J.Steinberg , *Simple relation between the temperature dependence of the density of liquid metals and their boiling temperatures*, Metallurgical Transactions **5**(6) (1974) pp. 1341-3.
- [Stagg93] B.J.Stagg and T.T.Charalampopoulos, *A method to account for window birefringence effects on ellipsometry analysis*, J. Phys. D.:Appl. Phys. **26** (1993) 2028-2035
- [Stobie75] R.Stobie et al., *Analysis of a Novel Ellipsometer Technique with Special Advantages for Infrared Spectroscopy*, J. Opt. Soc. Am. **65** (1975) 25
- [Sullivan86] D.E.Sullivan and M.M. Telo de Gama, *Wetting Transitions and Multilayer Adsorption at Fluid Interfaces* in C.A. Croxton
- [Swanson89] B.D.Swanson et al., *Layer-by-layer surface freezing of freely suspended liquid-crystal films*, Phys. Rev. Lett. **62** (1989) 909
- [Taborek92] P.Taborek and J.Rutledge, , Phys. Rev. Lett. 68 (1992) 2184
- [Takamichi93] I.Takamichi and R.Guthrie, *The physical properties of liquid metals*, Oxford (1993)
- [Tarazona83] P.Tarazona and R.Evans, *Wetting transitions at models of a solid-gas interface*, Molec. Phys., **48**(4) (1983) 799
- [Tostmann95] H.Tostmann, *Phasenübergänge an Grenzflächen fluider metallischer Systeme*

untersucht mit der Erzeugung der Zweiten Harmonischen, Dissertation, Karlsruhe (1995)

- [Tostmann96] H.Tostmann et al., *Wetting and Prewetting Transitions in Metallic Systems Studied by SHG*, J. Chem. Phys. **104** (1996) 8777
- [Tostmann97] H.Tostmann et al., *In-situ characterization of oxide films on liquid alkali metals using Second Harmonic Generation (SHG)*, Mater. Res. Soc. Symp. Proc. **451** (1997) 579
- [Tostmann00] H.Tostmann et al., *Microscopic Structure of the Wetting Film at the Surface of Liquid Ga-Bi Alloys*, Phys. Rev. Lett. **84** (2000) 4385
- [Tsekov03] R.Tsekov and W.Freyland, *Model calculations of surface phase transitions in Ga-Bi alloys: adsorption, wetting, surface freezing and melting*, J. Phys.: Condens. Matter **15** (2003) 6155
- [Turcanin02] A.Turchanin et al., *Surface freezing in liquid Ga-Bi alloys: optical second harmonic and plasma generation study*. Phys. Chem. Chem. Phys **4**(4) (2002) 647-654
- [Turcanin04] A.Turchanin et al., submitted CPL 2003.
- [Vani83] V.Vani et al., *Coexistence curve and critical point wetting in a binary liquid mixture cyclohexan+acetonitrile*, Phys. Rev. Lett., **99A** (1983) 441
- [Warren84] W.Warren et al., *Localization of Electrons in Ionic Liquids: NMR in Cs-CsI and CsI-I Solutions*, Phys. Rev. **B 30**(1) (1984) 65
- [Widom78] B.Widom, *Structure of the α interface*, J. Chem. Phys., **68** (1978) 3878
- [Winblatt98] P.Winblatt and D.Chatain, *Wetting and prewetting transitions in Ga-Pb alloys*, Ber. Bunsenges. Phys, Chem. **102** (1998) 1142
- [Yang99] B.Yang et al., *Structure of the liquid-vapor interface of a dilute alloy of Pb in Ga*, Phys. Rev. **B 62** (2000) 13111

Acknowledgments

In the end I would like to thank all who made it possible for me to accomplish this work:

- Prof. Dr. W. Freyland for giving me the opportunity to work in his research group at the University Karlsruhe (TH) and very interesting and challenging goal-settings,
- Prof. Dr. M. Kappes who was a co-referee of this work,
- Dr. Priv.-Doz. Detlef Nattland who introduced the ellipsometric technique to me and always helped with many practical advises on all stages of this work,
- Dr. S. Staroske who helped me a lot at the beginning, particularly for all tricks of the lasers alignment,
- to all people of mechanical workshop of the University who built the setup for Ga-Bi measurements and were very patient to all my technical ideas and heaps of sophisticated drawings. To H. Ernesti for valuable advises during the design of setup and correction of mechanical flaws and very accurate practical realization of his ideas,
- the people of electrical workshop for help with any “current” problems,
- J. Szepessy for professional help with any “soft- and hardware” troubles,
- G. Ritter for help with the preparation of high purity KCl and numerous orders of every sort and kind - from laser and sapphire to wire and gloves,
- Jens Dubielzig für zahlreiche Ausflüge sowohl mit seinem neuem als auch mit dem alten Auto in den Schwarzwald, nach Strasbourg, zur Tour de France Berg-Etappe etc.,
- the friendly and supportive atmosphere inherent to the whole PC I contributed essentially to the final outcome of my studies.

But above all, I am indebted to my wife, Jana, without hers constant support this thesis would not have been written.



Curriculum Vitae



Personal data

Name: Dogel Stanislav A.
Data and place of birth: 27th April 1976 Bryansk, Russia
Marital status: married, no children

Secondary education:

1983-1990 Secondary school
1990-1993 Specialized college with profound study of Physics and Math, Russia.

Tertiary education:

1993-1994 *University of Road Machinery Construction, Department of Machinery and Precision Tools, Bryansk, Russia*

1994-2000 *Moscow State Steel and Alloys University, Dep. of Phys. Chem.*
Speciality: "Physical chemical methods of investigation of processes and materials".

Feb. 2000 Diploma of Physical Chemistry
Title: "*Experimental determination of formation enthalpies of Zr-Cu-Al amorphous alloys*".

Ph.D. project

Jun. 2000 – University Karlsruhe (TH), Department of Condensed Matter,
Feb. 2004 Prof. Dr. W. Freyland, Germany
Title: "*Spectroscopic Ellipsometry of Interfacial Phase Transitions in Fluid Metallic Systems: K_xKCl_{1-x} and $Ga_{1-x}Bi_x$* ".

List of publications

Referred papers

- Turchanin, A. A.; Dogel, S. A.; Tomilin, I. A.; Inoue, A. ***Experimental investigation of the formation enthalpies of the Zr-Cu-Al amorphous alloys.*** Materials Science Forum (1999), 312-314(Metastable, Mechanically Alloyed and Nanocrystalline Materials), 653-658.
- Tomilin, I. A.; Turchanin, A. A.; Dogel, S. A.; Latuch, J.; Kulik, T. ***Experimental determination of the formation enthalpies of Al-Y and Al-Y-Ni amorphous alloys.*** Materials Science Forum (2000), 343-346(Pt. 1, Metastable, Mechanically Alloyed and Nanocrystalline Materials, Part 1), 37-42.
- Tomilin, I. A.; Dogel, S. A.; Latuch, J.; Kulik, T. ***The formation enthalpies of rapidly quenched amorphous alloys in the Al-Y-Ni system.*** Materials Science Forum (2001), 360-362 (Metastable, Mechanically Alloyed and Nanocrystalline Materials), 143-148.
- Dogel, Stanislav; Freyland, Werner; Hippler, Horst; Nattland, Detlef; Nese, Chandrasekhar; Unterreiner, Andreas-N. ***Ultrafast dynamics of excess electrons in a molten salt: Femtosecond investigation of K-KCl melts.*** Physical Chemistry Chemical Physics (2003), 5(14), 2934-2937
- Dogel, S.; Nattland, D.; Freyland, W. ***Wetting transitions in fluid K_xKCl_{1-x} revisited.*** Zeitschrift fuer Physikalische Chemie (München, Germany) (2003), 217(7), 879-892.
- Unterreiner, Andreas N.; Brands, Helge; Dogel, Stanislav; Freyland, Werner; Hippler, Horst; Lindner, Joerg; Nattland, Detlef; Nese, Chandrasekhar; Voehringer, Peter. ***Localized electrons in polar liquids and molten alkali metal-alkali halides: A femtosecond study.*** Abstracts of Papers, 226th ACS National Meeting, New York, NY, United States, September 7-11, 2003 (2003), PHYS-176.

Articles in preparation

- Dogel, S.; Nattland, D.; Freyland, W., ***Complete wetting transition at the fluid-vapour interface of Ga-Bi studied by spectroscopic ellipsometry,*** Thin Solid Films 2004 (accepted)
- Dogel, S.; Nattland, D.; Freyland, W., ***Optical properties of pure liquid Ga and Bi measured by spectroscopic ellipsometry between 0.8 and 4.6 eV.*** (in preparation)